UNIVERSITY OF STRATHCLYDE
Department of Physics

Colloidal quantum dot and hybrid lasers

by

Luke Jonathan McLellan

A thesis presented in fulfilment of the
requirements for the degree of
Doctor of Philosophy

January 2018

Declaration of Authorship

This thesis is the result of the author's original research. It has been composed by the author and has not been previously submitted for examination which has led to the award of a degree.

Signed: _____

Date: _____

Frontispiece

Off resonance fan-shape ASE emission from CQDs emitting at 630nm of CHDV DFB cavity.

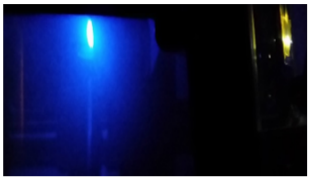

Super Yellow DFB laser submersed in deionised water demonstrating fan-shaped emission.

CQD/DFB laser with fan-shaped emission.

Alloyed-core/shell CdS_xSe_{1-x}/ZnS in toluene. Intrinsic PL 540nm, 575nm and 630nm.

Abstract

This thesis presents research on solution-processed semiconductor lasers, with an emphasis on colloidal quantum dot (CQD) lasers, aimed at progressing the state of the art of the technology. A particular focus is placed on demonstrating such lasers under long (>nanosecond) pulse pumping in order to bring this device technology closer to applications.

Alloyed-core CdSSe CQDs with a ZnS outer shell that emit in the visible are studied. These were prepared in a solid-state thin-film overcoated with a polymeric cladding (polyvinyl alcohol or PVA) to demonstrate a distributed feedback (DFB) laser having a bilayer waveguide structure. It is shown that the PVA symmetrises the laser structure and reduces the modal losses, in turn enabling the lowest threshold operation in the nanosecond regime for CQD lasers at the time; 13.5 $\mu J/cm^2$ at 5 ns. The format is also beneficial for the photostability of the laser.

The CQDs are also demonstrated as the gain material of a robust, orange-emitting Vertical-Cavity Surface-Emitting Laser (VCSEL). Oscillation threshold comprised between 1 and 20 mJ/cm^2 for 5ns pump pulse duration are obtained. For a broad area excitation (250 μm at $1/e^2$ radius), the operation is highly multimode and characterised by spatio-temporal instabilities. When pumped with a spot size at or below $100\mu m$ in radius, the VCSEL is observed to be single mode for low pump energies while additional longitudinal modes, as well as transverse mode, appear as the pumping level is increased. A study of the polarisation of the CQD laser emission for different polarisation of the pump was carried out and the Stokes parameters calculated. Results show that the pump polarisation has no significant effect on the VCSEL polarisation.

While the bulk of the research concerns CQDs, two types of organic semiconductors were also applied to the aforementioned DFB laser structure. Poly(paraphenylenevinylene) (PPV) copolymer Super Yellow leading to what is to the best of our knowledge, the only case of completely ambient lasing using Super Yellow. Refractive index sensing with the laser was attempted and results are summarised. The second type in fact consisted of two organic semiconductor materials from the

same novel family of autofluorescence molecules respectively named Blue 4 and Blue 6. These are investigated for the first time as laser materials. Both materials show signs of random lasing when prepared in a solid-state film. Single mode lasing in distributed feedback format is also demonstrated with Blue 4.

Acknowledgements

I would like to begin by thanking Professor Martin Dawson for granting me the opportunity to work as part of the Institute of Photonics. I would like to express a great amount of appreciation to my supervisor Dr Nicolas Laurand who, along with much patience for my ideas and ramblings, also offered support and guidance throughout my studies. I believe that without him I would not have been able to complete this Ph. D. In addition I would also like to show thanks to Dr Benoit Guilhabert for his advice and guidance throughout my studies.

I would like to express my gratitude to all the colleagues and, more importantly, friends I have made at the institute creating great memories and experiences. I would like to thank Sharon Kelly for all of her administration help as well as the help received on the general running of the group. Finally I would like to thank my family for providing me support and understanding not only throughout my studies but also day to day life. To my parents, Lydia and William McLellan, thank you. My mum for always pushing to get the support I needed and my dad for creating the interest in physics. If it was not for them pushing me, to not only better myself academically but as a person, I would not be where I am today.

I would also like to take this opportunity to thank former supervisors from my undergraduate and masters studies at the University of Glasgow, in particularly Professor Martin Hendry, Dr Nicolas Labrosse and Dr Harry Ward. I would also like to extend thanks to Ms Shona Robertson from the University of Glasgow's disability service and to my secondary school physics teacher Mr McKay.

Contents

List of Figures

List of Tables

Abbreviations

IOP	**I**nstitute **o**f **P**hotonics
AFM	**A**tomic **F**orce **M**icroscopy
ASE	**A**mplified **S**pontaneous **E**mission
CQD	**C**olloidal **Q**uantum **D**ot
CW	**C**ontinuous **W**ave
DBR	**D**istributed **B**ragg **R**eflector
DFB	**D**istributed **F**eedback
FSR	**F**ree **S**pectral **R**ange
FWHM	**F**ull **W**idth **H**alf **M**aximum
HOMO	**H**ighest **O**ccupied **M**olecular **O**rbit
LED	**L**ight **E**mitting **D**iode
LCP	**L**eft **C**ircularly **P**olarised
LUMO	**L**owest **U**noccupied **M**olecular **O**rbit
NC	**N**ano **C**rystal
NOA	**N**orland **O**ptical **A**dhesive
OLED	**O**rganic **L**ight **E**mitting **D**iode
OS	**O**rganic **S**emiconductor
PAG	**P**hoto **A**cid **G**enerator
PL	**P**hotoluminescence
PLQY	**P**hotoluminescence **Q**uantum **Y**ield
PVA	**P**oly (**v**inyl **a**lcohol)
RCP	**R**ight **C**ircularly **P**olarised
RoC	**R**adius **o**f **C**urvature

RL	**R**andom **L**aser
SoG	**S**pin **o**n **G**lass
TIR	**T**otal **I**nternal **R**eflecion
TE	**T**ransverse **E**lectric
TM	**T**ransverse **M**agnetic
UV	**U**ltraviolet
VCSEL	**V**ertical-**C**avity **S**urface-**E**mitting **L**aser
VSL	**V**ariable **S**tripe-**L**ength
WGM	**W**hispering **G**allery **M**ode
YAG	**Y**ttrium **A**luminium **G**arnet

To my family.

Part I

Introduction

Chapter 1

Introduction

This chapter introduces the background and motivations for the thesis research and presents the basic physics principles and properties of the materials and devices studied. Specifically, it covers fundamentals of lasers and gives information on solution-processed photonic materials (colloidal quantum dots and organic semiconductors) for application in lasers.

1.1 An introduction to lasers

Lasers are relatively common in today's world and can be found in a wide variety of devices, from household appliances to industrial machinery. Laser is an acronym, which stands for Light Amplification by Stimulated Emission of Radiation. The term was coined by Gordon Gould in 1957 based on the main physical process exploited in the generation of coherent light.

Laser action, or more precisely oscillation, was first demonstrated in 1960 by Theodore Maiman at Hughes Research Laboratories in a pulsed ruby laser pumped by flashlamps [1]. Maimans research followed on from the theoretical work of Charles Hard Townes and Arthur Leonard Schawlow that showed that masers (MASER= microwave amplification by stimulated amplification of radiation, a concept first demonstrated by Townes group at Columbia University in 1954) could be made to operate in the optical and infrared regions. In the same year the first gas laser (helium-neon laser [2]) was shown. The first laser diode, based on

the semiconductor gallium arsenide, was demonstrated in 1962. Over the years, and to this day, the development and applications of lasers have flourished.

Lasers differ from other light sources in that they emit coherently (typically combining spatial and temporal coherence). Spatial coherence enables directionality, allowing laser light to be focused to very small spots or be collimated for propagation over long distances with little divergence. Temporal coherence is what gives the laser light a narrow optical bandwidth, i.e. its pure colour/emission wavelength. Lasers can operate in continuous wave (CW), where they emit constantly, or can be pulsed with common pulse duration from microseconds down to a few attoseconds, although even shorter pulses have now been demonstrated. The properties of lasers have opened a wide range of applications. Everyday examples include disk drive, laser printers and barcode readers. They are also utilised in optical communications, medical tools for surgery, sensing, dermatology, heavy manufacturing, defence, and even in law enforcement apparatus.

While the basic physics principle stays the same, there are many types of lasers that differ in their mode of operation, implementation, emission wavelengths, output powers, the materials they are made of, and formats. New laser technologies are constantly emerging and solution-processed light-emitting semiconductors have recently attracted particular interest partly because of their compatibility with a vast range of materials and with soft material fabrication techniques. This in turn is paving the way to potential low cost fabrication of lasers in both existing and totally novel formats. For example these materials could enable mechanically-flexible laser devices, bringing the functionalities of lasers to applications in wearable technology. We note that photonics on mechanically-flexible substrates (so called flexible photonics) has already existing applications in bendable displays, electronic paper and solar cells. Flexible photonics is a sub-category of plastic electronics, a field that is predicted to be several billion pound worth by 2026 (http://www.idtechex.com/research/reports/oled-display-forecasts-2016-2026-the-rise-of-plastic-and-flexible-displays-000477.asp).

There are two main categories of solution-processed laser materials: (i) inorganic colloidal nanocrystals (including quantum dots) and (ii) organic semiconductors. This thesis studies lasers made from these materials with an emphasis on colloidal quantum dots. These are promising laser materials whose properties can be tailored by design of the shape, size and composition while retaining their solution processability.

1.2 Motivation and thesis outline

Colloidal quantum dots (CQDs) are minuscule inorganic crystals typically having a diameter less than 10 nm (i.e. they are nanocrystals). They have properties of narrow and tunable (size, shape and composition dependent) emission with the added benefit of being solution processable. This allows them to be compatible with a wide range of materials (to be deposited upon or even blended with) such as polymers while they can provide emission across the entire visible spectrum and up to the infrared by variation of their composition and size. CQDs also offer an improvement in luminescent operational lifetimes, retaining customisable designs and solution processability. Because of attractive properties, CQDs are utilised in a multitude of areas including in fluorescence (in-vivo and in-vitro) imaging techniques [3–9], photovoltaic cells [10, 11], photodetectors [12], in nuclear magnetic resonance spectroscopy [13, 14]. They have even seen commercial success as colour enhancers in LED-based LCD screens (for example quantum dot LEDs in the Samsung 4K TV) [15].

CQDs, because of the quantum confinement effect, have an energy spectrum approaching that of an atom. The electronic density of states of charge carriers is therefore increased compared to a bulk semiconductor, meaning that carriers are concentrated in a narrow energy range. In turn, optical gain in principle increases (less carriers are wasted to photons at other energies) and its temperature dependence diminishes, both important characteristics for laser performance. The most mature material technology for visible lasers is based on chalcogenide CQDs (composition using Cd, Se, S, Zn, S and Te). InP has also been investigated for lasers but performance is not yet as advanced.

Despite undeniable progress, CQD lasers are not yet a mature technology and performance is still limited. The purpose of this Ph. D. was to contribute to pushing their development and performance in different formats, including VCSELs. In particular, at the start of this work most of the report of CQD lasers made use of ultrafast optical pumping (pump pulses in the fs regime) meaning that the devices were far from being practical because they required bulky, expensive pump lasers. Our motivations were to demonstrate low threshold laser operation for longer pulse duration (nanosecond and above) so that pumping with more compact pump lasers can be considered.

The thesis comprises a total of six chapters separated into three main parts. Part I is an introductory section containing chapters 1 and 2. Part II is the results section containing chapters 3, 4 and 5. Finally part III contains chapter 6, which concludes this thesis and discusses outlooks. Chapter 1, in addition to this section, gives an introduction to lasers and their fundamentals. It also gives a description of the different materials utilised for lasers in this work and details the state of the art.

Chapter 2 discusses the principles of distributed feedback (DFB) lasers, of vertical-cavity surface-emitting lasers (VCSELs) and of so-called random lasers covering their fabrication and implementation. It also goes in depth about optical excitation and the characterisation methods used throughout the work in addition to illustrating the analytical models used in later chapters.

Chapter 3 is the first results chapter where CQD DFB lasers are reported on. The chapter gives a full description of the investigation into CQDs as a potential visible gain material, implementing them into an operational laser cavity and developing said cavity into an encapsulated device. Chapter 4 presents the experimental findings using the CQDs in an orange VCSEL. From the operation of this device a study on both the output polarisation, calculating the Stokes vectors, and pump dependencies is reported.

Chapter 5 expands on the scope of the materials introducing organic semiconductors with the primary aim to assess these gain materials for DFB laser-based refractive index sensing, which has potential applications for biosensing. Super Yellow, Blue 4 and Blue 6 are the materials employed in DFB format where the two latter materials demonstrate random lasing effects.

Chapter 6 concludes this thesis by giving a summary of the chapters of part two. It also conveys future work that will expand the application of these laser technologies.

1.3 How lasers work

Laser action is produced via the oscillation of light in a laser cavity that acts as an optical resonator. This consists in its most basic implementation of a pair of mirrors with the light circulating between them. Crucially the structure possesses

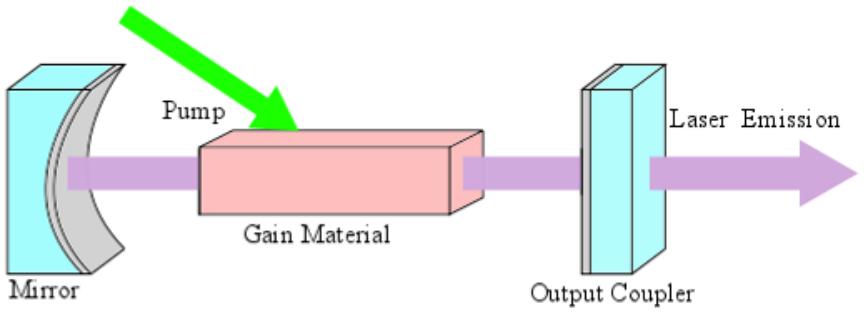

FIGURE 1.1: Schematic of basic Fabry-Pérot laser oscillator.

a gain material placed within the cavity, giving rise to the amplification of light through stimulated emission, figure 1.1. Omission of this material would result in the oscillating light becoming gradually weaker over each round trip (the distance travelled by a photon to return to its initial location, twice the cavity length) as it experiences losses at the mirrors upon reflection; and there would initially be no photons. When the gain material produces high enough gain, it compensates the overall cavity losses resulting in the amplification of the oscillating light. In order to achieve this an external excitation source must be applied. This is referred to as the pump source and often the laser is referred to as being pumped. Lasers are typically excited under optical or electrical pumping although other methods such as chemical pumping have been demonstrated. This is done either by the injection of light, from another laser, or through an applied electric current.

The pump energy needed to compensate the overall loss of the laser cavity is referred to as the laser threshold. Below this value non-coherent luminescence is emitted. When approaching threshold the power of the light within the cavity rapidly increases. The laser output versus the pump energy or power has a characteristic, dramatic increase in the slope when crossing threshold. Such transfer function of a laser is shown throughout this thesis to characterise devices. Due to this oscillation, the spectrum also narrows compared to the luminescence below threshold.

The laser emission itself escapes the cavity due to a partially transparent mirror (output coupler). In other resonators, there can be several output couplers or it can take another form than a mirror. This coupler can be optimised for optimum output power and slope efficiency of the laser, which is expanded upon in section 1.3.6.

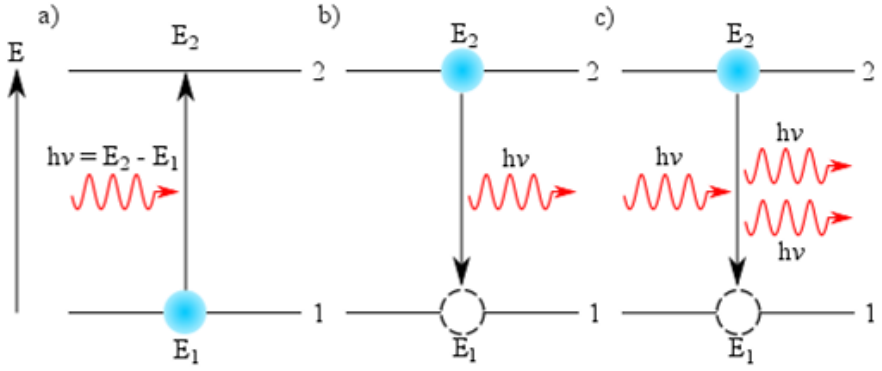

FIGURE 1.2: Energy level schematics of a) absorption on a photon exciting an electron to the higher energy level and creation of a hole b) spontaneous emission of a photon as electron recombines with hole and c) stimulated emission due to incident photon forcing recombination, duplicating the incident photon.

1.3.1 Absorption, spontaneous and stimulated emission.

In order to achieve laser operation, three fundamental light-matter processes must occur. These are absorption, stimulated emission and spontaneous emission, and are illustrated in figure 1.2 [16, 17]. To explain these a system composed of atoms or molecules is considered. The system has two possible energy levels, 1 and 2, each with their own energies, E_1 and E_2 respectively - for example these can be the energy levels occupied by the outermost electrons of the atoms constituting the system. E_1 is taken to be the ground energy level and E_2 as the excited energy level with their difference being,

$$h\nu = (E_2 - E_1). \tag{1.1}$$

In equation 1.1 h is the Planck's constant and ν the frequency corresponding to the transition between the energy levels.

At thermodynamic equilibrium when E_2-E_1 is greater than the thermal energy, the electrons are located in the ground state. If a photon, with an energy equal to that of $h\nu$, interacts with the system there is a probability that the photon will be absorbed. This results in the excitation of an electron into the E_2 energy level and the creation of a hole in the E_1 level - this is known as the absorption process.

With the electron having been excited into the E_2 state it will decay back down into the ground state. This is due to E_2 being unstable. The timescale of this phenomenon is known as the decay lifetime or the excited state. When the electron

relaxes back down to the ground state the recombination of electron and hole creates a photon of energy equal to $h\nu$. This process is called spontaneous emission where it can be described by applying the Einstein coefficient, A_{21}:

$$\left(\frac{dN_2}{dt}\right)_{21} = -A_{21}N_2, \tag{1.2}$$

$$A_{21} = \frac{1}{\tau_{sp}}. \tag{1.3}$$

Equation 1.2 describes the radiative transition between the upper, N_2, and lower level population, N_1, showing that the number of emitted photons at a given time is proportional to the population of the upper level and the Einstein coefficient. A_{21} is related to the radiative lifetime of the transition as expressed in equation 1.3. If spontaneous emission is the only occurring phenomena then the decay lifetime is equal to τ_{sp}. Unfortunately, the recombination process does not always result in the production of light. There can be non-radiative recombination processes taking place that contribute to the decay lifetime.

The third type of transition in this system is stimulated emission. Considering, again, an electron in the energy level E_2, an incoming photon of energy $h\nu$ can stimulate a downward emission transition (just as it does for the upward absorption transition), causing the electron and hole to recombine. The result is a coherent (stimulated) photon meaning that it has the same energy, phase and direction as the incident photon [16, 18–20]. This differs from spontaneous emission that has no definite phase nor direction. This is discussed further in section 1.3.3 when describing the absorption and emission cross sections. Stimulated emission is at the origin of optical gain, hence of laser oscillation.

1.3.2 Population inversion

In order to produce optical gain (the amplification of light), population inversion is required so that stimulated emission dominates over absorption. Consider the simplest case for laser transition of a two level non-degenerate system of energy levels E_1 and E_2 with the electrons populating the lowest available energy state, E_1, at thermal equilibrium. The electrons can be elevated into the higher energy level E_2 through absorption of a photon. At this point the populations of the two levels are equal ($N_1 = N_2$) and an incident photon has an equal probability to be

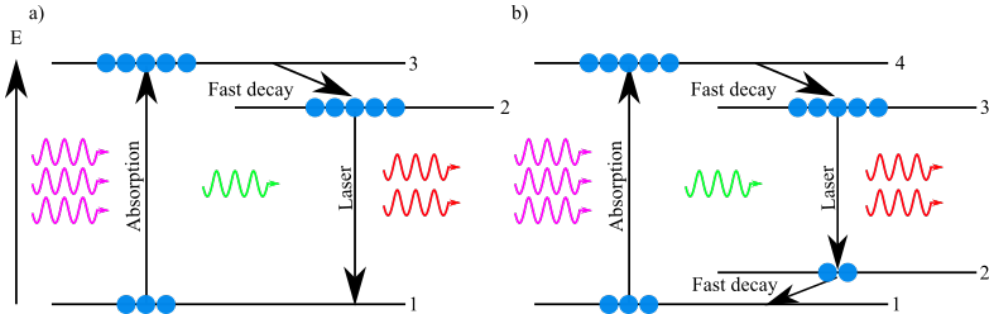

FIGURE 1.3: Schematic of population inversion in a a) three level energy system and b) four level energy system.

absorbed or to stimulate emission, which on average cancels out the contribution of both processes. Therefore, in a two level system, no significant quantity of electrons will further accumulate within the higher state and at best $N_1 = N_2$ otherwise $N_1 > N_2$. This means population inversion cannot be achieved.

In order to achieve population inversion, excitation to higher energy levels, through non-resonant pumping, is necessary to create the non-equilibrium conditions. More realistic models to understand this process are the three- and four-level systems, illustrated in figures 1.3a and 1.3b, and explained next.

Taking the three level system to start, when external excitation is applied to a gain material an electron is excited from the ground level, E_1, into the third energy level, E_3. In an effective gain material, the electron will immediately relax (de-excite/radiationless transition) from the E_3 level into the lower energy E_2 level. This allows population inversion to be acquired between E_2 and E_1.

For a four level energy system the electrons are directly excited from the ground level to the fourth energy level, E_4. Once this level is reached, the electrons relax down to the E_3 level. Here the population inversion is created between the E_3 and E_2 levels. The four-level system has the benefit that the population inversion is reached faster. It can be obtained at very low pump power/energy if the decay from level 2 to level 1 is really rapid. In principle, the four-level system yields a lower laser threshold when compared to the three level system because there is no absorption at the laser transition because of the fast de-excitation from E_2 to E_1 [16, 18–20]. The CQDs and organic semiconductors studied here can to a certain extent be considered as quasi-three level systems because there is some level of absorption (which depending on the Stokes shift of the materials can be relatively small thereby akin to a 4-level system) at the laser transition wavelength.

1.3.3 Absorption and emission cross section

In physics the term transitional cross section is used to describe the probability of particle-particle interactions. When discussing lasers this primarily refers to optically induced interactions such as the absorption and emission cross section. The values of the absorption and emission cross sections of the laser transition can be expressed as a function of the rate of absorption and stimulated emission. This behaviour dictates whether absorption or stimulated emission is activated for a population of the upper energy state and a particular photon flux. These cross sections are dependent on the specific transition experienced by the excited states, the photon wavelength and, material dependent, the photon polarisation.

Ref [18] describes the rate of absorption, R_{abs}, as

$$\left(\frac{dN_l}{dt}\right)_{abs} = -R_{abs}N_l, \tag{1.4}$$

$$R_{abs} = u_p\sigma_{abs}. \tag{1.5}$$

Here $\left(\frac{dN_l}{dt}\right)_{abs}$ is the transition rate due to absorption, σ_{abs} is the absorption cross section, u_p the photon flux and N_l the lower level population density. u_p is the number of photons per second per unit area and N_l refers to the number of states occupying the lower energy state per unit volume.

u_p can be expressed in terms of intensity (power per unit area), I, of the electromagnetic wave,

$$u_p = \frac{I}{h\nu}, \tag{1.6}$$

and the absorption cross section is described by [18],

$$\sigma_{abs} = \frac{2\pi^2}{3n\varepsilon_0 ch} \mid \mu \mid^2 \nu g(\nu), \tag{1.7}$$

where n is the gain material refractive index, ε_0 is the permittivity in free space, c the speed of light in a vacuum and g(ν) is a frequency dependent function describing the line profile of the transition.

The rate of stimulated emission, R_{em}, can be expressed in a similar manner to equation 1.4,

$$\left(\frac{dN_u}{dt}\right)_{em} = -R_{em}N_u, \tag{1.8}$$

$$R_{em} = u_p \sigma_{em}. \tag{1.9}$$

Here $\left(\frac{dN_u}{dt}\right)_{em}$ is the transition rate due to stimulated emission, σ_{em} is the stimulated emission cross section and N_u is the population density in the upper energy level (i.e. the excited state per unit volume). When in two non-degenerate energy levels, the rates of absorption and stimulated emission are equal for the transitions meaning that the absorption and emission cross sections are also equal. This is not the case for organic semiconductors (OS) nor CQDs as the absorption and emission peaks occur at different wavelengths. This translates to the absorption and emission cross sections as they are dependent on the wavelength [16, 18–20].

1.3.4 Rate equations

The dynamics of inter state light interaction within a gain material are modelled using rate equations. These are a series of differential equations that describe the evolution of the populations of electronic levels when optical excitation is applied. These equations are built from terms such as the absorption process, spontaneous/stimulated emission and energy transfers allowing for a numerical method to calculate the temporal evolution as well as approximating populations.

In order to explain this concept in more detail, a four level energy system will be considered, as in figure 1.3b. As seen in section 1.3.2, the population density, N_1 of the ground state, E_1 decreases as electrons are excited into the fourth energy level, E_4. This process is aided when the relaxation time from E_2 to E_1 is fast giving a larger N_1. Hence, the population density, N_2 is reduced by the relaxation process but is increased by either spontaneous or stimulated emission from the third energy level, E_3. The population density, N_3, in the E_3 level is reduced by spontaneous and stimulated emission where it is increased, similarly as E_1, by a fast relaxation process from E_4. The corresponding rated equations for the four level energy system are:

$$\frac{dN_1}{dt} = -u_p \sigma_{14} N_1 + R_{21} N_2, \tag{1.10}$$

$$\frac{dN_2}{dt} = \frac{N_3}{\tau_{sp}} + B_{32} S(N_3 - N_2) - R_{21} N_2, \tag{1.11}$$

$$\frac{dN_3}{dt} = R_{43} N_4 - \frac{N_3}{\tau_{sp}} - B_{32} S(N_3 - N_2), \tag{1.12}$$

$$\frac{dN_4}{dt} = u_p \sigma_{14} N_1 - R_{43} N_4. \tag{1.13}$$

Here the subscripts correspond to the relative energy level, u_p is the photon energy density at the excitation wavelength, σ_{ij} correspond to the absorption cross section for the $i^{th}j^{th}$ transition, R_{ij} is the rate of relaxation between the energy levels, τ_{sp} is the lifetime of the spontaneous emission in E_3, S is the photon density at the emission wavelength and B_{32} is the second Einstein coefficient for photon absorption and stimulated emission. This is equal to the absorption and emission cross sections at the emission wavelength of the laser transition. Note that the non-radiative relaxation processes have been ignored for the E_3 to E_2 transition.

S can also be related to the intensity as,

$$\frac{dS}{dt} = B_{32}(S+1)(N_3 - N_2) - \frac{S}{\tau_\phi}. \tag{1.14}$$

Here, τ_ϕ is the rate of photon loss and is dependent on the considered system (for example in the material of the cavity), and the "+1" takes into account spontaneous emission. In the next section, the case of a single optical wave or mode propagating in the gain material, in a single direction (1D problem), is considered. In this case, one can obtain an expression for the growth of the mode intensity as it propagates. Note that S is linked to the photon flux as,

$$u_p = v_g \frac{S}{h\nu}, \tag{1.15}$$

where v_g is the group velocity and,

$$I = h\nu u_p. \tag{1.16}$$

1.3.5 Amplified spontaneous emission

In a laser material that produces large gain the emission from the spontaneous emission can be amplified to higher power levels. Amplified spontaneous emission (ASE) was first observed in organic semiconductors by Hide *et al.* in MEH-PPV films comprising of TiO_2 nanoparticles [21]. ASE describes the phenomenon of the amplification of spontaneously emitted light by stimulated emission as it propagates through the gain material. This leads to spectral distortion and narrowing of the emission profile in comparison to the intrinsic photoluminescence (PL). This

is a consequence of the photons with energies close to the gain maximum that are favourably amplified resulting in them dominating the emission.

When determining ASE two equations have to be regarded [22, 23]. For ease of explanation a two level system will be considered, i.e. the transition between upper and lower levels (referred to as the transition between level 2 to 1). The probability of transition, W_{21} between these levels, during a period dt, is the sum of the contributions of spontaneous and stimulated emission. The Einstein coefficient, A_{21}, is introduced when considering the transition probability of spontaneous emission [18],

$$dW_{21} = A_{21}dt. \tag{1.17}$$

When stimulated emission is considered the transition probability of the electron, from E_2 to E_1, is,

$$dW_{21} = u_i B_{21}dt, \tag{1.18}$$

where B_{21} is the Einstein coefficient of stimulated emission and u_i is the photon energy density of the pump.

Equation 1.18 shows that stimulated emission is related to the photon energy density. Note this is not the case for spontaneous emission. When photon density is large enough, stimulated emission dominates spontaneous emission. As the spontaneously emitted photons travel through a medium where population inversion is present within the transition, section 1.3.2, they are amplified by the stimulated emission. This increases the photon density increasing the probability of stimulated emission. However, optical gain is a function of photon wavelength meaning that amplification will vary with different energies resulting in the spectrum around the gain peak undergoing the highest amount of amplification. This can lead to the spectral narrowing of the emission.

The narrowing phenomenon can be understood more broadly by considering the photon flux, u_p, propagating the gain material in the z-direction. As light propagates through the length of the material, dz, the change of flux, du_p, is the sum of the amplified component and the spontaneous emission in that direction. du_p indicates the difference between absorption and stimulated emission where it can be seen as,

$$du_p = \sigma_{em} u_p (N_2 - N_1)dz, \tag{1.19}$$

where u_p is the number of photons per unit area per unit time (photon flux). Equation 1.19 can then be expressed as a function of intensity, I, as,

$$dI = \sigma_{em} I(N_2 - N_1)dz, \tag{1.20}$$

or

$$\frac{dI(\lambda)}{dz} = g_{mat}(\lambda)I(\lambda). \tag{1.21}$$

Here g_{mat} is the material gain per unit length where equation 1.21 takes into account the transitions dependence to the wavelength.

The increase in light intensity due to spontaneous emission, coupled in the z-direction [18], can be expressed as,

$$\frac{dI(\lambda)}{dz} = \frac{A_{21}N_2hc}{\lambda}\frac{A}{4\pi L^2}. \tag{1.22}$$

L is the length of the gain material, A is the cross sectional area, and N_2 is the population density in the excited state.

When considering both the spontaneous and stimulated emission components, equations 1.21 and 1.22 are combined to give,

$$\frac{dI(\lambda)}{dz} = g_{mat}(\lambda)I(\lambda) + \frac{A_{21}N_2hc}{\lambda}\frac{A}{4\pi L^2}, \tag{1.23}$$

where the solution, to equation 1.23, is

$$I(\lambda, z) = \frac{A_{21}N_2hc}{\lambda g_{mat}(\lambda)}\frac{A}{4\pi L^2}(e^{g_{mat}(\lambda)z} - 1). \tag{1.24}$$

Equation 1.24 displays the intensity dependence of population inversion and the length z of the gain material. This results in more significant spectral narrowing occurring with longer lengths.

Chapter 2 will detail the experimental procedure to determine ASE (spectral narrowing of the emission spectra) in solution processed semiconductor films as it is a tell-tale sign of optical gain and a way to validate the use of a material as a laser material. These films are excited under optical pump where the observable intensity can be expressed by equation 1.24.

1.3.6 Gain and threshold

As mentioned previously, optical gain requires population inversion where laser operation can only be obtained using a laser oscillator, wherein the gain medium is enclosed within an optical cavity. At the operational threshold of the laser, the beam intensity is balanced precisely by the systems losses. For example, in a Fabry-Pérot cavity (section 2.6.1) these losses are due to the cavity mirrors, diffraction losses, as well as losses due to the active medium such as self-absorption and scattering. From this a minimum population inversion density is necessary to compensate for these systematic losses and from here on will be referred to as the threshold. Continuing the example of a Fabry-Pérot cavity the threshold condition can be modelled. The cavity has two mirrors with reflectivity R_1 and R_2 sandwiching the gain material. Radiation is amplified by oscillating back and forth between the mirrors dissecting the gain medium of length L. The cavity losses are symbolised as α and is the average loss per unit length where the optical gain coefficient, g (per unit length), is necessary to compensate for these losses [16, 18–20].

Initially, ignoring the losses, after a single pass of the gain material the intensity of the light is amplified by the factor G,

$$G = \frac{I_{out}}{I_{in}} = e^{gL}, \tag{1.25}$$

where

$$g = \sigma_{em}(N_u - N_l). \tag{1.26}$$

I_{out} and I_{in} are respectively the intensity at the start and end of a single pass.

As mentioned before, the radiation also experiences losses per round trip as it propagates through the gain material. Taking the initial intensity of the radiation, I_0, from the beginning of the cycle, starting at the first mirror, R_1, the losses of the intensity of the radiation arriving at the second mirror is taken into account, $I_0R_2e^{(g-\alpha)L}$. After a complete round trip of the cavity the radiation is $I_0R_1R_2e^{2(g-\alpha)L}$. When there is an amplifying medium in the form of a waveguide present (i.e. a CQD thin film) the factor Γ is introduced. This describes the overlap of the laser mode with the gain region and is expressed as $I_0R_1R_2e^{2\Gamma(g-\alpha)L}$. For the time being, Γ will be ignored but this overlap will be discussed further in section 2.5.1.

After the round trip the threshold is obtained when the amplification surpasses the cavity losses and can be expressed as,

$$R_1 R_2 e^{2(g-\alpha)L} \geq 1, \tag{1.27}$$

where the factor of two in the exponential is because the light passes the length of the cavity twice per round trip.

From equation 1.27 the material gain coefficient can be found as,

$$g \geq \alpha - \frac{ln(R_1 R_2)}{2L}, \tag{1.28}$$

where the density of population inversion necessary to achieve threshold is expressed as,

$$N_u - N_l = \frac{1}{\sigma}\left[\alpha - \frac{ln(R_1 R_2)}{2L}\right]. \tag{1.29}$$

Equations 1.28 and 1.29 display that when both the gain of the laser material and the sum of the cavity losses, for a round trip of light, is equal, threshold is achieved. It can also be noted that population inversion is related to the absorption of the pump power via the rate equations.

However, at high intensity, stimulated emission reduces the amount of gain by depleting the population. This is known as gain saturation and g in equation 1.27 can be substituted by the saturated gain (g_{sat}). Figure 1.4a shows the evolution of the gain as a function of the pump below and above threshold, P_{th}. Below threshold, the evolution is linear (it is considered that the pump is not high enough to start saturating the gain yet). At threshold the gain is clamped. In fact one can think about the system with gain momentarily exceeding the loss as the pump reaches threshold. In turn the intensity within the cavity increases exponentially to a point where it is strong enough to deplete the population inversion, reducing the effective gain to the saturated value g_{sat}. At the steady-state g_{sat} equals the loss of the cavity and is hence clamped. It is a self-limiting effect. Above threshold the additional pump power is transferred to the laser emission. Again the gain cannot increase as it would lead to exponentially growing intensity in the resonator. This locks the value of gain, for all pumping powers, at or above threshold, and equation 1.27 is fulfilled.

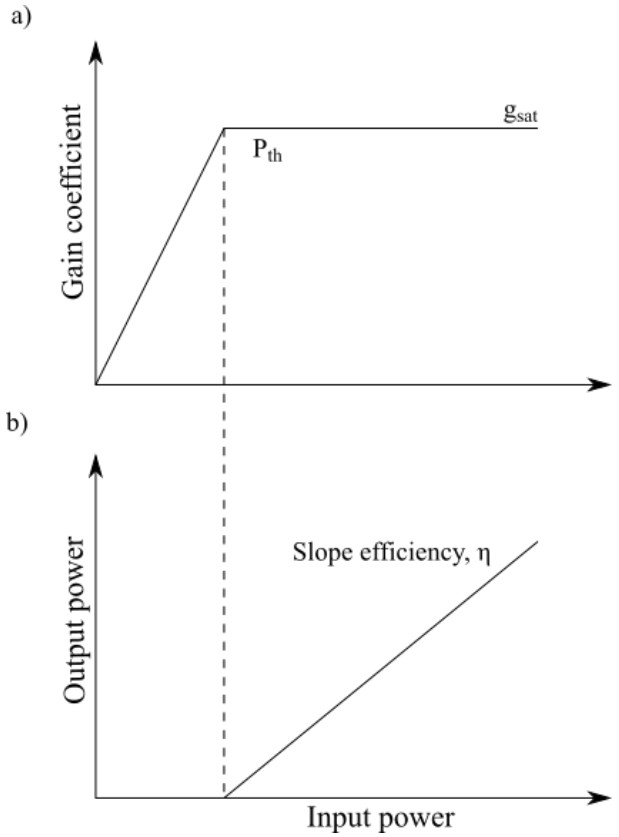

FIGURE 1.4: Plots of the emission intensity above and below threshold. a) Relation to gain with increasing pump power and b) output versus the input power, the slope efficiency.

The efficiency of the cavity can then be expressed as,

$$\eta = \frac{dI}{dP}. \tag{1.30}$$

This is known as the slope efficiency, or the differential efficiency, where the slope of the curve is defined by the laser output versus the pump power, figure 1.4b. Note that this curve is more or less linear allowing specification as a single value. However, in some cases, a non-linear slope can occur and are likely attributed to a quasi-three level system (requiring higher excitation densities introducing loss through fluorescence) or thermal effects (thermal roll-over as the gain materials temperature increases).

As mentioned previously, section 1.3.5, a significant factor of a laser is spectral narrowing ($\Delta\omega$) of the laser mode with pump power. Assuming that the optical mode is Lorentzian, section 2.6.3, the spectral intensity of the emission will grow due to the stimulated emission where the emission near the peak will grow faster than the wings of the function. This can be related to the average number of

photons, ϕ, as,

$$\Delta\omega = \frac{R_{sp}}{2\phi}, \tag{1.31}$$

with R_{sp} being the rate of spontaneous emission [16, 18].

1.3.7 Optical resonators

This section introduces various types of laser format. In particularly, the distributed feedback laser (DFB) and vertical-cavity surface-emitting laser (VCSEL) will be utilised in this thesis. These will be discussed in further detail in Chapter 2.

As mentioned previously, for laser operation an optical cavity, a gain material and a pump source are required. The cavity creates the amplification of light by generating optical feedback as it passes through the gain medium. There have been a number of different types of both CQD and OS laser resonators demonstrated [24, 25]. The simplest format consists of two parallel mirrors surrounding a gain material, figure 1.5a (and seen in figure 1.1). This configuration is known as a Fabry-Pérot cavity and is the stereotypical format that has been exploited in many laser systems [26–28]. Researchers have adapted the geometry of the Fabry-Pérot cavity where such an example is removing one mirror and polishing the opposite facet of the gain material as the output coupler to obtain Fresnel reflection [29–33], figure 1.5b. Figure 1.5 also displays other types of optical resonators used in CQD and OS lasers. Other such formats are vertical-cavity surface emitting lasers (VCSELs), vertical external cavity surface emitting organic laser (VECSOL) [34], distributed Bragg reflectors (DBR)[35–40], slab waveguides where feedback is produced by reflection from facet ends [41–51], doped optical fibres [52–54], Littman cavities (this uses a grating for colour-tuning and out-coupling) [44, 55–57], whispering gallery mode (WGM) lasers [50, 58–63] and random lasers [64–69] all depicted in figure 1.5.

Six years after the first demonstration of laser operation [1], lasing from organic molecules was reported [71]. These devices were based on fluorescent dye molecules in liquid solvents (see section 1.5.1.1). Dyes are now widely used in solid-state organic lasers where they have to be dispersed in a polymer matrix as otherwise the luminescence would quench when the individual molecules come close to one another. Over the years a number of solution based materials have emerged including

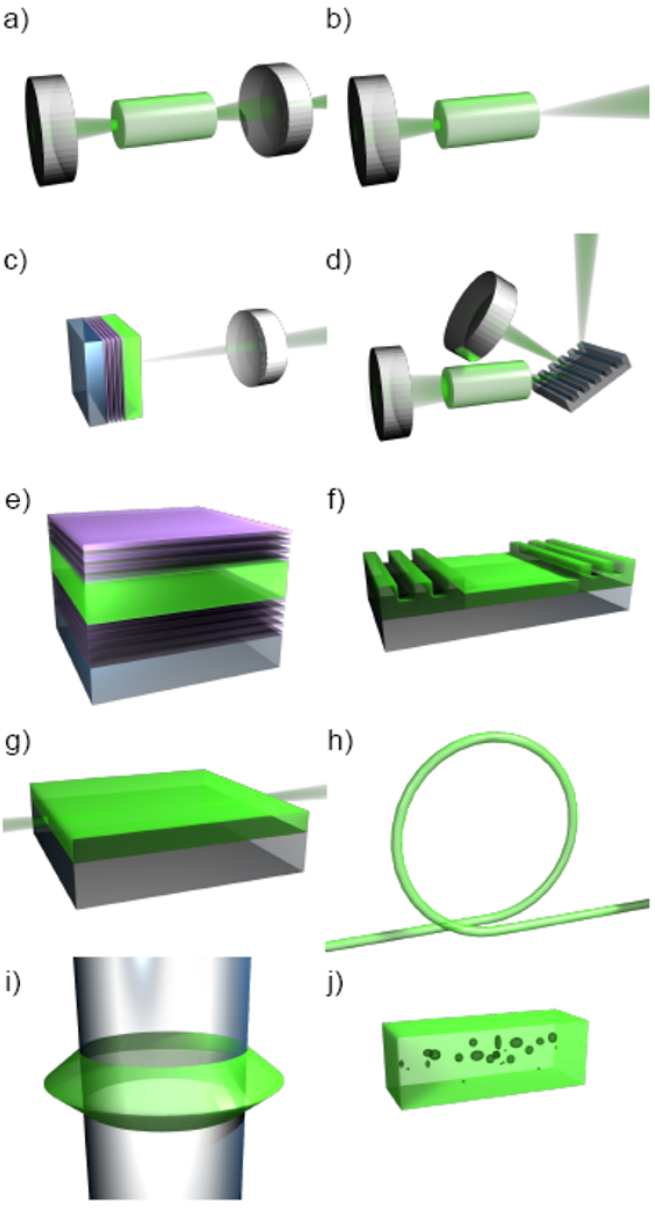

FIGURE 1.5: Laser cavity formats: a) classic Fabry-Pérot cavity, b) polished end facet of the rod as out-coupler, c) VECSOL, d) Littman cavity, e) VCSEL, f) DBR laser, g) slab waveguide with high-quality end-facets, h) doped fibre, i) WGM laser, j) random laser [70].

FIGURE 1.6: CQDs in solution with increasing diameter from left to right from Cytodiagnostics http://www.cytodiagnostics.com.

CQDs. Solution processed materials open new capabilities of fabrication including spin-coating, ink-jet printing, dip-pen nano-lithography and nano-imprint lithography. With these techniques, laser structures such as shown in figure 1.5 can be created with ease without the need for high-level clean room facilities or ultra-high vacuum systems. The next sections of this chapter describe the two families of such solution processed laser materials we are interested in.

1.4 Colloidal quantum dots

Semiconductor nanocrystals are an interesting type of inorganic chromophore. When metal-organic precursors of group II-VI or III-V semiconductors are heated and brought to a chemical reaction in coordinating solvent, the result is semiconductor crystals with dimensions of a few nanometres. These are known as colloidal quantum dots (CQDs) and their mean size, as well as their size distribution, can be dictated under the synthesis parameters such as temperature and reaction time [72] (synthesis techniques are discussed further in section 1.4.5). It is possible to overcoat them with another semiconductor material leading to a core/shell structure, figure 1.12a. CQDs have organic ligands attached to their surface (figure 1.6), which confers them their solubility in particular solvents and therefore their solution processability. They also determine the inter-particle separation in closely packed thin films, e.g. avoiding aggregation [72].

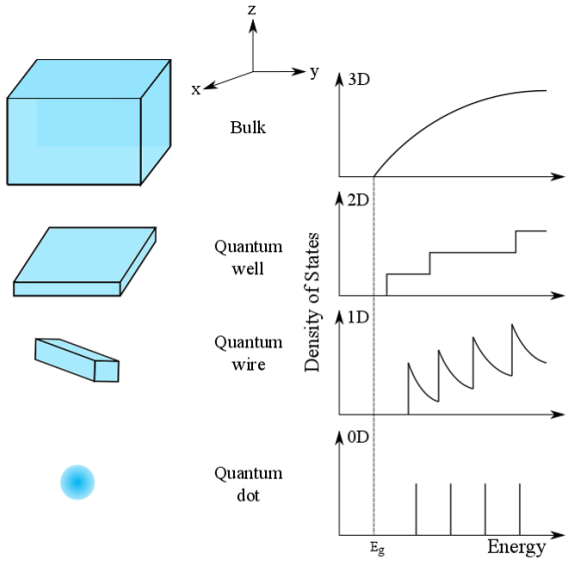

FIGURE 1.7: Schematic representation of semiconductors in bulk, quantum well, wire and dot format. Density of states functions for electrons in the conduction band of the semiconductor with band gap Eg for each corresponding structure.

1.4.1 Quantum confinement

Characteristics of a CQDs absorption and emission can be understood in terms of quantum confinement. Quantum confinement transpires when the physical structure of the nanocrystal is small enough to result in the potential confining energy being greater than the thermal energy. This affects the electronic structure of the CQDs in a manner that is proportional to the crystal size. Quantum confinement is observed when the size is equivalent to the de Broglie wavelength of the electrons and holes wave functions. Or if considering electron-hole pairs (excitons) when it is comparable to the Bohr exciton radius, a_0; the electron-hole Coulomb interaction establishes a_0. Confinement along one spatial direction refers to a quantum well, two dimensions to a quantum wire and three to a quantum dot. Shape dependency modifies the electrons wave function as well as the density of states, figure 1.7. CQDs impose the confinement potential on electron and holes (excitons) in three dimensions and is often referred to as a zero dimensional structure. Typically, chalcogenide CQDs as used in this work have diameter between 2 nm and 10 nm. Through the particle in a box example the relationship between the energy levels and their spacing can be approximated,

$$E(n_x, n_y, n_z) = \frac{\pi\hbar}{2m_e}\left(\frac{n_x^2}{d_x^2} + \frac{n_y^2}{d_y^2} + \frac{n_z^2}{d_z^2}\right), \tag{1.32}$$

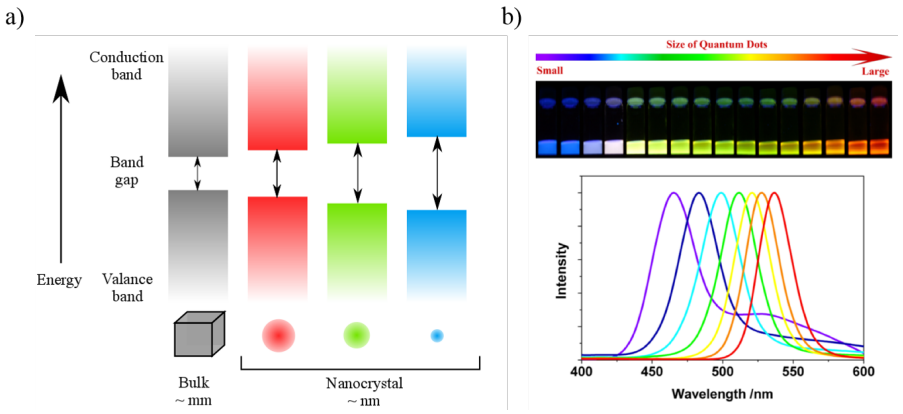

FIGURE 1.8: Band gap of CQDs is determined by their radial dimensions. a) Displays how the band structure alters and b) shows CQDs dispersed in solution with different diameters and spectra [13].

where n_x, n_y, and n_z are integer quantum numbers indicating the quantised levels, m_e is the mass of an electron, and d is the diameter of the CQD. A similar expression can be obtained for the quantization of the hole energy levels. The band edge transition energy between the lowest energy levels of holes and electrons is given by:

$$\hbar\omega(CQD) \approx E_g + \frac{\pi^2\hbar^2}{2\mu R_{CQD}^2} \tag{1.33}$$

where μ is the electron-hole reduced mass, E_g is the bandgap of the bulk material, R_{CQD} is the radius of the CQD [73].

This demonstrates that the size of the CQD controls the resulting band gap thus allowing tailoring of the emission wavelength by altering the CQD dimensions, figure 1.8a. This can also be seen in figure 1.8b where reducing the CQD size results in the blue shifting of the emission wavelength (increase energy). The transition energy is with this simple model inversely proportional to the square of the CQD diameter. The shift in wavelength can also be achieved by altering the material composition, hence E_g.

1.4.2 Energy levels and transitions

For a spherical confinement potential a series of states that can be classified by two quantum numbers n and L arises. This can be understood by looking at equation 1.32 and for dx=dy=dz. n is the number of the energy level and L corresponds to the angular momentum. L=0,1,2,3... is often labelled with the letters s, p, d...

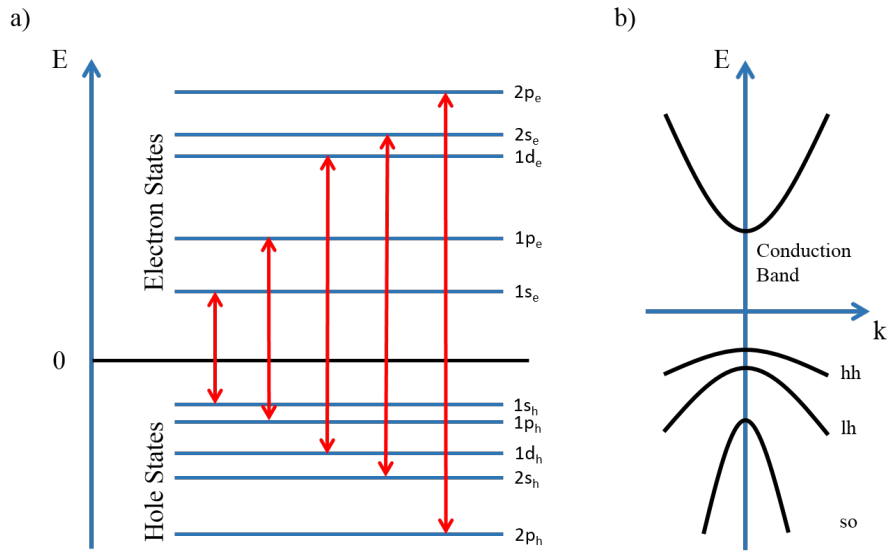

FIGURE 1.9: a) Depicts allowed transitions when creating an exciton pair and b) displays four energy bands corresponding to the conduction band, the heavy-hole (hh) band, the light-hole (lh) band and the spin orbit split off (so).

(or S, P, D...) in analogy with atomic spectroscopy notations. The energy levels for the holes and electrons are represented in figure 1.9a along with the allowed transitions, which are the ones that conserve n and L between the electron and hole states.

Trends in absorption and emission spectra can be broadly explained with such a simple picture. However, it does not accurately describe the spectra seen in experiments. For this more details on the valence band need to be considered. Most III-V and II-VI CQDs (such as those studied in this work) are of zinc blende or wurtzite crystal structure and therefore the valence band is made up of 3 sub-bands. In ideal zinc blende the top of the valence band is 6-fold degenerate at k=0 (with the 3 bands each having a 2-spin degeneracy) as depicted in figure 1.9b. Spin-orbit interaction, and crystal field splitting in wurtzite crystals, lift this degeneracy leading to three valence sub-bands called heavy-hole (hh), light-hole (lh) and spin orbit split-off (so) bands. The total angular momentum of these bands is given by J, a combination of the orbital momentum of the Bloch function and the angular momentum of the spin. J=3/2 for the hh and the lh bands and J=1/2 for so band [74].

Confinement in CQDs leads to a mixing of these hole sub-bands, meaning that J and L are inadequate independent quantum numbers to describe the hole energy levels. Instead one uses the total angular momentum F=J+L where the hole wave

functions are linear combinations of the different sub-bands [74]. J is the angular momentum from the Bloch function given the crystal lattice (i.e. related to the valence bands) and L is the orbital angular momentum of the envelope function obtained from the confinement problem. The hole energy states are then labelled as nL_F as shown in figure 1.10. Again the letter S is used for L=0, P for L=1 etc. The lowest energy state is then written as $1S_{3/2}$(h), h to indicate hole. The electron states can be described as before because of the unique (2-fold spin degenerate) conduction band. For example, the lowest energy state is written 1S(e). Figure 1.10a shows these electron and hole states, with the arrows indicating the allowed transitions that conserves n and F. Figure 1.10b displays the absorbance spectra of CdSe CQDs where four transitions corresponding to 1S and 1P electron states are resolved [75].

1.4.3 Emission - band-edge state fine structure

The confinement induced mixing of hole states accurately describes the absorption spectra of CQDs but does not totally explain the emission. For the latter, the fine structure of the band-edge state (i.e. the transition 1S(e) - $1S_{3/2}$(h)) needs to be considered. The origin of the fine structure is the electron-hole interaction, i.e. when considering the exciton involved in the transition. This excitonic interaction is strong in CQDs because of the confinement (strong electron-hole wavefunctions overlap). The band edge electron and hole state in such a case cannot be truly treated independently. Instead one considers the 1S(e) - $1S_{3/2}$(h) exciton with a total angular momentum $N = F_e + F_h$ with F_e=1/2 (projection +1/2 and -1/2) and F_h=3/2 (projections +3/2, 1/2, -1/2 and -3/2).

The exchange interaction lifts the degeneracy of the two resulting states N=1 and N=2. These two sub-states further split into five sub-levels due to crystal field and shape asymmetry (see figure 1.11). The projection of N, N_m, is used to label these states with a superscript indicating if it corresponds to the upper (U for N=1) or lower (L for N=2) levels. These are shown in figure 1.11. The lowest state is "dark" as N_m=2 does not couple, in the dipole model, with a photon that carries an angular momentum of 1. The second lowest sub-levels, is characterised by N_m =1 and is therefore "bright" (dipole allowed transition to the ground state). Bright states can absorb and emit photons and dark states cannot (although can still emit but over a much longer timescale). At low temperature, the luminescence of CQDs

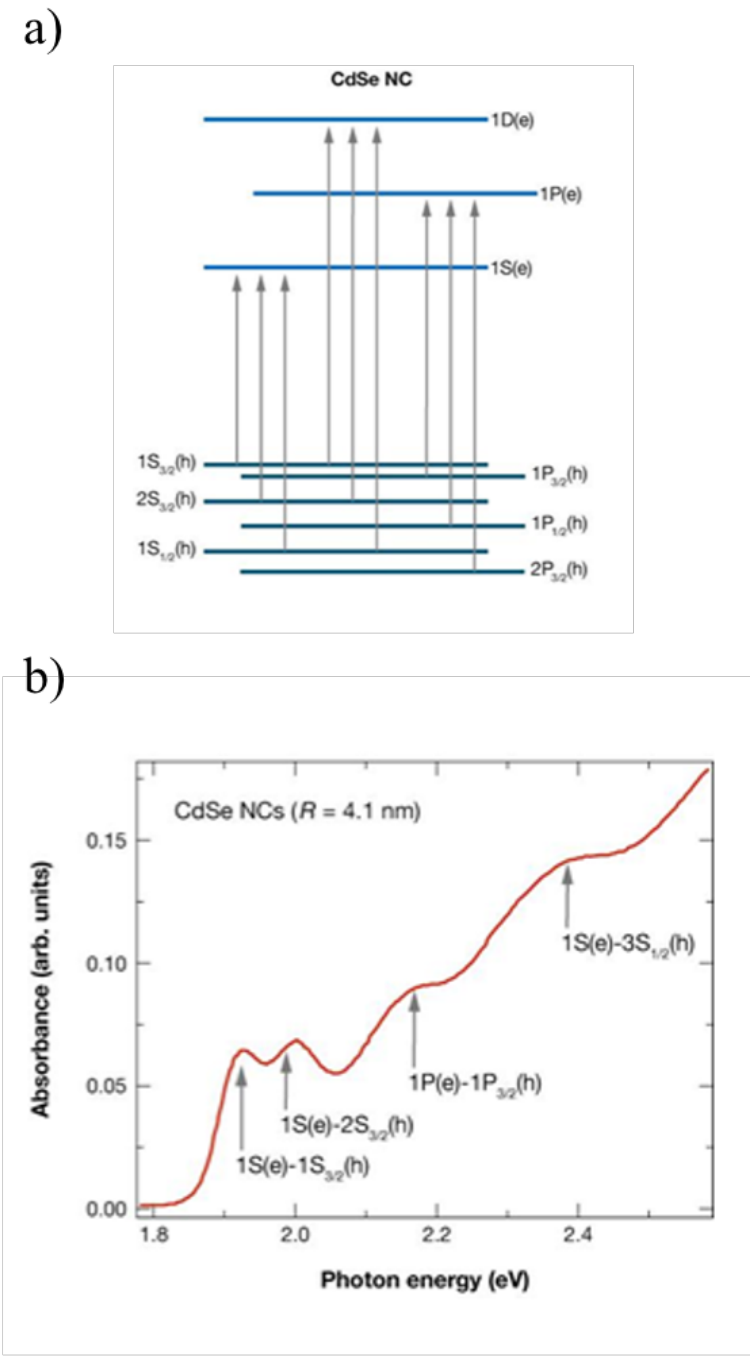

FIGURE 1.10: a) Band structure of a CdSe CQD and b) absorbance spectra of CdSe CQD displaying for transition [76].

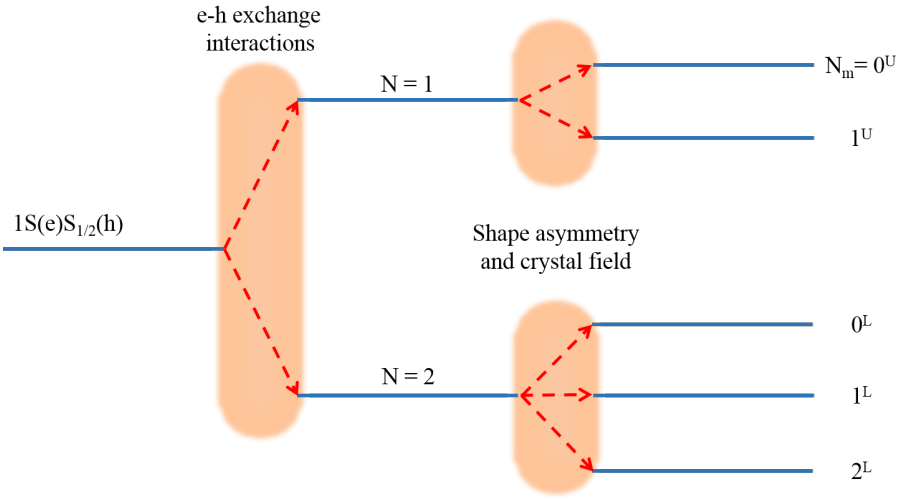

FIGURE 1.11: Representation of the bright-dark exchange interaction of the ground state excitation structure, the CQD shape asymmetry and crystal field.

is slow (microseconds) because it comes from the lowest dark state transition. At room temperature the exciton population is distributed over the lowest dark and bright states and the luminescence lifetime is on the order of a few nanoseconds to a few tens of nanoseconds.

This fine structure of the band-edge exciton also contributes to the Stokes shift between the photoluminescence peak and the absorption maximum of this first transition. A high Stokes shift is desirable to limit the effect of self absorption, which can increase laser threshold.

1.4.4 CQD structure classification

The majority of CQDs utilised today are typically of a core/shell or multishell structure. These structures consist of the CQD core overcoated with a shell made of another inorganic material. The latter encapsulates the core. In turn it passivates the trap sites on the cores surface that would otherwise promote the recombination of electrons and hole non-radiatively. Core/shell structure therefore enables higher photoluminescence quantum efficiency. Furthermore, the addition of the shell layer gives some protection from environmental degradation such as photo-oxidation. Organic ligands are still there, onto the surface of the shells, adding an additional passivation layer and preventing aggregation when in thin film format.

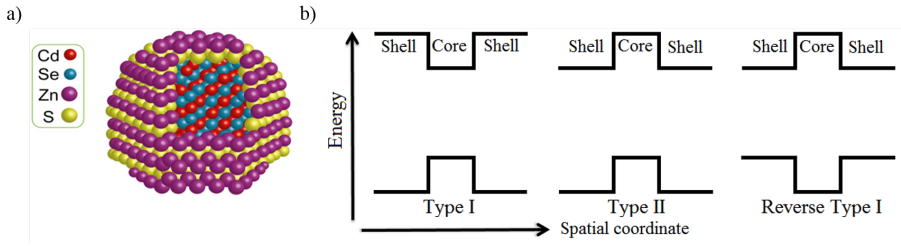

FIGURE 1.12: a) Schematic of spherical core/shell CQD b) electronic band structure representation of different types of CQD.

The respective band alignment of the core and shell material, along with the lattice parameters, allow engineering of so-called excitonics by controlling the overlap, and hence interactions, of electrons and holes. The relative position of the electronic bands leads to the classification of CQD as type I, type II or reverse type I heterostructures, see figure 1.12b.

A schematic of a typical spherical binary core/shell CQD can be seen in figure 1.12a where the spacing of the electronic bands is controlled by the semiconductor material chosen as well as the size (the confinement energy), in addition to the carriers effective mass and lattice strain [77].

Type I CQDs have been broadly investigated, and reported in this thesis, with typical formats resulting in the shell having larger band gap than the core [78–86]. Both absorption and emission are observed to red shift when adding shell material. This is due to the excitonic wave function being pulled into the shell lowering quantum confinement and the effective band gap energy [87]. This restricts the exciton pair to the core creating an overlap with the corresponding wave functions. In reverse type I the opposite is true as the shell is of lower band gap energy than the core resulting in the exciton pair wave function being localised within the shell [88–91].

On the contrary, type II CQDs core and shell bandgaps are designed to overlap one another, figure 1.12b. This alignment allows one charge carrier to be localised in the core and the other localised in the shell [92, 93]. The band gap energy of type II system can be smaller than that of the individual semiconducting materials. The Stark effect caused by the separation of holes and produces a redshift in the emission. A large Stokes shift can be obtained in such a way. However, type II CQDs usually have a lower emission efficiency.

Quasi-type II are structures in between type I and type II, i.e. one type of carrier is localised in either the core or shell while the other type of carrier is delocalised over the whole CQD. At lower wavelength, the alloyed core chalcogenide CQDs utilised in this work approaches the quasi-type II classification.

1.4.5 CQD synthesis

CQDs can be fabricated in a number of ways in a variety of material alloys (III-V, II-VI), and tailored to produce different shapes and compositions. The synthesis process involves wet chemistry fabrication and can be done with a number of methods such as hot-injection [94] and heat-up techniques [95]. The concept of the wet chemical fabrication process is demonstrated in figure 1.13. This displays a typical procedure that results in the decomposition of chalcogenides and metal-organics in a solvent at high temperature [73, 96]. The approach requires 3 main ingredients: (i) the desired seed materials for the CQDs, known as the precursors; (ii) a systematising organic solvent; and (iii) the ligands, which contributes to the controlled growth and stabilizes the CQDs. There are three stages to the procedure [97–99] and has been described as burst nucleation. Initially there is pyrolysis of the precursors of the chosen material. This is the breakdown of the precursors (stage 1) giving ions of the CQD constituting material. As this pyrolysis happens after injection, the ion concentrations increase to supersaturation. Once this is reached, nucleation begins with the formation of stable nuclei depleting ion concentration (stage two). When the ion concentration is low enough the formation of nuclei halts. After this the existing nuclei begin to expand and the CQDs grow (stage three), where the crystals are removed over time increments. Cadmium Selenide (CdSe) based CQDs have been extensively researched and as a consequence are the most developed where monodispersed nanocrystals are obtained through these methods; with other common alloy materials being CdS, ZnS, InP and PbS.

As mentioned before the photoluminescence quantum yield is improved when these core structures are encapsulated, here with the addition of a Zinc Sulphide (ZnS) shell, as dangling bonds are passivated; reducing carrier trapping [78, 80], where the addition of organic ligands allows solution processing like with organic semiconductors [96]. The shell can be applied to the core by either the dropwise addition

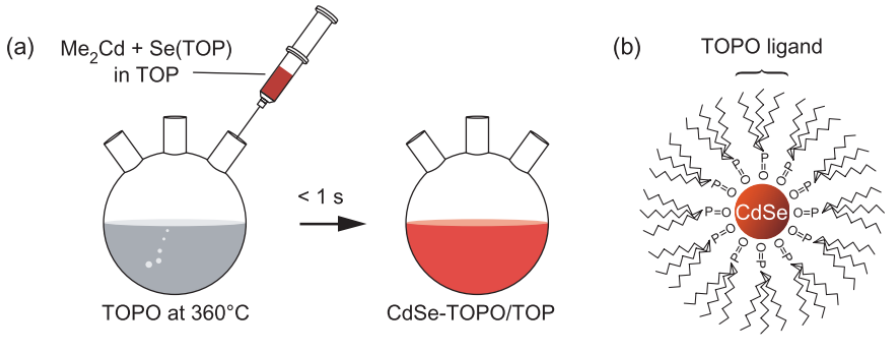

FIGURE 1.13: a) Schematic of the wet chemical reaction used for the synthesis of CdSe CQDs and b) adding organic ligands with TOPO: trioctylphosphine oxide and TOP: trioctylphosphine to the CdSe CQD adapted from [73].

[100, 101] or utilising the Successive Ion Layer Adsorption and Reaction (SILAR) technique [102].

The dropwise addition method requires an ensemble of the anion and cation precursors to be gradually added into the previously fabricated, core only, CQDs. Thus creating the core/shell architecture. There are certain drawbacks to this technique. A consequence of the high temperature fabrication process during the core nucleation process can cause the nucleation of the shell material as well as defects reducing the photoluminescence quantum yield.

SILAR is a method that manipulates, a monolayer at a time, shell growth via alternating injections of the of shell precursors into the core only CQD solution, at high temperature. The advantage here is the small probability that nucleation occurs within the shell precursors. After injection, and once the solution has cooled, the final product is isolated from the solvent. This is done with the addition of ethanol where the CQDs are separated by precipitation, via centrifuge, and re-dispersed in the desired solvent. The CQDs reported in this thesis are purchased dissolved in toluene.

The thickness of the shell is limited by the lattice mismatch between shell and core materials. For a CdSe/ZnS this thickness is only a couple of atomic layers because of the large lattice mismatch between CdSe and ZnS. A thicker layer would introduce defects detrimental to luminescence and laser operation. CdSe/CdS and CdSSe/ZnS CQDs mitigate this issue of lattice mismatch.

1.4.6 CQDs as a visible gain material

Since optical gain in a solid film of CQDs was first reported [75] in 2000, the field of research has significantly expanded. Due to their quantum size effect yielding large confinements, CQDs have the potential for low lasing threshold lasers coupled with narrow emission linewidth and improved temperature stability [73]. In addition to these aspects the solution processing capabilities allow them to be applied to a vast variety of substrates and the fabrication of complex structures.

To understand the basics of optical gain in CQDs, let's consider a band edge transition (1S(e) - $1S_{3/2}$(h)) with a single electron and hole state (each double spin degenerate). There are initially two electrons occupying the ground state, one spin up and the other spin down due to the Pauli exclusion principle, and an external excitation is applied. An electron can then be raised to the excited level, producing an exciton (electron-hole pair). In this condition, a photon incident on the material with an energy corresponding to the transition has an equal probability of (i) being absorbed, creating a second exciton, and of (ii) stimulating emission with the recombination of the electron-hole pair (see section 1.3.1). Therefore when N_{eh}= 1, where N_{eh} is the per-dot exciton occupancy, the material is in transparency: absorption at the transition energy and stimulated emission balance each other. It ensures that in such a system, biexcitons are needed for optical gain so that N_{eh} is superior to 1. This is the condition for population inversion of the first transition in CQDs. Of course, it is necessary to pump at higher energy (a 2-level system cannot produce optical gain as mentioned before). Excited carriers relax from higher excited states to the band edge state on a sub-ps timescale, faster than the PL lifetime, ensuring that there is a sufficient accumulation of carriers for population inversion.

The condition N_{eh} =1 for population inversion is valid for a transition between single electron and single hole states. However, this is not always the case for the latter as we have seen. The hole sub-states manifold discussed in section 1.4.2 increase the multiplicity of the excited state (excitonic state), which in turn, unless the energy separation between the sub-states is bigger than the thermal energy, increases the value of N_{eh} needed for threshold [103, 104].

There is one effect that can contribute to reducing the value of N_{eh} needed for optical gain. This effect is biexciton binding, which reduces the probability of self absorption (absorption of a photon at the transition energy) in CQDs by shifting

the biexcitonic energy state compared to the single exciton state [105, 106]. In principle, if the band-edge multiplicity can be reduced to its minimum (a single spin-degenerated for both electrons and holes) and if the biexciton binding energy is larger than the transition linewidth (for example by using a type II CQDs where the electron and hole are spatially separated) then optical gain in the single exciton regime is possible [107].

1.4.6.1 Non-radiative Auger recombination

As previously mentioned CQDs were first seriously considered as potential materials for visible lasers after optical gain was demonstrated in neat films of core-shell CdSe/ZnS CQDs [75]. The issue of Auger recombination in such core-shell CQDs (a non-radiative recombination effect impeding optical gain) was recognised early and the effect was shown to scale with the number of excitons, N_{eh}, and to decrease with increasing CQD volume [73]. Auger recombination is a major challenge in achieving laser operation. If it is significant, it accelerates the carrier recombination rate reducing the gain lifetime [73].

There has been a number of studies on the dynamics of optical amplification in CQDs and several device demonstrations followed, including whispering gallery mode lasers [61, 62, 108, 109], vertical-cavity surface-emitting lasers [110, 111], random laser [111] and distributed feedback (DFB) lasers [112–114]. Unfortunately, most of these reports utilised ultrafast (ps and fs) pumping as the optical pump source operates faster than the Auger decay time.

A method to alleviate the non-radiative recombination is through the design architecture of the CQD heterostructure. In this thesis, alloyed-core/shell structures were used as they are known to mitigate Auger in CQDs. Auger recombination is minimised in alloyed-core/shell CQDs because of the smoother transition between the core and shells [115]. The CQDs can be made bigger as well while tuning the wavelength through the composition.

We have seen that in CQDs with a single hole ground state, population inversion begins when the exciton occupancy $N_{eh} > 1$ [73, 75]. However, when $N_{eh} > 1$ Auger recombination becomes possible.

Auger recombination is an undesirable phenomenon that occurs within CQDs containing multiple excitons and is a Coulomb mediated non-radiative recombination

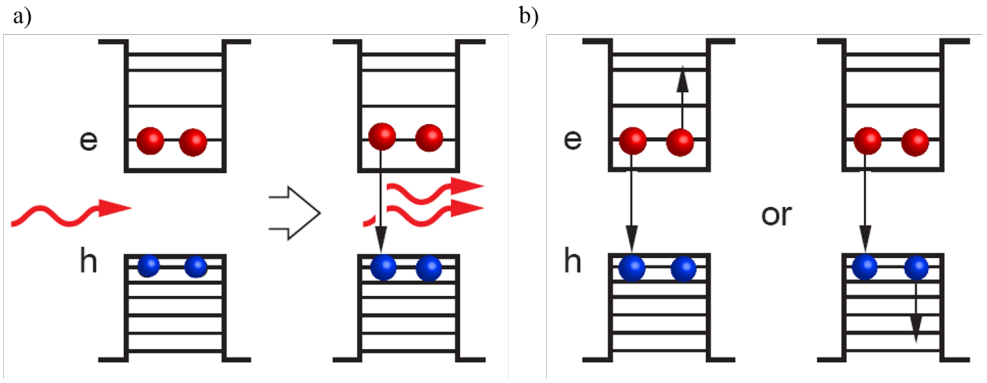

FIGURE 1.14: a) Modelling the lowest optical transition can be simply considered as a two-level system having two electrons in the valence band (the ground states). When an external excitation is applied an exciton pair is created. When another incident photon is applied the electron recombines with the hole emitting a photon. This process is known as stimulated emission. b) When the energy from the electron-hole recombination is transferred to either the electron or hole and it is known as non-radiative Auger recombination.

of the carriers. Here, the electron and hole recombine by transferring their energy to a third party carrier, figure 1.14. Typically, the energy is released via phonons rather than a photon and enhances device degradation [116]. The process is more prominent in CQDs, in comparison to bulk semiconductors, and is a result of their physical architecture, more precisely their small size and the abrupt interfaces between the core and shell materials as well as the interfaces between the CQD and ligands/solvent. It results in the relaxation of the momentum conservation getting rid of the thermal activation barrier [117]. The consequence is the decay of multiexcitons can be dominated by Auger recombination [118–120], which in turn can severely limit the lifetime of optical gain well below the ns, a problem when operating in the nanosecond regime and above.

The occurrence of optical gain within a medium therefore does not guarantee stimulated emission and laser operation. To overcome Auger recombination the accumulation of stimulated emission must occur faster than the Auger lifetime. This can be seen as the stimulated build-up time given by [75],

$$\tau_s = \frac{4\pi R^3}{3} \frac{n_r}{\xi \sigma_g c} \tag{1.34}$$

where R is the radius of the CQD, n_r is the sample refractive index, ξ is the packing density of the CQD, σ_g is the gain cross-section and c is the speed of light.

The biexciton lifetime, τ_2, and can be expressed as $\tau_2 = \beta R^3$ [121, 122], where β is a scaling factor giving the condition on the minimum packing density required to achieve stimulated emission. Thus stimulated emission occurs when $\tau_2 > \tau_s$ and occurs when,

$$\xi > \frac{4\pi n_r}{3\sigma_g \beta c}. \tag{1.35}$$

As this drastically affects CQD laser performance there has been a number of creative solutions to this ailment via physically and chemically adapting CQD architectures as briefly mentioned above.

Examples of such processes are the fabrication of giant core-shell CQDs where increasing their volume has demonstrated a reduction of Auger recombination [123, 124]. Another tactic is to smooth the transition between the core-shell interface giving a smoother alloyed layer and a graded confinement potential [125]. Finally, another method is to use alloyed or gradient structures, similar to the alloyed-core/shell arrangement of the CQDs investigated here [126–128].

1.4.6.2 Colloidal quantum dot lasers: State of the art

CQDs have been utilised in numerous formats as a visible gain medium as a highly dense film of the material can be easily fabricated. These films are typically placed within an optical cavity and produce stimulated emission as light is allowed to propagate through the medium. As more and more reflections of the photons occur within the cavity, a greater degree of monochromaticity, directionality and brightness is achieved. As stimulated emission being achieved led to a drive in producing more compact, efficient and tunable devices resulted in different groups exploring different formats of CQDs; such as their dimensionality [87, 104, 129–131] and physical size [125, 127, 132–135]. This section will discuss a selected overview of some of the accomplishments that have been made with CQD gain materials in the search for low operational thresholds, tunable laser emission and compact devices.

Typically, in order to achieve laser operation, the gain medium has to interact with an optical resonator. However, this is not always the case. A random laser (RL) is a device that when the gain material is in a thin film, produces scattering effects within the film resulting in laser-like emission. This format was once seen as both a promising industrial idea as it negates the need for the resonator fabrication

saving costs but is also seen by others as not real laser operation. Chen *et al* reported on type I CdSe/ZnS core/shell CQDs spin coated onto a 500 μm planar glass substrate [111]. The substrate had micron-scale groves etched into it via a diamond tip where an integrated emission (602-608nm) achieved thresholds of ∼25 mJ/cm^2. Augustine *et al* also demonstrated RL in solution by mixing CdSe CQDs with Rhodamine 6G in solution [136]. Here the dye allowed the CQD emission to be scattered throughout the material and RL emission ranging from ∼558-562 nm was observed.

DFB lasers have been extensively demonstrated utilising CQDs as a gain material. Here, a periodic structure is overcoated with the CQDs where they behave like a slab-waveguiding structure. Resonance is achieved via optical feedback provided by the periodically varying refractive indices (CQD and grating material) and is defined by Bragg scattering (section 2.2). This format is advantageous as it allows the tuning of these devices through altering the CQD size, film thickness and refractive indices, altering the effective refractive index of the device, under a constant grating period. Where the majority of CQD laser research has been extensively studied exploiting ultrashort optical excitation and has established many high quality results, state-of-the-art ns pulsed optical excitation have been demonstrated within our group. In [137], DFB lasers were fabricated using commercial type I core/shell CdSe/ZnS CQDs diluted with a Poly (methyl methacrylate) (PMMA) matrix and was the basis for this investigation. This CQD DFB laser was optically pumped under stripe excitation with 5ns pulses producing a threshold fluence of 0.5 mJ/cm^2, where the emission pattern appears fan-shaped and is attributed to laser emission of a one dimensional DFB cavity at 610 nm. This device was also tested in a liquid environment where a 4nm redshift was observed when immersed in water, demonstrating the potential of such lasers for sensing.

Advancement of this work was carried out where the CQD DFB laser was transferred onto an ultrathin (30μm) glass substrate [138]. The mechanical bending of the glass substrate resulting in a tunable emission over a range of 18nm with an average threshold fluence of 450 $\mu J/cm^2$ at 607 nm. Here the emission wavelength was red-shifted by applying a positive curvature and blue-shifted by a negative curvature as bending alters the grating period shifting the wavelength.

Eisler *et al* builds on the tunability of these devices enabling a tunable range of ∼ 56 nm (565-621nm) coverage by employing a variation of CdSe/ZnS core/shell CQD diameters with constant grating periodicity under fs pulsed optical pumping

[139]. Dang *et al* also displayed tunable devices by varying film thicknesses [140]. Where, through a 250nm and a 400nm CQD film achieved DFB laser emission at 608nm and 620nm with thresholds around 250 $\mu J/cm^2$. These measurements were again conducted using ultra fast pumping (ps). In the same year, Dang *et al* also reported on red, green and blue optically excited CQD/DFB lasers through size-dependent tuning [141]. Again this utilised ultra fast pumping producing thresholds between 250-350 $\mu J/cm^2$.

Both [137, 138] demonstrate that CQD laser emission, even in novel flexible formats, can be obtained with optical pumping with greater than ns-pump pulses and with thresholds that can be achieved with compact solid-state lasers. Unfortunately, this performance however is still out of the range of blue InGaN laser diodes. In addition to this, laser oscillation was demonstrated at wavelengths between 600 nm and 630 nm. Typically, emission at lower wavelengths are more difficult to achieve due of the reduction of pump absorption and of the increase of Auger recombination in correspondingly smaller sized CdSe/ZnS CQDs.

Vertical-cavity surface-emitting laser (VCSEL) formats have also been investigated using CQDs as their gain materials. These are formed by placing the CQDs between two highly reflective mirrors. These mirrors are typically build up of varying refractive indices (i.e. DBRs section 2.6.2) [25, 110]. VCSELs have laser emission perpendicular to their surface where, due to their small cavity length, have the ability to be compact with minimal scattering and absorption losses. This allows for low threshold laser operation to be achieved. Dang *et al* achieved multimode laser emission using a gradiented CdSe/ZnCdS CQD film within a wedged DBR structure made up of SiO_2/TiO_2 alternating layers [25]. Prior to this, Menon *et al* created a mechanically flexible VCSEL device [110]. Here, InGaP CQDs were chosen to be the gain material and place within solution processed DBR mirrors. The mirrors were made up by spin coating alternating poly-N (vinylcarbazole) (PVK), and cellulose acetate (CA) layers of quarter wavelength thickness onto glass. The device was then peeled off the substrate and the free-standing device emitted at 657 nm with a slope efficiency of 12 %.

Whispering gallery mode (WGM) lasers are not reported on in this thesis, but much work has been concluded on them with CQDs. WGM lasers use total internal reflection (TIR) to confine light within their structure (usually disk or sphere like). The strong photon confinement propagates the mode around its concave surface reducing thresholds and achieving quality factors as high as 10 million [142, 143].

By integrating CdSe/CdZnS CQDs onto dielectric microsphere surfaces, Snee *et al* devised an approach to produce stable and repeatable laser emission through silica and polystyrene [63]. Here the WGM produces multimodal laser emission spans a range of 620nm to 680nm where a variance in the microsphere dimensions (so that only one mode appears within the stop-band) allows the tuning of single mode emission. Chan *et al* built on the size tunability of microspheres using CdS/ZnS nanocrystals (NCs) (∼4.5nm) emitting in the blue (∼480nm) achieved laser oscillation [144]. Min *et al* demonstrated an ultra low threshold of ∼9fJ per pulse (fs excitation at 388nm) when employing toroidal microcavities [145]. Here, CdSe/ZnS NCs were spun cast onto the surface of the microcavity. A threshold this low is the result of the high Q-factors present in comparison to microsphere resonators with similar size [143]. This is due to lower mode volumes in addition to efficient evanescent coupling of the pump to the toroidal microcavity geometry via a tapered-fibre. These cavities also benefit as they can be fabricated through lithography allowing for predefined locations on silicon chips. The toroidal cavities resonances can also be tuned electrically in return tuning the laser emission. Armani *et al* demonstrated such structures [146] (although this has yet to be shown with CQD implementation).

1.5 Organic semiconductor gain media

1.5.1 Different types

In addition to CQDs, two types of organic semiconductors were also utilised for lasers as reported in Chapter 5. The optical properties of organic gain materials rely on electron delocalisation due to π-conjugation. The same phenomenon is the reason for the semiconducting properties of some organic materials. Organic gain media can be broadly divided in the following categories.

1.5.1.1 Dyes

Sorokin *et al* demonstrated the first organic laser through the use of small molecular dyes as a gain material [71]. Dyes have been extensively utilised as gain materials for organic solid state lasers where the most common being are Perylene, Coumarin, 4-(dicyanomethylene) - 2 - methyl - 6 - (4 - dimethylaminostyryl)

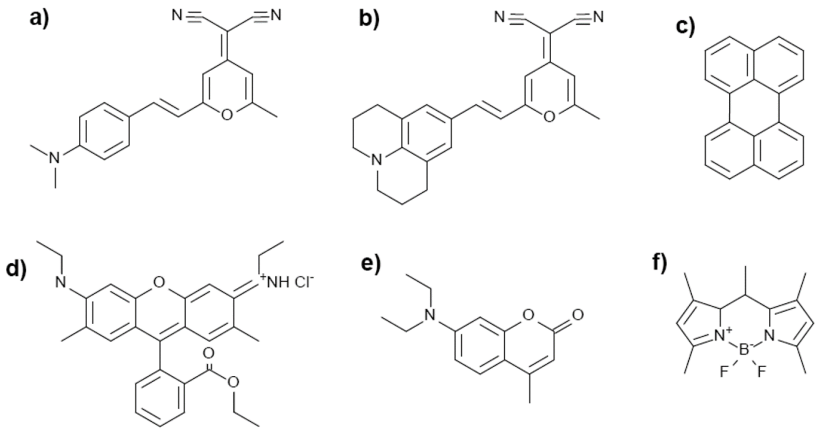

FIGURE 1.15: Popular dye materials and their molecular structure: a) 4- (dicyanomethylene) -2-methyl-6- (4-dimethylaminostyryl) -4H-pyran (DCM), b) 4- (dicyanomethylene) -2-methyl-6- (julolidin-4-yl-vinyl) -4H-pyran (DCM2), c) perylene, d) Rhodamine 6G (R6G), e) Coumarin 47, f) pyrromethane (PM) [70].

- 4H - pyran (DCM), 4 - (dicyanomethylene) - 2 - methyl - 6 - (julolidin - 4 - yl - vinyl) - 4H - pyran (DCM2), Pyrromethane and Rhodamine 6G [147–150], figure 1.15. The materials themselves are very small solution processable conjugated molecules consisting of around ten carbon atoms. As mentioned before, if the molecules are in close proximity to each other, non-radiative relaxation diminishes luminescence. To overcome this quenching, dye molecules have to be suspended in a solvent or a polymer matrix.

1.5.1.2 Conjugated polymers

Unlike small-molecule organic semiconductors, conjugated polymers are solution processable allowing for their incorporation into photonic devices by printing and soft-lithography techniques. Conjugated polymers are made up of a repeating monomer chains and their solubility comes from functional side groups or chains.

The monomers are of similar size to dye molecules. Some of the most commonly used building blocks are displayed in figure 1.16. Polyacetylene was the first conjugate polymer. It was fabricated in 1970s and is the precursor of all conjugated polymers [151]. Unfortunately, the electronic and semiconducting properties were not good as high quality films were hard to produce. Advances in synthesis techniques, in the mid 1980s to early 1990s, allowed more complex repetition containing benzene, thiophene, or similar ring structures, producing more stable molecular

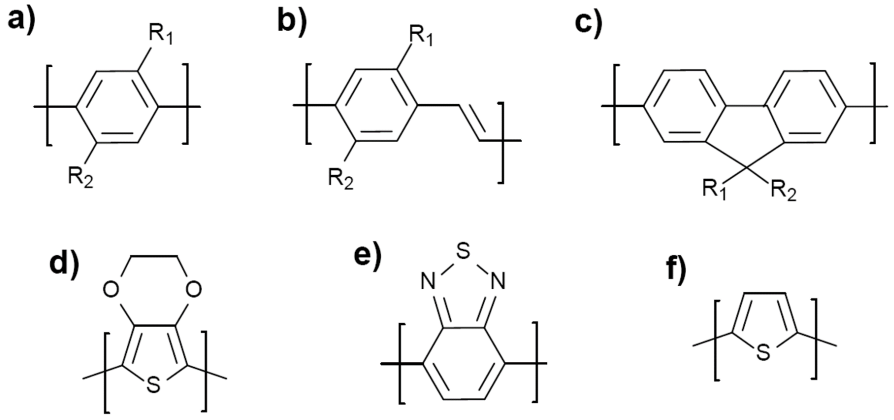

FIGURE 1.16: Common monomer building blocks: a) (poly) para phenylene (PPP), b)(poly) para phenylene vinylene (PPV), c) (poly) fluorene (PFO), d) (poly) ethylene dioxythiophene ((PEDOT), e) benzothiadiazole (BT), and f) (poly) thiophene (PT) [70].

conformation [151, 152]. Their optical properties (e.g. absorption and emission wavelengths) can be adapted by altering conjugation length or the addition of specific monomer units into the molecule. Derivatives of poly (phenylene vinylene) (PPV) [153] and polyfluorene (PFO) [154] are the main conjugated polymers utilised in gain materials in visible lasers.

1.5.1.3 Conjugated oligomers

Conjugated oligomers are similar to conjugated polymers. Typically, they are fabricated using the same building blocks and as a result have similar optical and electronic properties. The main difference is that where polymers consist of many repeating units, oligomers are made of only a few repeats, usually less than ten. In turn synthesis leads to monodispersed molecules with exactly the same number of repeating units. They are the same distinct reciprocal unit whereas polymers are long, one-dimensional thread-like chains.

Oligomers are solution processable and are a recent addition to semiconducting polymers. In particularly, they offer greater spectral overlap of optical transition and manipulation of the electronic and optical properties, via conjugation length, insertion of single different monomer species and self-organisation is exploited [155].

Another advantage of oligomers is the possibility to produce more complex structures from the monomers. Examples of these are highly branched structures known

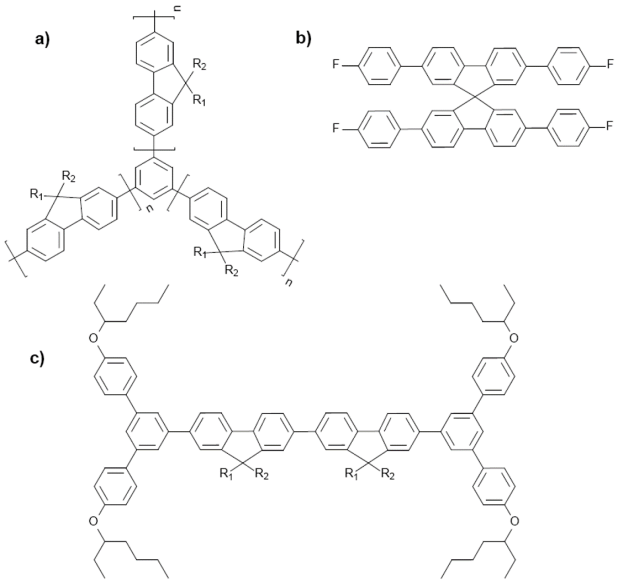

FIGURE 1.17: Structural examples of different oligomers: a) star-shaped oligofluorene benzene, b) spiro-bifluorene, and c) bisfluorene-cored dendrimer [70].

as dendrimers, star shaped molecules and structures integrating sprio-linked cyclopentadiene groups have been investigated allowing alterations influencing the optical and electronic properties [155]. These complex configurations are known to be oligomeric with some examples shown in figure 1.17.

1.5.2 Organic semiconductor lasers

1.5.2.1 Background

Organic lasers utilise carbon based materials forming molecules that act as a gain material. Kogelnik *et al* first demonstrated organic solid state lasers in 1971 [156] obtaining lasing from both a DBR and DFB resonator. In the follwing months, Kaminow *et al* expanded on this work [39]. In both studies dye-doped host polymers were employed as the active gain material. In 1992 the first laser fabricated out of a conjugated polymer in solution were reported [157]. Tessler *et al* reported the first organic laser using a π-conjugated polymer solid-state film in 1996 [158]. Organic semiconductor lasers have advanced since then and have been shown in many different formats with a wide range of gain materials thanks to advances in material synthesis and processing. The physical concept responsible for their electronic and main optical properties is described in the next 2 sections.

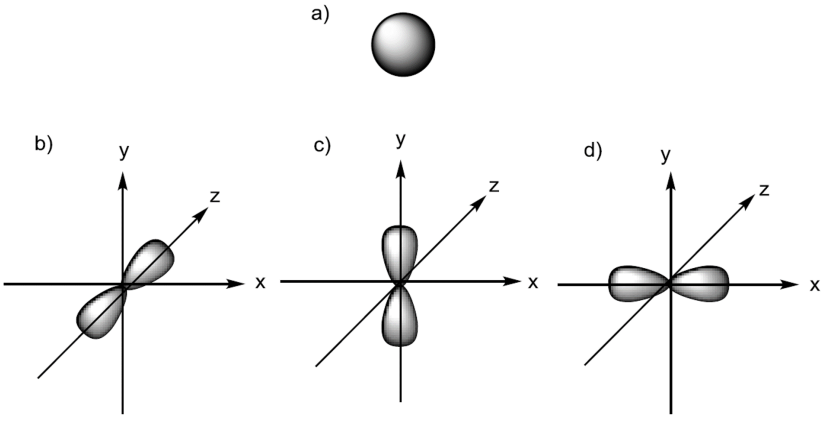

FIGURE 1.18: Representation of the a) 2s orbital and b), c) and d) the 2p orbitals.

1.5.2.2 Electronic properties

Carbon and hydrogen atoms are the main ingredients used to form organic semiconductors where the main structure of polymers is attained from long chains of carbon-carbon bonds. Observing how the atoms within the polymers form, and are bound together, gives an understanding of the electronic and photo-physical properties of the organic semiconductor.

An isolated carbon atom has an electronic configuration of $1s^2 2s^2 2p^2$ with four valence electrons. The 1s orbital contains the core electrons and do not contribute to the bonds. The four valence electrons are in the 2s and 2p orbitals and are responsible for the connection to other atoms. The spatial distribution of these orbitals can be seen in figure 1.18. The unpaired electrons in the 2p orbitals typically permits two bonds in this configuration. This is not always the case as when bonds form, the electronic configuration of the carbon atoms can hybridise. This means that there is mixing of the 2s and 2p orbitals that leads to, for example, an sp^3 hybridisation $1s^2 2s^1 2p^3$. This structure results in a more stable configuration as it enables four bonds in preference to two [159]. A representation of the sp^2 and sp^3 hybridisations is displayed in figure 1.19.

The geometry of the hybridisation depicts the bonding in organic molecules. When the carbon atoms are double bonded, for example ethane (C_2H_4), there are three half-filled sp^2 orbitals (from the 2s orbital) and an unhybridised 2p orbital. For this kind of molecule with sp^2 hybridisation, there are two types of bonds.

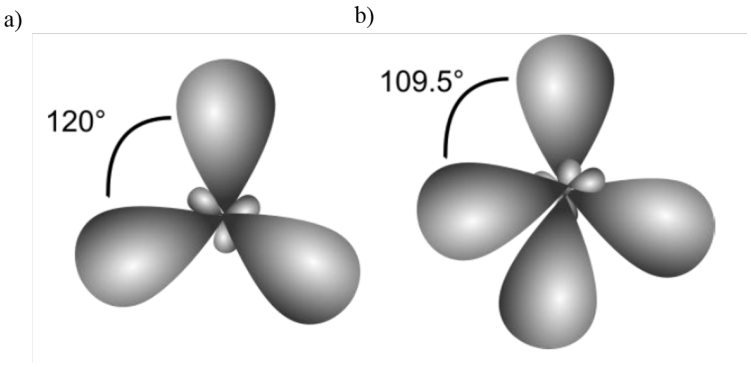

FIGURE 1.19: Depiction of the a) sp^2 and b) the sp^3 hybridisations.

These are σ bonds and π bonds. σ bonds are formed by three sp^2 orbitals of atoms opposite one another and the π bond is formed by the overlap of two parallel 2p orbitals [153, 156].

The σ bonds produce strong and stable links whereas the π bonds are weaker. σ bonds equate to single bonds and a $\sigma + \pi$ bond represents a double bond. In such a representation of a conjugated system the p-orbitals produces alternating single and double bonds between carbon atoms. The π bonds allow electron delocalisation across the overlapping, shared p-orbitals of a group of atoms. This is the foundation when considering conjugated polymers as organic semiconductors. In general, in conjugated molecules the π-electrons are delocalised over the entire molecule. Figure 1.20 is a representation of the ethylene molecule where the electrons in the hybridised π-orbitals are delocalised along the molecule; as it contains only one double bond. In larger molecules (such as benzene) the π-orbitals delocalise along the chain connecting them as there is more than one double bond (where the π bonds conjugate together), leading to a semiconductor-like electronic band-structure [153, 160, 161].

Figure 1.21 displays a phase representation of the wavefunctions of the electrons when a π bond is formed. They can be either in phase or out of phase. When they are out of phase they are said to be antibonding and referred to as π^* orbitals and in phase a π orbital. π^* bonded orbitals have a higher energy than π bonded orbitals. π^* is referred to as the lowest unoccupied molecular orbit (LUMO) and π the highest occupied molecular orbit (HOMO). The HOMO and LUMO orbitals refer to the valence and conduction bands in analogy with inorganic semiconductors and behave in the same manner. Due to the π^* orbital being partially empty the electrons are free to move around it under excitation. This produces conductivity and is directional if the molecule is linear. It is the radiative transition between

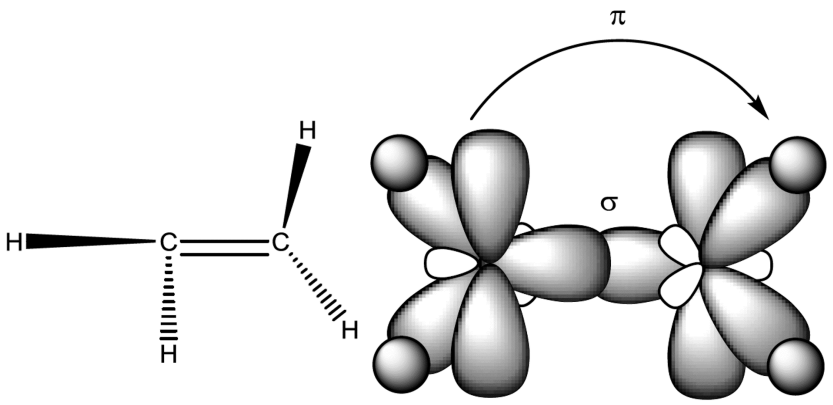

FIGURE 1.20: A schematic illustration the π-electron delocalisation in single and double bonds in an ethylene molecule.

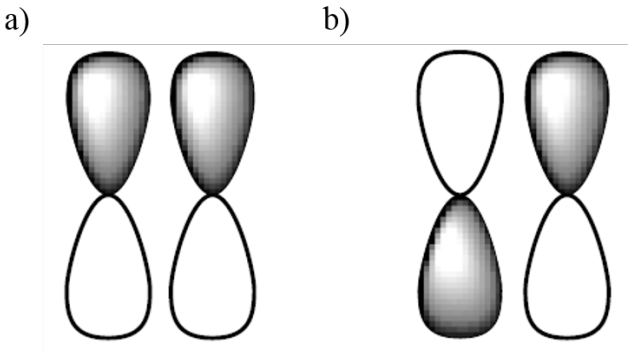

FIGURE 1.21: Phase representation for the wavefunctions of a) π and b) π^* orbitals.

these two orbitals (HOMO and LUMO) that is responsible for the production of light and laser emission in light-emitting organic semiconductors [153, 160].

The π and π^* energy levels can have two electrons each, resulting in four possible combinations of spin $\uparrow\uparrow$, $\downarrow\downarrow$, $\uparrow\downarrow$ and $\downarrow\uparrow$. The total spin dictates the spin states where a singlet state is obtained when the electron spins are paired resulting in a total spin of zero. When there are two unpaired electrons the total spin is one a triplet state is achieved. These excited states are called metastable with a lifetime lasting from microseconds to seconds. In comparison, singlet excited states have a lifetime of the order of nanoseconds [153, 160, 162].

1.5.2.3 Fluorescence and phosphorescence

In a conjugated molecule the optical absorption and emission properties are determined by the electronic transitions between the π and π^* orbitals (typically in

the visible). The conjugation length is a factor that determines the energy gap between them. Higher energy is required for electronic transitions with a short conjugation length resulting in a shorter absorption and emission wavelength [163]. In a way, it is similar to a CQD: a larger molecule confines less the excited carriers, hence the longer emission wavelength.

The emission of photons can be explained by the Franck-Condon principle, depicted in figure 1.22 [164]. External excitation only excites singlets from their ground state S_0 to their excited state S_1 as triplet-singlet transitions are dipole forbidden. These electronic states, S_0 and S_1, are each sub-divided into different vibronic state (caused by the different possible vibration modes of the molecule), where each state has a different energy. Once excited, carriers in a singlet state can relax radiatively to the lowest vibronic state S_0. However, typically the vibration modes of the molecule are different in S_0 and S_1. This means that the lowest vibronic states in S_0 and S_1 correspond to a different molecular arrangement. Upon excitation, a molecule reaches its excited state almost instantly. The molecule then "re-arranges" to minimise its vibrational energy. Upon emission of a photon, the molecule goes to the S_0 level in a higher vibronic level (like for absorption, emission is instantaneous on the time scale of molecular arrangement because electronic transitions are faster than molecular vibration). It then re-arranges to return to the ground state vibronic level. This process results in a red shift of the emission wavelength compared to the absorption. Figure 1.22 shows a typically separated absorption and emission (fluorescence) spectra. This separation of spectra is known as the Stokes shift. Other phenomena, for example absorption due to molecule dispersity, also contribute to the Stokes shift.

Different radiative processes produce different types of luminescence. Singlet state transitions as just discussed have a short lifetime on the order of the ns. This is called fluorescence whereas triplet states have a long lifetime and produce phosphorescence [160, 166, 167]. Singlet states have a probability to spin-flip to become a triplet state (called intersystem crossing). The rate of this intersystem crossing is slower (usually longer than several tens of ns to $> \mu$s depending on the material) than the $S_1 - S_0$ transition. Note that often triplets also absorb in the visible, overlapping with the emission of $S_1 - S_0$ transition, which is detrimental to laser action. This is in fact one reason why organic lasers operate only in the pulsed regime. Under continuous-wave excitation triplet population builds up, which takes away energy and increases absorption at the laser transition.

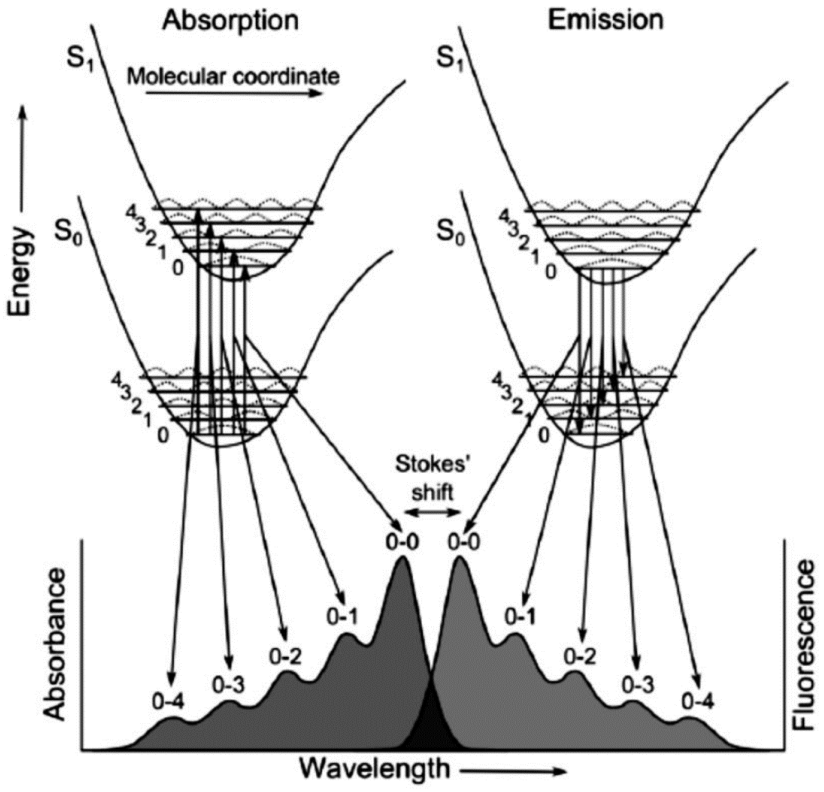

FIGURE 1.22: Absorption and emission spectra of photons illustrating optical transitions in between the S_0 and S_1 electronic states with corresponding fluorescence and absorption spectra displaying the transitions [165].

In terms of laser operation, a larger Stokes shift results in less re-absorption of luminescence. The larger the Stokes shift, the more the molecule approaches a 4-level system as can be intuitively understood from figure 1.22. This is known to lower laser operation thresholds and produce higher photoluminescence quantum yield [164, 168].

1.5.2.4 Organic lasers: State of the art

A literature review of organic lasers based on their properties (wavelength, operational threshold and their photostability) is compiled. The accumulated data contains information on numerous cavity formats including DFB lasers, facetted waveguide lasers, DBR lasers, VCSEL, VECSOL, micro-ring lasers, droplet lasers, doped fibre lasers, random lasers and Fabry-Pérot lasers. All organic lasers, like CQD lasers, are optically pumped.

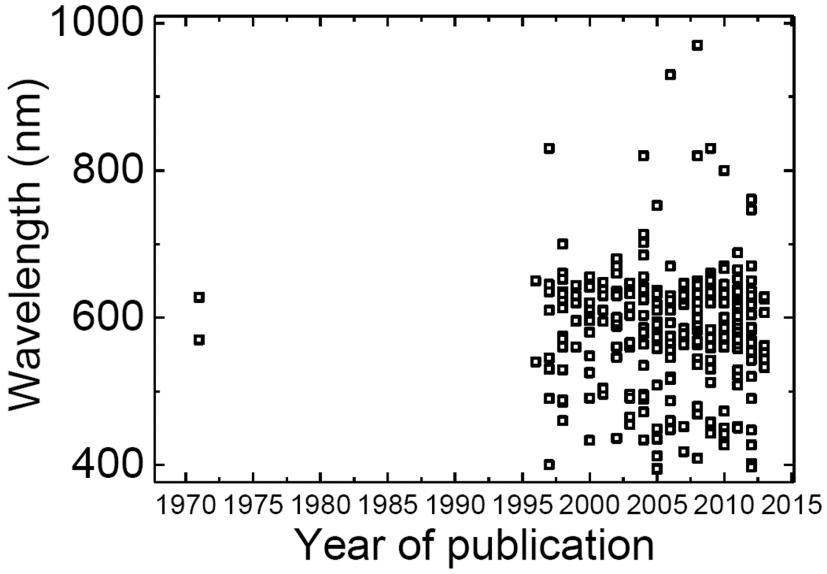

FIGURE 1.23: Overview of reported wavelengths of organic lasers, from [70].

1.5.2.5 Wavelength

Figure 1.23 depicts a synopsis of the emission wavelengths obtained via numerous laser formats. Organic semiconductors can be designed to emit over the entire visible spectrum due to the availability of chromophores. The shortest wavelength was recorded at 361.9nm and utilised spiro-terphenyl whereas the longest was 930nm and was obtained using IR-140 dye [169, 170]. Through the use of different organic materials, such as dyes (DCM, Coumarin, PM-597 etc.), conjugated polymers (BBEHP-PPV, MEH-PPV, DOO-PPV, etc.), and macromolecules (oligofluorene truxene, perylene, etc.), this wide range of emission wavelength can be achieved. There have been more that 350 organic lasers reported in the past 2 decades with the majority (more than two thirds) utilising the DFB laser format [26, 30, 33, 34, 38–40, 45, 147–150, 163, 164, 169–195].

1.5.2.6 Threshold

The values for threshold are typically referred to in terms of the lasers pump energy fluence, F_{th}, or by its power density. The pulse width of the laser emission determines the terminology as emission that is a lot longer than the singlet state lifetime the threshold is signified as the power density and when the pulse width is much shorter than the singlet lifetime, the threshold is expressed as fluence. Fluence is the defined as the time-integrated flux and is expressed as the energy

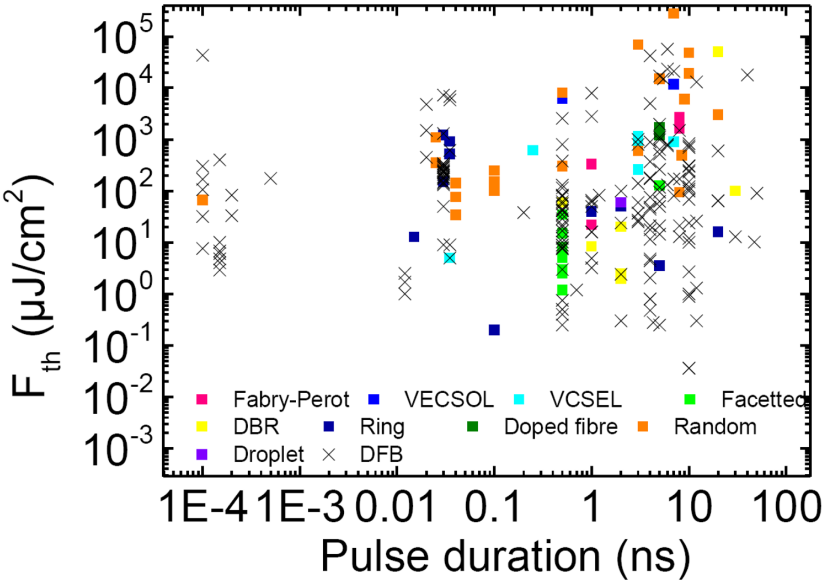

FIGURE 1.24: Overview of reported pump energy fluencies of organic lasers, from [70].

over area (i.e. $\mu J/cm^2$) and the power density is given in kW/cm^2. Figure 1.24 gives a summary of F_{th} reported in the literature as a function of the pump sources pulse duration for different types of organic lasers. Most of these use solid-state lasers or gas lasers as pump sources for optical pumping, where when threshold is low enough, were pumped by laser diodes or light emitting diodes (LEDs) [196–199]. For the majority the pulse duration of the pump sources ranges from 150 fs to 50 ns. As seen with wavelength, the lowest thresholds were obtained from DFB lasers with the lowest being obtained by Karnutsch *et al* [200] [26, 30, 33, 34, 38–40, 45, 147–150, 163, 164, 169–195].

1.5.2.7 Photostability

Under operation when employed as a visible gain material, organic semiconductors have a tendency to degrade. The main culprit of this degradation is photo-oxidation and will be expanded on in the next section, section 1.5.3. Compared with wavelength and threshold, there has been a smaller number of photostability studies carried out on organic semiconductor lasers. Figure 1.25 illustrates the reported values of photostability, F_{deg}, in J/cm^2 [34, 40, 147–150, 170, 171, 179, 201]. F_{deg} typically represents the intensity at the 1/e value of the total exposure from the initial value of intensity. However, some of the values shown in figure 1.25 display values of F_{deg} defined as the intensity drop to 10% or 50% as they are

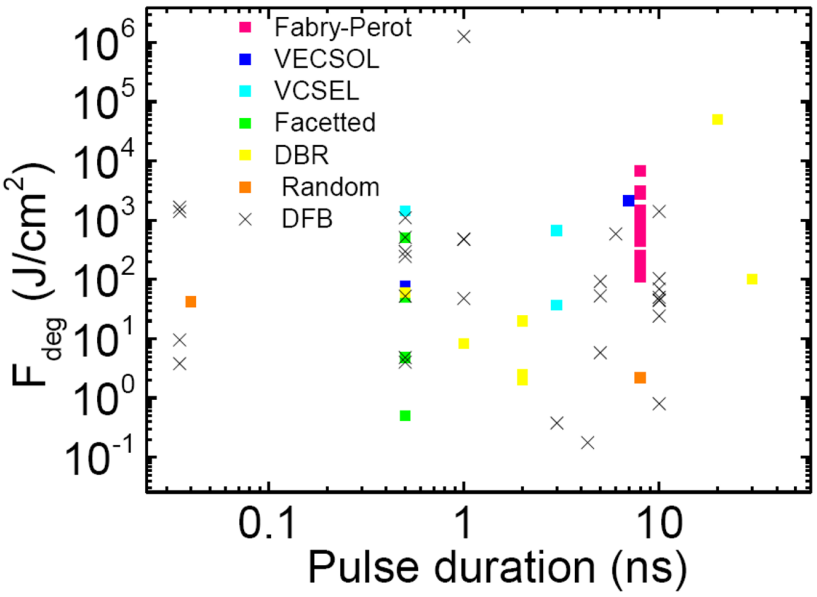

FIGURE 1.25: Overview of reported photostability of organic lasers, from [70].

taken from literature; where sometimes the value is not stated. This means that these values can only give a representation of the order of magnitude for the photostability of organic semiconductor lasers. The longest operational lifetime was achieved, by Richardson *et al* [201], by employing an DFB laser encapsulated in thick glass [180, 202].

1.5.3 Photodegradation

Organic semiconductors are limited in real-world application due to photodegradation. Chemical reactions can be triggered within the materials when exposed to certain conditions resulting in detrimental effects for laser operation. The main mechanisms responsible are heat, high energy and photo-oxidation [203].

As discussed earlier, section 1.5.2.3, the groups that studied the fluorescent and phosphorescent properties in organic semiconductors acknowledged these effects and reported on the mechanisms responsible for photo-induced chemical reactions in dyes [204]. Bleaching of the OSs emission is a consequence of this photo-induced oxidation. The photodegradation in PFO (polyfluorene) has been studied where observations of oxygen atom ketone-bond to the alkyl side chains or even replace them altogether [205, 206]. This is illustrated in figure 1.26a. Studies on MEH-PPV (2 - methoxy - 5 - (2' - ethyl hexyloxy) - p - (phenylene vinylene)) resulted in comparable reactions with photodegradation [207]. After oxidation, the PFO

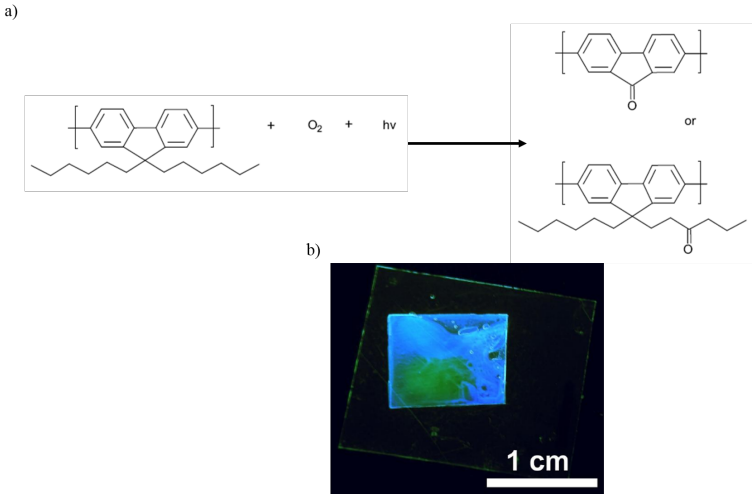

FIGURE 1.26: a) Molecular structure of photo-oxidation of fluorene units, b) photo-oxidation of the oligourene truxene under UV illumination where the green emission is produced from he photo-bleached pump spot.

molecules, usually known as fluorenones, have a reduction in pump absorption, a reduced photoluminescent quantum yield, a reduced intensity in the first (blue) vibronic transition but an increase in the higher (green) vibronic modes [205]. The later results in the polymer appearing greenish after photo-oxidation has taken place, figure 1.26b. This is understood as the polymer experiencing a strong electron-negativity of oxygen deforming, delocalising electrons and inducing non-radiative relaxation processes [206]. This is particularly true when the binding of the oxygen atom to the molecule is ketonic.

To put it another way, photo-oxidation is another means of a relaxation pathway for the excited S_1 state, where the bleaching of the organic light emitters occurs with the presence of oxygen. There are ways to mitigate this effect: device operation in a vacuum or inert (i.e. nitrogen) atmosphere, the addition of functional side-groups to the chromophore that prevent oxygen molecules coming into contact with the active part of the organic semiconductor, blending the chromophores in a protective polymer matrix and encapsulation of the device with another material to provide an oxygen barrier.

Encapsulation has proven to be the most practical and influential method and has been utilised in DFB devices reported in this thesis as it also increases the photo-stability of the device. This has also been exploited commercially with OLEDs employing encapsulation techniques based on inorganic oxygen barriers. Unfortunately, the drawback of this method is that the encapsulation hinder mechanically flexible devices resulting in further research into different suppressing techniques.

1.6 Conclusion

Solution processable gain materials are attractive for manufacturing, potentially at low-cost, visible lasers that are suitable for a range of applications including sensing, medical diagnostics and lab on a chip, spectroscopy, etc. They also allow innovative formats of lasers, e.g. for flexible photonics. However, in the case of organic semiconductors there are various obstacles hindering their utilisation, including photostability and the fact they can intrinsically only operate in a pulsed regime; as a consequence of the triplet state absorbing photons at the laser transitions in organics. CQDs provide an attractive alternative to organic semiconductors as they can be fabricated with the addition of inorganic materials. This is still a young field and, regardless of recent breakthroughs, CQD lasers are not as mature in comparison. In general, the performance of optically pumped CQD lasers in terms of threshold remains limited in the nanosecond regime [104]. But, CQDs are intrinsically more photostable and in principle could operate in continuous-wave.

This chapter has described fundamentals of lasers in view of CQDs and organic semiconductors. The basic physics and characteristics of these two class of colloidal materials was discussed. The work reported in the rest of this document targets the utilisation of both types of fluorescent materials for lasers and studies the resulting laser devices.

References

[1] T. H. MAIMAN. Stimulated Optical Radiation in Ruby. *Nature*, 187(4736):493–494, aug 1960.

[2] A. Javan, W. R. Bennett, and D. R. Herriott. Population inversion and continuous optical maser oscillation in a gas discharge containing a He-Ne mixture. *Physical Review Letters*, 6(3):106–110, 1961.

[3] Graziela V L Gomes, Mirella R. Sola, Luis F P Marostegan, Camila G. Jange, Camila P S Cazado, Ana C. Pinheiro, Antonio A. Vicente, and Samantha C. Pinho. Physico-chemical stability and in vitro digestibility of beta-carotene-loaded lipid nanoparticles of cupuacu butter (Theobroma grandiflorum) produced by the phase inversion temperature (PIT) method. *Journal of Food Engineering*, 192:93–102, 2017.

[4] Xianxian Yao, Xingxing Niu, Kexin Ma, Ping Huang, Julia Grothe, Stefan Kaskel, and Yufang Zhu. Graphene Quantum Dots-Capped Magnetic Mesoporous Silica Nanoparticles as a Multifunctional Platform for Controlled Drug Delivery, Magnetic Hyperthermia, and Photothermal Therapy. *Small*, 1602225:1–11, 2016.

[5] Yuan Gao, Guannan Yu, Yue Wang, Cuong Dang, Tze Chien Sum, Handong Sun, and Hilmi Volkan Demir. Green Stimulated Emission Boosted by Nonradiative Resonant Energy Transfer from Blue Quantum Dots. *Journal of Physical Chemistry Letters*, 7(14):2772–2778, 2016.

[6] Zhengbo Sun, Yuetao Zhao, Zhibin Li, Haodong Cui, Yayan Zhou, Weihao Li, Wei Tao, Han Zhang, Huaiyu Wang, Paul K. Chu, and Xue-Feng Yu. TiL4 -Coordinated Black Phosphorus Quantum Dots as an Efficient Contrast Agent for In Vivo Photoacoustic Imaging of Cancer. *Small*, (021):1602896, 2017.

[7] Kareem AbuBakr Soliman, Howida Kamal Ibrahim, and Mahmoud Mohammed Ghorab. Effects of different combinations of nanocrystallization technologies on avanafil nanoparticles: in vitro, in vivo and stability evaluation. *International Journal of Pharmaceutics*, 517(1-2):148–156, 2017.

[8] Chen Xie, Paul Kumar Upputuri, Xu Zhen, Manojit Pramanik, and Kanyi Pu. Self-quenched semiconducting polymer nanoparticles for amplified invivo photoacoustic imaging. *Biomaterials*, 119:1–8, 2017.

[9] Yuping Yan, Qi Yang, Jie Wang, Hongyu Jin, Jing Wang, Hong Yang, Zhiguo Zhou, Qiwei Tian, and Shiping Yang. Heteropoly blue doped polymer nanoparticles: an efficient theranostic agent for targeted photoacoustic imaging and near-infrared photothermal therapy in vivo. *J. Mater. Chem. B*, 5(2):382–387, 2017.

[10] Prashant V Kamat. Quantum Dot Solar Cells. Semiconductor Nanocrystals as Light Harvesters. *The Journal of Physical Chemistry C*, 112(October):18737–18753, 2008.

[11] István Robel, Vaidyanathan Subramanian, Masaru Kuno, and Prashant V Kamat. Quantum Dot Solar Cells. Harvesting Light Energy with CdSe Nanocrystals Molecularly Linked to Mesoscopic TiO 2 Films. *Journal of the American Chemical Society*, 128(7):2385–2393, feb 2006.

[12] Gerasimos Konstantatos, Ian Howard, Armin Fischer, Sjoerd Hoogland, Jason Clifford, Ethan Klem, Larissa Levina, and Edward H Sargent. Ultrasensitive solution-cast quantum dot photodetectors. *Nature*, 442(7099):180–183, 2006.

[13] Debasis Bera, Lei Qian, Teng-Kuan Tseng, and Paul H. Holloway. Quantum Dots and Their Multimodal Applications: A Review. *Materials*, 3(4):2260–2345, mar 2010.

[14] Laura Piveteau, Ta-Chung Ong, Aaron J Rossini, Lyndon Emsley, Christophe Coperet, and Maksym V. Kovalenko. The Structure of Colloidal Quantum Dots from Dynamic Nuclear Polarization Surface Enhanced NMR Spectroscopy. *Journal of the American Chemical Society*, page 151016160630009, 2015.

[15] Tae-Ho Kim, Kyung-Sang Cho, Eun Kyung Lee, Sang Jin Lee, Jungseok Chae, Jung Woo Kim, Do Hwan Kim, Jang-Yeon Kwon, Gehan Amaratunga, Sang Yoon Lee, Byoung Lyong Choi, Young Kuk, Jong Min Kim, and Kinam Kim. Full-colour quantum dot displays fabricated by transfer printing. *Nature Photonics*, 5(3):176–182, 2011.

[16] K. Thyagarajan and Ajoy Ghatak. *Lasers: Fundamentals and Applications*. Springer, 2nd edition, 2010.

[17] O Svelto, S Taccheo, and C Svelto. Analysis of amplified spontaneous emission: some corrections to the Linford formula. *Optics Communications*, 149(4-6):277–282, 1998.

[18] Orazio Svelto. *Principles of Lasers*. Springer, 1974.

[19] Frank Träger. *Springer Handbook of Laser and optics*. Springer, 2nd edition, 2012.

[20] Karl F. Renk. *Basics of Laser Physics, Graduate Texts in Physics*. Springer Berlin Heidelberg, 2012.

[21] Fumitomo Hide, Ma Diaz-Garcia, and Bj Schwartz. Semiconducting polymers: a new class of solid-state laser materials. *Science*, 273(5283):1833–1836, 1996.

[22] Y. Sorek, R. Reisfeld, I. Finkelstein, and S. Ruschin. Light amplification in a dye-doped glass planar waveguide. *Applied Physics Letters*, 66(10):1169–1171, 1995.

[23] K. L. Shaklee and R. F. Leheny. Direct determination of optical gain in semiconductor crystals. *Applied Physics Letters*, 18(11):475–477, 1971.

[24] I. D. W. Samuel and G. A. Turnbull. Organic Semiconductor Lasers. *Chemical Reviews*, 107(4):1272–1295, apr 2007.

[25] Cuong Dang, Joonhee Lee, Craig Breen, Jonathan S Steckel, Seth Coe-Sullivan, and Arto Nurmikko. Red, green and blue lasing enabled by single-exciton gain in colloidal quantum dot films. *Nature nanotechnology*, 7(5):335–9, may 2012.

[26] D N Kumar, J D Bhawalkar, and P N Prasad. Solid-state cavity lasing from poly(p-phenylene vinylene) silica nanocomposite bulk. *Appl. Optic.*, 37(3):510–513, 1998.

[27] Kenichi Yamashita, Masahiro Ito, Shuhei Sugimoto, Takashi Morishita, and Kunishige Oe. Optically end-pumped plastic waveguide laser with in-line Fabry-Pérot resonator. *Optics Express*, 18(23):24092, nov 2010.

[28] E. Yariv and R. Reisfeld. Laser properties of pyrromethene dyes in sol-gel glasses. *Optical Materials*, 13(1):49–54, 1999.

[29] Roberto Sastre, Virginia Martín, Leoncio Garrido, José Luis Chiara, Beatriz Trastoy, Olga García, Angel Costela, and Inmaculada García Moreno. Dye-doped polyhedral oligomeric silsesquioxane (poss)-modified polymeric matrices for highly efficient and photostable solid-state lasers. *Advanced Functional Materials*, 19(20):3307–3316, 2009.

[30] A. Costela, I. García-Moreno, C. Gómez, O. García, and R. Sastre. New organic-inorganic hybrid matrices doped with rhodamine 6G as solid-state dye lasers. *Applied Physics B: Lasers and Optics*, 75(8):827–833, 2002.

[31] Angel Costela, Inmaculada García-Moreno, Clara Gómez, Olga García, and Roberto Sastre. Enhancement of laser properties of pyrromethene 567 dye incorporated into new organic-inorganic hybrid materials. *Chemical Physics Letters*, 369(5-6):656–661, 2003.

[32] Inmaculada Garcia-Moreno, Francisco Amat-Guerri, Marta Liras, Angel Costela, Lourdes Infantes, Roberto Sastre, Fernando Lopez Arbeloa, Jorge Banuelos Prieto, and Inigo Lopez Arbeloa. Structural changes in the BODIPY dye PM567 enhancing the laser action in liquid and solid media. *Advanced Functional Materials*, 17(16):3088–3098, 2007.

[33] Roberto Sastre, Virginia Martín, Leoncio Garrido, José Luis Chiara, Beatriz Trastoy, Olga García, Angel Costela, and Inmaculada García Moreno. Dye-doped polyhedral oligomeric silsesquioxane (poss)-modified polymeric matrices for highly efficient and photostable solid-state lasers. *Advanced Functional Materials*, 19(20):3307–3316, 2009.

[34] Hadi Rabbani-Haghighi, Sébastien Forget, Sébastien Chénais, and Alain Siove. Highly efficient, diffraction-limited laser emission from a vertical external-cavity surface-emitting organic laser. *Optics letters*, 35(12):1968–1970, 2010.

[35] A E Vasdekis, G Tsiminis, J-C Ribierre, Liam O' Faolain, T F Krauss, G A Turnbull, and I D W Samuel. Diode pumped distributed Bragg reflector lasers based on a dye-to-polymer energy transfer blend. *Optics express*, 14(20):9211–9216, 2006.

[36] M Berggren, a Dodabalapur, R E Slusher, and Z Bao. Light amplification in organic thin films using cascade energy transfer. *Nature*, 389(6650):466–469, 1997.

[37] Naoto Tsutsumi and Takashi Ishibashi. Organic dye lasers with distributed Bragg reflector grating and distributed feedback resonator. *Optics express*, 17(24):21698–21703, 2009.

[38] a. Dodabalapur, M. Berggren, R.E. Slusher, Z. Bao, a. Timko, P. Schiortino, E. Laskowski, H.E. Katz, and O. Nalamasu. Resonators and materials for organic lasers based on energy transfer. *IEEE Journal of Selected Topics in Quantum Electronics*, 4(1):67–74, 1998.

[39] I. P. Kaminow, H. P. Weber, and E. A. Chandross. Poly(methyl methacrylate) dye laser with internal diffraction grating resonator. *Applied Physics Letters*, 18(11):497–499, 1971.

[40] Hadi Rabbani-Haghighi, Sébastien Forget, Sébastien Chénais, Alain Siove, Marie-Claude Castex, and Elena Ishow. Laser operation in nondoped thin films made of a small-molecule organic red-emitter. *Applied Physics Letters*, 95(3):033305, jul 2009.

[41] V. G. Kozlov, V. Bulovic, P. E. Burrows, M. Baldo, V. B. Khalfin, G. Parthasarathy, S. R. Forrest, Y. You, and M. E. Thompson. Study of lasing action based on Forster energy transfer in optically pumped organic semiconductor thin films. *Journal of Applied Physics*, 84(8):4096, 1998.

[42] V. G. Kozlov, V. Bulović, P. E. Burrows, and S. R. Forrest. Laser action in organic semiconductor waveguide and double-heterostructure devices. *Nature*, 389(September):362–364, 1997.

[43] V.G. Kozlov and S.R. Forrest. Lasing action in organic semiconductor thin films. *Current Opinion in Solid State and Materials Science*, 4(2):203–208, 1999.

[44] T. N. Kopylova, G. V. Maier, E. N. Telminov, V. A. Svetlichnyi, and and K. M. Degtyarenko. Optics and Spectroscopy a Double-Frequency Solid-State Laser on Organic Compounds. *Russian Physics Journal*, 52(7):3–8, 2009.

[45] S V Frolov, M Shkunov, Z V Vardeny, and K Yoshino. Ring microlasers from conducting polymers. *Physical Review B*, 56(8):R4363–R4366, 1997.

[46] Makoto Fukuda and Keiichi Mito. Laser oscillation of energy transfer solid-state dye laser with a thin-film ring resonator. *Japanese Journal of Applied Physics, Part 1: Regular Papers and Short Notes and Review Papers*, 39(6 A):3470–3471, 2000.

[47] Juhee Yang, Sang Bum Lee, Jeong Bo Shim, Songky Moon, Soo Young Lee, Sang Wook Kim, Jai Hyung Lee, and Kyungwon An. Enhanced nonresonant optical pumping based on turnstile transport in a chaotic microcavity laser. *Applied Physics Letters*, 93(6), 2008.

[48] Xiang Wu, Hao Li, Liying Liu, and Lei Xu. High quality direct photo-patterned microdisk lasers with organic-inorganic hybrid materials. *IEEE Journal of Quantum Electronics*, 44(1):75–80, 2008.

[49] Lei Shang, Liying Liu, and Lei Xu. Single-frequency coupled asymmetric microcavity laser. *Optics letters*, 33(10):1150–1152, 2008.

[50] Jin-Feng Ku, Qi-Dai Chen, Ran Zhang, and Hong-Bo Sun. Whispering-gallery-mode microdisk lasers produced by femtosecond laser direct writing. *Optics Letters*, 36(15):2871, aug 2011.

[51] Van Duong Ta, Rui Chen, and Han Dong Sun. Self-assembled flexible microlasers. *Advanced Materials*, 24(10), 2012.

[52] T Kobayashi and W J Blau. Laser emission from conjugated polymer in fibre waveguide structur. *Electronic Letters*, 38(2):67–68, 2002.

[53] Takeyuki Kobayashi, Werner J. Blau, Hartwig Tillmann, and Hans Heinrich Hörhold. Light amplification and lasing in a stilbenoid compound-doped glass-clad polymer optical fiber. *IEEE Journal of Quantum Electronics*, 39(5):664–672, 2003.

[54] Alexander Argyros, Martijn A van Eijkelenborg, Stuart D Jackson, and Richard P Mildren. Reply to comment on Microstructured polymer fiber laser. *Optics Letters*, 30(14):1829, jul 2005.

[55] A. Costela, I. García-Moreno, D. del Agua, O. García, and R. Sastre. Highly photostable solid-state dye lasers based on silicon-modified organic matrices. *Journal of Applied Physics*, 101(7):073110, 2007.

[56] G. Wegmann, H. Giessen, D. Hertel, and R.F. Mahrt. Blue-green laser emission from a solid conjugated polymer. *Solid State Communications*, 104(12):759–762, 1997.

[57] I. García-Moreno, A. Costela, M. Pintado-Sierra, V. Martín, and R. Sastre. Enhanced laser action of Perylene-Red doped polymeric materials. *Optics Express*, 17(15):12777, jul 2009.

[58] Matthew Pelton, Jelena Vučković, Glenn Solomon, Charles Santori, Bingyang Zhang, Jocelyn Plant, and Yoshihisa Yamamoto. An efficient source of single photons: A single quantum dot in a micropost microcavity. *Physica E: Low-Dimensional Systems and Nanostructures*, 17:564–567, 2003.

[59] Weiqiang Xie, Yunpeng Zhu, Tangi Aubert, Zeger Hens, Edouard Brainis, and Dries Van Thourhout. Fabrication and characterization of on-chip silicon nitride microdisk integrated with colloidal quantum dots. *Optics Express*, 24(2):A114, 2016.

[60] Yue Wang, Kah Ee Fong, Shancheng Yang, VanDuong Ta, Yuan Gao, Zeng Wang, Venkatram Nalla, Hilmi Volkan Demir, and Handong Sun. Unraveling the ultralow threshold stimulated emission from CdZnS/ZnS quantum dot and enabling high-Q microlasers. *Laser & Photonics Reviews*, 9(5):507–516, 2015.

[61] J. Schafer, J. P. Mondia, R. Sharma, Z. H. Lu, A. S. Susha, A. L. Rogach, and L. J. Wang. Quantum Dot Microdrop Laser. *Nano Letters*, 8(6):1709–1712, jun 2008.

[62] Christos Grivas, Chunyong Li, Peristera Andreakou, Pengfei Wang, Ming Ding, Gilberto Brambilla, Liberato Manna, and Pavlos Lagoudakis. Single-mode tunable laser emission in the single-exciton regime from colloidal nanocrystals. *Nature Communications*, 4(May):2376, aug 2013.

[63] P. T. Snee, Y. Chan, D. G. Nocera, and M. G. Bawendi. Whispering-Gallery-Mode Lasing from a Semiconductor Nanocrystal/Microsphere Resonator Composite. *Advanced Materials*, 17(9):1131–1136, may 2005.

[64] S. Frolov, Z. Vardeny, K. Yoshino, a. Zakhidov, and R. Baughman. Stimulated emission in high-gain organic media. *Physical Review B*, 59(8):R5284–R5287, 1999.

[65] R C Polson, A Chipouline, and Z V Vardeny. Random lasing in π-conjugated films and infiltrated opals. *Advanced Materials*, 13(10):760–764, 2001.

[66] Shiyoshi Yokoyama and Shinro Mashiko. Tuning of Laser Frequency in Random Media of Dye-Doped Polymer and Glass-Particle Hybrid. *Japanese Journal of Applied Physics*, 42(Part 2, No. 8A):L970–L973, 2003.

[67] Li Long, Daisi He, Weiying Bao, Menglei Feng, Peng Zhang, Dingke Zhang, and Shijian Chen. Localized surface plasmon resonance improved lasing performance of Ag nanoparticles/organic dye random laser. *Journal of Alloys and Compounds*, 693:876–881, 2017.

[68] Yanping Xu, Liang Zhang, Song Gao, Ping Lu, Stephen Mihailov, and Xiaoyi Bao. Highly sensitive fiber random-grating-based random laser sensor for ultrasound detection. *Optics Letters*, 42(7):1353, 2017.

[69] Chun-Wei Chen, Huai-Ping Huang, Hung-Chang Jau, Cheng-Yu Wang, Chih-Wei Wu, and Tsung-Hsien Lin. Polarization-asymmetric bidirectional random laser emission from a twisted nematic liquid crystal. *Journal of Applied Physics*, 121(3):033102, 2017.

[70] Johannes Herman Ludwig Hernnsdorf. *Organic Lasers and Nanostructured Organic Films for Hybrid Integration*. PhD thesis, University of Strathclyde, 2012.

[71] P. P. Sorokin and J. R. Lankard. Stimulated Emission Observed from an Organic Dye, Chloro-aluminum Phthalocyanine. *IBM Journal of Research and Development*, 10(2):162–163, 1966.

[72] C. B. Murray and C. R. Kagan. Synthesis and Characterization of Monodisperse Nanocrystals and Close-Packed Nanocrystal Assemblies. *Annual Review of Materials Science*, 30:545–610, 2000.

[73] Victor I Klimov. From fundamental photophysics to multicolor lasing. *Los Alamos Science*, (28):214–220, 2003.

[74] Ulrike Woggon. *Optical Properties of Semiconductor Quantum Dots*, volume 136. Springer Berlin Heidelberg, 1997.

[75] V. I. Klimov. Optical Gain and Stimulated Emission in Nanocrystal Quantum Dots. *Science*, 290(5490):314–317, oct 2000.

[76] Victor I Klimov. Spectral and Dynamical Properties of Multiexcitons in Semiconductor Nanocrystals. *Annual Review of Physical Chemistry*, 58(1):635–673, may 2007.

[77] Andrew M Smith, Aaron M Mohs, and Shuming Nie. Tuning the optical and electronic properties of colloidal nanocrystals by lattice strain. *Nature Nanotechnology*, 4(1):56–63, jan 2009.

[78] Margaret A. Hines and Philippe Guyot-Sionnest. Synthesis and Characterization of Strongly Luminescing ZnS-Capped CdSe Nanocrystals. *The Journal of Physical Chemistry*, 100(2):468–471, jan 1996.

[79] Xiaogang Peng, Michael C. Schlamp, Andreas V. Kadavanich, and A. P. Alivisatos. Epitaxial growth of highly luminescent CdSe/CdS core/shell nanocrystals with photostability and electronic accessibility. *Journal of the American Chemical Society*, 119(30):7019–7029, 1997.

[80] B O Dabbousi, J Rodriguez, F V Mikulec, J R Heine, H Mattoussi, R Ober, K F Jensen, and M G Bawendi. (CdSe)ZnS Core - Shell Quantum Dots : Synthesis and Characterization of a Size Series of Highly Luminescent Nanocrystallites. *J. Phys. Chem. B*, 101(97):9463–9475, 1997.

[81] Peter Reiss, Joël Bleuse, and Adam Pron. Highly Luminescent CdSe/ZnSe Core/Shell Nanocrystals of Low Size Dispersion. *Nano Letters*, 2(7):781–784, 2002.

[82] Jonathan S. Steckel, John P. Zimmer, Seth Coe-Sullivan, Nathan E. Stott, Vladimir Bulović, and Moungi G. Bawendi. Blue luminescence from (CdS)ZnS core-shell nanocrystals. *Angewandte Chemie - International Edition*, 43(16):2154–2158, 2004.

[83] Hsueh Shih Chen, Bertrand Lo, Jen Yu Hwang, Gwo Yang Chang, Chien Ming Chen, Shih Jung Tasi, and Shian Jy Jassy Wang. Colloidal ZnSe, ZnSe/ZnS, and ZnSe/ZnSeS quantum dots synthesized from ZnO. *Journal of Physical Chemistry B*, 108(44):17119–17123, 2004.

[84] Huaibin Shen, Hongzhe Wang, Xiaomin Li, Jin Zhong Niu, Hua Wang, Xia Chen, and Lin Song Li. Phosphine-free synthesis of high quality ZnSe, ZnSe/ZnS, and Cu-, Mn-doped ZnSe nanocrystals. *Dalton Trans.*, (47):10534–10540, 2009.

[85] Dingan Chen, Fei Zhao, Hang Qi, Michael Rutherford, and Xiaogang Peng. Bright and stable purple/blue emitting CdS/ZnS Core/Shell nanocrystals grown by thermal cycling using a single-source precursor. *Chemistry of Materials*, 22(4):1437–1444, 2010.

[86] Marco Cirillo, Tangi Aubert, Raquel Gomes, Rik Van Deun, Philippe Emplit, Amelie Biermann, Holger Lange, Christian Thomsen, Edouard Brainis, and Zeger Hens. Flash Synthesis of CdSe/CdS CoreShell Quantum Dots. *Chemistry of Materials*, 26(2):1154–1160, 2014.

[87] Renguo Xie, Ute Kolb, Jixue Li, Thomas Basché, and Alf Mews. Synthesis and Characterization of Highly Luminescent CdSeCore CdS/Zn 0.5 Cd 0.5 S/ZnS Multishell Nanocrystals. *Journal of the American Chemical Society*, 127(20):7480–7488, 2005.

[88] Sergei A. Ivanov, Jagjit Nanda, Andrei Piryatinski, Marc Achermann, Laurent P. Balet, Ilia V. Bezel, Polina O. Anikeeva, Sergei Tretiak, and Victor I. Klimov. Light amplification using inverted core/shell nanocrystals: Towards lasing in the single-exciton regime. *Journal of Physical Chemistry B*, 108(30):10625–10630, 2004.

[89] L. P. Balet, S. A. Ivanov, A. Piryatinski, M. Achermann, and V. I. Klimov. Inverted core/shell nanocrystals continuously tunable between type-I and type-II localization regimes. *Nano Letters*, 4(8):1485–1488, 2004.

[90] Xinhua Zhong, Renguo Xie, Ying Zhang, Thomas Basché, and Wolfgang Knoll. High-quality violet- To red-emitting ZnSe/CdSe core/shell nanocrystals. *Chemistry of Materials*, 17(16):4038–4042, 2005.

[91] Zhenxiao Pan, Hua Zhang, Kan Cheng, Yumei Hou, Jianli Hua, and Xinhua Zhong. Highly efficient inverted type-I CdS/CdSe core/shell structure QD-sensitized solar cells. *ACS Nano*, 6(5):3982–3991, 2012.

[92] Sungjee Kim, Brent Fisher, Hans-Jürgen Eisler, and Moungi Bawendi. Type-II quantum dots: CdTe/CdSe(core/shell) and CdSe/ZnTe(core/shell) heterostructures. *Journal of the American Chemical Society*, 125(38):11466–7, sep 2003.

[93] Renguo Xie, Xinhua Zhong, and Thomas Basche. Synthesis, characterization, and spectroscopy of type-II core/shell semiconductor nanocrystals with ZnTe cores. *Advanced Materials*, 17(22):2741–2745, 2005.

[94] Dmitri V. Talapin, Andrey L. Rogach, Andreas Kornowski, Markus Haase, and Horst Weller. Highly Luminescent Monodisperse CdSe and CdSe/ZnS Nanocrystals Synthesized in a HexadecylamineTrioctylphosphine OxideTrioctylphospine Mixture. *Nano Letters*, 1(4):207–211, apr 2001.

[95] Joel Van Embden, Anthony S R Chesman, and Jacek J. Jasieniak. The heat-up synthesis of colloidal nanocrystals. *Chemistry of Materials*, 27(7):2246–2285, 2015.

[96] C. B. Murray, D. J. Norris, and M. G. Bawendi. Synthesis and characterization of nearly monodisperse CdE (E = sulfur, selenium, tellurium) semiconductor nanocrystallites. *Journal of the American Chemical Society*, 115(19):8706–8715, sep 1993.

[97] Victor K. LaMer and Robert H. Dinegar. Theory, Production and Mechanism of Formation of Monodispersed Hydrosols. *Journal of the American Chemical Society*, 72(11):4847–4854, nov 1950.

[98] Z. Adam Peng and Xiaogang Peng. Nearly Monodisperse and Shape-Controlled CdSe Nanocrystals via Alternative Routes: Nucleation and Growth. *Journal of the American Chemical Society*, 124(13):3343–3353, apr 2002.

[99] Jongnam Park, Jin Joo, Gu Kwon Soon, Youngjin Jang, and Taeghwan Hyeon. Synthesis of monodisperse spherical nanocrystals. *Angewandte Chemie - International Edition*, 46(25):4630–4660, 2007.

[100] Sergei A. Ivanov, Andrei Piryatinski, Jagjit Nanda, Sergei Tretiak, Kevin R. Zavadil, William O. Wallace, Don Werder, and Victor I. Klimov. Type-II core/shell CdS/ZnSe nanocrystals: Synthesis, electronic structures, and spectroscopic properties. *Journal of the American Chemical Society*, 129(38):11708–11719, 2007.

[101] Jiwon Bang, Juwon Park, Ji Hwang Lee, Nayoun Won, Jutaek Nam, Jongwoo Lim, Byoung Yong Chang, Hyo Joong Lee, Bonghwan Chon, Junghan Shin, Jae Byung Park, Jong Hwa Choi, Kilwon Cho, Su Moon Park, Taiha Joo, and Sungjee Kim. ZnTe/ZnSe (core/shell) type-II quantum dots: Their optical and photovoltaic properties. *Chemistry of Materials*, 22(1):233–240, 2010.

[102] J. Jack Li, Y. Andrew Wang, Wenzhuo Guo, Joel C. Keay, Tetsuya D. Mishima, Matthew B. Johnson, and Xiaogang Peng. Large-scale synthesis of nearly monodisperse CdSe/CdS core/shell nanocrystals using air-stable reagents via successive ion layer adsorption and reaction. *Journal of the American Chemical Society*, 125(41):12567–12575, 2003.

[103] Marek Korkusinski, Oleksandr Voznyy, and Pawel Hawrylak. Fine structure and size dependence of exciton and biexciton optical spectra in CdSe nanocrystals. *Physical Review B - Condensed Matter and Materials Physics*, 82(24):1–16, 2010.

[104] Fengjia Fan, Oleksandr Voznyy, P Randy, Kristopher T Bicanic, Michael M Adachi, James R Mcbride, Kemar R Reid, Young-shin Park, Xiyan Li, Ankit Jain, Rafael Quinterobermudez, Mayuran Saravanapavanantham, Min Liu, Marek Korkusinski, Pawel Hawrylak, Victor I Klimov, Sandra J Rosenthal, Sjoerd Hoogland, and Edward H Sargent. Continuous-wave lasing in colloidal quantum dot solids enabled by facet-selective epitaxy. *Nature*, 544(7648):1–18, 2017.

[105] Younghwan Choi, Sangwan Sim, Seong Chu Lim, Young Hee Lee, and Hyunyong Choi. Ultrafast biexciton spectroscopy in semiconductor quantum dots: evidence for early emergence of multiple-exciton generation. *Scientific reports*, 3:3206, 2013.

[106] Victor I. Klimov, Sergei A. Ivanov, Jagjit Nanda, Marc Achermann, Ilya Bezel, John A. McGuire, and Andrei Piryatinski. Single-exciton optical gain in semiconductor nanocrystals. *Nature*, 447(7143):441–446, may 2007.

[107] Kwangdong Roh, Cuong Dang, Joonhee Lee, Songtao Chen, Jonathan S. Steckel, Seth Coe-Sullivan, and Arto Nurmikko. Surface-emitting red, green, and blue colloidal quantum dot distributed feedback lasers. *Optics Express*, 22(15):18800, jul 2014.

[108] A. V. Malko, A. A. Mikhailovsky, M. A. Petruska, J. A. Hollingsworth, H. Htoon, M. G. Bawendi, and V. I. Klimov. From amplified spontaneous emission to microring lasing using nanocrystal quantum dot solids. *Applied Physics Letters*, 81(7):1303, 2002.

[109] S. Hoogland, V. Sukhovatkin, I. Howard, S. Cauchi, L. Levina, and E. H. Sargent. A solution-processed 1.53 μm quantum dot laser with temperature-invariant emission wavelength. *Optics Express*, 14(8):3273, apr 2006.

[110] V. M. Menon, M. Luberto, N. V. Valappil, and S. Chatterjee. Lasing from InGaP quantum dots in a spin-coated flexible microcavity. *Optics Express*, 16(24):19535, nov 2008.

[111] Yujie Chen, Johannes Herrnsdorf, Benoit Guilhabert, Yanfeng Zhang, Ian M. Watson, Erdan Gu, Nicolas Laurand, and Martin D. Dawson. Colloidal quantum dot random laser. *Optics Express*, 19(4):2996, feb 2011.

[112] Yujie Chen, Benoit Guilhabert, Johannes Herrnsdorf, Yanfeng Zhang, Allan R. Mackintosh, Richard a. Pethrick, Erdan Gu, Nicolas Laurand, and Martin D. Dawson. Flexible distributed-feedback colloidal quantum dot laser. *Applied Physics Letters*, 99(24):241103, 2011.

[113] Francesco Todescato, Ilaria Fortunati, Samuele Gardin, Eleonora Garbin, Elisabetta Collini, Renato Bozio, Jacek J. Jasieniak, Gioia Della Giustina, Giovanna Brusatin, Stefano Toffanin, and Raffaella Signorini. Soft-Lithographed Up-Converted Distributed Feedback Visible Lasers Based on CdSe-CdZnS-ZnS Quantum Dots. *Advanced Functional Materials*, 22(2):337–344, jan 2012.

[114] V. C. Sundar, H.-J. Eisler, T. Deng, Y. Chan, E. L. Thomas, and M. G. Bawendi. Soft-Lithographically Embossed, Multilayered Distributed-Feedback Nanocrystal Lasers. *Advanced Materials*, 16(23-24):2137–2141, dec 2004.

[115] George E. Cragg and Alexander L. Efros. Suppression of Auger Processes in Confined Structures. *Nano Letters*, 10(1):313–317, jan 2010.

[116] Lin-Wang Wang, Marco Califano, Alex Zunger, and Alberto Franceschetti. Pseudopotential Theory of Auger Processes in CdSe Quantum Dots. *Physical Review Letters*, 91(5):056404, jul 2003.

[117] V.A. Kharchenko and M. Rosen. Auger relaxation processes in semiconductor nanocrystals and quantum wells. *Journal of Luminescence*, 70(1-6):158–169, 1996.

[118] Leeann Kim, Polina O. Anikeeva, Seth A. Coe-Sullivan, Jonathan S. Steckel, Moungi G. Bawendi, and Vladimir Bulovic. Contact Printing of Quantum Dot Light-Emitting Devices. *Nano Letters*, 8(12):4513–4517, dec 2008.

[119] Praket P. Jha and Philippe Guyot-Sionnest. Trion decay in colloidal quantum dots. *ACS Nano*, 3(4):1011–1015, 2009.

[120] Marco Marceddu, Michele Saba, Francesco Quochi, Adriano Lai, Jing Huang, Dmitri V Talapin, Andrea Mura, and Giovanni Bongiovanni. Charged excitons, Auger recombination and optical gain in CdSe/CdS nanocrystals. *Nanotechnology*, 23(1):015201, 2011.

[121] Victor I. Klimov. Optical Nonlinearities and Ultrafast Carrier Dynamics in Semiconductor Nanocrystals. *The Journal of Physical Chemistry B*, 104(26):6112–6123, 2000.

[122] V. I. Klimov, A. A. Mikhailovsky, D. W. McBranch, C. A. Leatherdale, and M. G. Bawendi. Quantization of Multiparticle Auger Rates in Semiconductor Quantum Dots. *Science*, 287(5455):1011–1013, 2000.

[123] V. I. Klimov. Quantization of Multiparticle Auger Rates in Semiconductor Quantum Dots. *Science*, 287(5455):1011–1013, feb 2000.

[124] R. D. Schaller and V. I. Klimov. High efficiency carrier multiplication in PbSe nanocrystals: Implications for solar energy conversion. *Physical Review Letters*, 92(18):186601–1, 2004.

[125] Florencio Garcia-Santamaria, Yongfen Chen, Javier Vela, Richard D. Schaller, Jennifer A. Hollingsworth, and Victor I. Klimov. Suppressed Auger Recombination in Giant Nanocrystals Boosts Optical Gain Performance. *Nano Letters*, 9(10):3482–3488, oct 2009.

[126] Wei Qin, Raman A. Shah, and Philippe Guyot-Sionnest. CdSeS/ZnS Alloyed Nanocrystal Lifetime and Blinking Studies under Electrochemical Control. *ACS Nano*, 6(1):912–918, jan 2012.

[127] Young-Shin Park, Wan Ki Bae, Thomas Baker, Jaehoon Lim, and Victor I. Klimov. Effect of Auger Recombination on Lasing in Heterostructured Quantum Dots with Engineered Core/Shell Interfaces. *Nano Letters*, 15(11):7319–7328, 2015.

[128] Robert E Bailey and Shuming Nie. Alloyed semiconductor quantum dots: tuning the optical properties without changing the particle size. *Journal of the American Chemical Society*, 125(23):7100–6, jun 2003.

[129] Joel Q. Grim, Sotirios Christodoulou, Francesco Di Stasio, Roman Krahne, Roberto Cingolani, Liberato Manna, and Iwan Moreels. Continuous-wave biexciton lasing at room temperature using solution-processed quantum wells. *Nature Nanotechnology*, 9(11):891–895, oct 2014.

[130] Yusuf Kelestemur, Murat Olutas, Savas Delikanli, Burak Guzelturk, Mehmet Zafer Akgul, and Hilmi Volkan Demir. Type-II Colloidal Quantum Wells: CdSe/CdTe Core/Crown Heteronanoplatelets. *Journal of Physical Chemistry C*, 119:21772185, 2015.

[131] Veena Hariharan Iyer, Rekha Mahadevu, and Anshu Pandey. Low Threshold Quantum Dot Lasers. *The Journal of Physical Chemistry Letters*, 7:1244–1248, 2016.

[132] Hyochul Kim, Kyung-Sang Cho, Heejeong Jeong, Jineun Kim, Chang-Won Lee, Weon-kyu Koh, Young-Geun Roh, Sung Woo Hwang, and Yeonsang Park. Single-Mode Lasing from a Monolithic Microcavity with Few-Monolayer-Thick Quantum Dot Films. *ACS Photonics*, page acsphotonics.6b00327, 2016.

[133] Peter Reiss, Myriam Protière, and Liang Li. Core/Shell semiconductor nanocrystals. *Small (Weinheim an der Bergstrasse, Germany)*, 5(2):154–68, feb 2009.

[134] Burak Guzelturk, Yusuf Kelestemur, Kivanc Gungor, Aydan Yeltik, Mehmet Zafer Akgul, Yue Wang, Rui Chen, Cuong Dang, Handong Sun, and Hilmi Volkan Demir. Stable and Low-Threshold Optical Gain in CdSe/CdS Quantum Dots: An All-Colloidal Frequency Up-Converted Laser. *Advanced Materials*, 27(17):2741–2746, 2015.

[135] Young Shin Park, Wan Ki Bae, Jeffrey M. Pietryga, and Victor I. Klimov. Auger recombination of biexcitons and negative and positive trions in individual quantum dots. *ACS Nano*, 8(7):7288–7296, 2014.

[136] Anju K Augustine, P Radhakrishnan, V P N Nampoori, and M Kailasnath. Enhanced random lasing from a colloidal CdSe quantum dot-Rh6G system. *Laser Physics Letters*, 12(2):025006, 2015.

[137] B. Guilhabert, C. Foucher, A-M. Haughey, E. Mutlugun, Y. Gao, J. Herrnsdorf, H.D. Sun, H.V. Demir, M.D. Dawson, and N. Laurand. Nanosecond colloidal quantum dot lasers for sensing. *Optics Express*, 22(6):7308, mar 2014.

[138] C. Foucher, B. Guilhabert, N. Laurand, and M. D. Dawson. Wavelength-tunable colloidal quantum dot laser on ultra-thin flexible glass. *Applied Physics Letters*, 104(14):141108, apr 2014.

[139] Hans Jürgen Eisler, Vikram C. Sundar, Moungi G. Bawendi, Michael Walsh, Henry I. Smith, and Victor Klimov. Color-selective semiconductor nanocrystal laser. *Applied Physics Letters*, 80(24):4614–4616, 2002.

[140] C. Dang, J. Lee, K. Roh, H. Kim, S. Ahn, H. Jeon, C. Breen, J. S. Steckel, S. Coe-Sullivan, and a. Nurmikko. Highly efficient, spatially coherent distributed feedback lasers from dense colloidal quantum dot films. *Applied Physics Letters*, 103(17), 2013.

[141] Cuong Dang and Arto Nurmikko. Beyond quantum dot LEDs: Optical gain and laser action in red, green, and blue colors. *MRS Bulletin*, 38(09):737–742, 2013.

[142] S M Spillane, S M Spillane, T J Kippenberg, T J Kippenberg, K J Vahala, and K J Vahala. Ultralow-threshold Raman laser using a spherical dielectric microcavity. *Nature*, 415:621–623, 2002.

[143] D K Armani, T J Kippenberg, S M Spillane, and K J Vahala. Ultra-high-Q toroid microcavity on a chip. *Nature*, 421(6926):925–8, 2003.

[144] Yinthai Chan, Jonathan S. Steckel, Preston T. Snee, J. Michel Caruge, Justin M. Hodgkiss, Daniel G. Nocera, and Moungi G. Bawendi. Blue semiconductor nanocrystal laser. *Applied Physics Letters*, 86(7):1–3, 2005.

[145] Bumki Min, Sungjee Kim, Koichi Okamoto, Lan Yang, Axel Scherer, Harry Atwater, and Kerry Vahala. Ultralow threshold on-chip microcavity nanocrystal quantum dot lasers. *Applied Physics Letters*, 89(19):2004–2007, 2006.

[146] Deniz Armani, Bumki Min, Andrea Martin, and Kerry J. Vahala. Electrical thermo-optic tuning of ultrahigh-Q microtoroid resonators. *Applied Physics Letters*, 85(22):5439–5441, 2004.

[147] S. Riechel, U. Lemmer, J. Feldmann, S. Berleb, A. G. Mückl, W. Brütting, A. Gombert, and V. Wittwer. Very compact tunable solid-state laser utilizing a thin-film organic semiconductor. *Optics Letters*, 26(9):593, may 2001.

[148] Yuji Oki, Shinichi Miyamoto, Masamitsu Tanaka, Duluo Zuo, and Mitsuo Maeda. Long lifetime and high repetition rate operation from distributed feedback plastic waveguided dye lasers. *Optics Communications*, 214(1-6):277–283, 2003.

[149] Ruidong Xia, Wen Yong Lai, Peter A. Levermore, Wei Huang, and Donal D C Bradley. Low-threshold distributed-feed back lasers based on pyrene-cored starburst molecules with 1,3,6,8attached oligo(9,9-Dialkylfluorene) arms. *Advanced Functional Materials*, 19(17):2844–2850, 2009.

[150] V. Trabadelo, A. Juarros, A. Retolaza, S. Merino, M. G. Ramírez, V. Navarro-Fuster, J. M. Villalvilla, P. G. Boj, J. A. Quintana, and M. A. Díaz-García. Highly photostable solid-state organic distributed feedback laser fabricated via thermal nanoimprint lithography. *Microelectronic Engineering*, 87(5-8):1428–1430, 2010.

[151] C. K. Chiang, C. R. Fincher, Y. W. Park, A. J. Heeger, H. Shirakawa, E. J. Louis, S. C. Gau, and Alan G. MacDiarmid. Electrical conductivity in doped polyacetylene. *Physical Review Letters*, 39(17):1098–1101, 1977.

[152] Alan J. Heeger. Semiconducting polymers: the Third Generation. *Chemical Society Reviews*, 39(7):2354, 2010.

[153] N. C. Greenham, I. D W Samuel, G. R. Hayes, R. T. Phillips, Y. A R R Kessener, S. C. Moratti, A. B. Holmes, and R. H. Friend. Measurement of absolute photoluminescence quantum efficiencies in conjugated polymers. *Chemical Physics Letters*, 241(1-2):89–96, 1995.

[154] Ashu K. Bansal, Arvydas Ruseckas, Paul E. Shaw, and Ifor D W Samuel. Fluorescence quenchers in mixed phase polyfluorene films. *Journal of Physical Chemistry C*, 114(41):17864–17867, 2010.

[155] Neil A. Montgomery, Jean Christophe Denis, Stefan Schumacher, Arvydas Ruseckas, Peter J. Skabara, Alexander Kanibolotsky, Martin J. Paterson, Ian Galbraith, Graham A. Turnbull, and Ifor D W Samuel. Optical excitations in star-shaped fluorene molecules. *Journal of Physical Chemistry A*, 115(14):2913–2919, 2011.

[156] H. Kogelnik and C. V. Shank. Stimulated emission in a periodic structure. *Applied Physics Letters*, 18(4):152–154, 1971.

[157] Daniel Moses. High quantum efficiency luminescence from a conducting polymer in solution: A novel polymer laser dye. *Applied Physics Letters*, 60(26):3215–3216, 1992.

[158] N. Tessler, G. J. Denton, and R. H. Friend. Lasing from conjugated-polymer microcavities. *Nature*, 382(6593):695–697, aug 1996.

[159] Th Forster. Energiewanderung und Fluoreszenz. *Die Naturwissenschaften*, 33(6):166–175, 1946.

[160] Mark Fox. *Optical Properties of Solids*. Oxford university press, 2001.

[161] R. C Haddon. Hybridization and the orientation and alignment of π-orbitals in nonplanar conjugated organic molecules: π-orbital axis vector analysis (POAV2). *Journal of the American Chemical Society*, 108(11):2837–2842, may 1986.

[162] Ruidong Xia, George Heliotis, Yanbing Hou, and Donal D.C. Bradley. Fluorene-based conjugated polymer optical gain media. *Organic Electronics*, 4(2-3):165–177, 2003.

[163] Georgios Tsiminis, Yue Wang, Paul E. Shaw, Alexander L. Kanibolotsky, Igor F. Perepichka, Martin D. Dawson, Peter J. Skabara, Graham A. Turnbull, and Ifor D W Samuel. Low-threshold organic laser based on an oligofluorene truxene with low optical losses. *Applied Physics Letters*, 94(24):1–4, 2009.

[164] G. Heliotis, R. Xia, G. a. Turnbull, P. Andrew, W. L. Barnes, I. D. W. Samuel, and D. D. C. Bradley. Emission Characteristics and Performance Comparison of Polyfluorene Lasers with One- and Two-Dimensional Distributed Feedback. *Advanced Functional Materials*, 14(1):91–97, 2004.

[165] A. Jabłoński. Über den Mechanismus der Photolumineszenz von Farbstoffphosphoren. *Zeitschrift für Physik*, 94(1-2):38–46, 1935.

[166] Gilbert N. Lewis and Michael Kasha. Phosphorescence and the Triplet State. *Journal of the American Chemical Society*, 66(12):2100–2116, 1944.

[167] D. Hertel, S. Setayesh, H. G. Nothofer, U. Scherf, K. Müllen, and H. Bässler. Phosphorescence in Conjugated Poly (para-phenylene) -Derivatives. *Advanced Materials*, 13(1):65–70, 2001.

[168] Jenny Clark and Guglielmo Lanzani. Organic photonics for communications. *Nature Photonics*, 4(7):438–446, 2010.

[169] T. Spehr, A. Siebert, T. Fuhrmann-Lieker, J. Salbeck, T. Rabe, T. Riedl, H. H. Johannes, W. Kowalsky, J. Wang, T. Weimann, and P. Hinze. Organic solid-state ultraviolet-laser based on spiro-terphenyl. *Applied Physics Letters*, 87(16):1–3, 2005.

[170] P. Del Carro, A. Camposeo, R. Stabile, E. Mele, L. Persano, R. Cingolani, and D. Pisignano. Near-infrared imprinted distributed feedback lasers. *Applied Physics Letters*, 89(20), 2006.

[171] Johannes Herrnsdorf, Benoit Guilhabert, Yujie Chen, Alexander Kanibolotsky, Allan Mackintosh, Richard Pethrick, Peter Skabara, Erdan Gu, Nicolas Laurand, and Martin Dawson. Flexible blue-emitting encapsulated organic semiconductor DFB laser. *Optics Express*, 18(25):25535, dec 2010.

[172] V. Bulovi. Transform-Limited, Narrow-Linewidth Lasing Action in Organic Semiconductor Microcavities. *Science*, 279(5350):553–555, 1998.

[173] Christoph Vannahme, Florian Maier-Flaig, Uli Lemmer, and Anders Kristensen. Single-mode biological distributed feedback laser. *Lab on a Chip*, 13(14):2675, 2013.

[174] Leonid M. Goldenberg, Victor Lisinetskii, Yuri Gritsai, Joachim Stumpe, and Sigurd Schrader. Second order DFB lasing using reusable grating inscribed in azobenzene-containing material. *Optical Materials Express*, 2(1):11, 2012.

[175] Bodo H. Wallikewitz, Gueorgui O. Nikiforov, Henning Sirringhaus, and Richard H. Friend. A nanoimprinted, optically tuneable organic laser. *Applied Physics Letters*, 100(17):17–20, 2012.

[176] Ran Ding, Hong-Hua Fang, Ying Wang, Shi-Yang Lu, Xu-Lin Zhang, Lei Wang, Jing Feng, Qi-Dai Chen, and Hong-Bo Sun. Distributed feedback lasing from thin organic crystal based on active waveguide grating structures. *Organic Electronics*, 13(9):1602–1605, 2012.

[177] Cameron L. C. Smith, Johan U. Lind, Claus H. Nielsen, Mads B. Christiansen, Thomas Buss, Niels B. Larsen, and Anders Kristensen. Enhanced transduction of photonic crystal dye lasers for gas sensing via swelling polymer film. *Optics Letters*, 36(8):1392–94, 2011.

[178] Johannes Herrnsdorf, Yue Wang, Jonathan J D Mckendry, Zheng Gong, David Massoubre, Benoit Guilhabert, Georgios Tsiminis, Graham A. Turnbull, Ifor D W Samuel, Nicolas Laurand, Erdan Gu, and Martin D. Dawson. Micro-LED pumped polymer laser: A discussion of future pump sources for organic lasers. *Laser and Photonics Reviews*, 7(6):1065–1078, 2013.

[179] O. V. Sakhno, J. Stumpe, and T. N. Smirnova. Distributed feedback dye laser holographically induced in improved organic-inorganic photocurable nanocomposites. *Applied Physics B: Lasers and Optics*, 103(4):907–916, 2011.

[180] C. Foucher, B. Guilhabert, A. L. Kanibolotsky, P. J. Skabara, N. Laurand, and M. D. Dawson. Highly-photostable and mechanically flexible all-organic semiconductor lasers. *Optical Materials Express*, 3(5):584, apr 2013.

[181] Andrea Camposeo, Pompilio Del Carro, Luana Persano, and Dario Pisignano. Electrically tunable organic distributed feedback lasers embedding nonlinear optical molecules. *Advanced Materials*, 24(35):221–225, 2012.

[182] Wenbin Huang, Zhihui Diao, Lishuang Yao, Zhaoliang Cao, Yonggang Liu, Ji Ma, and Li Xuan. Electrically tunable distributed feedback laser emission from scaffolding morphologic holographic polymer dispersed liquid crystal grating. *Applied Physics Express*, 6(2), 2013.

[183] Guojian Yang, Xiao Chen, Yiquan Wang, and Shuai Feng. Lasing characteristic of organic octagonal quasicrystal slabs with single-defect microcavity at low-index contrast. *Optics Express*, 21(9):11457, 2013.

[184] Stefano Toffanin, Sunghwan Kim, Susanna Cavallini, Marco Natali, Valentina Benfenati, Jason J. Amsden, David L. Kaplan, Roberto Zamboni, Michele Muccini, and Fiorenzo G. Omenetto. Low-threshold blue lasing from silk fibroin thin films. *Applied Physics Letters*, 101(9), 2012.

[185] Georgios Tsiminis, Yue Wang, Alexander L. Kanibolotsky, Anto R. Inigo, Peter J. Skabara, Ifor D W Samuel, and Graham A. Turnbull. Nanoimprinted organic semiconductor laser pumped by a light-emitting diode. *Advanced Materials*, 25(20):2826–2830, 2013.

[186] Yue Wang, Georgios Tsiminis, Alexander L. Kanibolotsky, Peter J. Skabara, Ifor D.W. Samuel, and Graham A. Turnbull. Nanoimprinted polymer lasers with threshold below 100 W/cmˆ2 using mixed-order distributed feedback resonators. *Optics Express*, 21(12):14362, jun 2013.

[187] Tamao Aoki-Matsumoto, Hitoshi Mizuno, Masao Ichida, Hiroaki Ando, Takeshi Hirai, and Ken-ichi Mizuno. Room-temperature lasing from fluorene thin-film crystals densely doped with anthracene. *Optics letters*, 37(23):4880–2, 2012.

[188] Oussama Mhibik, Tatiana Leang, Alain Siove, Sebastien Forget, and Sebastien Chenais. Broadly tunable (440-670 nm) solid-state organic laser with disposable capsules. *Applied Physics Letters*, 102(4), 2013.

[189] Y. Kawabe, Ch Spiegelberg, A. Schülzgen, M. F. Nabor, B. Kippelen, E. A. Mash, P. M. Allemand, M. Kuwata-Gonokami, K. Takeda, and N. Peyghambarian. Whispering-gallery-mode microring laser using a conjugated polymer. *Applied Physics Letters*, 72(2):141–143, 1998.

[190] Hong-Hua Fang, Ran Ding, Shi-Yang Lu, Xu-Lin Zhang, Jing Feng, Qi-Dai Chen, and Hong-Bo Sun. Flexible lasers based on the microstructured single-crystalline ultrathin films. *Journal of Materials Chemistry*, 22(45):24139, 2012.

[191] Manuel G Ramirez, Pedro G Boj, Victor Navarro-Fuster, Igor Vragovic, José M Villalvilla, Ibon Alonso, Vera Trabadelo, Santos Merino, and María A. Díaz-García. Efficient organic distributed feedback lasers with imprinted active films. *Optics Express*, 19(23):22443–22454, 2011.

[192] Luana Persano, Andrea Camposeo, Pompilio Del Carro, Pierpaolo Solaro, Roberto Cingolani, Patrizia Boffi, and Dario Pisignano. Rapid prototyping encapsulation for polymer light-emitting lasers. *Applied Physics Letters*, 94(12):1–4, 2009.

[193] Yujie Chen, Johannes Herrnsdorf, Benoit Guilhabert, Alexander L. Kanibolotsky, Allan R. MacKintosh, Yue Wang, Richard A. Pethrick, Erdan Gu, Graham A. Turnbull, Peter J. Skabara, Ifor D W Samuel, Nicolas Laurand, and Martin D. Dawson. Laser action in a surface-structured free-standing membrane based on a pi-conjugated polymer-composite. *Organic Electronics: physics, materials, applications*, 12(1):62–69, 2011.

[194] T. Riedl, T. Rabe, H. H. Johannes, W. Kowalsky, J. Wang, T. Weimann, P. Hinze, B. Nehls, T. Farrell, and U. Scherf. Tunable organic thin-film laser pumped by an inorganic violet diode laser. *Applied Physics Letters*, 88(24):2004–2007, 2006.

[195] Sönke Klinkhammer, Nico Heussner, Klaus Huska, Tobias Bocksrocker, Felix Geislhöringer, Christoph Vannahme, Timo Mappes, and Uli Lemmer. Voltage-controlled tuning of an organic semiconductor distributed feedback laser using liquid crystals. *Applied Physics Letters*, 99(2):2–5, 2011.

[196] Herbert Lifka, Cristina Tanase, Dave Mcculloch, Peter Van De Weijer, and Ian French. Ultra-Thin Flexible OLED Device. *Electronics*, pages 1599–1602, 2007.

[197] Sujan Rajbhandari, Jonathan J D Mckendry, Johannes Herrnsdorf, Hyunchae Chun, Grahame Faulkner, Harald Haas, Ian M Watson, Dominic O Brien, and Martin D Dawson. A review of Gallium Nitride LEDs for multi-gigabit-per-second visible light data communications. *Semiconductor Science and Technology*, 32(2):1–44, 2016.

[198] Bernd Gruska and Sven Peters. Organic Light Emitting Diodes. *Homo*, 20:1–12, 2005.

[199] Ebinazar B. Namdas, Minghong Tong, Peter Ledochowitsch, Sarah R. Mednick, Jonathan D. Yuen, Daniel Moses, and Alan J. Heeger. Low Thresholds in Polymer Lasers on Conductive Substrates by Distributed Feedback Nanoimprinting: Progress Toward Electrically Pumped Plastic Lasers. *Advanced Materials*, 21(7):799–802, feb 2009.

[200] C. Karnutsch, C. Pflumm, G. Heliotis, J. C. DeMello, D. D C Bradley, J. Wang, T. Weimann, V. Haug, C. Gärtner, and U. Lemmer. Improved organic semiconductor lasers based on a mixed-order distributed feedback resonator design. *Applied Physics Letters*, 90(13):1–4, 2007.

[201] S. Richardson, O. P M Gaudin, G. A. Turnbull, and I. D W Samuel. Improved operational lifetime of semiconducting polymer lasers by encapsulation. *Applied Physics Letters*, 91(26):1–4, 2007.

[202] C. Foucher, B. Guilhabert, J. Herrnsdorf, N. Laurand, and M. D. Dawson. Diode-pumped, mechanically-flexible polymer DFB laser encapsulated by glass membranes. *Optics Express*, 22(20):24160, sep 2014.

[203] N. Grassie and N. A. Weir. The photooxidation of polymers. IV. A note on the coloration of polystyrene. *Journal of Applied Polymer Science*, 9(3):999–1003, 1965.

[204] James Franck and Robert Livingston. Remarks on the Fluorescence, Phosphorescence and Photochemistry of Dyestuffs. *The Journal of Chemical Physics*, 9(2):184–190, 1941.

[205] Linlin Liu, Shi Tang, Meirong Liu, Zengqi Xie, Wu Zhang, Ping Lu, Muddasir Hanif, and Yuguang Ma. Photodegradation of polyfluorene and fluorene oligomers with alkyl and aromatic disubstitutions. *Journal of Physical Chemistry B*, 110(28):13734–13740, 2006.

[206] Egbert Zojer, Alexander Pogantsch, Emmanuelle Hennebicq, David Beljonne, Jean Luc Brédas, Patricia Scandiucci De Freitas, Ullrich Scherf, and Emil J W List. Green emission from poly(fluorene)s: The role of oxidation. *Journal of Chemical Physics*, 117(14):6794–6802, 2002.

[207] M Atreya, S Li, E T Kang, K G Neoh, Z H Ma, K L Tan, and W Huang. Stability studies of poly(2-methoxy-5-(2'-ethyl hexyloxy)-p-(phenylene vinylene) [MEH-PPV]. *Polymer Degradation and Stability*, 65:287–296, 1999.

Chapter 2

Nanoparticle lasers: design and models

This chapter expands on the notions of DFB lasers and VCSELs. It gives information on device fabrication, modelling and concepts that are used in subsequent chapters.

2.1 Introduction

Section 2.2 of this chapter explains the principles of second-order DFB lasers. The fabrication of the DFB lasers that are studied in following chapters is detailed in section 2.3 and a brief description of the optical pumping characterisation arrangements including that for ASE measurements, are given in section 2.4. Information on the transfer matrix modelling that is used in subsequent chapters to discuss DFB laser results is included in section 2.5.

Basics of VCSELs are covered in section 2.6, including cavity format, DBR and beam properties. In Chapter 4 polarisation measurements of a CQD VCSEL under a spin-polarised pump is carried out and therefore some background information on spin excitation in semiconductors is given in section 2.7. Finally, the concept of random lasers is touched upon in section 2.8 as it is a phenomenon that can occur in CQDs and OSs that is mentioned in Chapter 5.

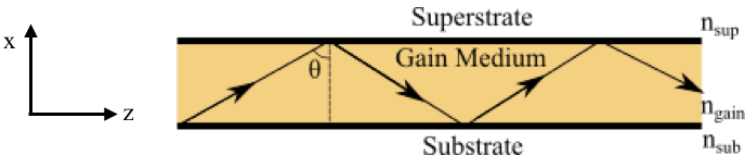

FIGURE 2.1: Example of a one layer planar slab waveguide.

2.2 Distributed feedback laser

A DFB laser differs from a Fabry-Pérot laser in that the resonator optical feedback is distributed over the whole physical structure of the device. DFB lasers, in their simplest form, consist of a thin film of a gain material overcoating a periodic structure. The periodic architecture is responsible for the reflection of the propagating light throughout the gain material as it diffracts it back and fourth through the thin film due to Bragg scattering. The DFB lasers reported in this thesis are fabricated with the gain medium cast directly on the surface of a grating structure. Three main conditions are required: (i) the gain material must have a higher refractive index than that of the cavity substrate and superstrate media so that a planar waveguide can be achieved, figure 2.1; (ii) the film of the gain medium must be thick enough to allow transverse mode propagation, ideally privileging the fundamental transverse electric (TE_0 which is the electric field parallel to the plane of the waveguide interface) and; (iii) the grating periodicy must be chosen to provide optical feedback for the desired mode at the desired wavelength [1].

Figure 2.1 does not take the grating period into consideration. It is a schematic to describe how the light is confined within the film. In the structure illustrated the light is confined by total internal reflection (TIR) and travels in the z-direction with no divergence in the x-direction. In order for TIR to take place, condition (i) must be fulfilled, the refractive index of the substrate and superstrate must be less than that of the gain medium [1, 2] i.e. $n_{gain} > n_{sub}$ and $n_{gain} > n_{sup}$. The modes that propagate through the structure are solutions of Maxwell's equations that satisfy the systems boundary conditions. As the wave passes through the medium, with a propagation constant related to the effective refractive index n_{eff}, in the x-direction the transverse profile remains unaltered. This allows the mode to be seen as only propagating in the z-direction confined within a medium of index n_{eff}.

It is also possible to calculate n_{eff} by solving the dispersion equation. This is important as n_{eff} affects resonance within the laser cavity. By considering the

interface condition in the transverse x-direction, the dispersion relation can be expressed as,

$$\frac{4\pi d}{\lambda}\sqrt{n_{gain}^2 - n_{eff}^2} = \phi_{sub} + \phi_{sup} = 2m\pi. \tag{2.1}$$

Here λ is the wavelength, d is the thickness of the gain medium, m is an integer, n_{gain} is the refractive index of the gain material and ϕ_{sub} and ϕ_{sup} are the phase shifts present upon TIR at the substrate, superstrate interfaces respectively.

ϕ_{sub} and ϕ_{sup} are dependent on the polarisation of the light, therefore, two cases must be considered. Firstly, when the electric field, E, is along in the y-direction (TE) and can be expressed as,

$$\phi_{sub} = 2tan^{-1}\sqrt{\frac{n_{eff}^2 - n_{sub}^2}{n_{gain}^2 - n_{eff}^2}}, \tag{2.2}$$

$$\phi_{sup} = 2tan^{-1}\sqrt{\frac{n_{eff}^2 - n_{sup}^2}{n_{gain}^2 - n_{eff}^2}}, \tag{2.3}$$

and secondly when the magnetic field, M, propagates along the y-direction (TM),

$$\phi_{sub} = 2tan^{-1}\frac{n_{gain}^2}{n_{sub}^2}\sqrt{\frac{n_{eff}^2 - n_{sub}^2}{n_{gain}^2 - n_{eff}^2}}, \tag{2.4}$$

$$\phi_{sup} = 2tan^{-1}\frac{n_{gain}^2}{n_{sup}^2}\sqrt{\frac{n_{eff}^2 - n_{sup}^2}{n_{gain}^2 - n_{eff}^2}}. \tag{2.5}$$

The number of modes that the waveguide can produce is determined by its thickness; the thickness of the gain material here. When $n_{sub} = n_{sup}$, the TE_0 and TM_0 have no cut-off in a planar waveguide, however, when $n_{sub} \neq n_{sup}$ there is a cut-off for each mode. Thus, there has to be a minimum thickness, d_0, that when the film is thinner than the TE_0 mode (or any mode) is not guided. However, when a thicker film is present, multiple modes can be observed such as the TE_1 mode, and so on. This is the same for the TM modes, although, the cut-off thicknesses tend to differ.

Figure 2.2 plots the dispersion of the first few transverse modes for $n_{sub} = 1.526$, $n_{sup} = 1$ and $n_{gain} = 1.996$ at a wavelength of 530 nm [3]. To re-emphasise, the film thickness dictates the number of transverse modes that can propagate and potentially lase. It is therefore an important parameter for single transverse mode regime of the laser.

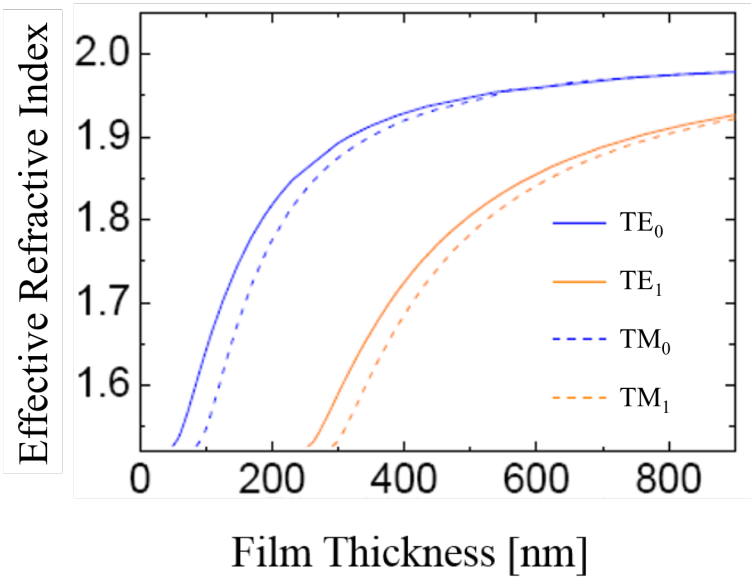

FIGURE 2.2: Example of the transverse mode effective refractive index as a function of film thickness.

Again considering thin films, the n_{eff} of the TE mode polarisation is higher than that of the TM mode. This signifies that there is stronger confinement for the TE mode, and as a result, it interacts more with the gain material. In turn, lower laser operation thresholds are typically achieved for the TE_0 mode (compared to the TM_0 mode).

With the basis of the waveguiding effect in thin films discussed, lets apply this to a full resonator and use coupled-wave theory to describe the effect of optical feedback, figure 2.3. Here it is considered that there is only one transverse mode, TE_0, where the wave propagates in both directions within the waveguide. When the wave travels in the positive z-direction, it is said to be a forward guided wave, and when in the negative z-direction, a backward guided wave. This is an approximation as the gain material thickness is averaged taking the grating depth into account. These diffractive grating structures can be designed and have a one-dimensional grating [4], or even a two-dimensional [5, 6] or three-dimensional corrugated structures. Chapters 3 and 5 report on DFB laser formats utilising one-dimensional second-order grating structures.

The periodic change in refractive index (and modal gain) causes coupling between the forward and backward propagating waves in the gain medium through Bragg diffraction. From this phenomena the total intra-cavity electric field mode can be

expressed as the sum of the forward and backward propagating modes:

$$E(z) = \phi(x)\big[A(z)e^{-ik_b z} - B(z)e^{ik_b z}\big]. \tag{2.6}$$

Here $\phi(x)$ represents the transverse amplitude of the "uncorrugated" guided mode, A and B are the amplitudes of the forward and backward propagating waves respectively and k_b is the wave vector. This corresponds to the Bragg vector in DFB lasers and is defined by the Bragg equation,

$$k_b = \frac{2\pi n_{eff}}{\lambda_b} = \frac{m\pi}{\Lambda}. \tag{2.7}$$

Here n_{eff} is the effective refractive index of the mode, λ_b is the Bragg wavelength, m is the diffraction order that determines the direction of the laser emission and Λ is the period of the grating [7, 8]. The diffraction order also provides in-plane feedback due to the m^{th} scattering order in a DFB grating with additional orders being coupled out of the waveguide.

In a first order DFB laser, where $m = 1$, there is only one order of diffraction, which is in the plane of the laser and thereby provides feedback (coupling of the two counter-propagating waves). This results in the laser emission exiting the edge of the gain film. This reduces equation 2.7 to,

$$\frac{2n_{eff}}{\lambda_b} = \frac{1}{\Lambda}, \tag{2.8}$$

and is represented in figure 2.3a.

In the case of a second order DFB laser, where $m = 2$, the laser emission exits the device perpendicularly from the surface (note that light is emitted from both sides of the device). This is due to the first order diffraction outputting the light out of the waveguide at 90^0 and the second order diffracted light providing the optical feedback in plane. Equation 2.7 can the be expressed as,

$$\frac{n_{eff}}{\lambda_b} = \frac{1}{\Lambda}, \tag{2.9}$$

and is represented in figure 2.3b.

Equation 2.9 shows the importance of cavity design and how n_{eff} is an important choice when choosing a grating periodicity. This means that for a specific

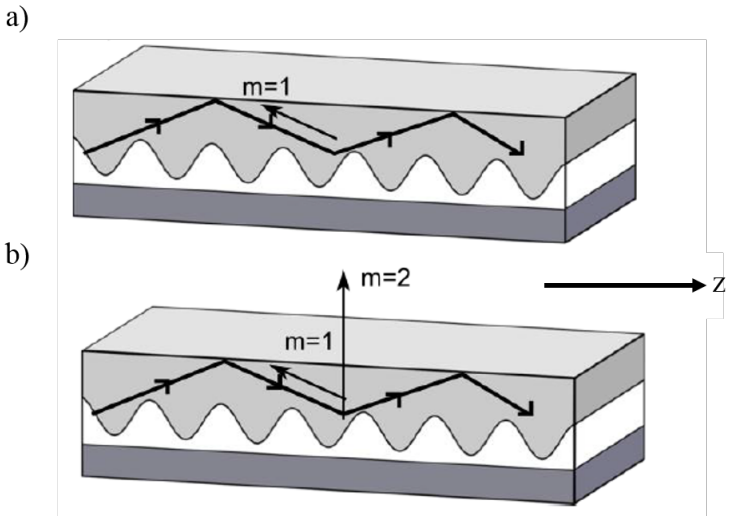

FIGURE 2.3: Examples of DFB laser structures of a) first order ($m = 1$) and b) second order (m= 2).

grating period, the n_{eff} aligns the Bragg resonance to the desired emission wavelength. This also permits tuning of the device as varying film thickness allows different grating periods to be used providing flexibility in obtaining the emission wavelength; as varying film thickness varies n_{eff}.

As discussed earlier, equation 2.6 describes the field inside the DFB waveguide as having two waves, $A(z)$ and $B(z)$, that are amplified as they propagate through the z-direction. With equation 2.6 and the wave theory for the Bragg wavelength region, the propagation of the coupled waves, $A(z)$ and $B(z)$, can be found,

$$\frac{\partial}{\partial z}A - \left(\frac{g}{2} - i\delta\right)A = -i\kappa B, \tag{2.10}$$

$$\frac{\partial}{\partial z}B - \left(\frac{g}{2} - i\delta\right)B = i\kappa A. \tag{2.11}$$

g is the gain coefficient, $\delta \approx \beta - \beta_{Bragg}$ where β is the modal propagation constant, κ is the coupling coefficient that depends on the laser structure, grating depth, difference of material refractive index and the overlap of the mode between the gain material and grating structure as well as possibly on the gain. The solutions of the coupled wave equations are,

$$A = a_1 e^{\gamma z} + a_2 e^{-\gamma z}, \tag{2.12}$$

and

$$B = b_1 e^{\gamma z} + b_2 e^{-\gamma z}. \tag{2.13}$$

Here γ is the complex propagation constant given by,

$$\gamma^2 = \kappa^2 + \left(\frac{g}{2} - i\delta\right)^2. \tag{2.14}$$

There are three possible scenarios for the propagation constant γ depending on g and κ. When κ is real this results in pure index coupling, when κ is imaginary it gives pure gain coupling, and the intermediate case when κ is complex both gain and index coupling occur. For pure index coupling, the spectral region is close to the Bragg wavelength and γ has real values. No waves can propagate here and it is known as the photonic bandgap. In this case the laser does not emit at the Bragg wavelength, however, it emits at wavelengths near the so call photonic bandgap, at the band edge. This happens for relatively deep gratings. The DFB lasers reported in this thesis contain shallow gratings resulting in complex coupling. Unlike index coupling, gain coupled DFB lasing can occur in the bandgap near the Bragg wavelength. This results in the Bragg wavelength being adequate for design purposes.

2.3 DFB fabrication

DFB lasers are utilised in Chapters 3 and 5. The fabrication process for these solution-processed DFB lasers are explained in this section. The reported devices follow the architecture of a gain material layer deposited onto the surface of a second-order one-dimensional grating structure that acts as the DFB reflector. The deposition of the gain material is achieved by spin coating and drop casting methods, which are described in the subsequent sections. Spin-coating is done by dropping the gain material, in solution, onto the grating pattern and spinning at speeds between 1 to 8 krpm, where the spinning speed dictates the film thickness [5]. In addition to this, all reported devices are fabricated in completely ambient conditions.

2.3.1 Master grating

In order to produce repeatable grating structures a master grating is used where negative imprints create the reflector used in experiment. These are silica substrates approximately 1cm x 1cm where the grating is produced by electron beam

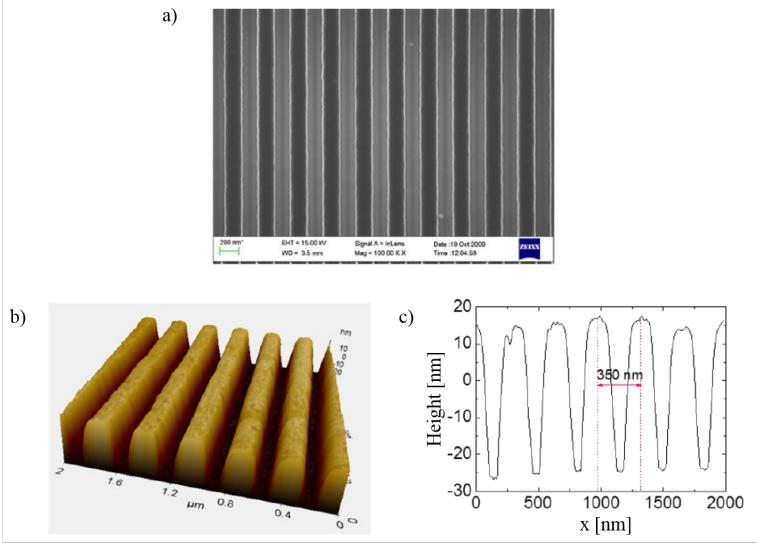

FIGURE 2.4: Silica master grating with Λ = 350nm, modulation depth 50nm a) SEM image, b) AFM image and c) AFM profile scan.

lithography. These have modulation depths of 50 nm and a period, Λ, chosen for particular emission wavelengths. A master grating with Λ = 350 nm is displayed in figure 2.4. The copies of the master grating are created using an ultraviolet-transparent and photo-curable epoxy material Norland NOA 65. This material was chosen due to its refractive index, n = 1.52, as the refractive index of the grating substrate must be lower than that of the gain material as the higher the index contrast, the more efficient the DFB effect.

When fabricating the structures a drop of NOA 65 is placed directly on the grating surface of the master grating. A small sheet of acetate, approximately 0.1mm thick, is then placed on top of the epoxy and pressed down ensuring that it completely covers the grating structure. The acetate then acts as an underlying substrate. This is then photo-cured under a UV lamp, 370 nm at a 300 mJ/cm^2 dose, for one minute. The acetate, with the NOA 65 attached, is then pealed off and post-cured for one hour under the same UV lamp. This process reproduces a negative image of the master grating where figure 2.4b displays a typical atomic force microscopy (AFM) image and figure 2.4c a profile scan.

2.3.2 Neat lasers

We refer to "neat lasers" when the gain material is deposited dispersed in solvent applied to the grating substrate with no additional encapsulation layers or no

host matrix. This results in the gain layer being made up of purely CQDs or purely OS, initially dissolved in solvent and then cast onto a grating substrate (note in chapter 3 neat refers to non-encapsulated). The solvents used are chosen based on their boiling points as well as their compatibility with the gain material. This allows film thickness tuning as a higher boiling point results in a thinner films. Information on the solvents used are discussed in the relevant chapters. As mentioned previously, the film thickness of the gain layer are important as propagation of at least the TE_0 mode has to be ensured. This is determined by the spinning speed at deposition and the solvents used.

2.3.3 Nanocomposite lasers

Nanocomposite lasers differ from neat lasers as the gain material is embedded in a polymer matrix. For these devices the fabrication process is the same as the neat laser differing only in the gain material being mixed in a matrix before deposition. In this thesis poly (methacrylate) (PMMA) is utilised with CQDs.

2.3.4 Encapsulated lasers

The encapsulation process is an additional step taken in device fabrication. The devices are fabricated as described in the previous two sections but the gain layer is further overcoated with the encapsulant layer. In Chapters 3 and 5, polyvinyl alcohol (PVA) was used as well as parylene C and spin-on-glass (SoG) in Chapter 5.

The PVA was prepared by mixing an 89% hydrolysed PVA powder, with a molecular weight in the range of 85000 to 124000 g/mol, with deionised (DI) water until a concentration of 50 mg.mL^{-1} was obtained. This solution was then stirred until completely dissolved (approximately one hour) at 80^{0}C. Once complete the solution is spun cast over the gain layer and annealed in an ambient atmosphere at 35^{0}C for 72 hours ensuring total evaporation of the DI water. This low temperature ensures that the gain material is not heat damaged and produces a good crystalline cohesion [9]. Utilising AFM, this produces a PVA film of 180 $\pm$ 20 nm thick.

When determining the thickness of the PVA layer the solution was prepared as described above and spun cast onto a planar glass substrate. A scratch was made on the film and the depth, of the scratch, was measured using AFM. This is the same method used to determine the film thicknesses throughout this document.

Parylene C is used in Chapter 5 and is an ideal material for its barrier properties, cost, and most importantly is biologically compatible. It was deposited in the IoP clean room suite by Dr Robert Scharf by vapour deposition process with refractive index of approximately 1.64. Spin-on-glass from Desert Silicon was also tested for these devices. This is a non-doped spin-on titanate known for uniform coatings, index matching, transparent in the visible and UV absorbing. This is applied directly onto the gain layer and spin coated at 3.5 krpm leaving a 2000 $\mathring{A}$ layer. Typically heated at 200^0C for 5 minutes to cure, here the same annealing time and temperature was used as PVA to protect the OSs.

2.4 Optical characterisation setup

The optical pump source used throughout the experiments is a frequency tripled Nd: YAG Q-switched laser pulsed at 5 ns at a wavelength of 355 nm with a 10Hz repetition rate. The emission of the excited device is collected via 50μm core optical fibre connected to an Avantes CCD spectrometer. A number of channels were utilised on the spectrometer. These were the "Master" channel with resolution 2.5 nm covering 176 nm to 1100 nm, "Slave 1" with resolution of 0.5nm covering a spectral range 400 nm to 635 nm, and "Slave 3" with resolution 0.13nm with a spectral range of 420 nm to 653 nm. Samples were placed either perpendicular to the pump or at a slight angle with respect to the beam axis prohibiting the direct coupling measured of the pump photons in the optical fibre. The full-width at half-maximum (FWHM) size of the pump was deduced via knife edge measurements [10–12]. Due to different materials and additional optics the pump spot size varied throughout the different experiments and is stated in their respected chapters.

For each laser, the corresponding power transfer function and spectra were recorded, and in section 3.4.2 the photodegradation of CQD films was measured. The pump energy is controlled by scanning through a quarter-wave plate, angle α, and having a neutral attenuator wheel, angle β, set throughout the measurement along with

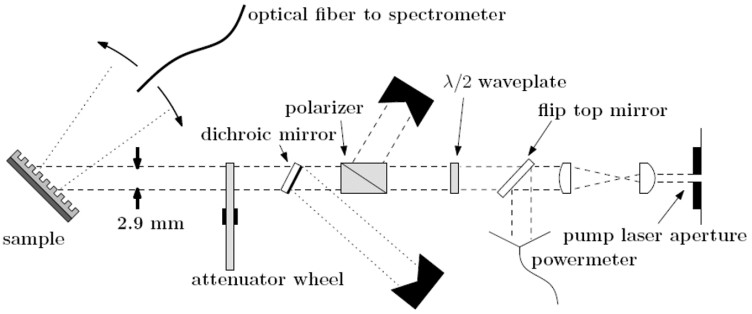

FIGURE 2.5: Optical set up utilised in DFB lasing measurements.

various optics manipulating the pump beam into a stripe. There is also a dichroic mirror that removes any "green" light from the pump (532 nm) as the pump laser is frequency-tripled from 1064 nm. A schematic of the optical set up for DFB lasers can be seen in figure 2.5 where the VCSEL set up is discussed in chapter 4.

2.4.1 Amplified spontaneous emission set up

Measurement of ASE, discussed in section 1.3.5, can indicate whether a material is suitable as a laser gain material and is the initial step in the investigation. Thin films of the desired gain material are spun cast on planar glass substrates and the emission (and eventual ASE) is detected through edge. For such experiment, the pump was shaped in a stripe configuration and placed near the edge of the sample, figure 2.6. The films were pumped orthogonally to the surface exciting the material from the top. The stripe geometry creates a guiding effect that results in possible ASE detection at the film edge via optical fibre connected to the Avantes.

When in this configuration, the tell-tale sign of ASE is the occurence of spectral narrowing (section 1.3.5). If this spectral redistribution of the emission for the material is observed, after reaching a certain threshold energy, ASE is present. Plotting the intensity, or the intensity integrated on the range of wavelengths where narrowing occurs, as a function of the pump energy gives a threshold-like behaviour where above this threshold energy the slope of the detected intensity versus pump energy increases.

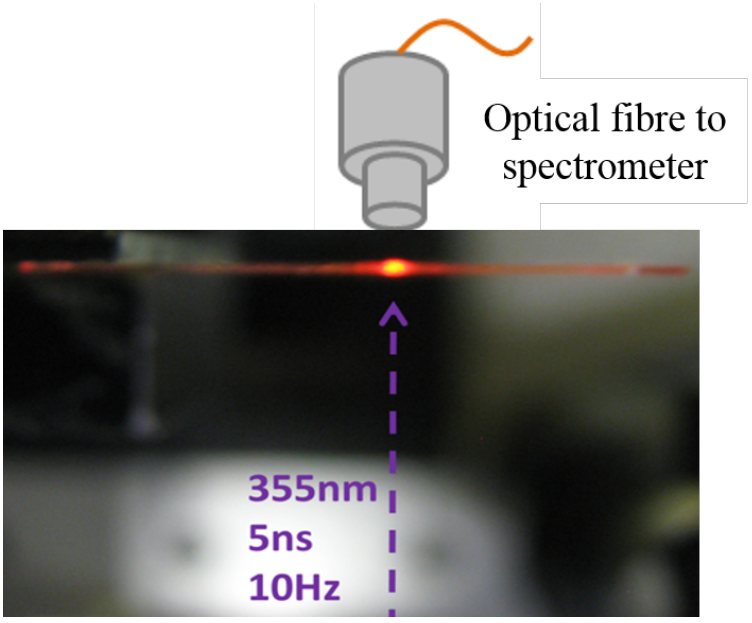

FIGURE 2.6: Plain view schematic of pump on thin film sample in the search for ASE.

2.5 DFB modelling

In the results chapters reporting on DFB operation, the laser mode transverse profile and its overlap with the gain region is often discussed for different structures. The overlap is an important parameter as it indicates confinement of the mode in the gain region and has a direct effect on the modal gain. A more confined mode usually results in a higher modal gain and a lower threshold. This is expanded on below. Dr Nicolas Laurand scripted this model using Mathcad where the calculations are made when analysing slab waveguides representative of the laser structures characteristics (the corresponding refractive indices and film thicknesses of the materials) using a multilayer matrix model. This model determines the TE_0 intensity profile across the entire laser structure and is adapted from [13, 14] where the principles of this method are described. The components of this model will be discussed below.

2.5.1 Transfer matrix

The effective refractive index of the laser mode is an important parameter that needs to be calculated in order to model the mode profile of the DFB laser. This is done by considering a matrix that describes the boundary conditions for respective

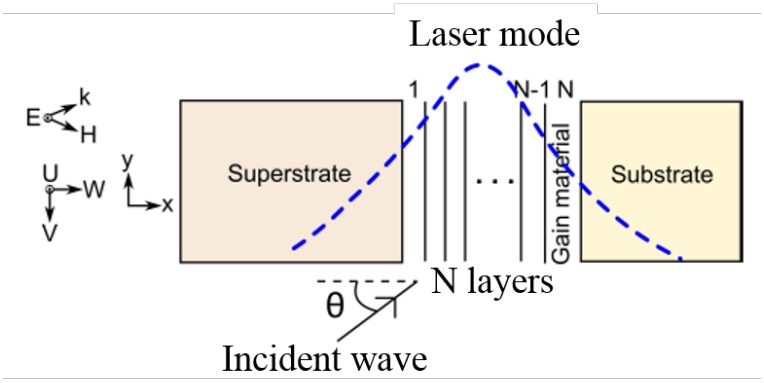

FIGURE 2.7: Representation of multilayer stack of N thin films surrounded by substrate and superstrate layers, with a propagating laser mode indicated by the blue dashed curve.

layers of the DFB structure. This structure is used for the calculation of the transfer matrix and is depicted in figure 2.7. Figure 2.7 shows a multilayer architecture comprised of N number of thin films sandwiched between semi-infinite substrate and superstrate. The boundaries of the confined layers are numbered from 1 to $N-1$, where the superstrate is layer 0 and the substrate N. The matrix is derived by considering a plane wave incident on the structure at an angle θ. Here, the direction cosines are given by $\alpha = ncos\theta = \sqrt{n^2 - \beta^2}$ where β is the propagation constant of the mode being constant for all layers and is given by $\beta = nsin\theta$.

This transfer matrix method allows for additional layers to be added on top of the gain material accurately producing the profile mode of the laser. This is used in Chapters 3 and 5 where the DFB lasers are encapsulated, by a number of different materials, and the corresponding TE_0 mode is calculated.

The transfer matrix of the DFB device is built up of transfer matrices for each of the corresponding layers linking the field amplitude to the layer boundaries, equation 2.15.

$$M_n = \begin{bmatrix} cos\Phi_n & \frac{-i}{\gamma_n} sin\Phi_n \\ -i\gamma_n sin\Phi_n & cos\Phi_n \end{bmatrix} \tag{2.15}$$

Here Φ_n represents the phase thickness, $\Phi_n = k\alpha_n(x_n - x_{n-1})$ and γ as α/z_0 (z_0 is the impedance of free space). The matrix is derived from Maxwell's equations when applied to a stratified medium where full details on the calculations are reported in ref [14].

Once M_n for each layer is known the DFB structure can be calculated as the product of the individual layers, equation 2.16 [15]. Equation 2.16 describes the overall matrix structure linking the field amplitudes to the substrate and superstrate boundaries.

$$M = \prod_{n=1}^{n} M_n = \begin{bmatrix} m_{11} & m_{12} \\ m_{21} & m_{22} \end{bmatrix}. \tag{2.16}$$

2.5.2 Effective refractive index

As discussed in the previous section, section 2.5.1, the field amplitude between the substrate and superstrate interfaces can be linked to the transfer matrix by equation 2.16. This can then be seen to satisfy,

$$\begin{pmatrix} U_{sup} \\ V_{sup} \end{pmatrix} = M \begin{pmatrix} U_{sub} \\ V_{sub} \end{pmatrix}, \tag{2.17}$$

where "*sub*" and "*sup*" represent substrate and superstrate. From Maxwell's equations,

$$U = \frac{1}{ik\gamma\alpha}\frac{dV}{dx}, \tag{2.18}$$

$$V = \frac{\gamma}{ik\alpha}\frac{dU}{dx}. \tag{2.19}$$

For guided modes in the ideal system, the energy is confined within the stack of thin films due to total internal reflections as well as the amplitudes of the field being independent of the y- and z-directions. The radiation condition states that when the waves are negative they propagate through the substrate, $U = U_{sup}e^{-ik\alpha_{sup}x}$, and when positive they propagate through the superstrate, $U = U_{sub}e^{ik\alpha_{sub}(x-x_{sub})}$. In the real world, the field observed in the substrate and superstrate are temporal resulting in α_{sub} and α_{sup} being imaginary. Equation 2.17 can then be expressed as

$$\begin{pmatrix} 1 \\ -\gamma_{sup} \end{pmatrix} U_{sup} = M \begin{pmatrix} 1 \\ \gamma_{sub} \end{pmatrix} U_{sub}. \tag{2.20}$$

Equation 2.20 can be solved finding the modal-dispersion function for the bound modes as

$$\chi(\beta) = \gamma_{sup}m_{11} + \gamma_{sup}\gamma_{sub}m_{12} + m_{21} + \gamma_{sub}m_{22} = 0. \tag{2.21}$$

The solutions to equation 2.21, if any, represent the effective refractive indices for the TE_0, TE_1, TE_2, etc, modes, where the largest value represents the TE_0 mode. For a single layer (the gain film), this relation is equivalent to equation 2.1.

2.5.3 Mode profile

Now that the effective refractive index of the TE mode has been found, it is possible to plot the distribution of the field between the boundaries of the N layers. For this an arbitrary value for one of the field amplitudes is chosen where the remainder of the field amplitude values, at other points in the laser structure, are found using,

$$\begin{pmatrix} U_{n-1} \\ V_{n-1} \end{pmatrix} = M \begin{pmatrix} U_n \\ V_n \end{pmatrix}. \tag{2.22}$$

Here, an arbitrary value of U = 1 is taken for the boundary between the gain layer and the substrate. The mode profile can then be plotted using,

$$E(x) = U_n cos[k\alpha_n(x - x_n)] + \frac{i}{\gamma_n} sin[k\alpha_n(x - x_n)]. \tag{2.23}$$

The mode profile is then plotted against the refractive index of the laser structure where the intensity profile of the mode is $|E(x)|^2$. Where the modal intensity overlap with the gain region can be expressed as,

$$\Gamma = \frac{\int_0^t |E(x)|^2 dx}{\int_{-\infty}^{\infty} |E(x)|^2 dx}, \tag{2.24}$$

with t being the thickness of the gain layer. Lower laser thresholds are typically obtained when there is a greater overlap.

2.6 VCSEL

CQD VCSELs are reported in Chapter 4 and this section introduces the design and concept elements of VCSELs.

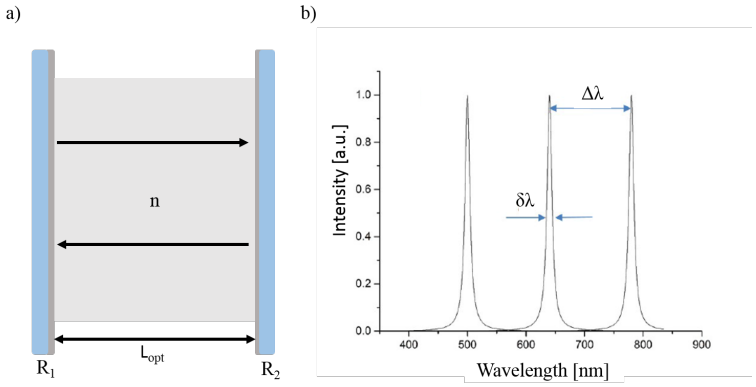

FIGURE 2.8: a) Schematic of a Fabry-Pérot cavity with length L_{opt} and gain region with refractive index n, b) normalised optical cavity modes with FWHM ($\delta\lambda$) and FSR ($\Delta\lambda$).

2.6.1 Fabry-Pérot

The cavity structures of VCSELs are similar to that of a Fabry-Pérot. These are planar cavities containing two opposing mirrors with reflectivities R_1 and R_2 separated by the optical cavity length, L_{opt}. This is demonstrated in figure 2.8a. One of the cavities key features is the finesse, F. This determines the cavity properties and can be thought of as the number of round trips a photon will make before it exits the cavity [16]. The finesse can be expressed as,

$$F = \frac{\pi(R_1R_2)^{\frac{1}{4}}}{1-\sqrt{R_1R_2}}. \tag{2.25}$$

The cavity length is equal to an integer number of half wavelengths when the cavity is in resonance with cavity length,

$$L_{opt} = \frac{q\lambda}{2}, \tag{2.26}$$

where q is number of antinodes located between the mirrors. Optical modes (peaks) in the cavity transmission are obtained when wavelengths satisfy equation 2.26. These occur at their relative spectral position demonstrated in figure 2.8b. The number of photons inside the cavity decay at an exponential rate due to the reflectivities of the mirrors being less than unity ($R_1, R_2 < 1$). The Fourier transform of this decay produces modes in the spectral domain that have a Lorentzian line shape with finite spectral linewidth, $\delta\upsilon$ (in Hz). The photon decay rate (κ) is related to the linewidth by $\kappa = 1/\tau_{cav} = 2\pi\delta\upsilon$, where τ_{cav} is the cavity decay time.

The cavity length can be calculated using the spectrum shown in figure 2.8b by rearranging equation 2.26 and differentiating, with respect to the wavelength,

$$\frac{dq}{d\lambda} = -\frac{2L_{opt}}{\lambda^2}. \tag{2.27}$$

Here $d\lambda = \Delta\lambda$ and is known as the free spectral range (FSR). This is the spectral deviation between the adjacent modes ($\Delta q = 1$). Equation 2.27 gives the cavity length as,

$$L_{opt} = \frac{\lambda^2}{2\Delta\lambda}. \tag{2.28}$$

The Q-factor is the quality factor and describes the strength of the damping of its oscillations, or for the relative linewidth within any geometry of resonator. This can be expressed as,

$$Q = \frac{\upsilon_0}{\delta\upsilon} = \frac{\lambda}{\delta\lambda}, \tag{2.29}$$

where $\delta\lambda$ is is the cavity linewidth. The Q-factor is proportional to the time a photon remains within the cavity and can be thought of as the number of oscillations it makes before decaying. The Q-factor is also related to the finesse by,

$$Q = qF. \tag{2.30}$$

This can be linked to the threshold of a Fabry-Pérot cavity as previously discussed in section 1.3.6. To remind the reader, threshold is determined when the gain of the cavity is equal to the sum of the cavity loses (the sum of the intrinsic and mirror transmission losses). Finesse is related to cavity gain as it too is determined by the losses occurring within the cavity; although not on the cavity length. This can then be related to the cavities Q factor when divided by the cavities FSR.

2.6.2 Distributed Bragg reflectors

A distributed Bragg reflector (DBR) is a mirrored structure build up of layers with different optical properties. When high finesse is desired, the resonant photons within the cavity must be confined efficiently. Using metallic mirrors is one method used to achieve this, however, the reflectivity of these mirrors tends not to exceed 95%. This is due to the losses induced when the electric field interacts with

the electrons in the metal. Evaporated silver mirrors have achieved high reflectivities [17] but a higher degree of photon confinement can be obtained by utilising dielectric mirrors. The DBRs used in Chapter 4 are SiO_2/TiO_2 dielectric mirrors. These are based on an architecture of alternating high, low refractive index layers. The thickness of each layer is taken as the optical depth and is equal to $\lambda/4n_{layer}$, where λ is the desired wavelength and n_{layer} the refractive index of the subsequent layer. The materials are chosen so that the thicknesses correspond to the path length differences for all reflections from low-index layers being integer multiples of wavelength (when the photons exit the high refractive index layer encounters the low index layer interface). A half-wavelength path difference is present in reflections from the high index (when the photons exit the low refractive index layer encounters the high index layer interface). This results in there being a π-phase shift upon reflection meaning that all reflected rays, from all interfaces, are in phase.

Fresnel equations describe the reflection and transmission amplitude coefficients of light at the layer interfaces [14, 15, 18]. When modelling the multilayer dielectric structures, reflections and interference effects from all interfaces must be taken into account. A convenient way is to again use the transfer matrix method approach, akin to that disscussed in section 2.5.1, which is explained in more detail in Chapter 4 for VCSEL formats. A full description can be found in [14, 15, 18]. The model takes the electric and magnetic fields surrounding each individual dielectric layers as a matrix and takes the product of all. The final matrix can be generalised into an arbitrary number of interfaces and is used to calculate the reflectivity and transmissivity of the DBRs, and then VCSELs.

Figure 2.9 displays the reflectivity spectrum, overlaid with the transmissivity spectrum, of a DBR containing 20 pairs of alternating high low refractive index dielectric layers, $n_{high} = 2.6$ and $n_{low} = 1.46$, incorporating the semi-infinite substrate and superstrate, calculated with the transfer matrix model. From the figure it can be seen that for the a range of wavelength, of roughly 500 nm to 700 nm, the reflectivity values are approximately unity. This is know as the stop-band.

The penetration depth, L_{DBR}, is an interesting property as it is a measure of how deep the electric field travels through the DBR layers. This property is subject to the various interfaces (DBR layer) the electric field encounters. When an incident

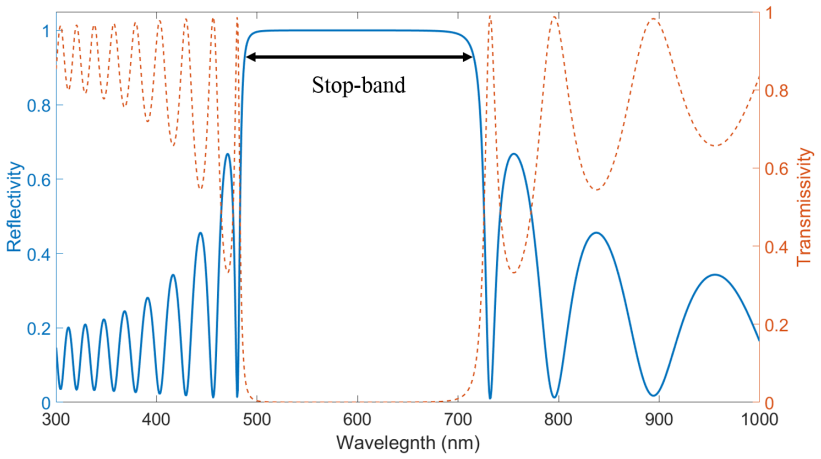

FIGURE 2.9: Typical reflectivity spectrum of a DBR strucuture (solid blue line) overlaid by the corresponding transmissivity spectrum (orange dashed line).

photon encounters a high index layer L_{DBR} is given by [19]

$$L_{DBR,h} = \frac{\lambda n}{a n_{av} \Delta n}, \tag{2.31}$$

and for a low index layer,

$$L_{DBR,l} = \frac{\lambda n_{av}}{4 n \Delta n} + \frac{\lambda \Delta n}{2\pi^2 n n_{av}}. \tag{2.32}$$

Here $\Delta n = n_h - n_l$ and $n_{av}^{-1} = 2(n_h^{-1} + n_l^{-1})$. The total penetration depth of a cavity is the sum of the values for each mirror, $L_{DBR} = L_{DBR,1} + L_{DBR,2}$ where $L_{DBR,1}$ and $L_{DBR,2}$ are the respective penetration depths of two DBRs. The total cavity length, L, can then be taken as the sum of the physical separation of the mirrors, L_C, where the total penetration depth is,

$$L = L_C + L_{DBR}, \tag{2.33}$$

and the optical cavity length is,

$$L_{opt} = n L_C + n_{av} L_{DBR}. \tag{2.34}$$

2.6.3 Gaussian beam optics in a cavity

Lasers such as VCSELs emit beams which can be considered Gaussian and are described as the spatial distribution of the optical modes formed by the cavity

formats. Details on higher order cavity modes will be expanded on in sections 2.6.4 and 2.6.5 and are referred to as either Hermite-Gaussian or Laguerre-Gaussian modes. A more in-depth derivation of these modes can be found in references [14, 15, 20–23]. To start, the Helmholtz equation is used. This describes the propagation of the spatial part of the electric field, E(r), when there is no charges or current present,

$$(\nabla^2 + k^2)E(r) = 0, \tag{2.35}$$

where k is the wavevector and $\nabla^2 = \frac{\partial^2}{\partial x^2} + \frac{\partial^2}{\partial y^2} + \frac{\partial^2}{\partial z^2}$ is the Laplacian operator. Solving equation 2.35 gives,

$$E(r) = U(r)e^{-ikz}, \tag{2.36}$$

where U(r) is the complex amplitude. This can be simplified by taking the angle that the light diverges (θ) from the direction of propagation to be small (the paraxial approximation). This means U(r) in equation 2.36 slowly varies as a function along the z-direction so that $\frac{\partial^2 U}{\partial z^2} \ll k\frac{\partial U}{\partial z} \ll k^2 U$. Substituting equation 2.36 into equation 2.35 results in the paraxial Helmholtz equation,

$$\nabla_T^2 - 2ik\frac{\partial U}{\partial z} = 0, \tag{2.37}$$

where $\nabla_T^2 = \frac{\partial^2}{\partial x^2} + \frac{\partial^2}{\partial y^2}$ is the transverse Laplacian operator. The Gaussian beam shape is described by the solution to equation 2.37,

$$E(r) = U_0\frac{\omega_o}{\omega(z)}e^{-\frac{r^2}{w(z)^2}}e^{-ikz}e^{-ik\frac{r^2}{2\beta(z)}}e^{i\zeta(z)}. \tag{2.38}$$

Here $r = \sqrt{x^2 + y^2}$, ω(z) is the 1/e value of the beam radius at z and can be seen in figure 2.10. In a cavity comprised of a planar mirror, M_1, and a curved mirror, M_2, when z = 0, ω_0 and U_0 are the radius of the beam and the amplitude located at the surface for the first mirror, M_1. The radius of curvature (RoC) of the second mirrors, M_2, phase profile and the Gouy phase shift are $\beta(z)$ and $\zeta(z)$. Thus the Gaussian mode profile is given by the first term in equation 2.38 and is dependent on $\omega(z)$. The wave propagation is in a positive direction due to the second term in equation 2.38 providing k is positive. The third term defines the RoC of the wavefronts in the z-direction and the fourth contains the Gouy phase factor. The Gouy phase factor induces a phase shift to a propagating Gaussian beam. This phase shift differs from a plane wave but the optical frequency is the same playing

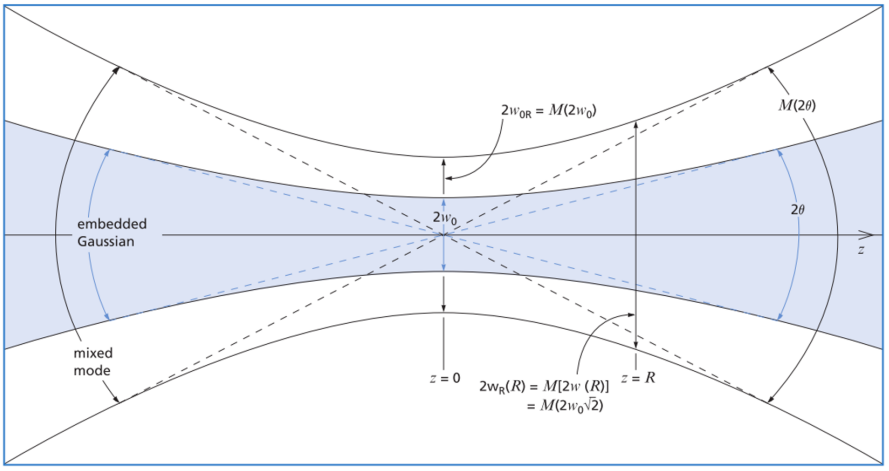

FIGURE 2.10: Schematic of a Gaussian bean cavity of optical length, L_{opt}. Here w_0 is the waist radius at the first (planar) mirror, M_1, z_R is the Rayleigh range, the angle of divergence θ and the two mirrors with RoC M_1, M_2, R_1 and R_2 respectively [20].

an important role determining the resonant frequencies of the cavities.

The Gouy phase shift, along with the beam waist and RoC, can be expressed in terms of the Rayleigh range, z_R. This is the distance along the z-axis where the beam is equal to $\sqrt{2}w_0$, figure 2.10,

$$z_R = \frac{\pi\omega_0^2}{\lambda}, \tag{2.39}$$

where the Gouy phase shift is expressed by [23, 24],

$$\psi(z) = (N+1)arctan\left(\frac{z}{z_R}\right), \tag{2.40}$$

where N is defined by l+m (transverse mode values),

$$\omega(z) = \omega_0\sqrt{\left(1+\left(\frac{z}{z_R}\right)^2\right)}, \tag{2.41}$$

$$\beta(z) = z + \frac{z_R^2}{z}, \tag{2.42}$$

and

$$\zeta(z) = tan^{-1}\left(\frac{z}{z_R}\right). \tag{2.43}$$

Taking a more general case giving each mirror a finite RoC, the minimum mode waist, w_0, for the mirrors, w_1, w_2, can be defined by,

$$g_i = 1 - \frac{L_{geo}}{R_i}, \tag{2.44}$$

where g_i is a parameter, $L_{geo} = nL_C$ and is the geometrical cavity length, n is the refractive index and R_i is the RoC of each mirror. From this, the beam radius can be further defined by,

$$\omega_0 = \left(\frac{\lambda L_{opt}}{\pi}\right)^{\frac{1}{2}} \left(\frac{g_1 g_2 (1 - g_1 g_2)}{(g_1 + g_2 - 2g_1 g_2)^2}\right)^{\frac{1}{4}}, \tag{2.45}$$

$$\omega_1 = \left(\frac{\lambda L_{opt}}{\pi}\right)^{\frac{1}{2}} \left(\frac{g_2}{(g_1(1 - g_1 g_2)}\right)^{\frac{1}{4}}, \tag{2.46}$$

$$\omega_2 = \left(\frac{\lambda L_{opt}}{\pi}\right)^{\frac{1}{2}} \left(\frac{g_1}{(g_2(1 - g_1 g_2)}\right)^{\frac{1}{4}}. \tag{2.47}$$

Equation 2.45 shows that in order for w_0 to be a positive value the numerator must obey the following,

$$0 \leqslant g_1 g_2 \leqslant 1, \tag{2.48}$$

and is the benchmark for a stable resonator.

It should also be noted here that the device reported on in Chapter 4 utilises planar mirrors (RoC $= \infty$) and therefore the cavity is in principle at the limit of stability ($g_1 g_2 = 1$). This means the beam diverges as it travels back and forth within the cavity. This, in return, will cause more loss. However, in our case, gain guiding plays the role of a focuser for the modes, stabilising the cavity. The description of the modes as Gaussian is still valid however it is very difficult to predict the mode sizes and diffraction losses are still non-negligible, increasing threshold. For this reason, it is hard to control the number of oscillating modes. We will see in Chapter 4 that the CQD VCSEL tends to operate on a multitude of transverse modes.

2.6.4 Hermite-Gaussian

The Hermite-Gaussian beam is made up of higher order transverse electromagnetic (TEM) modes. Equation 2.38 in section 2.6.3 discusses the lowest order of these

modes, TE_0 mode, however, other higher order modes can exist in optical cavities. These higher modes are also solutions to the paraxial Helmholtz equation and are known as Hermite-Gaussian beams. Hermite-Gaussian beams have the general form,

$$E_{l,m}(r) = U_0 \frac{\omega_0}{\omega(z)} H_l\left[\sqrt{2}\frac{x}{\omega(z)}\right] H_m\left[\sqrt{2}\frac{y}{\omega(z)}\right] e^{-\frac{r^2}{\omega(z)^2}} e^{-ikz} e^{-ik\frac{r^2}{2\beta(z)}} e^{i(l+m+1)\zeta(z)}. \tag{2.49}$$

This is a more general solution of optical modes where it contains the lowest-order solutions. The two additional factors $H_l\left[\sqrt{2}\frac{x}{\omega(z)}\right]$ and $H_m\left[\sqrt{2}\frac{y}{\omega(z)}\right]$ are the Hermite polynomials where l and m denote their order (Hermite polynomials have the typical form $\frac{d^2y}{dx^2} - 2z\frac{dy}{dx} + 2\alpha y = 0$ with α being a constant). These cavity modes also have an additional transverse mode structure compared to the Gaussian shape discussed previously (for a Gaussian beam $l = m = 0$). They also obtain an additional phase shift of $e^{i(l+m)\zeta(z)}$. The cavity modes in equation 2.49 are known as "transverse electric and magnetic field" and are represented by TEM_{lm}.

A combination of these modes are displayed in figure 2.11. The lowest-order mode (TEM_{00}) is known as the fundamental mode and is non-degenerate. The higher-order modes have spatial profiles and are energetically degenerate for symmetrical cavities.

Returning to equation 2.49, by integrating this equation, an expression for the optical cavity volume, V_{opt}, can be found [15, 22–25],

$$V_{opt} = \frac{\pi\omega_0^2 L_{opt}}{4}. \tag{2.50}$$

2.6.5 Laguerre-Gaussian

Laguerre-Gaussian modes differ from Hermite-Gaussian modes as they have rotational symmetry along their propagation axis. As well as this they have properties of intrinsic rotational orbital angular momentum. The modes are built up of functions using generalised Laguerre polynomials, L_p^l, and are written in cylindrical coordinates (these generalised Laguerre polynomials have the form $x\frac{d^2y}{dx^2} + (1-x)\frac{dy}{dx} + \alpha y = 0$, where α is a constant) [20, 22, 23, 26, 27]. As in the case of Hermite-Gaussian modes, section 2.6.4, the transverse modes are denoted by two integer values. These are the radial index, p, where $p \geqslant 1$ and the

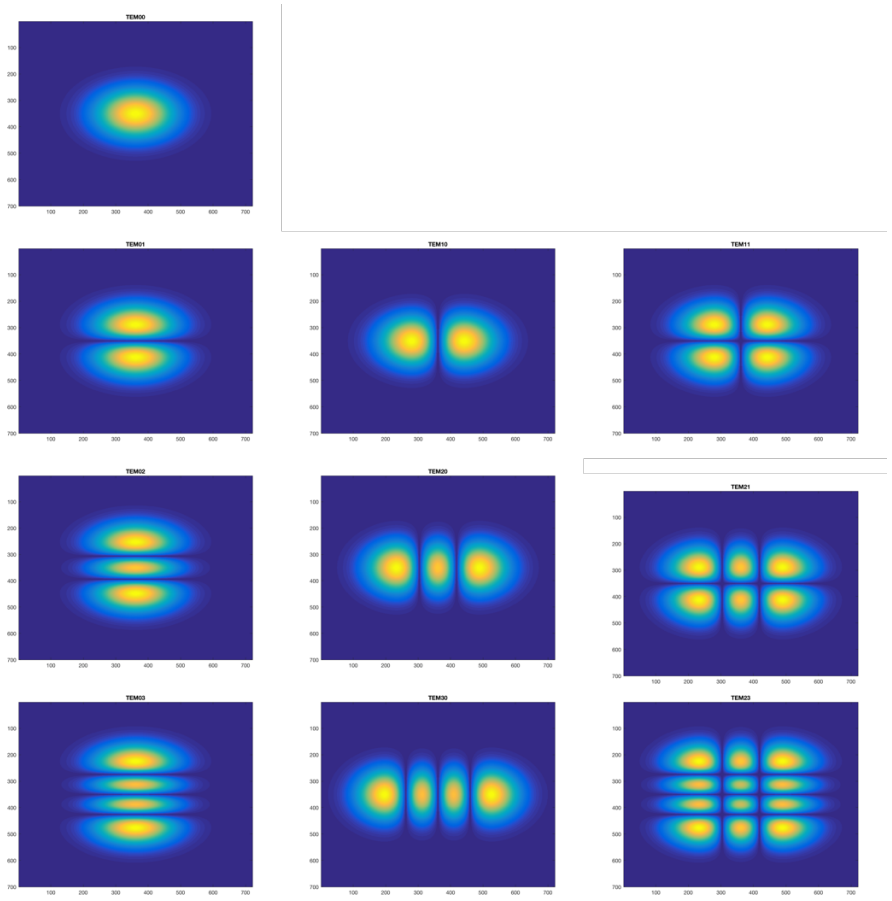

FIGURE 2.11: Hermite-Gaussian electric field distribution of various modes based, starting with a Gaussian mode, on the device utilised in Chapter 4.

azimuthal index, l, that can be any integer value (equivalent to l and m in section 2.6.4). The paraxial equation, in cylindrical coordinates, is expressed by,

$$\left(\frac{1}{r}\frac{\partial}{\partial r}\left(r\frac{\partial}{\partial r}\right)+\frac{1}{r^2}\frac{\partial^2}{\partial\phi^2}+2ik\frac{\partial}{\partial z}\right)u(r,\phi,z)=0. \tag{2.51}$$

The circular beam profile, in the simplest form, can then be expressed as,

$$u(r,\phi,z)=\frac{C_{lp}^{LG}}{\omega(z)}\left(\frac{r\sqrt{2}}{\omega(z)}\right)^{|l|}e^{\left(-\frac{r^2}{\omega(z)^2}\right)}L_p^{|l|}\left(\frac{2r^2}{w(z)^2}\right)e^{\left(-ik\frac{r^2}{2R(z)}\right)}e^{(-il\phi)}e^{(-ikz)}e^{(i\psi(z))}. \tag{2.52}$$

Here C_{lp}^{LG} is a normalisation constant, $\omega(z)$ is the radius of the field at the 1/e value, and $R(z)$ is the radius of curvature of the beams wave-front at a distance

z. The Laguerre-Gauss mode can is then given as [24, 26],

$$E_{p,l}(r,\phi) = E_0\sqrt{\left(\frac{2r^2}{w(z)^2}\right)}L_p^l\left(\frac{2r^2}{w(z)^2}\right)e^{\left(-\frac{r^2}{w(z)^2}\right)}e^{(il\phi)} \tag{2.53}$$

Note that the first minimum occurs at $x^2 + y^2 = 0$ and of the amplitudes are rotationally symmetric around the z-axis. The Gouy phase shift is exaggerated in Laguerre-Gaussian modes, the same as in Hermite-Gaussian modes, by a factor of N+1 (equation 2.40) where $N = |l| + 2p$. This also contains the transverse amplitudes including the Gaussian drop off in r but with the product of the Laguerre polynomial. The rotational mode number, l, not only has impact on the Laguerre polynomial but also the phase factor ($e^{-il\phi}$). Here the beam profile is either advance by, or retarded by, l where it completes one rotation (2π) around the beam. This behaviour is an example of an optical vortex associated with the orbital angular momentum of light. Due to the randomly multimodal nature of the device reported in Chapter 4 it is not certain that the excited modes have either Hermite- or Laguerre-Gaussian properties. As the change in location produces varying output conditions and the laser emission not being collimated it is difficult to observe the superposition of the modes. Figure 2.12 displays a number of iterations of the Laguerre-Gaussian modes.

2.7 Spin Injection

Spin dependences of laser devices have been heavily investigated with particular interest in the effects of how a polarised pump source (master laser) alters the devices (slave laser) functionality and characteristics [28–30]. This polarised pump injects spin polarised carriers into the active region of the laser creating imbalances in the polarisation of carrier populations and can lead to a polarised emission from the slave laser. All devices reported in this thesis are optically excited using the Nd: YAG laser discussed in section 2.4. In Chapter 4 the polarisation of the VCSEL is also studied for different polarisation states of the pump, including linear and circular polarisation.

When a medium is optically excited by an external pump source with linearly or circularly polarised light that is resonant with the materials transitional levels, the medium becomes spin polarised. This is due to the population transfer between

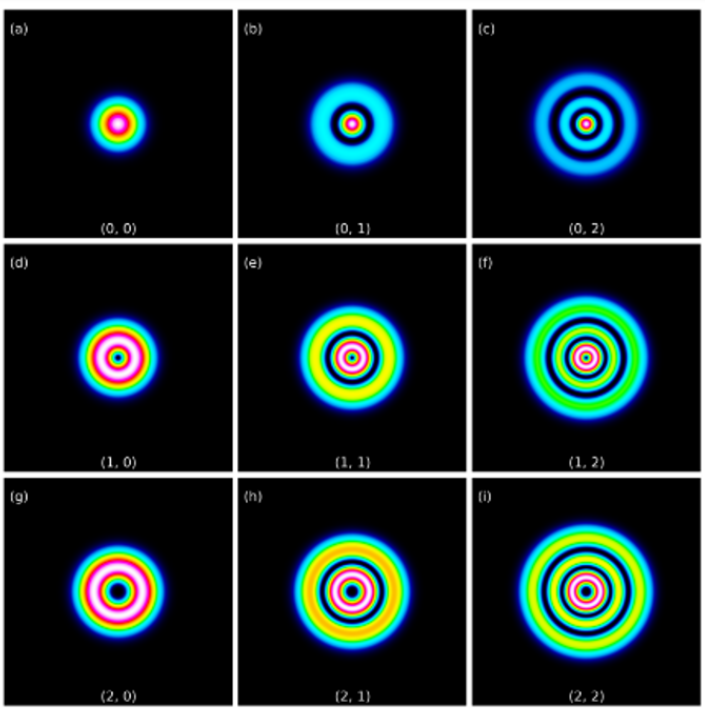

FIGURE 2.12: Spatial energy distribution of Laguerre-Gaussian modes. Image is taken from Lucas Hofer, "M^2 and High-order Modes," http://www.dataray.com/blog-m2-high-order-modes.html, 07/06/2017.

the magnetic sub-levels shifting between either the absorption or the emission of photons where the light polarisation can be chosen as π (linearly) of $\sigma^{\pm}$ (left- or right-circularly polarised) designated by the polarisation of the pump [29, 31–39].

In the following, background information on this topic is given.

2.7.1 Electron spin interactions

Electrons have the intrinsic property of being spin S = 1/2 and are characterised as having their intrinsic angular momentum quantum number = 1/2. From the quantised angular momentum [23], the total angular momentum can be seen as,

$$S = \sqrt{\frac{1}{2}\left(\frac{1}{2}+1\right)}\hbar = \frac{\sqrt{3}}{2}\hbar. \tag{2.54}$$

Equation 2.54 results in a fine structure that give rise to two possibilities along the z-axes,

$$S_z = \pm\frac{1}{2}\hbar. \tag{2.55}$$

This results in an energy split linking the spin to the magnetic moment of the electron,

$$\mu = \frac{e\hbar}{2mc}, \tag{2.56}$$

resulting in physical parameters the electron experiences [29]. In the 1920s, two investigations arose giving experimental values of the electron properties. The first is the splitting of the hydrogen spectral lines, known as fine structure. The second was the Stern-Gerlach experiment (1922) demonstrating that a beam of silver atoms split in two when sent through an inhomogeneous magnetic field. Both experiments validated the arguments of the electrons intrinsic angular momentum and magnetic moment where this property was coined electron spin, where equation 2.55 can be expressed as,

$$S_z = m_s\hbar, \tag{2.57}$$

where $m_s = \pm 1/2$.

2.7.2 Pauli exclusion principle

Due to electrons being fermions, S = 1/2, no two electrons in an atom can have the same quantum numbers. The Pauli exclusion principle is a quantum mechanical principle that states that two or more identical fermions per quantum state is not allowed.

2.7.3 Semiconductor energy bands

As p- and s-states are referred to in the subsequent sections a brief description will be given. The semiconductors that are considered (for example the II-VI CdSe semiconductor making the CQDs) have all four valence electrons per atom in the crystal. Here the valence electrons are derived from the s and p orbitals in a four-valent atom. Figure 2.13 displays the evolution of the p- and s-like atomic states through s and p bonding and anti-bonding orbitals of a molecule transitioning to the conduction bands of a bulk semiconductor. It is apparent from figure 2.13 that the top of the valence band has a p-like character whereas the bottom of the conduction is s-type. We note that the transition between such

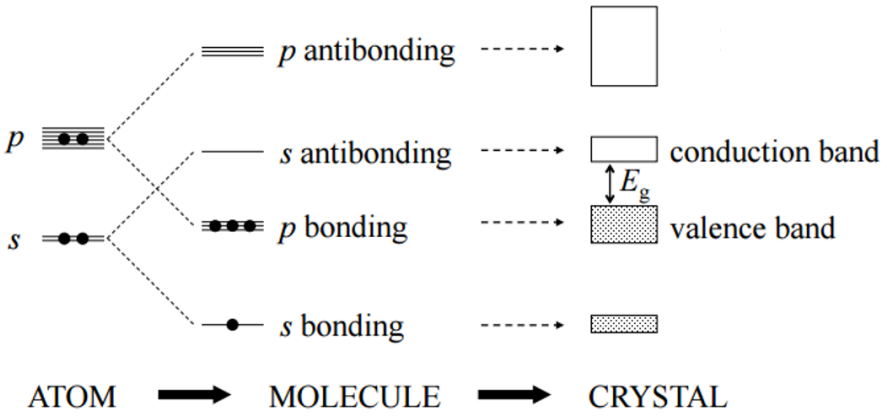

FIGURE 2.13: Schematic diagram from [16] of a semiconductor made up of four-valent atoms where the p- and s-states are hybridised forming bonding and anti-bonding molecular orbits that evolve into conduction and valence band of the semiconductor.

a valence (p) and conduction (s) bands is dipole allowed [16]. Because of the p-type character, the valence band is constituted of 3 sub-bands (corresponding to the 3 p-bonding orbitals), which are called heavy hole, light-hole and spin-orbit bands (see also section 1.4.2) each two spin degenerate. The conduction band is unique (but 2-spin degenerate) because of its s-type character. In the following sections, to discuss spin excitation, these levels/bands are identified by their total angular momentum J. We will see that consequently, 8 sub-states (2 for the s-like conduction band and 6 for the p-like valence band) are involved in transition phenomena.

2.7.4 Bulk III-V semiconductors

To explain the concept of spin injection, first consider a bulk semiconducting material, as described in [16]. When no magnetic field is present electrons in the conduction band have equal probability of being either spin up (m_s = +1/2) or spin down (m_s = -1/2). This results in there being no net spin. However, when absorption of circularly polarised light occurs a net electron spin can be created. This is known as spin injection.

This is possible because the circularly polarised light has an angular momentum component ±h that travels along the z-axis (the direction of propagation). The angular momentum is dependent on the direction of light polarisation, being +h for σ^+ (positive polarisation) and -h for σ^- (negative polarisation). This demonstrates

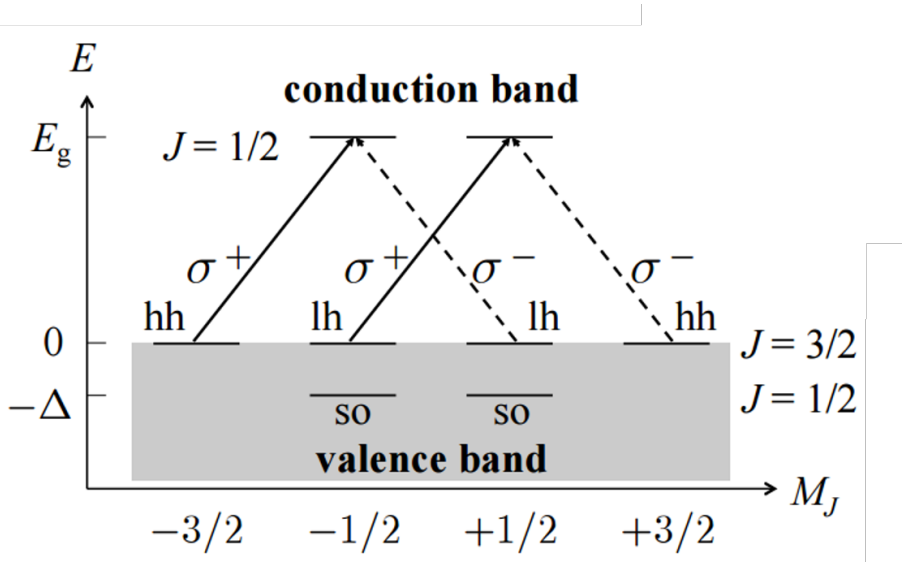

FIGURE 2.14: Detailed sub-level schematic of a bulk III-V semiconductor with direct band gap and $k = 0$. Circularly polarised excitation dictates the electron transitions with energy E_g shown from the degenerate valence bands to the conduction band, with no magnetic field present from [16].

that the absorption of circularly polarised light transmits angular momentum onto the medium resulting in a net spin.

Consider a direct band-gap III-V (or II-VI) semiconductor where the transitions are at the fundamental band edge where the heavy- and light-holes are degenerate. An angular momentum quantum number of L = 0 is obtained for the conduction band in s-like atomic states, with L = 1 for the valence band derived from p-like states. This results in the conduction band, remaining degenerate, having a single J = 1/2 level and the valence band having a four-fold degeneracy (M_J (the sub-level splitting) = 3/2, 1/2, -1/2, -3/2) level. In the latter, the spin-orbit energy (from the doubly degenerate state M_J = 1/2, -1/2), Δ, separates the two J levels.

Figure 2.14 displays a detailed sub-level plot of the conduction and valence band when $k = 0$ (the wave vector) and considers the M_J states. The conduction band has a single degenerate sub-level with $M_J = \pm 1/2$, however, the valence band is more complicated from the heavy- and light-holes degeneracy, for the J = 3/2 sub-level. The heavy-hole band has $M_J = \pm 3/2$ and the light-hole band $M_J = \pm 1/2$. The spilt-off hole band corresponds to the J = 1/2 level in the valence band.

When excited by circularly polarised light, selection rules only allow for specific transitions to occur. If the semiconductor is excited by σ^+ source then transition containing $\Delta M_J = +1$ are created. When excited by an σ^- source $\Delta M_J = -1$

transitions are created. Figure 2.14 illustrates all of the transitions when photon energy is greater than E_g. As can be seen, with σ^+ the electron in the heavy-hole sub-level M_J = -3/2 is promoted to M_J = -1/2 electron sub-level. This is also true for the light-hole, where the transition from the M_J = -1/2 light-hole sub-level promotes an electron to the M_J = 1/2 electron-level. When the semiconductor is excited by σ^- light the transition directions are reversed, as seen in figure 2.14 by the dashed arrows. Heavy-hole transitions are three times more likely than light-hole transitions (square of the matrix element) [16] resulting in three times as many electrons with M_J = -1/2 rather than M_J = 1/2. This allows the electron spin polarisation to be seen as,

$$\Pi = \frac{N(+1/2) - N(-1/2)}{N(+1/2) + N(-1/2)}, \tag{2.58}$$

where N(+1/2) and N(-1/2) are the number of electron with spin $\pm 1/2$ respectively. For σ^+ $\Pi = -50\%$ and for σ^- $\Pi = 50\%$. Therefore, bulk III-V semiconductors produce only 50% of spin polarised electron population.

2.7.5 Spin injection in quantum wells

This can then be extended, from bulk semiconductors, into quantum well structures. In quantum well structures the degeneracy of the heavy- and light-holes is lifted. This results in the generation of completely spin polarised electrons, i.e. $\Pi = 100\%$.

Figure 2.15 displays the optical transitions in a quantum well structure when optically excited by circularly polarised light. As discussed previously, the valence band is obtained by the splitting of the p-states by the spin-orbit interaction. This produces heavy- and light-hole levels with J = 3/2 with sub-levels $M_J = \pm 3/2$ and $M_J = \pm 1/2$. The conduction band remains the same with the sub-levels $M_J = \pm 1/2$ (spin up/down) in the J = 1/2 level. σ^+ pumping results in well defined circular polarisations as the transitions between the sub-levels are well defined ($M_J = \pm 1$), demonstrated in figure 2.15.

Comparing figures 2.14 and 2.15 it can be seen that the main difference is the shift in states. This shift is due to the quantum confinement and results in the hole levels losing degeneracy. This results in the heavy- and light-hole energies, hh1 $\rightarrow$ e1 and lh1 $\rightarrow$ e1, transitions being split by the difference in hh1 and lh1

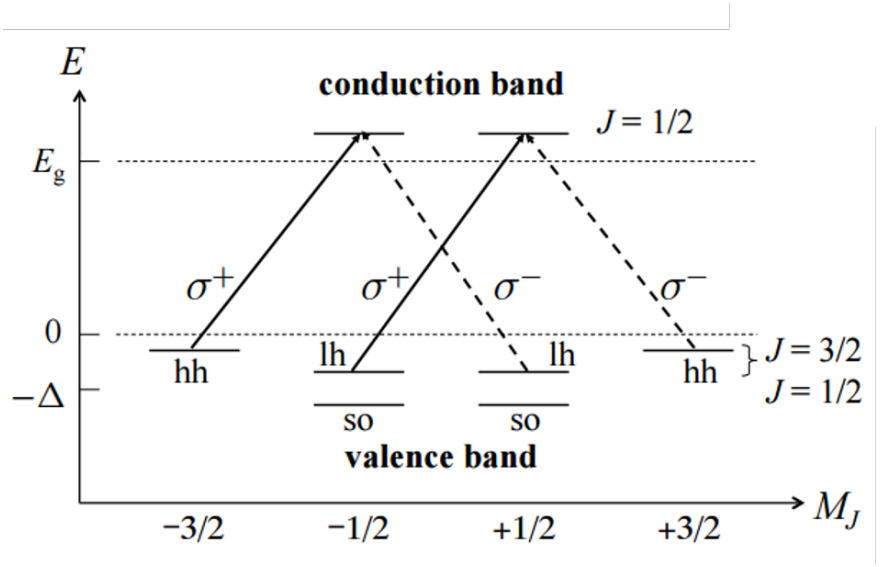

FIGURE 2.15: Detailed sub-level schematic of a zinc-blende quantum well band structure dipicting the selection rules under circularly polarised optical pump from [16].

confinement energies. Using circularly polarised light in an energy range of,

$$E_g + E_{e1} + E_{hh1} \leqslant \hbar\omega \leqslant E_g + E_{e1} + E_{lh1}, \tag{2.59}$$

allows for complete spin polarisation of electrons where the direction is dependent on the pump polarisation ($\sigma^{\pm}$).

Note that the effect of quantum confinement splitting the heavy- and light-holes is an important phenomenon. In bulk semiconductors, at $k = 0$, the heavy- and light-holes have degenerate bands, known as mixed character, with a hole relaxation lifetime of $\tau_h = 10^{-12}s$ and is typically shorter than the electron relaxation lifetime [36]. In a quantum well structure this is no longer true as the $M_J = \pm 3/2$ states are pure eigenstates and due to the circularly polarised photons having an energy range as in equation 2.59, 100% spin-polarised heavy-holes and electrons are produced.

2.7.6 Quantum dots

Circular polarisation switching and polarisation bistability have been shown in VCSEL structures [31], circularly polarised laser pulses due to spin polarised excitation [28] and in GaN nanowire lasers [44]. These results are the basis in the curiosity of CQD behaviour under such conditions and lead onto the Stokes parameters for the device reported in Chapter 4 being calculated.

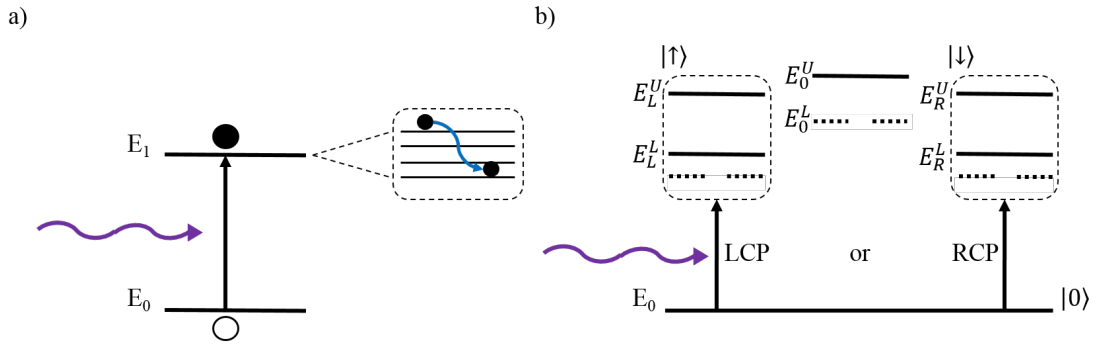

FIGURE 2.16: a) A two-level degenerate system with the conduction band splitting magnified. This shows the excited electron relaxing from a circularly polarised state into a linear polarised state before emission. b) $1S_{3/2}$-$1S_e$ structure indicating the exciton pair dependence on polarisation. E_0^U and E_0^L represent the linear polarised levels, E_L^U and E_L^L represent LCP levels and E_R^U and E_R^L with RCP. $|0>$, $|\uparrow>$ and $|\downarrow>$ representative of the different polarisation outputs.

Chalcogenide CQDs as studied in this work can be considered of the zinc-blende or wurtzite crystal structure and the exciton fine structure of the $1S_{3/2} - 1S_e$ transition is shown in figure 2.16. Three states (dashed lines) are dark and five are bright. One of these bright states can be excited with linear polarisation and the other four with either right or left circular polarisation. Therefore, like for quantum wells, specific spin states can be specifically addressed. For this, the CQDs have to be suitably oriented, with the excitation light having a propagation component non-nil along the CQD c-axis (representative of the z-axis). Consequently, in a random spatial distribution of CQDs, obtaining a significant spin bias of excitons is not evident. However, even a small difference in the spin of the exciton population has the potential to translate to a strongly spin-polarised emission in the laser regime. In Chapter 4, we therefore utilised a spin-polarised pump excitation and record the polarisation of the CQD VCSEL to see if such a behaviour can be seen. While the explanations above were on resonant excitation of spin states, it is also possible to pump out of resonance (as is often done in experiments on VCSELs) as relaxation is fast enough so the spin are conserved. This is what is done, and explained further, in Chapter 4.

2.8 Random lasing

When assessing a material as a potential gain material for a lasers, ASE is initially sought out as it in an indicator if the material is suitable. This is the phenomenon of the spectral narrowing characterised by a threshold-like behaviour of the power-transfer function and is discussed in section 1.3.5. However, a smooth ASE spectrum is not always observed in OS or CQD thin films but instead there can be characteristic narrow peaks dominating in intensity superposed onto it. These peaks are caused by random scattering in the film when optical gain is present. The scattering can in certain cases increase the photon interaction with the gain medium in a way that is wavelength dependent. This is at the origin of the narrow spectral spikes and such behaviour is attributed to phenomena related to what is termed random lasing (RL). RL was first reported by Lethokov *et al* [45, 46] in the 1960s whilst investigating the limits of classical cavity structures. There was a lack of enthusiasm until the 1990s when unexpected spectral features were observed in polycrystalline semiconductors [47] and particle-doped dye-based gain materials [48]. This led onto an active research area exploring the localisation of light [49], complex interference phenomena [50–52] and phase transition [53]. This has led to RL demonstrations particularly in organic semiconductor films, where scattering was unintentional [54]. RLs are reported on in Chapter 5 section 5.4 and are produced in OSs.

As stated throughout this thesis, the basic concept of a laser cavity can be understood with a Fabry-Pérot cavity, depicted in figure 1.1. Comprising a three- or four-level optical gain medium the optical cavity architecture determining the output properties of the laser. The emission is usually expected to be directional, coherent, narrow-linewidth and of a specific state of polarisation. In addition to this, lasers need to achieve population inversion in order to produce gain within the energy levels demonstrating clear threshold levels establishing the "kick" in the power transfer function. However, researchers have explored unique cavity formats such as lasers without inversion [55], zero threshold laser action [56] and mirrorless lasers [57]. The latter being where RLs fall into place. RLs lack some of the properties mentioned resulting in some scientists to have conflicting views.

Typically, RLs emit spiky optical spectra comprised of numerous, or single, narrow-linewidth peaks. However, it has been shown that phase transitions from spiky to non-spiky spectra has been demonstrated through varying the pump geometry

[53]. It was shown that through pumping organic films with a narrow geometry, highly multimode laser emission with narrow linewidth (< 1meV) peaks were recorded. These peaks were not periodically separated as other cavity formats such as Fabry-Pérot or whispering gallery mode lasers would produce.

2.9 Conclusion

In this chapter the principles of DFB lasers, VCSELs and RLs were explained. For DFB laser the main concepts and fabrication techniques were described including encapsulation method exploited in the work reported in this thesis. The characterisation methods were also addressed discussing the corresponding experimental set-ups; although more details are given in the later chapters. The theoretical models used in these chapters were also expanded upon as their outputs are used in the discussion of the experimental results.

The main properties of Fabry-Pérot cavities was also covered including the physical and optical elements. As a polarisation study is carried out in Chapter 4 a basis into molecular spin is given with examples leading from bulk semiconductor to quantum dots for comparison.

The experimental results of this thesis and the related discussions are given in the next part.

References

[1] I. D. W. Samuel and G. A. Turnbull. Organic Semiconductor Lasers. *Chemical Reviews*, 107(4):1272–1295, apr 2007.

[2] A. V. Malko, A. A. Mikhailovsky, M. A. Petruska, J. A. Hollingsworth, H. Htoon, M. G. Bawendi, and V. I. Klimov. From amplified spontaneous emission to microring lasing using nanocrystal quantum dot solids. *Applied Physics Letters*, 81(7):1303, 2002.

[3] Caroline Foucher. *Solution-processable, mechanically-flexible lasers*. PhD thesis, 2015.

[4] M. D. McGehee, M. A. Díaz-García, F. Hide, R. Gupta, E. K. Miller, D. Moses, and A. J. Heeger. Semiconducting polymer distributed feedback lasers. *Applied Physics Letters*, 72(13):1536–1538, 1998.

[5] Johannes Herrnsdorf, Benoit Guilhabert, Yujie Chen, Alexander Kanibolotsky, Allan Mackintosh, Richard Pethrick, Peter Skabara, Erdan Gu, Nicolas Laurand, and Martin Dawson. Flexible blue-emitting encapsulated organic semiconductor DFB laser. *Optics Express*, 18(25):25535, dec 2010.

[6] K. Yoshino, S. Tatsuhara, Y. Kawagishi, M. Ozaki, A. A. Zakhidov, and Z. V. Vardeny. Amplified spontaneous emission and lasing in conducting polymers and fluorescent dyes in opals as photonic crystals. *Applied Physics Letters*, 74(18):2590–2592, 1999.

[7] Patrick Görrn, Marcus Lehnhardt, Wolfgang Kowalsky, Thomas Riedl, and Sigurd Wagner. Elastically tunable self-organized organic lasers. *Advanced Materials*, 23(7):869–872, 2011.

[8] M. G. Moharam, T. K. Gaylord, Eric B. Grann, and Drew A. Pommet. Formulation for stable and efficient implementation of the rigorous coupled-wave analysis of binary gratings. *Journal of the Optical Society of America A*, 12(5):1068, 1995.

[9] Andrea Camposeo, Pompilio Del Carro, Luana Persano, and Dario Pisignano. Electrically tunable organic distributed feedback lasers embedding nonlinear optical molecules. *Advanced Materials*, 24(35):221–225, 2012.

[10] Johannes Herrnsdorf, Yue Wang, Jonathan J D Mckendry, Zheng Gong, David Massoubre, Benoit Guilhabert, Georgios Tsiminis, Graham A. Turnbull, Ifor D W Samuel, Nicolas Laurand, Erdan Gu, and Martin D. Dawson. Micro-LED pumped polymer laser: A discussion of future pump sources for organic lasers. *Laser and Photonics Reviews*, 7(6):1065–1078, 2013.

[11] Hyochul Kim, Kyung-Sang Cho, Heejeong Jeong, Jineun Kim, Chang-Won Lee, Weon-kyu Koh, Young-Geun Roh, Sung Woo Hwang, and Yeonsang Park. Single-Mode Lasing from a Monolithic Microcavity with Few-Monolayer-Thick Quantum Dot Films. *ACS Photonics*, page acsphotonics.6b00327, 2016.

[12] C. Foucher, B. Guilhabert, J. Herrnsdorf, N. Laurand, and M. D. Dawson. Diode-pumped, mechanically-flexible polymer DFB laser encapsulated by glass membranes. *Optics Express*, 22(20):24160, sep 2014.

[13] John Chilwell and Ian Hodgkinson. Thin-films field-transfer matrix theory of planar multilayer waveguides and reflection from prism-loaded waveguides. *Journal of the Optical Society of America A*, 1(7):742, 1984.

[14] Max Born and Emil Wolf. *Principles of Optics*. 7th edition, 1999.

[15] Shun Lien Chuang. *Physics of Photonic Devices*. John Wiley & Sons Inc, 2nd edition, 2009.

[16] Mark Fox. *Optical Properties of Solids*. Oxford university press, 2001.

[17] Hiram W. Edwards and Robert P. Petersen. Reflectivity of evaporated silver films. *Physical Review*, 50(9):871, 1936.

[18] Eugene Hecht. *Optics*. Addison Wesley Longman Inc, 4th edition, 1998.

[19] L. R. Brovelli and U. Keller. Simple analytical expressions for the reflectivity and the penetration depth of a Bragg mirror between arbitrary media. *Optics Communications*, 116:343–350, 1995.

[20] Paul N. Butcher and David Cotter. Gaussian beam optics. *The Elements of Nonlinear Optics*, pages 319–320.

[21] Bahaa E. A. Saleh and Malvin Carl Teich. *Fundamentals of photonics*. Wiley New York, 1991.

[22] Graham Woan. *The Cambridge Handbook of Physics Formulas*. Cambridge University Press, 2003.

[23] Karl F. Renk. *Basics of Laser Physics, Graduate Texts in Physics*. Springer Berlin Heidelberg, 2012.

[24] A. V. Volyar and T. A. Fadeeva. Laguerre-Gaussian beams with complex and real arguments in a uniaxial crystal. *Optics and Spectroscopy*, 101(3):450–457, 2006.

[25] William T. Silfvast. *Laser Fundamentals*. Cambridge University Press, 2004.

[26] M. Mohamadi, M. Mostamand, M. Moosavi, and M. Soltanolkotabi. Selective Transverse Modes in a Diode End-Pumped Nd : Yag Pulsed Laser. *International Journal of Mathematical, Computational, Physical, Electrical and Computer Engineering*, 5(10):324–327, 2011.

[27] Frank Träger. *Springer Handbook of Laser and optics*. Springer, 2nd edition, 2012.

[28] Omar Qasaimeh. Novel closed-form solution for spin-polarization in quantum dot VCSEL. *Optics Communications*, 350:1–7, 2015.

[29] M. I. Dyakonov. Basics of Semiconductor and Spin Physics. In *Spin Physics in Semiconductors*, pages 1–28. Springer, 2008.

[30] Paul A. Williams. Rotating-wave-plate Stokes polarimeter for differential group delay measurements of polarization-mode dispersion. *Applied Optics*, 38(31):6508, nov 1999.

[31] S. S. Alharthi, A. Hurtado, V. M. Korpijarvi, M. Guina, I. D. Henning, and M. J. Adams. Circular polarization switching and bistability in an optically injected 1300 nm spin-vertical cavity surface emitting laser. *Applied Physics Letters*, 106(2), 2015.

[32] Z. Yu, W. Li, J. A. Hagen, Y. Zhou, D. Klotzkin, J. G. Grote, and A. J. Steckl. Photoluminescence and lasing from deoxyribonucleic acid (DNA) thin films doped with sulforhodamine. *Applied Optics*, 46(9):1507, mar 2007.

[33] M. Paillard, X. Marie, P. Renucci, T. Amand, A. Jbeli, and J. M. Gérard. Spin relaxation quenching in semiconductor quantum dots. *Physical Review Letters*, 86(8):1634–1637, 2001.

[34] A. Imamolu, E. Knill, L. Tian, and P. Zoller. Optical Pumping of Quantum-Dot Nuclear Spins. *Physical Review Letters*, 91(1):017402, 2003.

[35] Beth Schaefer, Edward Collett, Robert Smyth, Daniel Barrett, and Beth Fraher. Measuring the Stokes polarization parameters. *American Journal of Physics*, 75(2):163–168, feb 2007.

[36] Ahmad Khastehdel Fumani and Jesse Berezovsky. Spin-Pumping Efficiency in Room-Temperature CdSe Nanocrystal Quantum Dots. *The Journal of Physical Chemistry C*, 118(48):28202–28206, dec 2014.

[37] Gregory D. Scholes. Selection rules for probing biexcitons and electron spin transitions in isotropic quantum dot ensembles. *The Journal of Chemical Physics*, 121(20):10104–10110, nov 2004.

[38] Gregory D. Scholes and David L. Andrews. Resonance energy transfer and quantum dots. *Physical Review B*, 72(12):125331, sep 2005.

[39] Kai Jun Yuan, Szczepan Chelkowski, and Andre D. Bandrauk. Rotations of molecular photoelectron angular distributions with intense ultrashort circularly polarized attosecond laser pulses. *Journal of Chemical Physics*, 138(13), 2013.

[40] Guido Burkard, Daniel Loss, and David P. DiVincenzo. Coupled quantum dots as quantum gates. *Physical Review B*, 59(3):2070–2078, 1999.

[41] D. Gammon, Al. L. Efros, T. A. Kennedy, M. Rosen, D. S. Katzer, D. Park, S. W. Brown, V. L. Korenev, and I. A. Merkulov. Electron and Nuclear Spin Interactions in the Optical Spectra of Single GaAs Quantum Dots. *Physical Review Letters*, 86(22):5176–5179, 2001.

[42] Vasilios Deligiannakis, Siddharth Dhomkar, Haojie Ji, Daniela Pagliero, Igor L. Kuskovsky, Carlos A. Meriles, and Maria C. Tamargo. Spin dynamics of ZnSe-ZnTe nanostructures grown by migration enhanced molecular beam epitaxy. *Journal of Applied Physics*, 121(11), 2017.

[43] Mete Atatüre, Jan Dreiser, Antonio Badolato, Alexander Högele, Khaled Karrai, and Atac Imamoglu. Quantum-Dot Spin-State Preparation with Near-Unity Fidelity. *Science*, 312(5773):551–554, 2006.

[44] A. Hurtado, H. Xu, J. B. Wright, Sheng Liu, Q. Li, G. T. Wang, T. S. Luk, J. J. Figiel, K. Cross, G. Balakrishnan, L. F. Lester, and I. Brener. Polarization switching in GaN nanowire lasers. *Applied Physics Letters*, 103(25), 2013.

[45] R. V. Ambartsumyan, N. G. Basov, P. G. Kryukov, and V. S. Letokhov. A Laser with a Nonresonant Feedback. *IEEE Journal of Quantum Electronics*, 2(9):442–446, 1966.

[46] V. S. Lethokov. Stimulated emission of an ensemble of scattering particles with negative absorption, 1967.

[47] H. Cao, Y. G. Zhao, H. C. Ong, S. T. Ho, J. Y. Dai, J. Y. Wu, and R. P H Chang. Ultraviolet lasing in resonators formed by scattering in semiconductor polycrystalline films. *Applied Physics Letters*, 73(25):3656–3658, 1998.

[48] R. M. Balachandran, D. P. Pacheco, and N. M. Lawandy. Laser action in polymeric gain media containing scattering particles. *Applied Optics*, 35(4):640, feb 1996.

[49] Diederik S. Wiersma, Paolo Bartolini, Ad Lagendijk, and Roberto Righini. Localization of light in a disordered medium. *Nature*, 390(6661):671–673, 1997.

[50] X. Wu, W. Fang, A. Yamilov, A. A. Chabanov, A. A. Asatryan, L. C. Botten, and H. Cao. Random lasing in weakly scattering systems. *Physical Review A - Atomic, Molecular, and Optical Physics*, 74(5):1–11, 2006.

[51] C. Vanneste, P. Sebbah, and H. Cao. Lasing with resonant feedback in weakly scattering random systems. *Physical Review Letters*, 98(14):1–4, 2007.

[52] Seung Ho Choi and Young L. Kim. Random lasing mode alterations by single-nanoparticle perturbations. *Applied Physics Letters*, 100(4), 2012.

[53] Marco Leonetti, Claudio Conti, and Cefe Lopez. The mode-locking transition of random lasers. *Nature Photonics*, 5(10):615–617, 2011.

[54] S. Frolov, Z. Vardeny, K. Yoshino, a. Zakhidov, and R. Baughman. Stimulated emission in high-gain organic media. *Physical Review B*, 59(8):R5284–R5287, 1999.

[55] Marlan O. Sully and Michael Fleischhauer. Lasers without inversion. *Science*, 263(5154):337–338, 1994.

[56] F. De Martini and G. R. Jacobovitz. Anomalous spontaneous stimulated-decay phase transition and zero-threshold laser action in a microscopic cavity. *Physical Review Letters*, 60(17):1711–1714, 1988.

[57] Lee W. Casperson. Threshold characteristics of mirrorless lasers. *Journal of Applied Physics*, 48(1):256–262, 1977.

Part II

Results

Chapter 3

CQD DFB lasers

This chapter presents and discusses the demonstration of a CQD DFB laser with state-of-the-art threshold performance for >ns duration pumping. This progress in performance compared to previous works is enabled by the utilisation of alloyed-core/shell quantum dots encapsulated in a multilayer waveguide structure. The overcoating of the gain material with PVA symmetrises the laser structure and reduces the modal losses, in turn enabling the lowest threshold operation in the ns regime for CQD lasers. Main results presented in this Chapter are published in Optics Express (L. J. McLellan, B. Guilhabert, N. Laurand, and M. D. Dawson, "CdS_xSe_{1-x}/ZnS semiconductor nanocrystal laser with sub $10kW/cm^2$ threshold and 40nJ emission output at 600 nm," Opt. Express 24, A146 (2016)).

3.1 Introduction

CQDs, as explained in Chapter 1, are nanoscopic semiconductor crystals that confine charge carriers in three dimensions. They are solution processable and their emission and absorption energies can be flexibly tuned by varying their size and composition. With the capability to emit at wavelengths typically difficult to access with other semiconductor materials, e.g. in the yellow-orange part of the spectrum [1–3], CQDs are attractive for visible lasers. Their solution processing also enables the fabrication of innovative laser cavity formats. Nevertheless, although intensive studies and developments have been achieved in the last two decades, a practical demonstration of CQD lasers has yet to be shown. In order to accomplish this, optical pumping with nanosecond or longer pulses must

be achieved so that the technology is compatible with compact solid-state pump lasers [4–7] or, the end goal, with laser diode pumping. The main objective of this chapter was to push the performance of CQD DFB lasers operating in a ns temporal regime. The chapter reports on a distributed feedback laser (DFB) with a bilayer planar waveguide structure that helps minimise resonator losses and hence enhances the modal gain. The CQDs used as gain material are alloyed-core/shell CdS_xSe_{1-x}/ZnS CQDs as the alloyed design is known to help mitigate the issue of Auger recombination, significant in CdSe/ZnS [8, 9].

3.2 Design and fabrication of the CQD DFB structure

3.2.1 Bragg equation

The principles of DFB lasers are explained in Chapter 2 (section 2.2). As a reminder to the reader such a laser utilises a grating structure to create optical feedback, distributed over the whole resonator structure, through Bragg scattering for producing laser oscillation. The optical feedback is obtained at the Bragg wavelength, λ_B, and is defined by

$$m\lambda_B = 2n_{eff}\Lambda, \tag{3.1}$$

where m corresponds to the desired order of emission (here being the second order), n_{eff} is the effective refractive index of the device and Λ is the period of the grating.

3.2.2 2nd order bilayer DFB laser

A schematic of the DFB laser is shown in figure 3.1. The design is based on a second order DFB cavity with a bi-layered, planar waveguiding structure. The grating itself is a rectangular nanopatterned fused silica substrate, with refractive index of 1.46, which has a period of $\Lambda = 380$ nm and a modulation depth of 50 nm. The period is selected to create a second order DFB effect, i.e. optical feedback is obtained for $m = 2$. The laser emits vertically, perpendicular to the devices surface, through the first order of diffraction. The mask for the grating was

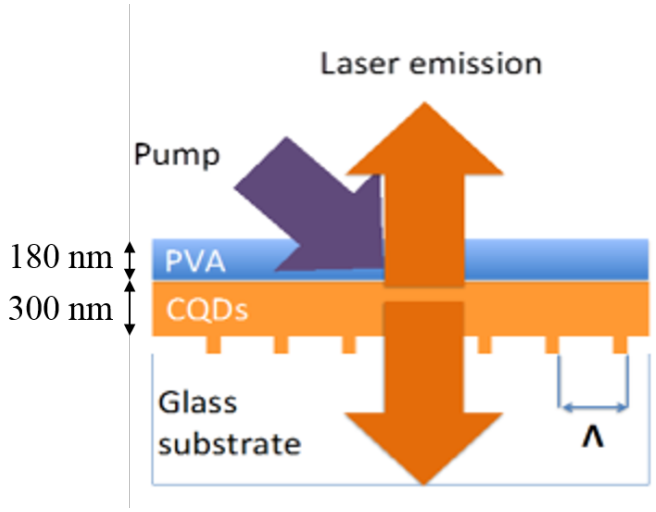

FIGURE 3.1: Schematic of the second order DFB laser structure with grating substrate, $\Lambda = 380$nm, 50nm modulation depth, 300nm CQD layer and 180nm PVA layer. The laser is pumped at an angle (purple arrow) and has vertical emission (orange arrows).

fabricated by e-beam lithography and its transfer into the fused silica substrate via etching (see Chapter 2).

The gain layer consisted of a 300nm thick film of CQDs that was directly applied to the surface of the patterned substrate. The encapsulant overcoating the CQD film (the second layer of the bilayer design) is polyvinyl alcohol (PVA). It plays two roles here. First it acts as an oxygen barrier [10] improving the photostability of the gain material, and secondly it symmetrises the refractive index profile of the overall DFB laser structure. The latter increases the confinement of the laser mode within the waveguiding structure. It also reduces the losses by reducing scattering at the interface of the CQD film. This in turn increases the modal gain, which is vital to enable low threshold operation.

The PVA layer used in this investigation was chosen to be 180 nm, $n_{PVA} = 1.55$. This provides a good compromise between confinement, overlap of the mode with the CQD layer and barrier properties [10]. This is shown in figure 3.2 for both a neat device (a single layer DFB laser, i.e. with no PVA) and an encapsulated device (the bilayer laser incorporating PVA). The figure was plotted using the transfer matrix method described in Chapter 2. It is expected that the addition of PVA would result in both an improved overlap with the gain region (see section 2.5.3) and a reduced field intensity at the air interface (hence reducing scattering loss at the laser surface). However, in reality, the addition of the PVA layer does not significantly alter the overlap with the CQDs (∼82%). The figure (figure 3.2)

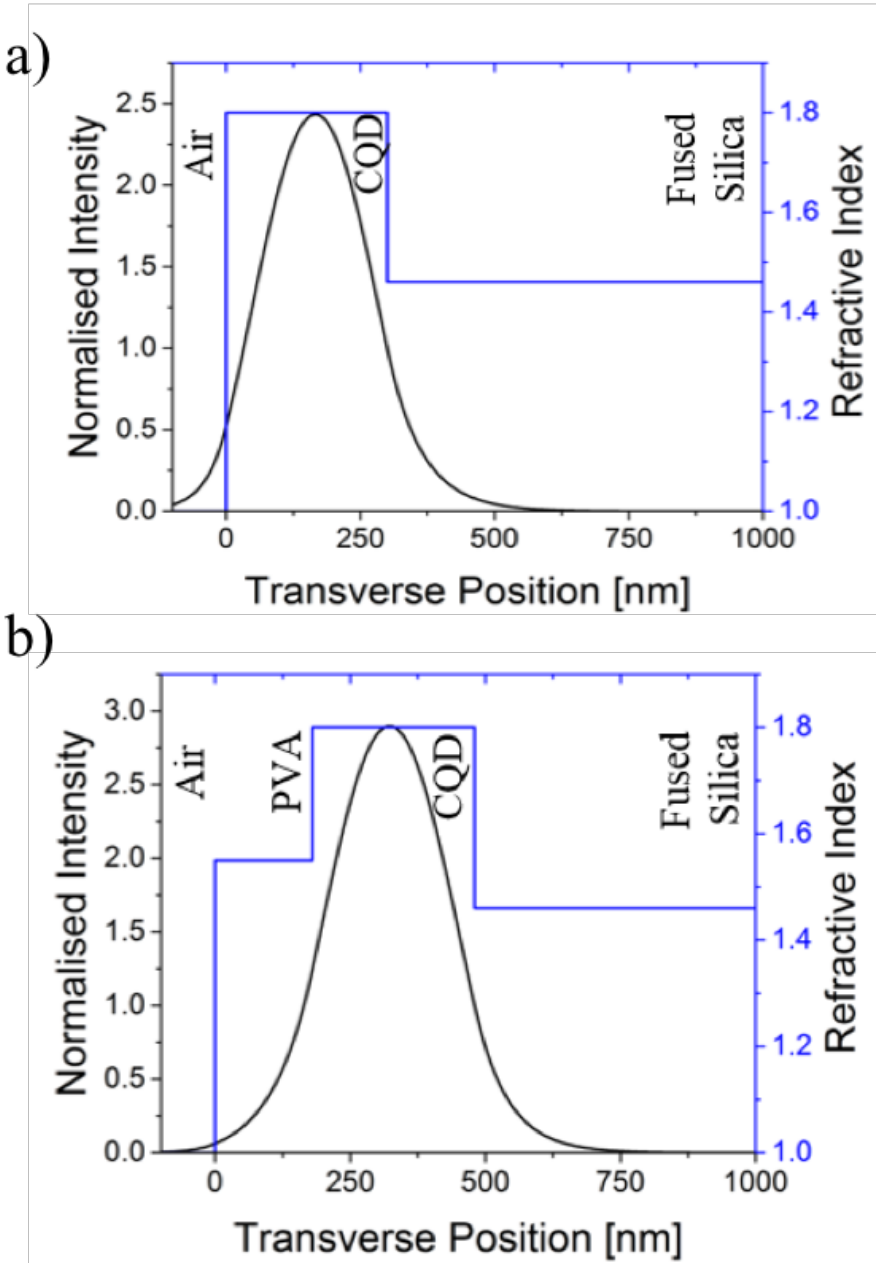

FIGURE 3.2: Mode and refractive index profile of a a) neat waveguide structure and b) PVA encapsulated waveguide structure.

does display a symmetrising effect present on the mode, confining a larger coverage within the gain material. Both modes, for neat and encapsulated films, have an approximately equal size where the encapsulated mode is again centralised within the CQD film, creating a more symmetrical mode. Figure 3.2 also depicts that the addition of PVA allows a more symmetrised mode within the CQD film. Thus, reducing the losses at the device surface; as PVA produces a smooth interface whereas the CQD PMMA matrix would be less homogeneous.

3.2.3 Alloyed-core/shell CdS_xSe_{1-x}/ZnS

The CQDs selected for this study were alloyed-core/shell CdS_xSe_{1-x}/ZnS CQDs (Trilite^{TM} from Cytodiagnostics). Although a number of wavelengths were tested only two, intrinsic PLs centred at 575nm and 630nm, were found to develop ASE in our set-up. These CQDs are spherical type I alloyed-core/shell structures with an average diameter of 6 nm and oleic acid as surface ligands. Type I CQDs are known to suffer from Auger recombination due to having stronger confinement, which increases their recombination lifetimes but also the likelihood for Auger effect when there are two or more excitons present. As discussed in Chapter 1, this is a factor that diminishes laser performance. The Auger effect is increased by an abrupt core/shell interface and its effects have been shown to be intensified in CQDs of smaller size [8, 9]. Utilising the alloyed-core design [11] allows CQDs to retain a relatively large size for a range of emission wavelengths (e.g. 6nm diameter for emission from 450 nm to 665 nm for Trilite^{TM} CQDs) as these are selected by tailoring the composition of the core. The alloyed design also results in a smoothing of the core/shell interface, also reducing the Auger recombination.

The CQDs were initially dispersed in toluene at a concentration of 1 mg.mL^{-1}. Figure 3.3 shows the absorption and the PL spectra of the 575nm and 630nm emitting CQDs in solution. For the 575nm CQDs it can be seen that the first absorption peak appears at 557 nm and the Stokes shift is 21 nm (maximum value of PL occurs at 578.2 nm) comparable to that of typical core/shell CdSe/ZnS CQDs [12, 13]. For the 630nm CQDs the first absorption peak occurs at 611 nm and Stokes shift can be seen to be 11 nm (maximum value of PL occurs at 622 nm). Note that any redshift due to the reabsorption of the CQDs is minimised in a solution with low concentration (dilute solution). Note that at longer wavelengths the absorption spectra does not go to zero. The experimental procedure is discussed in section 3.3.1 where the "dark" is measured in toluene. Toluene has a lower refractive index (at longer wavelengths) than the CQDs allowing more light to pass through causing the non-zero values.

Normally a large Stokes shift (as long as emission stays efficient) is desirable for lasers as it minimises reabsorption in the gain material. Here, because the absorption overlays the emission spectra, there will be reabsorption present within the film as the CQDs partially absorb in their emission wavelength. This correlates with the redshift in the solid-state emission discussed later in section 3.3.2.

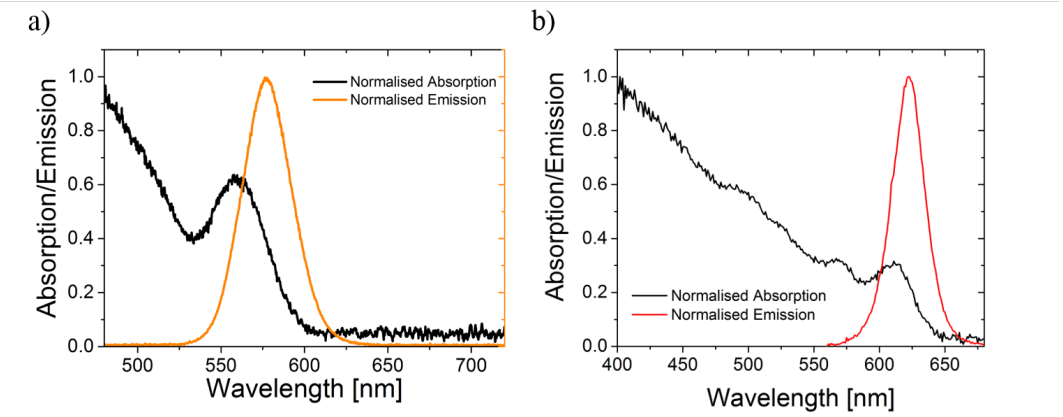

FIGURE 3.3: Absorption and intrinsic PL spectra of CQDs dispersed at 1mg.mL^{-1} in toluene for a) 575nm emitting CQDs and b) 630nm emitting CQDs.

DFB lasers were demonstrated with 575nm CQDs deposited onto glass gratings, although ASE from 630nm CQDs on polymer grating was also shown during initial studies (see section 3.4.1). For these demonstrations solutions of CQDs were taken and the toluene was evaporated using a vacuum pump, thereby yielding the CQDs in powder form. The CQDs were then rediluted to 50 mg.mL^{-1} in a Poly (methyl methacrylate) (PMMA): chloroform mix with a weight ratio of PMMA to chloroform of 1.6:1. The solution was spun cast onto the planar glass substrate. After deposition of the PVA, also by spin-coating, the sample was annealed at 30^{0}C for 72 hours. PVA can be found in many everyday appliances such as food packaging, biomedicine and photonics. It has also been used in photonic crystal sensors, waveguides and as protective encapsulant in organic solar cell. PVA has also shown a reduction in lasing threshold as it alters the modal confinement in the waveguide that occurs during laser resonance [14, 15].

3.2.4 Initial studies using polymeric gratings

Although the main results discussed in this chapter use a fused silica grating to create the cavity, initial studies with polymeric gratings were attempted. In these initial studies optical adhesives chosen to have specific refractive indices and transparencies at certain wavelengths have been utilised: Norland NOA 65 and Cyclohexyldimethanol divinylether (CHDV).

NOA 65 is transparent at visible wavelengths, can be cured under a UV lamp (370 nm with power density 200 mW/cm^2) and has a refractive index of approximately

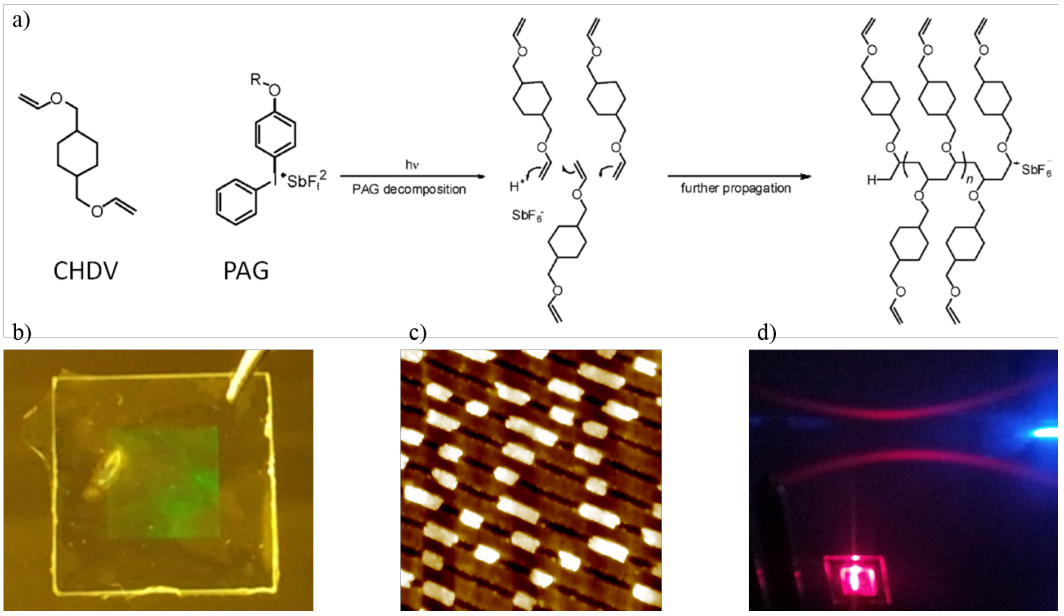

FIGURE 3.4: a) Chemical structure of CHDV and the PAG. Upon exposure to light, the monomers are linked through their vinyl ether units [18] b) CHDV grating under torch illumination shows the grating structure through its diffracted light (green colour) c) AFM image of CHDV grating with contamination of PDMS from the lithography process d) 630 nm CQDs emitting ASE on CHDV grating.

1.52. This material has been used before in demonstrations of organic lasers [10, 15–17] under nanosecond pulsed pumping. However, we found previously that CdSe/ZnS CQDs had the tendency to aggregate with this material. In this work with the alloyed-core/shell CQDs we saw no evidence of optical gain in ASE measurements and it is not discussed further.

CHDV [18], figure 3.4, has previously been successfully engineered with CdSe/ZnS CQDs [19]. As CHDV is a rigid material it cannot be directly applied to a master grating. When fabricating the CHDV gratings, a negative copy of the master grating is created using a flexible Polydimethylsiloxane (PDMS) film to reproduce the desired periodicity for a second-order DFB. Once the PDMS has set the CHDV is drop cast onto the grating surface. Before deposition the CHDV is mixed with Photo Acid Generator (PAG) at 0.1% by weight, figure 3.4a. After deposition the solution is cured under the same UV lamp used previously. Once set the CHDV grating was peeled off the PDMS resulting in a copy of the master grating, figure 3.4b, and the (re-diluted) CQDs are spun cast onto the grating surface.

A priori CHDV is an ideal material as it is transparent in the visible and near UV, it has low refractive index , $n_{CHDV} = 1.47$, (lower than typical epoxies such

as NOA 65 that typically increases the DFB efficiency because of the higher index contrast with the CQDs, leading to greater strength in the propagating mode), is very robust and the grating structures are reusable.

Unfortunately, even though there are a lot of benefits to this material, there are a number of drawbacks. Although the rigidity of the material is initially desired, it is also one of its main downfalls for fabrication as the CHDV literally rips apart the PDMS grating leaving impurities. This can be seen in figure 3.4c, where the light sections are remnants of the PDMS being physically ripped off. CHDV is also known to shrink under curing, which can alter the periodicity, create non-linear periods, and decreases the modulation depth.

Despite these difficulties, we had some success with this material with the 630nm emitting CdS_xSe_{1-x}/ZnS CQDs. Figure 3.4d displays fan shaped emission from the CHDV grating indicating that ASE occurs and is diffracted by the grating. If the feedback was in resonance, laser emission would happen and these fans would overlap (with laser emission as a line in the centre). In our case though the periodicity is not adequate. We had no grating with a periodicity large enough for such wavelength range (>630nm) and given the difficulty with replication of the grating in CHDV, we decided to focus on using directly the silica gratings with 575nm CQDs. This is what is discussed in the rest of the chapter.

3.3 Optical Characterisation

3.3.1 Emission and absorption

When measuring the absorption and PL of the CQDs in solution, figure 3.3, as small amount of the CdS_xSe_{1-x}/ZnS CQDs, as purchased, at 1mg.mL^{-1} in toluene was placed into a 1mm-path glass cuvette. For the PL measurement the film was optically excited via a CW 10mW UV laser diode emitting at 371 nm where the beam shaped as a 6.1±0.4 mm by 1.7±0.2 mm stripe onto the film surface. The emission from the edge of the film was then collected with a microscope objective (60 X magnification, NA 0.85) and the spectrum was recorded with a TRIAX 550 spectrometer at a resolution of 0.03 nm.

For absorption measurements a tungsten lamp replaced the laser diode. The light from the lamp was transmitted through the cuvette and the spectrum recorded using the aforementioned spectrometer. Measurements were calibrated with respect to the transmission data taken through the cuvette filled only with toluene.

3.3.2 ASE and photostability

The characteristics for the PL and ASE for both neat (single layer) and PVA encapsulate (bilayer) devices reported in section 3.4.3 were initially tested independently of the DFB laser cavity by constructing the corresponding waveguide structure onto a glass substrate containing no grating. In order to authenticate the effect of the PVA layer a CQD film on smooth glass (this structure is called "CQD sample") and a CQD film, also on smooth glass, over coated with PVA (such structure is called "CQD/PVA sample" in the following) were tested for ASE.

For the detection of ASE (please refer to section 2.4.1 for details) both samples were optically excited by a Nd:YAG solid-state laser emitting at 355 nm at a repetition rate of 10 Hz with 5ns pulses. The pump beam was shaped as a stripe with dimensions 8.3 mm by 1.0 mm on the film surface, near the substrate edge, and the emission was directly collected from the edge of the sample by a $50\mu m$-core optical fibre placed approximately 0.5cm away. The optical fibre was connected to a CCD spectrometer (Avantes, 2.5nm resolution) where the evolution of the spectra was recorded over increasing energies; from below to above threshold.

3.3.3 DFB Characterisation

When characterising the DFB lasers the same optical pump source was used; the pump spot was 0.74 ± 0.01 mm by 4.4 ± 0.2 mm. The devices were placed at a slight angle and their vertical emission was collected using the same optical fibre and CCD spectrometer used before, however, the resolution was increased to 0.13 nm.

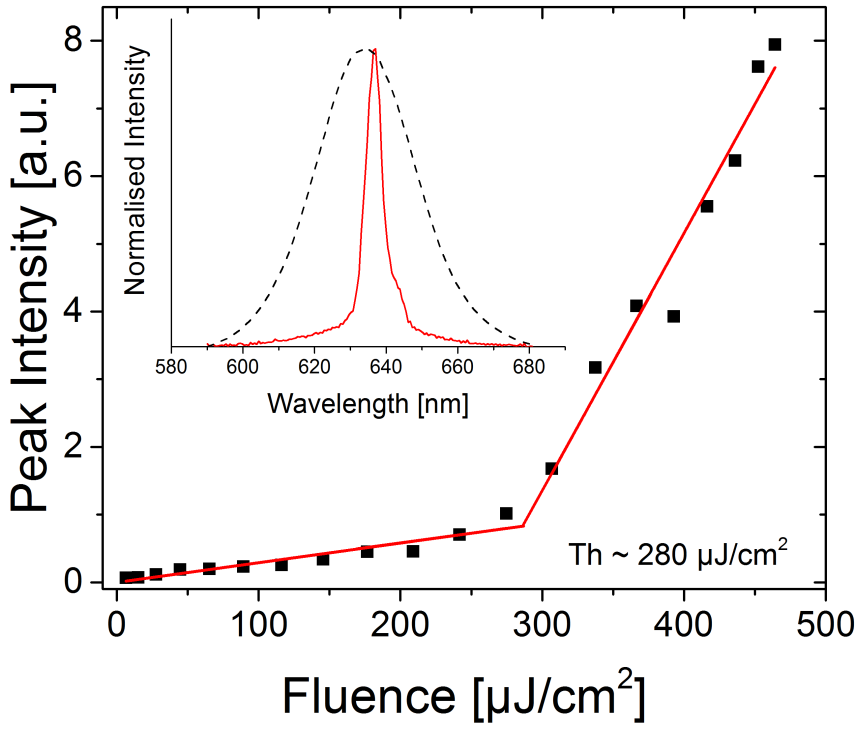

FIGURE 3.5: Transfer functions for the detection of ASE for the 630 nm CQDs with concentration 50 mg.mL^{-1} inset display the corresponding ASE spectra and edge emission from CW stripe excitation.

3.4 Results and discussion

3.4.1 Study of ASE

Initially the red CQDs were investigated in search for ASE. For the 630nm, at the same concentration and spin rate as the 575nm CQDs discussed later (50mg.mL^{-1} and 4krpm), the threshold energy is seen to occur at 280 $\mu J/cm^2$. Above this energy the shape of the spectra changes developing a second, spectrally narrower peak. This second peak has a full-width at half-maximum (FWHM) of 5.7nm and develops on the red side of the PL where it is centred at 637nm, inset figure 3.5.

Once the pump energy levels surpass threshold the ASE peak dominates the overall edge emission. A threshold-like behaviour can be seen when plotting the corresponding intensity evolution versus the pump fluence at this secondary peak wavelength (see figure 3.5) validating that ASE is observed. The observed redshift of the ASE peak in comparison to the edge PL, which is due to the biexcitonic binding energy, typical of type I CQDs [20, 21]. It was also noticed that, above

threshold, the value for the ASE peak also redshifts for increasing pump energies, an effect that has been observed in other types of CQDs. This behaviour is attributed to the population of the sub-level. Overall, the behaviour and ASE threshold performance of the 630nm CdS_xSe_{1-x}/ZnS CQDs are very similar to red-emitting CdSe/ZnS CQDs (data not shown).

ASE was also achieved with the 575nm emitting CQDs. Figure 3.6 displays the normalised spectra for the CQD and CQD/PVA encapsulated films, along with the edge emission for comparison, when excited with energies approximately 5 times that for the onset of stimulated emission. We note that the ASE threshold is lower for the CQD/PVA sample as is discussed further (figure 3.7). The edge PL emission in figure 3.6 was taken from the samples under low intensity CW excitation by laser diode, section 3.3.1. The PL taken from a dilute solution and from the edge PL of a film (figures 3.3 and 3.6) can be compared. The edge PL of the CQD sample is centred at 584 nm with a FWHM of 35 nm. There is approximately a 10nm redshift between this edge PL and the PL from the dilute solution. This redshift is expected and is due to the greater CQD density in the solid state enhancing reabsorption within the CQD film.

Above the ASE threshold, the CQD and CQD/PVA spectra are constructed of an edge PL base with the addition of a narrower ASE peak. Figure 3.6 decomposes the spectra by fitting two Gaussians to the data of the CQD sample (red dash-dot curve) and the CQD/PVA sample (solid blue line). The CQD sample has a PL centred at 585nm with a marginally wider FWHM of 38 nm - it is similar to the edge PL under CW excitation. The ASE peak occurs at 589 nm, a 4nm red-shift when compared with the edge PL, which is ascribed to the balance of gain and reabsorption within the CQD film. The FWHM of the ASE peak is 8 nm. The CQD/PVA sample has a PL centred at 587 nm with a corresponding FWHM of 36 nm. The ASE peak occurs at 598 nm with a FWHM of 6 nm. This is an 11nm red-shift from the PL, which is coherent with a quasi-3 level laser system as the addition of PVA increases the modal confinement within the structure, in turn increasing the modal gain, figure 3.2. In a quasi-3 level system the absorption is non-nil at the transition wavelength and therefore the spontaneous emission that is guided (and possibly amplified) is reabsorbed predominantly at the lower wavelengths, causing the redshift. A higher modal gain means a lower pump level is needed to reach the onset of ASE. A lower pump level also means higher

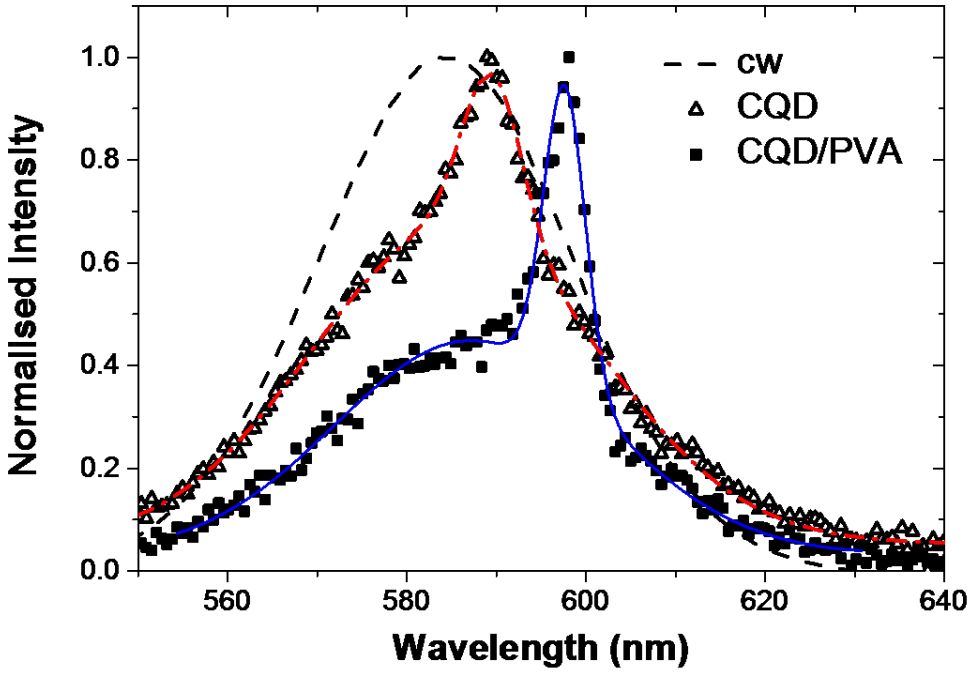

FIGURE 3.6: Emission profiles for 575 nm CQDs with CW edge PL (black dash line), CQD sample edge emission (data: open black triangles; fit: red dash-dot line) and CQD/PVA sample edge emission (data: black square; fit: blue solid line) under 5ns-pulse pumping.

reabsorption or lower net gain at the shorter wavelengths and hence the ASE peak develops at a longer wavelength.

The ASE intensity transfer functions for both CQD and CQD/PVA samples are plotted in figure 3.7. The recorded intensity is displayed as a function of pump fluence. The trend for both samples is similar. Initially, when at low fluence, as the pump is increased, the intensity increases sublinearly. This is a typical behaviour observed for PL when there is no noticeable ASE. As pump energies are further increased, towards and beyond threshold (for the CQD sample values greater than 800 $\mu J/cm^2$ and for the CQD/PVA sample values greater than 380 $\mu J/cm^2$), the trend becomes supralinear, a more characteristic trend for ASE. The overall emission can be understood as the combination of two main components. Firstly, there is the unamplified emission component obtained from the PL. This comes from the spontaneous emission of the main guided modes of the planar waveguide structure as well as from the leaky modes and higher lateral modes. Lateral guiding is due to the physical size (width) of the excitation stripe creating guiding effects in two dimensions. Secondly there is the amplified component itself from the modes that are primarily confined within the length of the excitation

stripe. This contribution relates to lower order lateral modes. At low fluence the sublinear behaviour of the unamplified PL is attributed to (i) an anti-guiding effect and (ii) from the emission saturation due to non-radiative multi-excitonic recombination (discussed in more details further). Antiguiding has a negative effect on the coupling of the CQD emission into the fibre with increasing fluence. This could be related to the carrier induced change of the CQDs refractive index and is a currently researched area [22]. The amplified component appears and then dominates at higher fluences, where the emission domination arises from the amplified component: the spontaneously emitted photons guided within the CQD layer are amplified significantly by stimulated emission. As the change in spectral linewidth occurs, from a broad PL peak to a narrower ASE peak (figure 3.6), the intensity of the ASE increases exponentially as long as the gain saturation limit is not reached. Figures 3.6 and 3.7 show that the addition of the PVA encapsulant creates a greater net optical gain resulting in the activation of ASE at a lower fluence. This is a direct consequence of the PVA mitigating scattering losses at the surface of the CQD film, reducing film roughness, and aiding in the confinement of the mode.

Bearing in mind the two aforementioned components of the samples edge emission, the data of figure 3.7 can be fitted giving greater accuracy for the value of ASE threshold. The development of the ASE is given by [23]:

$$I_{ASE} = \frac{\Omega}{g}\big(e^{gL} - 1\big). \tag{3.2}$$

Here $\Omega = A \cdot F$ is the amount of spontaneous emission coupled into the stripe-defined guide, F is the pump fluence, A is a coupling factor, g the net gain coefficient and L is the length of the stripe. The net gain is defined as $g = B \cdot F$, where B is proportional to the gain factor of the CQD layer. However, the unamplified component has to also be taken into account. This is done phenomenologically with the addition of a saturating term I_{naPL} that is proportional to the spontaneous emission. The total edge emission is the sum of these two components:

$$I_{edge} = I_{ASE} + I_{naPL} = \frac{\Omega}{g}\big(e^{gL} - 1\big) + \frac{C.F}{1 + \frac{F}{F_C}}. \tag{3.3}$$

I_{edge} is the peak intensity observed. I_{naPL} is the saturating phenomenon with factors C and F_C (the fluence at saturation). The fit parameters are therefore A, B, C and F_C where fitting requires a 2-step method. First the data at low

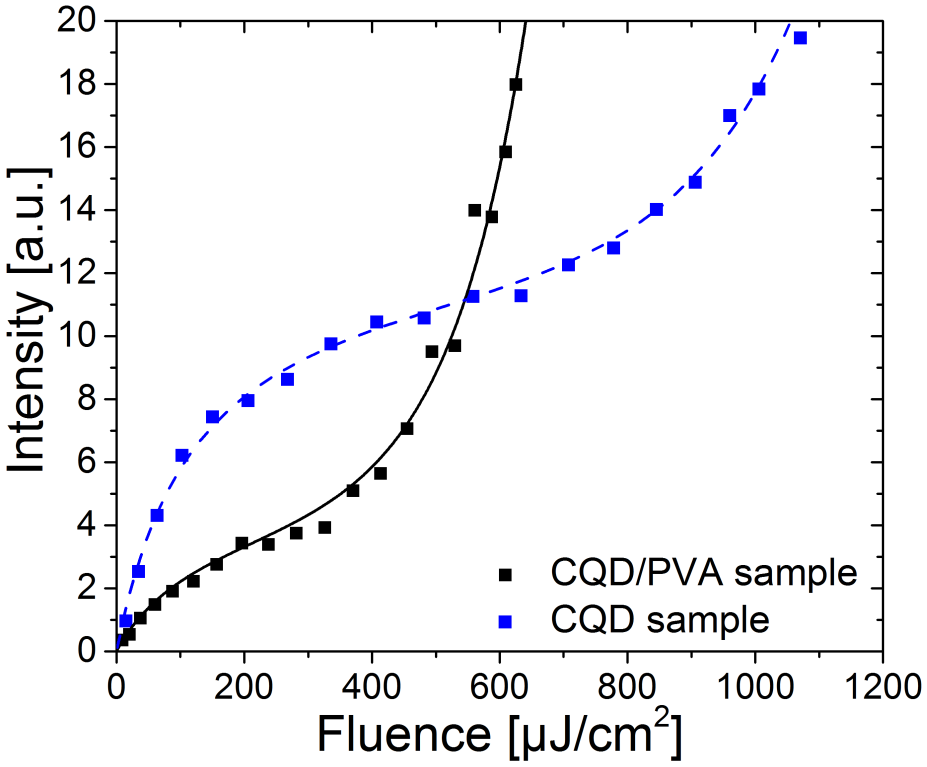

FIGURE 3.7: Edge PL peak intensity versus pump fluence for the CQD sample (blue data points and dashed line) and CQD/PVA sample (black data points and solid line).

fluence is fitted disregarding the I_{ASE} term as its contribution is minimum, i.e. considering only I_{naPL}, enabling solutions for C and F_C to be found. After this the entire range of fluence values are fitted over using equation 3.3 where the values of C and F_C, found previously, remain constant leaving only A and B as parameters.

Figure 3.7 displays the fits calculated from equation 3.3 where the blue dash-dot line represents the CQD sample and the black solid line represents the CQD/PVA sample. The values and parameters used in the fitting, including the goodness of the fit (given as the adjusted R^2) are shown in Table 3.1. The CQD/PVA sample has a higher B factor that corresponds to a larger net model gain when compared with the CQD sample at the same fluence.

For example, when a fluence of 600 $\mu J/cm^2$ is taken the net gain, g, is 4.5 ± 0.5 cm^{-1} and 7.2 ± 0.5 cm^{-1} for the corresponding CQD and CQD/PVA samples. The encapsulant layer produces a higher net modal gain benefical to low threshold laser performance. At threshold, when the values of spontaneous and stimulated emission are equal along the stripes edge, produces $g(= \mathrm{B}.F_{th})\mathrm{L} \approx 1.256$ [23], where

TABLE 3.1: Parameters for the fits used when plotting figure 3.7.

Parameters	CQD Sample	CQD/PVA Sample
A ($cm^2.\mu J^{-1}$)	$(10 \pm 1).10^{-2}$	$(5.1 \pm 0.2).10^{-2}$
F_C ($\mu J.cm^{-2}$)	140 ± 15	310 ± 5
B ($cm.\mu J^{-1}$)	$(7.5 \pm 0.8).10^{-3}$	$(12 \pm 0.8).10^{-3}$
L (cm)	0.8	0.8
C ($cm^2.\mu J^{-1}$)	9.8 ± 0.6	3.1 ± 0.2
Adj R^2	98.9%	98.7%

F_{th} is the fluence at threshold. This equates to a $F_{th} = 210\ \mu J/cm^2$ for the CQD sample and $F_{th} = 130\ \mu J/cm^2$ for the CQD/PVA sample noting that the values of A and C are larger for the CQD sample. This is due to higher confinement as the CQD air interface has a higher refractive index contrast compare to the CQD PVA interface.

Another interesting way to understand the saturation term of the PL in equation 3.3 is to relate to the phenomenon to the excitonic population in CQDs (the average exciton number $\langle N \rangle$ per dot) assuming a decrease in PL efficiency at multi-exciton levels. If we write β_i the quantum efficiency for the i^{th} exciton, k as the number of excitons in a CQD and P(k) the Poisson distribution of k in the CQD ensemble with average exciton number $\langle N \rangle$, then the contribution of PL intensity from the CQDs can be written as:

$$I_{naPL} = P(1)\beta_1 + P(2)(\beta_1 + \beta_2) + P(3)(\beta_1 + \beta_2 + \beta_3) + \cdots , \tag{3.4a}$$

where this can be expressed as,

$$I_{naPL} = \sum_{i}^{\infty} \beta_i \left(\sum_{n=0}^{i-1} P(k) \right). \tag{3.4b}$$

This equation simply means that the emission is produced from the recombination of excitons. Due to Auger recombination in CQDs being an efficient process (in CdSe/ZnS CQDs the Auger lifetime of biexcitons is on the order of 100ps and smaller for higher multi-exciton levels whereas the single exciton lifetime is 10 ns or more [7, 24, 25]), the emission is often approximated as coming from the radiative recombination of single and biexcitons only, as the radiative efficiency of the multi-excitons is considered low (assuming a negligible contribution). In this

TABLE 3.2: Fit parameters with Auger recombination as main detrimental effect.

Parameters	CQD Sample	CQD/PVA Sample
A ($cm^2.\mu J^{-1}$)	$(3.2 \pm 2.5).10^{-2}$	$(5.4 \pm 3).10^{-2}$)
B ($cm.\mu J^{-1}$)	$(8.5 \pm 1.5).10^{-3}$	$(15 \pm 0.2).10^{-3}$
I_{sat}	1088.4 ± 18.9	631.1 ± 22.6
I_{bi}	0 ±50.2	0
F_s ($\mu m^2.\mu J^{-1}$)	144.3 ± 11.6	312.5 ± 24.0
Adj R^2	98.8%	98.7%

case:

$$I_{naPL} = \sum_{i}^{\infty} \beta_i \left(\sum_{k=0}^{i-1} P(k) \right) = P(1)\beta_1 + P(2)(\beta_1 + \beta_2). \tag{3.5}$$

P(k) is the probability of this occurring and is expressed by Poisson distribution where,

$$P(k) = \frac{\langle N \rangle^k e^{-N}}{k!}. \tag{3.6}$$

Taking the probability of the intensity as proportional to $\langle N \rangle$, and assuming that all CQDs are excited, the I_{naPL} component in equation 3.3 is transformed by equation 3.4 reducing to,

$$I_{naPL} = I_{sat}\left(1 - e^{-\frac{F}{F_s}}\right) + I_{bi}\left(1 - \frac{F}{F_s}e^{-\frac{F}{F_s}} - e^{-\frac{F}{F_s}}\right). \tag{3.7}$$

Here, I_{sat} is the intensity proportional to β_1, I_{bi} is proportional to β_2, F is the fluence and F_s is the fluence at unity. Equation 3.7 describes the saturating trend of the PL with increasing pump fluence.

Adapting the I_{naPL} component in equation 3.3 with equation 3.7 similar values (of the same magnitude) for the parameters can be found as in table 3.1. These are displayed in table 3.2. Restating that the biexciton component is near negligible results in these similarities. However, varying this aspect will alter the other parameters.

This method is not ideal in this case. Yes, Auger recombination is a factor that will have effect in the measurements. However, fitting equation 3.7 has the same outcome as equation 3.3 when examining this phenomenon. In the Auger fit the collection of 100% of light, both PL and ASE, is presumed. Whereas, unlike ASE that is directional, PL is inhomogeneous and not all photons are coupled

into the optical fibre. The fit also presumes that there is zero contribution from multi-excitons.

The values established for the fluences are far greater than the measured values when the CQDs are applied to a DFB cavity, section 3.4.3.

3.4.2 Photostability

The photostability of the ASE was measured. The samples were fabricated (the same as for ASE measurements) and were excited with a stripe (same as before), located close to the substrate edge, connected to an Avantes spectrometer (resolution 2.5 nm). This was run over a number of hours where the spectra were recorded at 30-second intervals.

Here the intensity of the ASE peak for both the CQD and CQD/PVA composite films, on a grating-less planar glass substrate, were optically excited. However, the optical excitation energy was approximately 1500 $\mu J/cm^2$ more than 10 times greater than the threshold of the CQD/PVA sample. Figure 3.8 shows that the PVA encapsulant delays the decay experienced by the ASE intensity thus increasing the CQDs operational lifetime. This can clearly be observed by the intensity pedestal occurring in the first 15 minutes of operation. This can be attributed to the PVA acting as an oxygen barrier that has been shown to improve photostability in gain materials [10].

The 575 nm CQDs in this section establishes two points. Firstly, that CdS_xSe_{1-x}/ZnS behaves like a quasi-3 level as can be seen from the redshifts of the edge PL and ASE peaks. Secondly, in spite of the quasi-3 level manner of the CQDs a low threshold is achieved from a nanosecond pumping regime. The bi-layered waveguide structure examined here reduces the ASE threshold fluence to 130 $\mu J/cm^2$ with an extended operational lifetime.

3.4.3 Laser characterisation

Having demonstrated ASE, in this section, both CQD and CQD/PVA waveguide structures are applied to lasing in a DFB cavity. The performance of these two designs of DFB lasers is characterised and compared. The neat CQD DFB laser

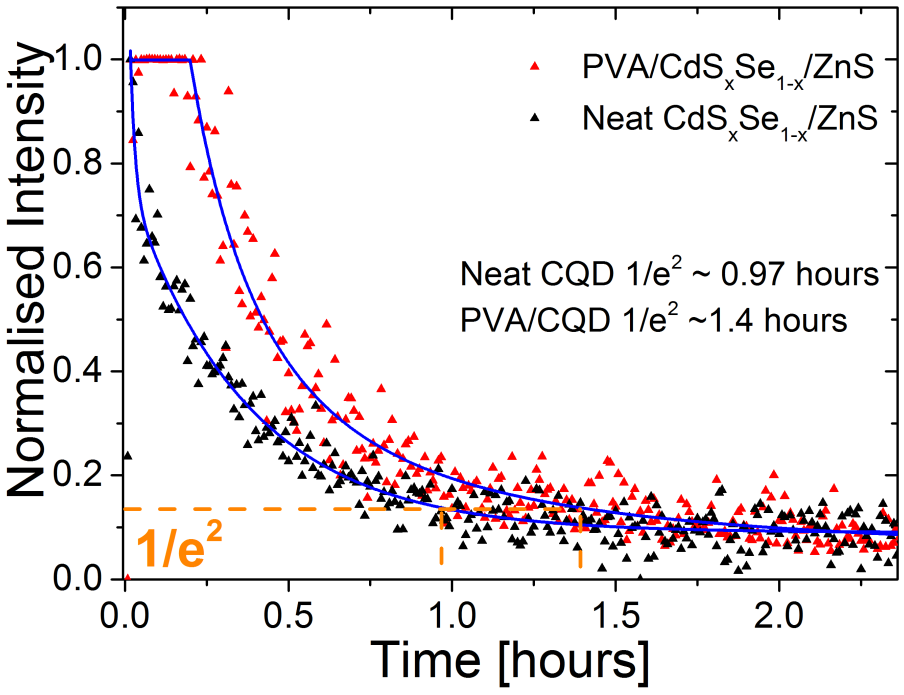

FIGURE 3.8: Photo-degeneracy of the ASE peak intensity versus time CdS_xSe_{1-x}/ZnS film and PVA encapsulated film.

transfer function can be seen in figure 3.9a along with the related spectrum (fluence 163 $\mu J/cm^2$) in the inset. The device emits on the TE_0 mode at 589.9 nm, FWHM of 0.43 nm (at fluence 163 $\mu J/cm^2$) and has a threshold fluence of 85 $\pm$ 8.5 $\mu J/cm^2$ (17 kW/cm^2). The CQD sample displays improvement when compared with previously reported CQD DFB lasers. Prior to this work, in the nanosecond regime, typical threshold fluences were in the range 500 to 4000 $\mu J/cm^2$ [19]. The second observable peak occurring at 588.5 nm corresponds to the TM_0 mode that has a threshold fluence of approximately 160 $\mu J/cm^2$ (32 kW/cm^2).

With the addition of the PVA encapsulating layer the CQD/PVA DFB laser emits on the TE_0 mode at 600 nm with a FWHM of 0.45 nm (when at fluence 24.4 $\mu J/cm^2$). The threshold fluence of the device is 13.5 $\pm$ 2.5 $\mu J/cm^2$ (2.7 kW/cm^2) and to best knowledge is the lowest reported by a solution processed CQD laser [26], figure 3.9b. This is also an improvement of a factor of 6 when compared to the CQD DFB laser. Because of the stronger confinement, the TM_0 mode also oscillates at lower fluence. Its wavelength is 597 nm and the threshold fluence is approximately 18 $\mu J/cm^2$.

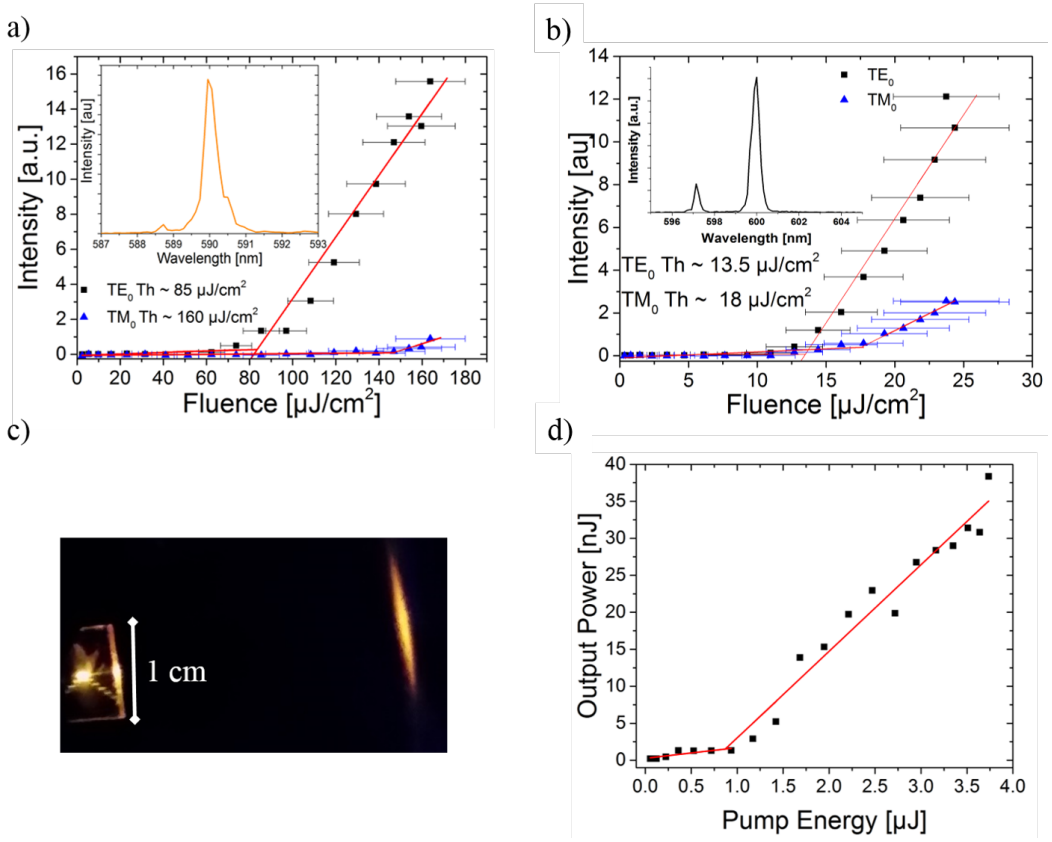

FIGURE 3.9: Transfer function of a) CQD/DFB Neat laser, b) PVA/CQD/DFB lasers with nanosecond optical pump source, displaying corresponding TM_0 modes. Inserts show laser emission spectra. c) PVA/CQD/DFB laser emission under optical pump d) output energy verses pump energy of PVA/CQD DFB laser.

When comparing the primary laser (TE_0) emission wavelengths of the CQD and CQD/PVA samples a 10nm shift is observed. This is due to the PVA layer that increases the effective refractive index for the mode (1.55 for CQD vs 1.58 for CQD/PVA). The limiting factor contributing to the FWHMs observed for both samples is due to the presence of lateral modes caused by the lateral size of the pump excitation. The improvement in the laser operation is attributed to the addition of the PVA encapsulant layer resulting in the higher modal gain that reduces the threshold value.

Replacing the spectrometer with an energy meter, an output pulse energy of 40 nJ was measured for a pump fluence 2.67 μJ. The total efficiency of the device is therefore around 3% considering the top and bottom laser emission, figure 9d. This value is comparable with other studies utilising CQDs with ns pump regimes (typically $< 10\%$) with the addition of lower threshold [27], however lower to what has been obtained with ultrafast pump regimes [28].

3.5 Conclusion

This chapter reported on a visible yellow-orange CQD DFB laser based on a bilayer-waveguide structure. The bilayer structure obtained by overcoating the CQD gain film with PVA was seen to increase the modal gain of the structure, subsequently lowering the threshold values for the onset of ASE. The addition of the PVA encapsulant was also shown to improve the photostability in an excitation regime well above the ASE threshold. Such a bilayer structure enabled the demonstration of a DFB laser, pumped with 5ns excitation pulses, with a fluence at threshold of 13.5 $\mu J/cm^2$ ($10kW/cm^2$). This was for a time the lowest threshold for CQD laser operation under nanosecond optical pumping. Fan *et al* has since demonstrated thresholds of $20kW/cm^2$ for thin films of CQD dispersed onto a two-dimensional DFB greating and SoG encapsulation under microsecond pump giving encouraging signs that laser diode (LD) pumping is possible [29].

There are still challenges ahead before taking this technology out of the laboratory. A first step would be LD pumping. High-performance, multi-watts GaN LDs emit at 405nm or 450nm and not 355 nm. Absorption would be lower at such wavelengths. However, LD can be pulsed in the nanosecond regime and reaching above 10 kW/cm^2 is certainly feasible if the resonator size is reduced further than what it was in this work. This is feasible in a DFB structure by improvements of the grating design to increase the feedback strength - for example using a first order DFB grating structure.

Two-dimensional nanoplatelet technology has recently been studied as an optical gain material. In [30] CdSe colloidal nanoplatelets excited initially in the femtosecond regime were found to have an exciton binding energy of 132 meV and a biexciton binding energy 30 meV with lifetimes of 438 ps and 124 ps. These nanoplatelets displayed threshold at $6\mu J/cm^2$ under the femtosecond pump and claim to demonstrate CW pumped lasing producing a threshold of 6.5 W/cm^2 [29]. Cadmium based nanoplatelets have also displayed ASE obtaining threshold of 41 $\mu J/cm^2$ and gain coefficents up to 650 cm^{-1} under two photo absorption methods [31]. These nanoplatelets where also utilised in VCSEL format obtaining thresholds as low as 2.49 mJ/cm^2. Although the pulsed threshold is approximately half of what is reported above with the use of a one-dimensional material minimising the Auger recombination effects. PVA encapsulated PPV materials with similar lasing threshold under ns pump have shown successful operation with ns pulsed

laser diodes [15]. Incorporating this with the CQDs would make this technology appealing as it could lead to out-of-the-lab application.

References

[1] Peter Reiss, Myriam Protière, and Liang Li. Core/Shell semiconductor nanocrystals. *Small (Weinheim an der Bergstrasse, Germany)*, 5(2):154–68, feb 2009. ISSN 1613-6829. doi: 10.1002/smll.200800841. URL `http://www.ncbi.nlm.nih.gov/pubmed/19153991`.

[2] V. I. Klimov. Optical Gain and Stimulated Emission in Nanocrystal Quantum Dots. *Science*, 290(5490):314–317, oct 2000. ISSN 00368075. doi: 10.1126/science.290.5490.314. URL `http://www.sciencemag.org/cgi/doi/10.1126/science.290.5490.314`.

[3] V. M. Menon, M. Luberto, N. V. Valappil, and S. Chatterjee. Lasing from InGaP quantum dots in a spin-coated flexible microcavity. *Optics Express*, 16(24):19535, nov 2008. ISSN 1094-4087. doi: 10.1364/OE.16.019535. URL `http://www.ncbi.nlm.nih.gov/pubmed/19030039https://www.osapublishing.org/oe/abstract.cfm?uri=oe-16-24-19535`.

[4] Francesco Todescato, Ilaria Fortunati, Samuele Gardin, Eleonora Garbin, Elisabetta Collini, Renato Bozio, Jacek J. Jasieniak, Gioia Della Giustina, Giovanna Brusatin, Stefano Toffanin, and Raffaella Signorini. Soft-Lithographed Up-Converted Distributed Feedback Visible Lasers Based on CdSe-CdZnS-ZnS Quantum Dots. *Advanced Functional Materials*, 22(2):337–344, jan 2012. ISSN 1616301X. doi: 10.1002/adfm.201101684. URL `http://doi.wiley.com/10.1002/adfm.201101684`.

[5] V. C. Sundar, H.-J. Eisler, T. Deng, Y. Chan, E. L. Thomas, and M. G. Bawendi. Soft-Lithographically Embossed, Multilayered Distributed-Feedback Nanocrystal Lasers. *Advanced Materials*, 16(23-24):2137–2141, dec 2004. ISSN 0935-9648. doi: 10.1002/adma.200400033. URL `http://doi.wiley.com/10.1002/adma.200400033`.

[6] B. Guilhabert, C. Foucher, A-M. Haughey, E. Mutlugun, Y. Gao, J. Herrnsdorf, H.D. Sun, H.V. Demir, M.D. Dawson, and N. Laurand. Nanosecond colloidal quantum dot lasers for sensing. *Optics Express*, 22(6):7308, mar 2014. ISSN 1094-4087. doi: 10.1364/OE.22.007308. URL `https://www.osapublishing.org/oe/abstract.cfm?uri=oe-22-6-7308`.

[7] Cuong Dang and Arto Nurmikko. Beyond quantum dot LEDs: Optical gain and laser action in red, green, and blue colors. *MRS Bulletin*, 38(09):737–742, 2013. ISSN 0883-7694. doi: 10.1557/mrs.2013.183. URL `http://www.journals.cambridge.org/abstract{_}S0883769413001838`.

[8] George E. Cragg and Alexander L. Efros. Suppression of Auger Processes in Confined Structures. *Nano Letters*, 10(1):313–317, jan 2010. ISSN 1530-6984. doi: 10.

1021/nl903592h. URL http://www.ncbi.nlm.nih.gov/pubmed/20017564http://pubs.acs.org/doi/abs/10.1021/nl903592h.

[9] Erfan Baghani, Stephen K. O'Leary, Igor Fedin, Dmitri V. Talapin, and Matthew Pelton. Auger-Limited Carrier Recombination and Relaxation in CdSe Colloidal Quantum Wells. *The Journal of Physical Chemistry Letters*, page 150302175751004, 2015. ISSN 1948-7185. doi: 10.1021/acs.jpclett.5b00143. URL http://pubs.acs.org/doi/abs/10.1021/acs.jpclett.5b00143.

[10] C. Foucher, B. Guilhabert, A. L. Kanibolotsky, P. J. Skabara, N. Laurand, and M. D. Dawson. Highly-photostable and mechanically flexible all-organic semiconductor lasers. *Optical Materials Express*, 3(5):584, apr 2013. ISSN 2159-3930. doi: 10.1364/OME.3.000584. URL http://www.opticsinfobase.org/abstract.cfm?URI=ome-3-5-584.

[11] Robert E Bailey and Shuming Nie. Alloyed semiconductor quantum dots: tuning the optical properties without changing the particle size. *Journal of the American Chemical Society*, 125(23):7100–6, jun 2003. ISSN 0002-7863. doi: 10.1021/ja035000o. URL http://www.ncbi.nlm.nih.gov/pubmed/12783563.

[12] T. Liptay, L. Marshall, P. Rao, R. Ram, and M. Bawendi. Anomalous Stokes shift in CdSe nanocrystals. *Physical Review B*, 76(15):155314, oct 2007. ISSN 1098-0121. doi: 10.1103/PhysRevB.76.155314. URL http://link.aps.org/doi/10.1103/PhysRevB.76.155314.

[13] Abhishek Joshi, K. Y. Narsingi, M. O. Manasreh, E. A. Davis, and B. D. Weaver. Temperature dependence of the band gap of colloidal CdSe/ZnS core/shell nanocrystals embedded into an ultraviolet curable resin. *Applied Physics Letters*, 89(13):89–92, 2006. ISSN 00036951. doi: 10.1063/1.2357856.

[14] Yuxi Xu, Wenjing Hong, Hua Bai, Chun Li, and Gaoquan Shi. Strong and ductile poly(vinyl alcohol)/graphene oxide composite films with a layered structure. *Carbon*, 47(15):3538–3543, dec 2009. ISSN 00086223. doi: 10.1016/j.carbon.2009.08.022. URL http://www.sciencedirect.com/science/article/pii/S0008622309005296.

[15] C. Foucher, B. Guilhabert, J. Herrnsdorf, N. Laurand, and M. D. Dawson. Diode-pumped, mechanically-flexible polymer DFB laser encapsulated by glass membranes. *Optics Express*, 22(20):24160, sep 2014. ISSN 1094-4087. doi: 10.1364/OE.22.024160. URL http://www.opticsinfobase.org/abstract.cfm?URI=oe-22-20-24160.

[16] C. Foucher, B. Guilhabert, A. L. Kanibolotsky, P. J. Skabara, N. Laurand, and M. D. Dawson. RGB and white-emitting organic lasers on flexible glass. *Optics Express*, 24(3):2273, 2016. ISSN 1094-4087. doi: 10.1364/OE.24.002273. URL https://www.osapublishing.org/abstract.cfm?URI=oe-24-3-2273.

[17] B. Guilhabert, N. Laurand, J. Herrnsdorf, Y. Chen, a. L. Kanibolotsky, C. Orofino, P. J. Skabara, and M. D. Dawson. Mechanically Flexible Organic Semiconductor Laser Array. *IEEE Photonics Journal*, 4(3):684–690, jun 2012. ISSN 1943-0655. doi: 10.1109/JPHOT.2012.2195651. URL http://ieeexplore.ieee.org/lpdocs/epic03/wrapper.htm?arnumber=6188505.

[18] Alexander J. C. Kuehne, David Elfström, Allan R. Mackintosh, Alexander L. Kanibolotsky, Benoit Guilhabert, Erdan Gu, Igor F. Perepichka, Peter J. Skabara, Martin D. Dawson, and Richard A Pethrick. Direct Laser Writing of Nanosized Oligofluorene Truxenes in UV-Transparent Photoresist Microstructures. *Advanced Materials*, 21(7):781–785, feb 2009. ISSN 09359648. doi: 10.1002/adma.200802656. URL `http://doi.wiley.com/10.1002/adma.200802656`.

[19] Yujie Chen, Benoit Guilhabert, Johannes Herrnsdorf, Yanfeng Zhang, Allan R. Mackintosh, Richard a. Pethrick, Erdan Gu, Nicolas Laurand, and Martin D. Dawson. Flexible distributed-feedback colloidal quantum dot laser. *Applied Physics Letters*, 99(24): 241103, 2011. ISSN 00036951. doi: 10.1063/1.3659305. URL `http://scitation.aip.org/content/aip/journal/apl/99/24/10.1063/1.3659305`.

[20] Victor I. Klimov, Sergei A. Ivanov, Jagjit Nanda, Marc Achermann, Ilya Bezel, John A. McGuire, and Andrei Piryatinski. Single-exciton optical gain in semiconductor nanocrystals. *Nature*, 447(7143):441–446, may 2007. ISSN 0028-0836. doi: 10.1038/nature05839. URL `http://www.ncbi.nlm.nih.gov/pubmed/17522678http://www.nature.com/doifinder/10.1038/nature05839`.

[21] Ahmet Fatih Cihan, Yusuf Kelestemur, Burak Guzelturk, Ozan Yerli, Ulas Kurum, Halime Gul Yaglioglu, Ayhan Elmali, and Hilmi Volkan Demir. Attractive versus repulsive excitonic interactions of colloidal quantum dots control blue- to red-shifting (and non-shifting) amplified spontaneous emission. *Journal of Physical Chemistry Letters*, 4(23):4146–4152, 2013. ISSN 19487185. doi: 10.1021/jz402211m.

[22] R A Ganeev, A I Ryasnyansky, R I Tugushev, and T Usmanov. Investigation of nonlinear refraction and nonlinear absorption of semiconductor nanoparticle solutions prepared by laser ablation. *Journal of Optics A: Pure and Applied Optics*, 5(4):409–417, 2003. ISSN 1464-4258. doi: 10.1088/1464-4258/5/4/317.

[23] Luis Cerdan, Angel Costela, and Inmaculada Garcia-Moreno. Variable Stripe Length method for optical gain measurements: Characteristic lengths. In *2011 Conference on Lasers and Electro-Optics Europe and 12th European Quantum Electronics Conference (CLEO EUROPE/EQEC)*, volume 27, pages 1–1. IEEE, may 2011. ISBN 978-1-4577-0533-5. doi: 10.1109/CLEOE.2011.5942846. URL `http://ieeexplore.ieee.org/document/5942846/`.

[24] Marco Marceddu, Michele Saba, Francesco Quochi, Adriano Lai, Jing Huang, Dmitri V Talapin, Andrea Mura, and Giovanni Bongiovanni. Charged excitons, Auger recombination and optical gain in CdSe/CdS nanocrystals. *Nanotechnology*, 23(1):015201, 2011. ISSN 0957-4484. doi: 10.1088/0957-4484/23/1/015201.

[25] V. Klimov, J. McGuire, R. Schaller, and V. Rupasov. Scaling of multiexciton lifetimes in semiconductor nanocrystals. *Physical Review B*, 77(19):195324, may 2008. ISSN 1098-0121. doi: 10.1103/PhysRevB.77.195324. URL `http://link.aps.org/doi/10.1103/PhysRevB.77.195324`.

[26] L. J. McLellan, B. Guilhabert, N. Laurand, and M. D. Dawson. CdSxSe1-x/ZnS semiconductor nanocrystal laser with sub 10kW/cmˆ2 threshold and 40nJ emission output at 600 nm. *Optics Express*, 24(2):A146, 2016. ISSN 1094-4087. doi: 10.1364/OE.24.00A146. URL https://www.osapublishing.org/abstract.cfm?URI=oe-24-2-A146.

[27] C. Dang, J. Lee, K. Roh, H. Kim, S. Ahn, H. Jeon, C. Breen, J. S. Steckel, S. Coe-Sullivan, and a. Nurmikko. Highly efficient, spatially coherent distributed feedback lasers from dense colloidal quantum dot films. *Applied Physics Letters*, 103(17), 2013. ISSN 00036951. doi: 10.1063/1.4826147.

[28] Kwangdong Roh, Cuong Dang, Joonhee Lee, Songtao Chen, Jonathan S. Steckel, Seth Coe-Sullivan, and Arto Nurmikko. Surface-emitting red, green, and blue colloidal quantum dot distributed feedback lasers. *Optics Express*, 22(15):18800, jul 2014. ISSN 1094-4087. doi: 10.1364/OE.22.018800. URL https://www.osapublishing.org/oe/abstract.cfm?uri=oe-22-15-18800.

[29] Fengjia Fan, Oleksandr Voznyy, P Randy, Kristopher T Bicanic, Michael M Adachi, James R Mcbride, Kemar R Reid, Young-shin Park, Xiyan Li, Ankit Jain, Rafael Quintero-bermudez, Mayuran Saravanapavanantham, Min Liu, Marek Korkusinski, Pawel Hawrylak, Victor I Klimov, Sandra J Rosenthal, Sjoerd Hoogland, and Edward H Sargent. Continuous-wave lasing in colloidal quantum dot solids enabled by facet-selective epitaxy. *Nature*, 544(7648): 1–18, 2017. ISSN 0028-0836. doi: 10.1038/nature21424. URL http://dx.doi.org/10.1038/nature21424.

[30] Joel Q. Grim, Sotirios Christodoulou, Francesco Di Stasio, Roman Krahne, Roberto Cingolani, Liberato Manna, and Iwan Moreels. Continuous-wave biexciton lasing at room temperature using solution-processed quantum wells. *Nature Nanotechnology*, 9(11):891–895, oct 2014. ISSN 1748-3387. doi: 10.1038/nnano.2014.213. URL http://www.ncbi.nlm.nih.gov/pubmed/25282045http://www.nature.com/doifinder/10.1038/nnano.2014.213.

[31] Burak Guzelturk, Yusuf Kelestemur, Murat Olutas, Savas Delikanli, and Hilmi Volkan Demir. Amplified Spontaneous Emission and Lasing in Colloidal Nanoplatelets. *ACS Nano*, 8(7):6599–6605, jul 2014. ISSN 1936-0851. doi: 10.1021/nn5022296. URL http://pubs.acs.org/doi/abs/10.1021/nn5022296.

Chapter 4

CQD-VCSEL

This chapter presents and discusses the demonstration of a solution processed yellow/orange VCSEL utilising alloyed-core/shell CQDs injected into a DBR cavity structure. Remaining with operation in the ns regime, oscillation threshold comprised between 1 and 20 mJ/cm^2 are obtained. For a broad area excitation (250 μm $1/e^2$ radius), the operation is highly multimode and characterised by spatio-temporal instabilities. When pumped with a spot size at or below 110μm in radius, the VCSEL is observed, in certain cases, to be single mode for low pump energies while additional longitudinal modes as well as transverse modes appear at higher pumping levels. Further to this, a study of the polarisation of the CQD laser emission under different pump polarisations is carried out.

4.1 Introduction

Expanding on the work carried out in Chapter 3, the CQD technology was applied to a different laser format, the vertical-cavity surface-emitting laser (VCSEL). VCSELs are a class of semiconductor lasers where the emission is perpendicular to the surface of the structure (see section 2.6, Chapter 2 and also figure 4.1). They are made up of two highly reflective planar mirrors, distributed Bragg reflectors (DBRs), which sandwich an active region. The high reflectivity of the DBRs compensates for the typical small thickness (1 to 10's of λ) of the gain region, hence the small single-pass gain, in such devices. Ultimately, a very thin gain region enables the oscillation of only one longitudinal mode. This helps reducing the level for threshold, producing lower power consumption [1]. The mirrors themselves

can be made of a metallic film but usually utilise DBRs. These are made up of multiple layers of interchanging materials selected to provide an alternating high/low refractive index modulation. The optical thickness of each individual layer is equal to a quarter of the chosen emission wavelength so the reflections from the layers interfaces add up in phase as explained in section 2.6.2. In epitaxial semiconductor VCSELs, the active region, also known as the gain structure, is characteristically made up of one or several quantum wells (QWs) or groups of QWs [2]. The QWs are a number of nanometres in thickness, designed to emit and provide optical gain centred at a selected wavelength. Because of their geometry, VCSELs benefit from a symmetrical beam profile with low beam divergence (at least for single mode VCSELs), which, compared to edge-emitting lasers, allows the emission to be easily coupled into an optical fibre or collimated.

Obtaining laser oscillation in a VCSEL structure with a new colloidal material is typically more challenging than in a planar laser like a DFB because of the smaller active region thickness and the necessary balance between gain, pump absorption, losses and DBR reflectivity.

In this chapter, we start by giving some general information and background on the VCSEL technology and highlight the difficulty to obtain VCSELs emitting in the yellow-orange wavelength range when using epitaxial semiconductor materials. We then present our solution-processed gain VCSEL material approach for emission at such wavelengths and the different characterisation studies conducted. In particular, we look at optically-pumped VCSEL operation under different excitation spot sizes and study the VCSEL polarisations for different polarisation states of the pump.

4.1.1 Background

The first demonstration of a VCSEL was reported by Iga in 1979 [3]. This was under a current pulsed excitation, at 77 K, and InGaAsP/InP was the semiconductor material system. Pulsed operation was observed at room temperature using GaAs/AlGaAs in 1983, and continuous wave (CW) operation was achieved in 1988 using the same materials [4, 5]. The rapid advances in VCSEL technology was supported by the expansion of epitaxial growth and microfabrication methods, as well as the oxidation process developed by Holonyak in 1990 for defining current apertures in electrically-driven devices being notable [6–11].

Electrical pumping is usually the preferred excitation method [12–14], as it removes the need for large/bulky pump sources, although compact optical pumping has also been demonstrated. With electrical pumping, tens of milliwatts are commonly used to excite the active region resulting in output powers varying over a few milliwatts (where higher input currents will produce multimodal lasing due to the oscillation onset of higher order transverse modes). Current is applied by creating a diode junction with the addition of p and n contacts directly manufactured onto both sides of the VCSEL. In this case, the DBRs need to be conductive. The p contact is often designed as a ring electrode enabling the laser beam to pass through freely [7]. Intracavity contacting is sometimes used to circumvent the need for conductive DBRs; for example, if dielectric DBRs are used.

VCSELs are sometimes designed to operate as single transverse mode emitters for a high quality output beam. For this, a very small current aperture is needed to only, or predominantly, excite the fundamental transverse mode, which in turn restricts the achievable output power (below the mW up to a few mW). This single mode emission function also confers the ability of emission wavelength tunability, by changing of the optical length, e.g. via the manipulation of the active region temperature or by actively modifying the position of one of the DBRs [14–17].

VCSELs are used in many applications. Examples of these are optical fibre communications as they can have gigahertz modulation frequencies because of their short resonator round trip periods, leading onto broadband signal transmission [10, 18–20]. VCSELs have also been exploited in absorption spectroscopy and in consumer electronic appliances such as laser printers and computer mice [14, 21–26]. VCSELs are also used in research for an atomic clock, in biochemical sensing techniques and even utilised in smart phones, via SPADs (single-photon avalanche diodes, ST Microelectronics), for time-of-flight ranging [27–29].

4.1.2 Epitaxial VCSELs

VCSELs are typically made, entirely or partly, of semiconductor materials and fabricated by epitaxy. Epitaxy is the accumulation of additional crystalline material built up layer by layer deposition on a substrate. The term is coined from the ancient Greek origins where epi-taxis ($\acute{\epsilon}\pi\grave{\iota} - \tau\acute{\alpha}\xi\iota\zeta$) refers to above - an ordered manner describing how the process is carried out (it can also be translated

to"arranging upon"). Supplementary layers are labelled as epitaxial films or layers. There are different processes and different crystal configurations that can be employed for epitaxial growth.

The various types of epitaxial growth can be separated into different groups: homoepitaxy [30]; heteroepitaxy that utilises a substrate; heterotopotaxy, which is similar to heteroepitaxy but differs as growth occurs in two-dimensions resulting in a thin-film material; and pendeo-epitaxy and is again similar to heteroepitaxy [31] with the addition of lateral growth allowing structures such as nanorods.

The techniques for epitaxial growth include vapour phase epitaxy [32–34], liquid phase epitaxy [33] and solid phase epitaxy [35]. These processes can be implemented in different ways. Examples of such implementations are chemical vapour deposition (MOCVD also known as metalorganic vapour phase epitaxy (MOVPE)) [32, 35–38] and molecular-beam epitaxy (MBE) [36, 39–41], which both lead to the highest quality materials. MOCVD uses metal organic precursors. This produces thickness controlled, high quality epitaxial layers (of III-V, II-VI or others) and is used in the fabrication of quantum wells. MBE requires a controlled environment. In a very high vacuum (approximately 10^{-8} Pa) the substrate is bombarded by one or more evaporated beams of atoms allowing for lower temperature growth. Through these methods the growth of groups I, II, III, IV and V semiconductor groups are accomplished.

4.1.3 The "Yellow/green gap"

The use of different epitaxial semiconductor alloys enables optoelectronic devices and lasers on a wide range of wavelengths, from the UV to the mid-infrared. However, there are a few spectral windows, including the yellow-green gap as discussed further, where it is currently difficult to obtain such devices. The typical operational range is between 720 nm to 1300 nm when based on GaAs/AlGaAs [42–44], with the majority of red emitting devices based on AlInGaP [45, 46]. AlGaAs alloys have demonstrated 670 nm to 800 nm [47]. Dilute nitrides (GaInNAs and GaInNAsSb) can achieve longer wavelengths up to and beyond 2 μm [48–51] with a growth still on GaAs. InGaAs and InGaAsP grown on InP are widely used in telecommunications [52]. The most established wavelength for VCSELs is 720nm-850nm (AlGaAs/GaAs), but they are also developed (on a much smaller scale)

at 650 nm (AlInGaP), and 1550 nm (InP-based) and 2000 nm (e.g. Sb-based material).

However, at lower wavelengths in the visible there are few examples of reliable VCSEL operation. This is an active area of research where a number of groups have endeavoured to produce VCSEL structures emitting from the UV to the green. Some progress has been made by employing mixtures of current driven semiconductor and dielectric DBRs and all-dielectric DBRs [53–57]. At such wavelengths devices have exploited InGaN and other GaN material systems [58, 59]. GaN devices, although working well in the blue/ultraviolet, lose in efficiency at longer wavelengths (>500nm). This is a direct consequence of high levels of strain and dislocations in the crystal structure. It is also due to strong polarisation effects that lead to a strain induced piezoelectric field resulting in the Stark effect [57–60]. This has been a noticeable and studied effect in the fabrication InGaN quantum wells [59]. The combination of diminishing quantum efficiencies under high injection currents and strain effects is causing obstacles for visible emission in the green-orange region. This issue is known as the yellow gap (also green gap) [58, 61, 62].

Various groups have attempted to mitigate these issues by applying different methods. One method is to change the growth substrate for reducing the number of defects and the polarisation issue. Traditionally grown on c-plane sapphire the quantum well structure can be grown on GaN and then transferred onto the DBR structures increasing the growth quality and reducing the Stark effect [63, 64]. Another approach is to refigure the p contact configuration and deposition to allow for a smoother current transit and improved thermal management [57, 65, 66]. Unfortunately, these methods have only slightly advanced the technology so far. The replacement of the growth substrate from sapphire to GaN and the inclusion of epitaxially grown InGaN QDs has enabled VCSELs operating with low thresholds and CW lasing at room temperature up to 560 nm [59, 67, 68]. However, this recent, cutting edge device suffers from a complicated design and fabrication, and the emission is limited to 560 nm and below.

4.1.4 The solution based approach

Here, a solution-based gain material has been explored as an alternative for achieving VCSEL emission at these desirable wavelengths. While such an approach is

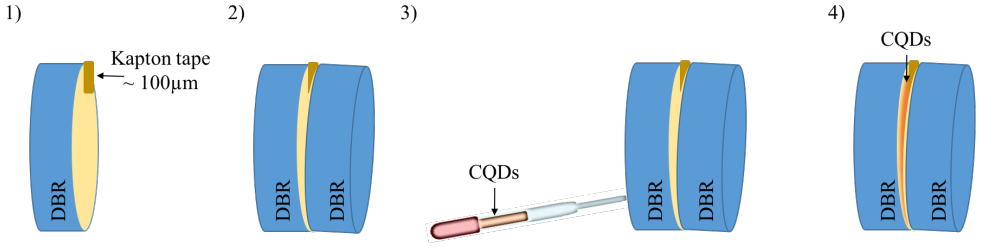

FIGURE 4.1: Systematic fabrication techniques to create CQD-VCSEL.

unlikely to lead in the near future to electrically driven VCSELs, it has some attractiveness. For one thing, it negates the use of complicated, time consuming and expensive epitaxial growth methods. Secondly, the library of solution-processed light-emitting materials, including CQDs, enables operation in the yellow-green gap. Thirdly, optical pumping with compact blue InGaN devices is possible. Finally, solution processing allows for new structure formats to be created permitting the use of different cavity designs, for example for the fabrication of flexible devices [69–76]. In the following, using commercially available CQDs and dielectric DBRs such a VCSEL is demonstrated and its characteristics explored.

4.2 VCSEL design and fabrication

The schematic of the CQD-VCSEL and the main fabrication steps can be seen in figure 4.1. The CQDs were the same alloyed-core/shell CdS_xSe_{1-x}/ZnS as in Chapter 3. These are type I alloyed-core/shell structures (tending towards quasi-type II at lower wavelengths) with an average diameter size of 6 nm with oleic acid as ligands. Their intrinsic PL is centred at 575 nm with an approximate PL FWHM of 40 nm.

The preparation for the CQDs deposition slightly differed from the DFB laser work as they were purchased at higher starting concentrations; whereas in Chapter 3 the CQDs were initially in toluene at 1 $mg.mL^{-1}$ here the initial concentration is 50 $mg.mL^{-1}$. As in section 3.2.3, the solvent of the CQD solution was evaporated under vacuum leaving the CQDs in powder form. They were re-diluted into a PMMA chloroform mix at 1.6:1 weight ratio.

Three different SiO_2/TiO_2 DBRs with respective maximum reflectivity of 70% (SLS optics), and two high reflectivity $>$ 99% from SLS optics, 585 nm to 685

nm, and Thorlabs, broadband, were utilised in this study. Laser operation was achieved using the high reflectivity DBRs.

For fabrication of the full VCSEL, the broadband DBR had a small piece of Kapton tape, 100 μm thick, attached to the edge of its reflective surface (step 1, figure 4.1). Re-diluted CQDs were then deposited onto the DBRs surface and the cavity was closed by placing the other high reflectivity DBR on top [70]; step 2 figure 4.1. Capillary bonding holds these mirrors together. Once the solvent was evaporated at room temperature additional CQDs were injected from the side, as shown in step 3 in figure 4.1. The solvent from the additional CQDs is allowed to evaporate and the process is repeated until satisfactory coverage is obtained. The final VCSEL is shown in step 4 of figure 4.1. The wedge in the cavity ensures a thickness for the gain region suitable for laser oscillation to be found. Reaching oscillation in a VCSEL is not straightforward especially with solution-processed materials with possible scattering limiting the achievable modal gain. The wedge therefore ensures that, if laser oscillation is possible, an appropriate gain thickness for a given cavity reflectivity and given gain material (here CQDs) will be found.

4.3 Optical setup

In this section, we summarise the methods and set-ups used for the experiments carried out, which are discussed in details afterwards.

The same pump laser as in Chapter 3 was utilised (355nm emission in 5ns pulses at a repetition rate of 10 Hz). The pulse duration is longer than the accepted value of Auger decay in standard core/shell CdSe based quantum dots of 360 ps [77], although the biexcitonic lifetime is unknown the CQDs reported in this thesis and it is presumed that in alloyed-core structures it is in the range of a few 100's of ps to a few ns.

The emission from the VCSEL is coupled into a 50μm core optical fibre, and connected to an Avantes CCD spectrometer. Throughout this study two of the spectrometers channels were employed depending on the particular nature being explored. These channels were the master slave with a 2.5nm resolution and slave 3 with 0.13 nm resolution. The VCSEL was investigated for two pump spot sizes of radius ($1/e^2$); 250 μm and 110 μm. These were obtained utilising optics discussed further. The plane-plane laser cavity here is stabilised by the gain guiding, hence

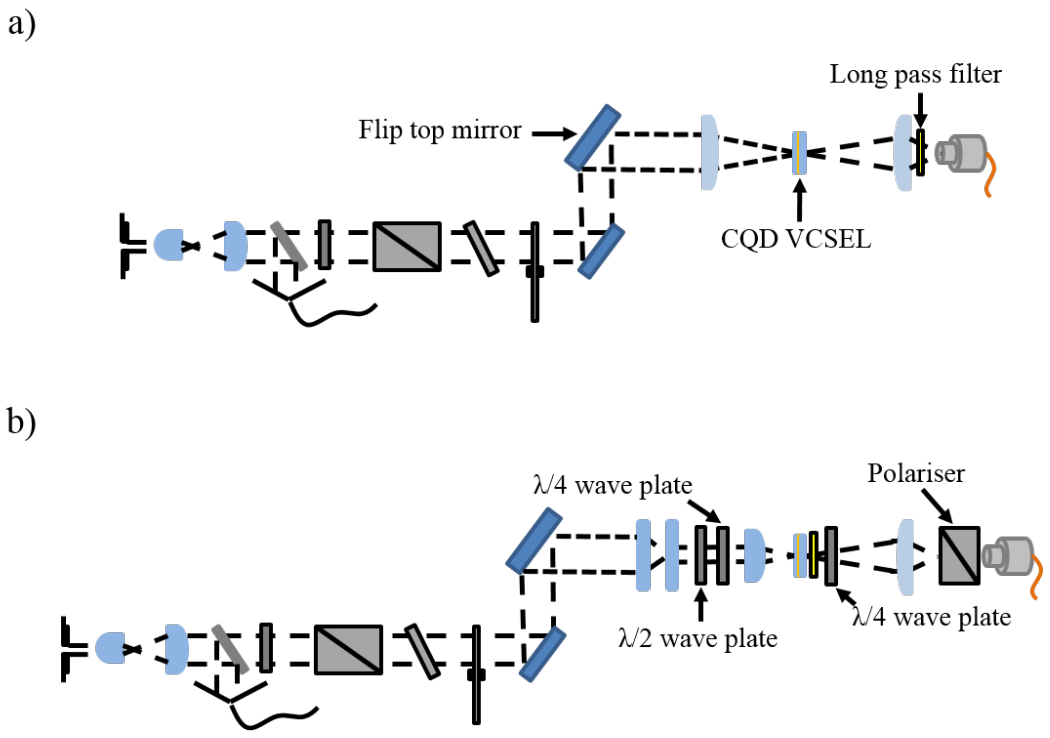

FIGURE 4.2: Experimental setups for CQD-VCSEL investigation.

changing the pump spot size changes the mode sizes and the F number of the cavity. The optical setup for pumping was similar to Chapter 3 with an attenuator stage (wave-plate + polariser + neutral density) allowing for the control of the pump energy incident on the surface of the sample. Flip mirrors then redirects the beam. These elements can be seen in figures 4.2a and 4.2b.

After the flip mirrors the pump went through a focusing optics, figure 4.2a. The optics were an asphere condenser (3.2cm focal length) and the pump spot at focus was measured with a 12 bit CCD camera. The VCSEL device was placed on an xyz stage. This stage permitted the sample to be easily repositioned, as well as allowing excitation of different regions. The detection was done behind the device. A second asphere condenser (3.2cm focal length) was placed 8cm distance away from the VCSEL to image the output into the optical fibre, through a long-pass filter.

A large spot size favours highly multimodal lasing due lateral modes being excited with the large surface area that the spot covers. To reduce the number of oscillating modes in our devices the simplest method is to reduce the pump spot size by utilising a focusing lens of shorter focal. In order to reduce the spot size, the pump beam was first demagnified so it could fill in the aperture of a 4.51mm

focusing lens with no significant losses. This was done using a contribution of a plano-convex lens and an asphere condenser (3.2cm focal length), figure 4.2b. The resulting collimated beam was measured to be 338 ± 12 by 368 ± 29 μm, i.e. slightly elliptical. It was then focused onto the device with the aspheric lens of 4.51mm focal length down to a spot of 55 ± 10 μm by 50 ± 10 μm (again measured using the beam profiler).

Knowing the spot size when collimated and at focus allows an estimate of the M^2 (quality of beam) value to be calculated. Approximating the beam waist assuming that the optical pump beam is Gaussian, the M^2 was determined by,

$$M^2 = \frac{\pi \omega_f \omega_l}{f\lambda}, \tag{4.1}$$

where ω_f is the waist (spot) size of the beam, ω_l is the radius of the collimated beam, f is the focal length, λ is the wavelength and M^2 can be estimated to be roughly 12, where ω_f is calculated to be $4.2\mu m$ under perfect conditions.

The error on the fluence threshold in section 4.4.3 is not negligible because of the tighter focus and the passive alignment of the device. Passive alignment means that the sample is placed at focus but the position is not fine adjusted based on the emission characteristics like threshold. Assuming that the M^2 value is 12 equation 4.2 can be used to calculate the beam radius at a distance z.

$$\omega_R(z) = \omega_{0R}\left[1 + \left(\frac{z\lambda M^2}{\pi \omega_{0R}^2}\right)^2\right]^{\frac{1}{2}}. \tag{4.2}$$

Here ω_R is the beam radius, ω_{0R} is the beam waist, and z is the distance. The beam radius increases from 50 μm at focus to 500 μm 10mm away. We estimate that the sample is placed in position within ±3mm of the true focus when the alignment is done passively. This has no significant effect on the effective excitation area when the pump beam waist is 250 μm but when it is 50 μm the effective pump spot radius in the CQD region can almost triple. This can translate into an error in the fluence by a factor of 10. In the following we take the excitation as the average of the size at focus within this placement range. It corresponds to an effective beam radius of 110 μm. The threshold is also quoted in terms of pump energy and not only the fluence. Such a size is still large but we will see that single peak emission is achievable at least when the pump level is not too high.

For the polarisation study, which was carried out on the VCSEL excited with the reduced spot size, a set of polarisers and wave-plates were used. To observe the polarisation-resolved VCSEL emission, a linear polariser was placed before the detection. To study the VCSEL polarisation dependence on the pump polarisation, a quarter wave-plate (QWP) was used behind the VCSEL, while a combination of a half wave-plate and a QWP before the VCSEL allowed the polarisation of the pump beam to be altered between linear and right-hand and left-hand circular.

4.4 CQD-VCSEL

4.4.1 Free spectral range

For the first experiment, the CQDs were deposited onto a >99% reflectivity DBR and the cavity was closed with the addition of a 70% reflectivity DBR. The device was then optically pumped through the high reflectivity mirror and the spectra recorded as it exited from the lower reflectivity mirror. The detected emission spectrum, excited with energy up to 11.1 μJ, displays eight peaks identified as the cavity longitudinal modes, the spacing between them corresponding to the free spectral range (FSR), figure 4.3.

The wavelengths of the resonant modes are typically compared with the central, dominant, mode. In figure 4.3 the central mode occurs at 578.6 nm (FWHM 5.6 nm) where the closest mode, the first mode, is taken to occur at 571.1 nm (FWHM 5.3 nm). The FSR in wavelength is 7.5 nm, where applying equation 4.3 the cavity length (approximating the CQD film thickness) can be estimated to be 12 μm.

$$L = \frac{\lambda^2}{2n_{QD}\Delta\lambda} \tag{4.3}$$

In equation 4.3, L is the film thickness, λ is the central peak wavelength, $\Delta\lambda$ is the FSR and n_{QD} is the refractive index of the CQD region, taken to be approximately 1.8 [78, 79].

Analysing the spectra obtained in figure 4.3 it is clear that laser oscillation is not achieved. This is because the limited single-pass gain cannot compensate for the overall low cavity reflectivity. Given the expression of the single-pass gain in the cavity (see chapter 2), the net modal gain needed to reach threshold here

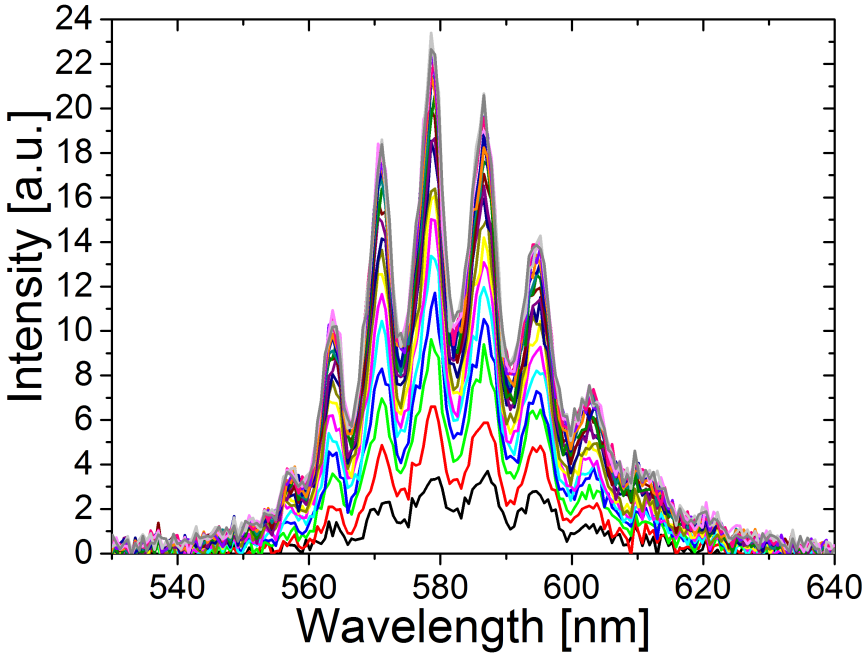

FIGURE 4.3: Spectra of 575 nm CQDs in closed cavity of 70% and 99% reflectivity DBRs (no wedge).

is above 150 cm^{-1}, which represents the highest optical gain ever reported for colloidal quantum dots [80, 81]. Therefore, reaching threshold with such a structure would be extremely challenging, especially when pumped in the nanosecond regime. Figure 4.3 allows an estimate of the expected Q factor (this is the quality factor describing the damping of photon number in the cavity). This can be calculated by dividing the emission wavelength by the FWHM of the longitudinal modes. Fitting a Gaussian over the central mode at 578.6nm (data not shown) the FWHM is 5.6 nm, resulting in a Q factor of 103. Typical VCSELs have Q factor in excess of 1000, or at least 500 for (relatively) thick gain region. So overall, not reaching threshold with this structure could be expected.

Fitting a single Gaussian over the entire PL spectrum also enables extraction of the "unfiltered" PL, i.e. the PL as emitted by the CQD film within the cavity. In turn this information can be used to model the theoretical cavity PL emission aligning the spectra with the transmissivity of the cavity calculated by the transfer matrix method. This was done and results are shown in figure 4.4a. Figure 4.4b displays the theoretical cavity reflectivity of the equivalent cold cavity, i.e. ignoring absorption of the CQDs.

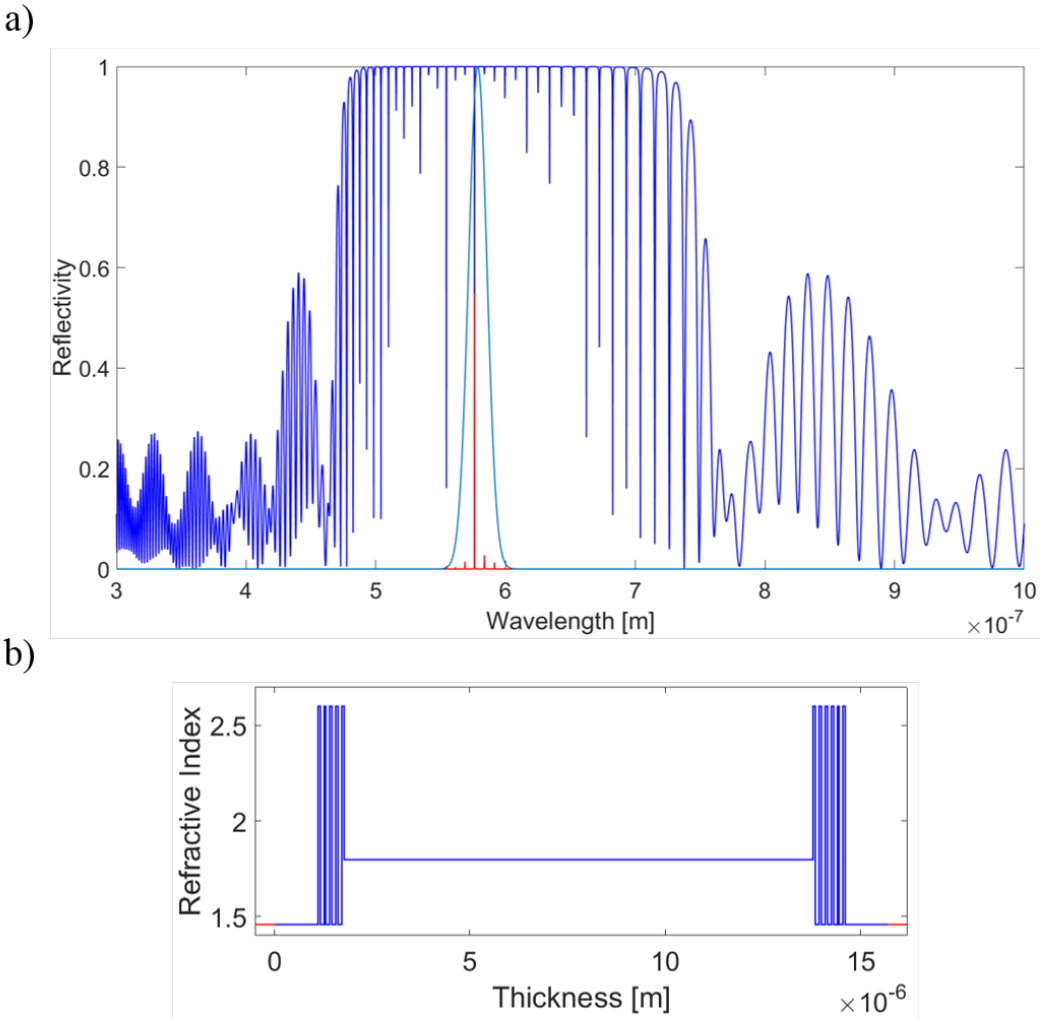

FIGURE 4.4: a) Model of the cavities FSR using the transfer matrix method, b) refractive index of CQD-VCSEL representing the structure.

The reflectivity diagram is obtained in a number of steps. Initially the VCSEL structure is created, taking into account the DBR glass substrates. The reflectivity is then calculated using the transfer matrix method [82, 83]. Here the model is based on a layered structure of homogeneous dielectric films where the refractive index and layer thickness, h, (optical depth) remain constant. From this a unimodular matrix can be constructed,

$$\mathbf{M}(h) = \begin{bmatrix} cos(k_0 nhcos\theta) & -\frac{i}{p}sin(k_0 nhcos\theta) \\ -ipsin(k_0 nhcos\theta) & cos(k_0 nhcos\theta) \end{bmatrix}, \tag{4.4}$$

where

$$p = ncos\theta P + \frac{1-P}{n}cos\theta, \tag{4.5}$$

where P is the polarisation, n the refractive index, k_o the wavenumber and θ

the angle of the incident photon (taken to be zero). There is a corresponding matrix for each layer constituting the cavity, i.e. for the DBR layers, and the active region. The characteristic matrix for the cavity is then the product of the matrices corresponding to each layer of the structure,

$$\mathbf{M} = \prod_{j=1}^{N} \mathbf{M}_j(h). \tag{4.6}$$

The elements of this matrix allow the calculation of the reflection (and transmission) coefficients,

$$r = \frac{R}{A} = \frac{(m_{11} + m_{12}p_{sub})p_{sub} - (m_{21} + m_{22}p_{sub})}{(m_{11} + m_{12}p_{sub})p_{sub} + (m_{21} + m_{22}p_{sub})}, \tag{4.7a}$$

$$t = \frac{T}{A} = \frac{2p_{sub}}{(m_{11} + m_{12}p_{sub})p_{sub} + (m_{21} + m_{22}p_{sub})}, \tag{4.7b}$$

where A, R and T are amplitudes of the electric vectors of the incident, reflected and transmitted waves. The intensity reflectivity and transmissivity can then be calculated from,

$$\Re = |r|^2, \tag{4.8a}$$

$$\Im = \frac{p_{sub}}{p_1}|t|^2. \tag{4.8b}$$

Next the spectral transmissivity of the structure is multiplied by a Gaussian that represents the unfiltered PL of the CQDs, as extracted by fitting the data of figure 4.3. This gives a model of the cavity modes corresponding to the spectra observed in figure 4.3. The modelled Gaussian is then plotted over the calculated spectra as a representation of the PL.

Figure 4.4b gives a schematic view of the refractive index profile versus physical length of the modelled cavity structure. This shows the fused silica (the substrate of the DBRs), the DBRs and the CQD gain material. Note that the model ignored the absorption of the CQDs and simply enables a representation of the device profile regarding the refractive indices. The model also negates to include the DBR substrate air interfaces and contribution from TM modes in addition to any angles alleviated from the pump to the DBR substrate surface as a perpendicular excitation geometry is desired.

4.4.2 250 μm diameter broad area VCSEL

The experiment of the previous section indicates that there is a cavity effect and, knowing the CQD material can provide amplification, the next step is to achieve laser operation by increasing the cavity Q factor. This can be done by increasing the reflectivity of the DBRs to increase the confinement within the cavity or by increasing the thickness of the gain material, thereby increasing the single-pass gain. However, increasing the thickness of the material gain is not the preferred option because it would further increase the number of potential longitudinal modes by reducing the FSR. Too thick a gain region would also exacerbate the effect of self-absorption, scattering and pump depletion.

Consequently, the 70% reflectivity DBR is replaced by a $R > 99\%$ broadband DBR. As a result, the overall reflectivity and Q of the cavity are increased (expected $Q \approx \frac{4\pi L}{\lambda(1-R_1R_2)} \approx 2180$ for a $12\mu m$ CQD thickness) producing a greater number of round trips through the gain material. However, a negative consequence of this is a lower output transmission.

Laser oscillation is obtained in this configuration. Figure 4.5a displays the multimode lasing spectrum (resolution 0.13 nm) obtained above approximately 2.1 mJ/cm^2. The main peak is centred at 591.1 nm with a FWHM of 0.2 nm. There are 6 modes visible between 580 nm and 602 nm. From the FSR equation, equation 4.3, it can be seen that there are 5 groups of longitudinal modes, with the remaining modes being transverse, figure 4.5a. The FSR is ∼6nm corresponding approximately to a $16\mu m$ thickness. The transfer function of the central mode at 591.1 nm is shown in figure 4.5b where the spectral threshold energy is observed at 2.1 ± 0.3 mJ/cm^2. The scattered values of intensity above threshold are attributed to the multimodal nature of the device. There is a competition of modes occurring within the gain material causing spectral fluctuations.

This highly multimode nature is not surprising given the wide lateral extension of the excitation area, which leads to a high Fresnel number, F, of the cavity. F is calculated by dividing the radius of the pump spot squared by the product of the film thickness with the emission wavelength,

$$F = \frac{a^2}{L_{opt}\lambda}. \tag{4.9}$$

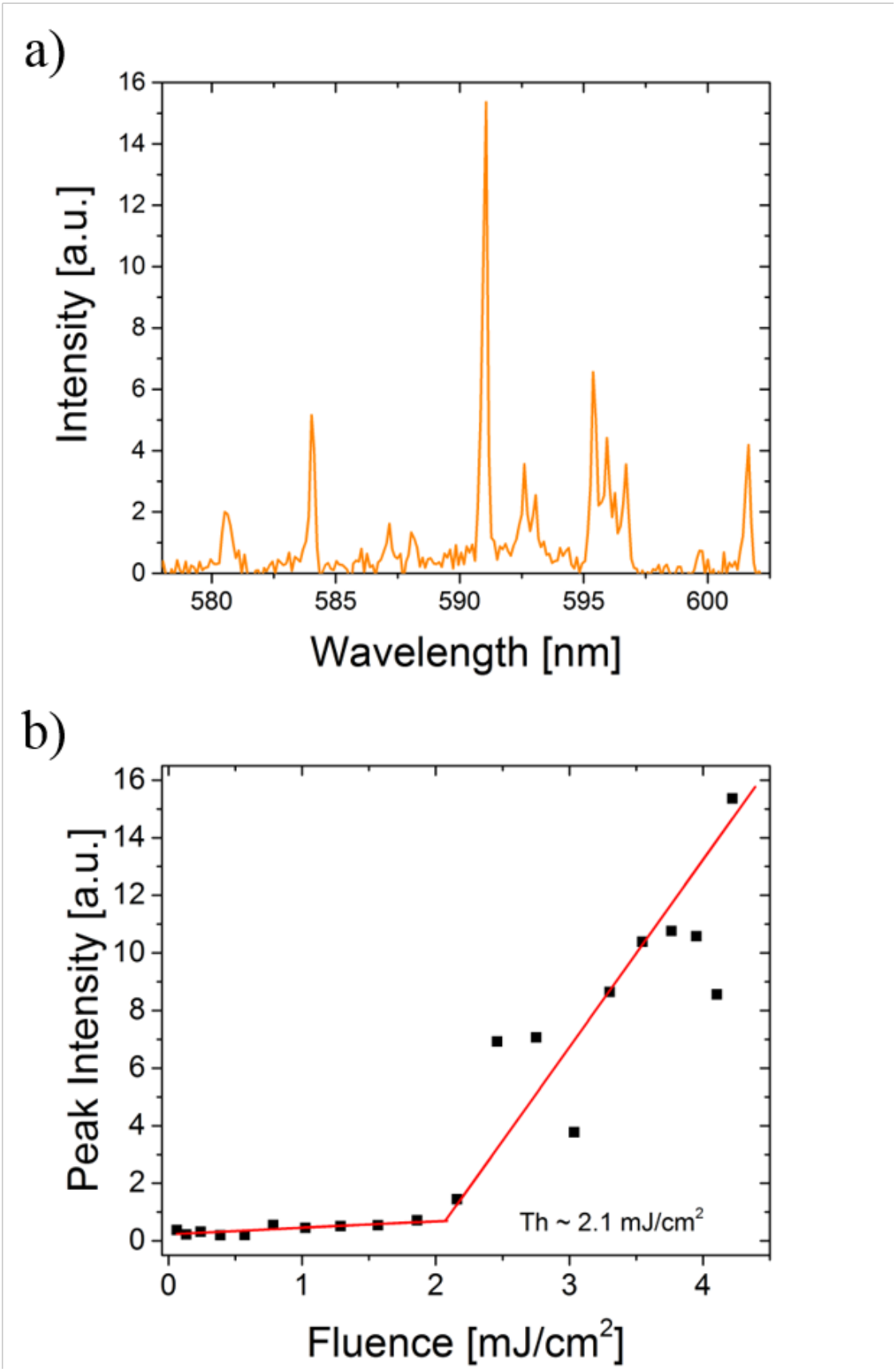

FIGURE 4.5: a): CQD-VCSEL optically pumped with 250μm spot multimode emission spectra with main peak occurring at 591.1nm with longitudinal modes present b) transfer function for the 591.1nm central peak with threshold energy 2.1 mJ/cm^2.

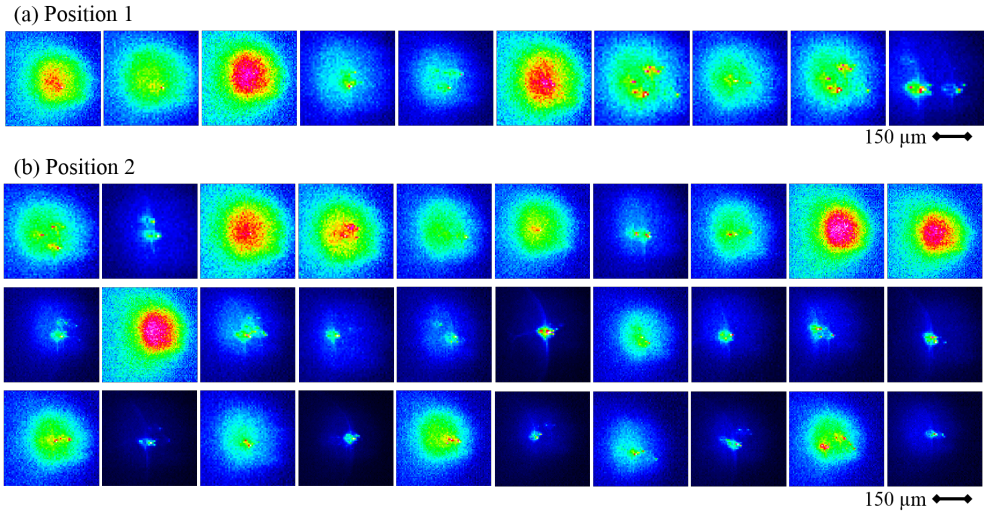

FIGURE 4.6: Images of CQD VCSEL emission beam observed by the Thorlabs beam profiler at two different excitation positions. Each image corresponds to a lapse in time. Spatio-temporal instabilities are observed with occurrences of narrow spectral "spikes" or "beams" associated with spatial solitons.

A high F-number indicates overall lower diffraction losses thereby favouring multimodal emission. The Fresnel number here is F = 3172, explaining the highly multimode nature of the VCSEL.

Spatio-temporal fluctuations are expected in such broad-area VCSELs and are also evidenced here when recording the VCSEL spatial emission [84–90]. The emission of the CQD-VCSEL was recorded with the Thorlabs beam profiler with the pump laser at approximately 5 μJ ($\approx$ 8 mJ/cm^2). Figure 4.6 displays two different equivalent positions on the device that were recorded at different time intervals. In both data sets the beam fluctuates between a spatially extended emission corresponding to the excitation area (the "broad" beam with maximum intensity near the centre) and spatially confined "single" spikes. These spikes are attributed to spatial solitons produced in the cavity [91–94]. These are isolated waves, or modes, that maintain their structure because of a balance between nonlinear and diffractive effects. There is nothing here to control and "lock" such solitons and their appearance and disappearance is chaotic.

4.4.3 110 μm VCSEL pump spot

Reducing the spot radius to between 50 μm and 145 μm enables a reduction of the F number to roughly between 90 and 760 for a mitigation of the highly multimodal

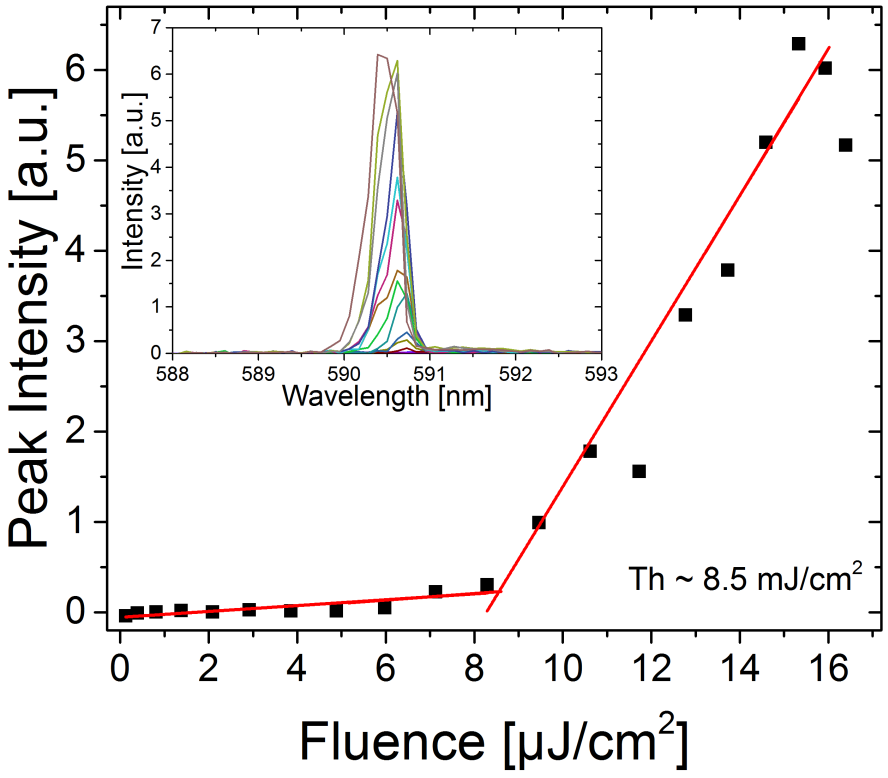

FIGURE 4.7: Transfer function of the CQD-VCSEL when excited with small pump spot with threshold energy 8.5 mJ/cm^2 inset: single, longitudinal mode lasing spectra.

behaviour. We note that this is still a high F number (as $F \gg 1$) but as we will see next, it enables single peak emission in our device, at least for a limited range of fluence.

Figure 4.7 displays the transfer function of the single mode CQD-VCSEL laser emission where the threshold energy occurs at 8.5 mJ/cm^2. Above a fluence of 16 mJ/cm^2 one can notice the start of a roll over of the intensity, which is attributed to the apparition of additional modes and to non-linearities as well as possible damage of the gain region at such high fluence. It could also be due to additional diffraction losses at higher thresholds because the gain guiding stabilises the plane-plane cavity here as there is no thermal effect; although additional study would be required to validate this. The threshold in terms of fluence is higher than for the bigger pump spot size, although the error is also significantly larger in this case, 3.2 μJ (and can be up to an order of magnitude).

The inset of figure 4.7 displays the corresponding spectra of the CQD-VCSEL and

its evolution over a range of energies from below to above the threshold value. The spectrum is centred at 590.5 nm and has a FWHM of 0.4 nm. The peak value of the laser emission slightly blue shifts as pump energies increase. In CQD thin films, such behaviour was also seen in ASE measurements and can be attributed partly to an increasing number of CQDs reaching saturation of the first excited energy states, reducing self-absorption. In a VCSEL the wavelength is fixed by the cavity. The optical thickness of the cavity can be affected by changes in the refractive index of the gain medium with pump level. This effect results in the reduction of the gain region refractive index (hence blue shift) as the pump excitation is increased. It also means that the gain region does not fully clamp at threshold.

While the laser remains single peak for a range of fluence, it is not systematically the case. Multimode emission was seen when slightly changing the excitation position. This is probably due to inhomogeneities in the CQD region and possibly the mirror surfaces. However, single peak emission could be obtained at several different positions, which was not possible with the bigger pump spot size.

4.4.4 Slope efficiency

The optical fibre, in figure 4.2, was then replaced by a photodiode connected to a Thorlabs power meter and the output energy was measured. The power meter was used because we had no energy meter sensitive enough for this measurement. The device emits at 10Hz and the averaged output power can be converted into the output energy per pulse. Figure 4.8 displays the VCSEL output energy versus the input energy of the CQD-VCSEL yielding a slope efficiency of approximately 2%. This is a relatively low efficiency that is explained by the gain guiding nature of the VCSEL and the high reflectivity of the output mirror [20, 74].

The threshold energy occurs at $2\mu J$ approximately equal of that detected via optical fibre. Figure 4.8 displays a zoomed in section representative of threshold location. Unfortunately, this is close to the detection limit of the photo diode resulting in higher pump energies being used in the detection. Above this, figure 4.8 can be seen to "kick" two more times. This is due to the detection of unsaturated PL being coupled into the detector. It is also possible that ASE being detected. This would be occurring within the film where the focusing optics used would couple it into the photo diode.

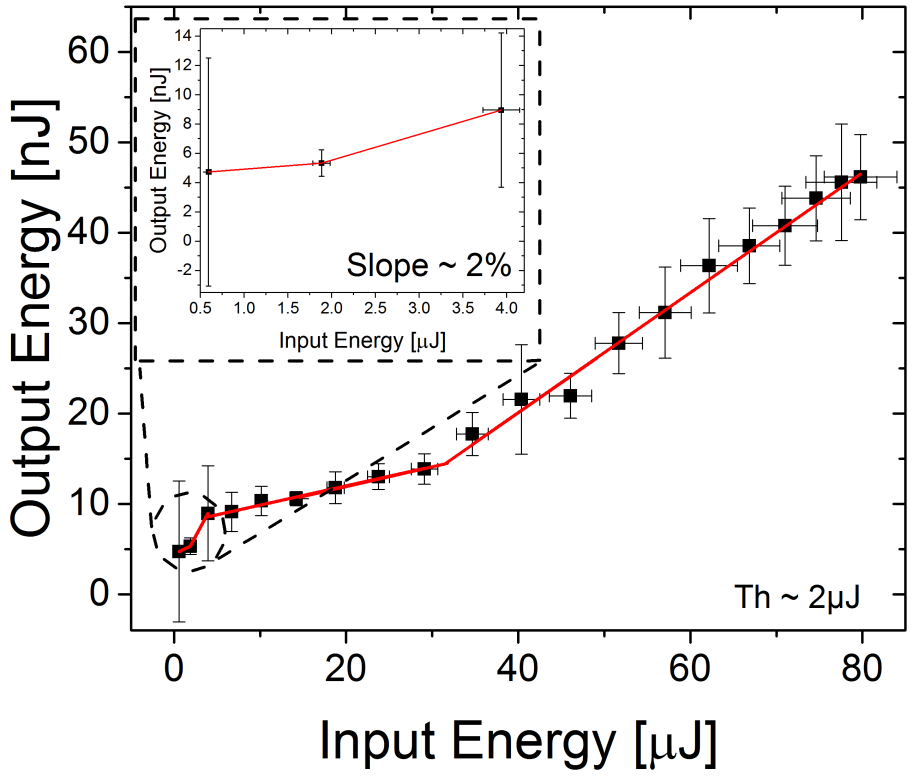

FIGURE 4.8: Slope efficiency of 2% for CQD-VCSEL with 110μm pump spot.

4.5 VCSEL polarisation

Reported in this section, an investigation into the CQD-VCSEL polarisation and the effect of the pump polarisation was carried out.

4.5.1 Linearly polarised excitation

Having demonstrated single longitudinal mode laser emission from a solution processed CQD VCSEL (under certain conditions) the polarisation properties of the VCSEL were investigated. Initially, the pump polarisation was left unchanged (linear along the vertical, i.e. in the $0^0/180^0$ direction). The long pass filter used to cut the optical pump was relocated directly behind the CQD-VCSEL and a linear polariser, mounted in a rotating wheel, placed just before the detection element (see figure 4.2). The polariser was rotated (clockwise) from 0^0 to 360^0. Figure 4.9a displays the normalised integrated intensity (integration over emitted wavelengths) versus angle of polarisation. The data is also represented in the 2D

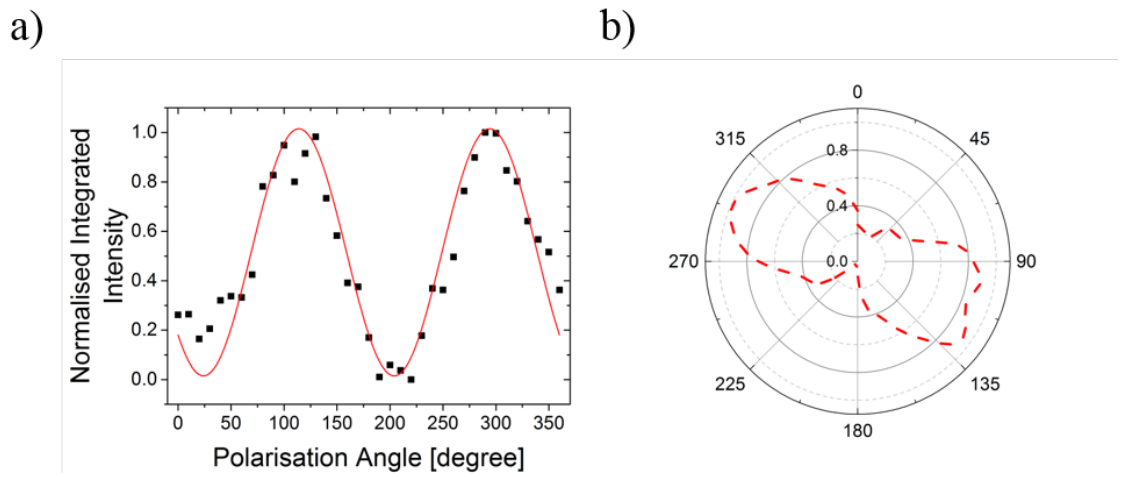

FIGURE 4.9: a) The intensity of the CQD-VCSEL emission versus angle of polariser b) detected laser intensity as a function of the polarisation angle.

polar coordinate map of figure 4.9b. The oscillatory period of 90^0 ($\pi/2$) with the minimum intensity close to (but not quite) nil confirms the mostly linear polarisation. The polarisation axis of the VCSEL is aligned along the $115^0/295^0$ line. It can also be observed that the intensity does not totally go to zero (polarisation appears slightly elliptical). This can be attributed to the additional PL being coupled within the detection or that the VCSEL is not entirely linearly polarised. A slight intensity drop at 115^0 can also be seen in the data, attributed to modal instability and possible pump intensity fluctuations.

4.5.2 The Stokes parameters

The Stokes parameters are a set of values that describe the state of polarisation of a light wave. We will use them in our following study. A quick reminder on polarisation and these Stokes parameters is given first.

4.5.2.1 Stokes parameter

Around 1670 Christiaan Huygens proposed that light propagating through a crystal displayed a vectorial nature. In 1818 Fresnel and Arago were able to describe the interference pattern of Youngs double slit experiment as two perpendicularly oscillating transverse waves having no longitudinal component. The polarisation ellipse, shown in figure 4.10a, is a representation of these transverse electromagnetic waves. It is taken that the waves propagate in the z-direction and can be

expressed as,

$$\vec{E}_x = E_{0x}cos(kz - \omega t)\hat{x}, \tag{4.10a}$$

$$\vec{E}_y = E_{0y}cos(kz - \omega t + \delta)\hat{y}, \tag{4.10b}$$

where δ is a phase term. Removing the amplitudes, manipulating the double angle formula, squaring and combining the above expressions, equation 4.10, allows the equation of the ellipse to be expressed as,

$$\frac{E_x^2}{E_{0x}^2} + \frac{E_y^2}{E_{0y}^2} - 2\frac{E_x}{E_{0x}}\frac{E_y}{E_{0y}}cos\delta = sin^2\delta. \tag{4.11}$$

The ellipse identifies 4 quantities. These are the size of the major and minor axes and the direction of rotation of the polarisation (clockwise or counter clockwise). When E_{0x} is zero there is only a y-component resulting in vertically polarised light and when E_{0y} is zero the light is horizontally polarised (if the y-axis is chosen as the vertical and x-axis as the horizontal). 45^0 polarisation is obtained when there is no phase difference, and $E_{0x} = E_{0y}$ (and $E_x = E_y$). Other linear polarisation are also characterised by $\delta = 0$. For $\delta \neq 0$, the polarisation rotation slope is either positive or negative depending upon the relative phase shift between the x and y components. Circular polarisation occurs when and $E_{0x} = E_{0y}$ (hence $E_x/E_{0x} = cos\psi$ and $E_y/E_{0y} = sin\psi$). Equation 4.11 then becomes,

$$\frac{E_x^2}{E_{0x}^2} + \frac{E_y^2}{E_{0y}^2} = cos^2\psi + sin^2\psi = 1, \tag{4.12}$$

and is the equation of a circle.

Both the linear and circular polarisation states remain related to the elliptical polarisation (= linear + circular polarisation) with the angles of the elliptical rotation, χ and ψ figure 4.10a, to be calculated.

In 1852 Sir George Gabriel Stokes discovered that the polarisation states could be characterised by a set of experimentally measurable parameters: the Stokes parameters. The polarisation ellipse is a function of time and equation 4.11 can be expressed as,

$$\left(\frac{E_x^2(t)}{E_{0x}^2(t)}\right)^2 + \left(\frac{E_y^2(t)}{E_{0y}^2(t)}\right)^2 - 2\frac{E_x(t)}{E_{0x}(t)}\frac{E_y(t)}{E_{0y}(t)}cos\delta = sin^2\delta. \tag{4.13}$$

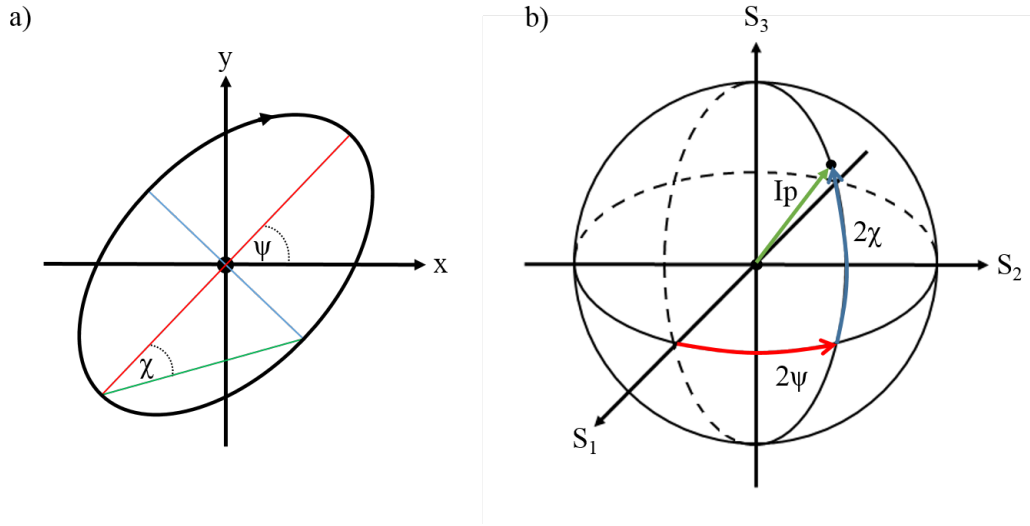

FIGURE 4.10: a) Polarisation ellipse including direction and angles of ellipticity. b) Poincaré sphere.

Integrating equation 4.13 over time results in the expression of the Stokes parameters,

$$(E_{0x}^2 + E_{0y}^2)^2 - (E_{0x}^2 - E_{0y}^2)^2 - (2E_{0x}E_{0y}cos\delta)^2 = (2E_{0x}E_{0y}sin\delta)^2. \tag{4.14}$$

Stokes gave a more approachable technique to describe light developing a method formed around the light intensity, I, the degree of polarisation, P, and relation to the shape parameters of the polarisation ellipse, figure 4.10a. These can be expressed as,

$$S_0 = E_{0x}^2 + E_{0y}^2 = I \tag{4.15a}$$

$$S_1 = E_{0x}^2 - E_{0y}^2 = IPcos(2\psi)cos(2\chi) \tag{4.15b}$$

$$S_2 = 2E_{0x}E_{0y}cos\delta = IPsin(2\psi)cos(2\chi) \tag{4.15c}$$

$$S_3 = 2E_{0x}E_{0y}sin\delta = IPsin(2\chi) \tag{4.15d}$$

where S_0, S_1, S_2 and S_3 are the Stokes parameters. These four parameters characterise the state of polarisation and can be transferred onto a Poincaré sphere for a 3D representation, figure 4.10b. These can be expressed as,

$$2\psi = atan\left(\frac{S_2}{S_1}\right), \tag{4.16a}$$

$$2\chi = atan\left(\frac{S_3}{\sqrt{S_1^2 + S_2^2}}\right). \tag{4.16b}$$

Stokes' experimental method was to allow a polarised beam to propagate sequentially through a QWP and a linear polariser. The wave-plate decomposes the beam photons into two axes, the ordinary and the extraordinary axes, where a phase shift, of a quarter of the wavelength of the polarised beam, is introduced between these. The intensity of the beam after the polariser is given by,

$$I(\theta,\phi) = \frac{1}{2}(S_0 + S_1 cos2\theta + S_2 sin2\theta cos\phi - S_3 sin2\theta sin\phi), \tag{4.17}$$

where θ is the angle of the linear polariser and ϕ the phase difference imparted by the QWP between the x and y axes.

The measurement entails measuring four intensity values. Initially the wave-plate is omitted (ϕ=0) and the intensity is measured with the linear polariser set at angles at 0^0, 45^0 and 90^0. The fourth measurement involves inserting the wave-plate into the optical setup with its fast axis along x, before the linear polariser, which is set at an angle of 45^0, and again measuring the intensity of the beam with the linear polariser at 90^0. From these measurements the Stokes parameters can be determined by [95],

$$S_0 = I(0^0, 0^0) + I(90^0, 0^0), \tag{4.18a}$$

$$S_1 = I(0^0, 0^0) - I(90^0, 0^0), \tag{4.18b}$$

$$S_2 = 2I(45^0, 0^0) - S_0, \tag{4.18c}$$

$$S_3 = S_0 - 2I(45^0, 90^0). \tag{4.18d}$$

Although the Stokes parameters are relatively simply obtained through this method, it is not as straightforward as it seems. It requires precision alignment of both polarising elements. As well as this, the addition of the QWP reduces the beam intensity at detection. Finally, this method only collects data at 4 locations increasing the chance of systematic errors.

4.5.2.2 Rotating quarter wave-plate

An alternative method for measuring the Stokes parameters is the rotating QWP measurement. Here a QWP, paired with a linear polariser at a fixed angle, is rotated and the intensity of the beam measured for the different angles. This is

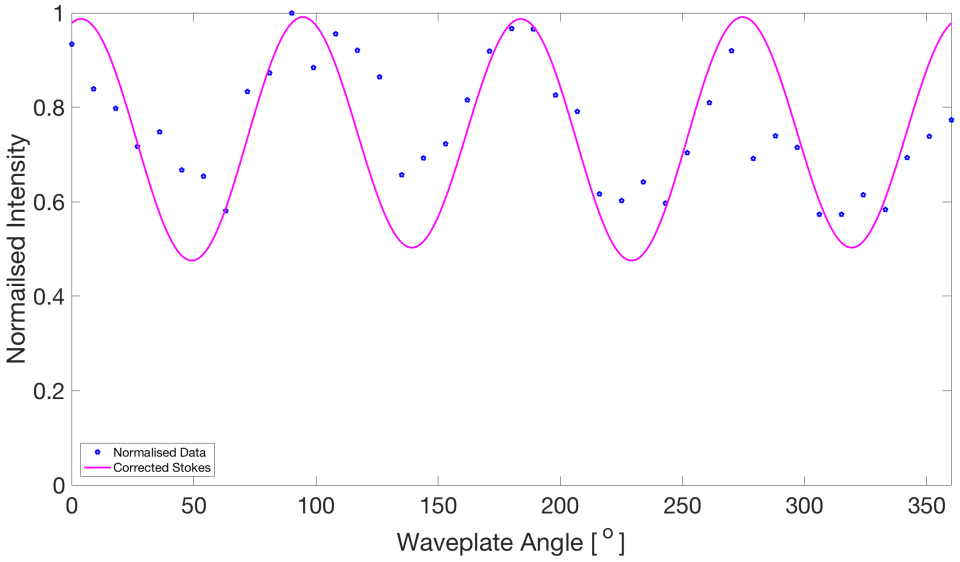

FIGURE 4.11: Normalised CQD intensity as a function of rotating QWP overlaid with modelled intensity from Stokes parameters.

the method used in our furthering of the polarisation study of the VCSEL. A QWP, fixed in a rotational mount, was placed into the setup directly behind the long pass filter and the polariser was set at 74^0 allowing for the maximum transmission of the laser emission to pass through (see figure 4.2). Without changing the linear polariser, the QWP was then rotated clockwise from 0^0 to 360^0 in increments of 10^0 with the addition of 45^0, 135^0, 225^0 and 315^0. This allows the calculation of the Stokes parameters for the CQD-VCSEL, figure 4.2b.

The optical intensity of the laser emission recorded is then normalised by the values of maximum intensity. Figure 4.11 shows the behaviour of emission as the QWP is passed through a complete rotation depicting a 90^0 ($\pi/2$) oscillatory period giving indication that the CQD-VCSEL structure is linearly polarised (scatter plot).

The Stokes parameters are extracted by fitting the data with:

$$I(\theta) = \frac{1}{2}(S_0 + S_1 cos^2 2\theta + S_2 cos2\theta sin2\theta + S_3 sin2\theta), \tag{4.19}$$

where S_0, S_1, S_2 and S_3 are the Stokes parameters, I is the intensity and θ is the rotational angle of the QWP. Using the techniques discussed in [95] trigonometric half-angled identities convert the intensity in equation 4.19 into truncated Fourier series, seen in equation 4.20.

$$I(\theta) = \frac{1}{2}(A + Bsin2\theta + Ccos4\theta + Dsin4\theta), \tag{4.20}$$

where

$$A = S_0 + \frac{S_1}{2} = \frac{2}{N}\sum_{n=1}^{N} I_n, \tag{4.21a}$$

$$B = S_3 = \frac{4}{N}\sum_{n=1}^{N} I_n sin2\theta, \tag{4.21b}$$

$$C = \frac{S_1}{2} = \frac{4}{N}\sum_{n=1}^{N} I_n cos4\theta, \tag{4.21c}$$

$$D = \frac{S_2}{2} = \frac{4}{N}\sum_{n=1}^{N} I_n sin4\theta. \tag{4.21d}$$

It results in three multiple angle harmonic terms coupled with a constant expression.

The standard (uncorrected) Stokes vector is built up, by rearranging, equation 4.19 giving

$$S = \begin{pmatrix} S_0 \\ S_1 \\ S_2 \\ S_3 \end{pmatrix}. \tag{4.22}$$

Taking possible coupled PL into account, which adds an unpolarised component to the elliptically polarised light, equation 4.22 becomes,

$$S = (1-P)S_{UNP} + PS_{ELP} \Rightarrow S = \begin{pmatrix} 1 \\ 0.55 \\ 0.17 \\ -0.02 \end{pmatrix} \left[S_{ELP} = \begin{pmatrix} 1.00 \\ 0.96 \\ 0.29 \\ -0.03 \end{pmatrix} \right], \tag{4.23}$$

where P is the degree of polarisation, S_{UNP} and S_{ELP} are the equivalent Stokes vectors of the unpolarised PL and the polarised emission contributions for the total intensity detected. Figure 4.11 displays the fit (from which the Stokes parameters are obtained) superimposed on top of the normalised spectra.

This fit transcribes well to the normalised data following the sinusoidal modulation giving validation of the linear polarisation with a period of 90^0 ($\pi/2$). The determined values of the Stoke vector, seen in equation 4.23, are also indicative of linear polarisation. Inserting these values into equation 4.16b it can be seen that the polarisation of the emission is at 82^0 from the vertical axes ($\psi = 8^0$ and is

measured from the x-axis), showing that the polarisation is not perfectly horizontal. The difference with the polarisation found in section 4.5.1 (115^0) is probably because the position of the excitation spot on the VCSEL is not the same.

The degree of polarisation (DOF) gives the percentage of how much of the overall emitted light is polarised and is obtained using the Stokes values via;

$$P = \frac{\sqrt{S_1^2 + S_2^2 + S_3^2}}{S_0} = \sqrt{S_1^2 + S_2^2 + S_3^2}. \tag{4.24}$$

For the operation observed in figure 4.11 the DOF can be calculated from the fit, given by equation 4.23, to be $P = 0.58$. Thus indicating that the PL contribution from the CQD-VCSEL has significant contribution as $P = 1$ if the emission was made up of entirely polarised light (only laser emission).

The VCSEL emission is thus linearly polarised, at least when optically-pumped with a linear polarisation. The polarisation was not found to be in the same direction as the pump. The polarisation is probably set by anisotropy in the laser cavity, caused by the CQD region itself - the elliptical excitation spot might also have a role.

4.5.2.3 Spin-polarised excitation

A linear polarisation state was observed from the CQD-VCSEL excited by a linearly polarised pump. Next, an additional QWP was inserted into the optical setup before the VCSEL to measure whether the VCSEL polarisation is dependent on the polarisation state of the pump. The additional QWP allows us to study of the VCSEL polarisation under excitation by, for example, a circularly polarised optical pump.

Let's look closer at the fine structure of the $1S_{3/2}$ - $1S_e$ band transitions of CQDs [96]. Figure 4.12b displays the eight excitation sub-states with lifted degeneracies where E_0^U and E_0^L represent the levels coupling to linearly-polarised radiation (in the z-axis direction of the crystal), E_L^U and E_L^L represent levels coupling to LCP and E_R^U and E_R^L represent levels coupling to RCP (U is for upper and L for lower). The dashed levels represent dark states, i.e. forbidden transition states that do not couple in principle to radiation. $|0>$, $|\uparrow>$ and $|\downarrow>$ are labels for each of the spin states. When the CQDs are excited via LCP the electron

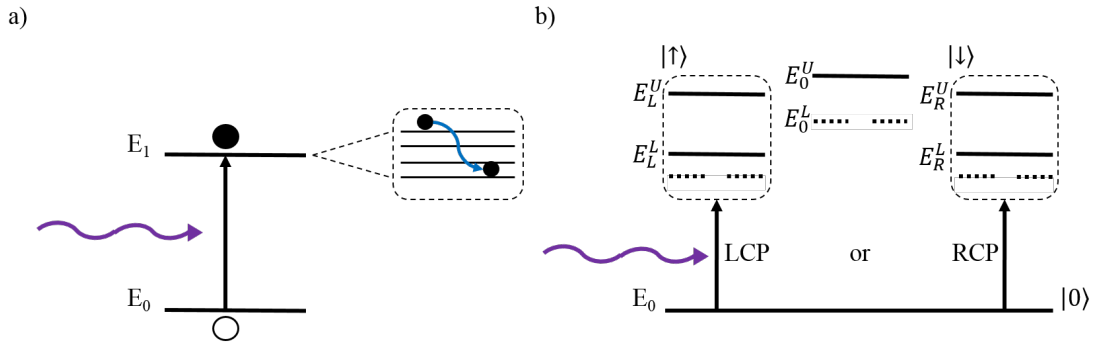

FIGURE 4.12: a) A two-level degenerate system with the conduction band splitting magnified. This shows the excited electron relaxing from a circularly polarised state into a linear polarised state before emission. b) $1S_{3/2}$ - $1S_e$ structure indicating the exciton pair dependence on polarisation. E_0^U and E_0^L represent the linear polarised levels, E_L^U and E_L^L represent LCP levels and E_R^U and E_R^L with RCP. $|0>$, $|\uparrow>$ and $|\downarrow>$ representative of the different polarisation outputs.

is excited into a LCP level. The same occurs with RCP excitation exciting the electron into a RCP level. The emitted photon would also follow this trend; where LCP absorption results in LCP emission, etc., unless decoherence of the spin states occurs before photon emission. Polarisation selective absorption however is dependent on the orientation of the CQDs. In a randomly distributed population (3D rotationally averaged) of CQDs, it is expected that a linear pump polarisation can excite all these different sub-levels. But is it possible to still preferentially bias the CQD population in the $|\uparrow>$ or $|\downarrow>$ using circularly-polarised pump in a 3D distribution of CQDs? Some reports in the literature seems to indicate that no [97], although the specificity of spin states can still be resolved in randomly oriented CQD distribution in non-linear optics experiments [97]. It is also known that in epitaxial VCSELs even a small difference in the population of spin-states can lead to a full spin-controlled laser emission, even when pumping out of resonance [98]. While the physics subtleties are relatively complicated, our aim here is simple: to assess if yes or no a spin-polarised laser emission can be obtained in our CQD-VCSEL through polarisation-controlled optical pumping. If that was the case, it could open up the study of CQD-based spin VCSELs. The additional QWP was also fixed in a rotational mount and was placed after the pump de-magnification and before the pump focusing lens.

Initially the angle of this QWP was set to zero degrees (along the vertical), exerting no phase change on the incoming optical pump beam, which therefore remains

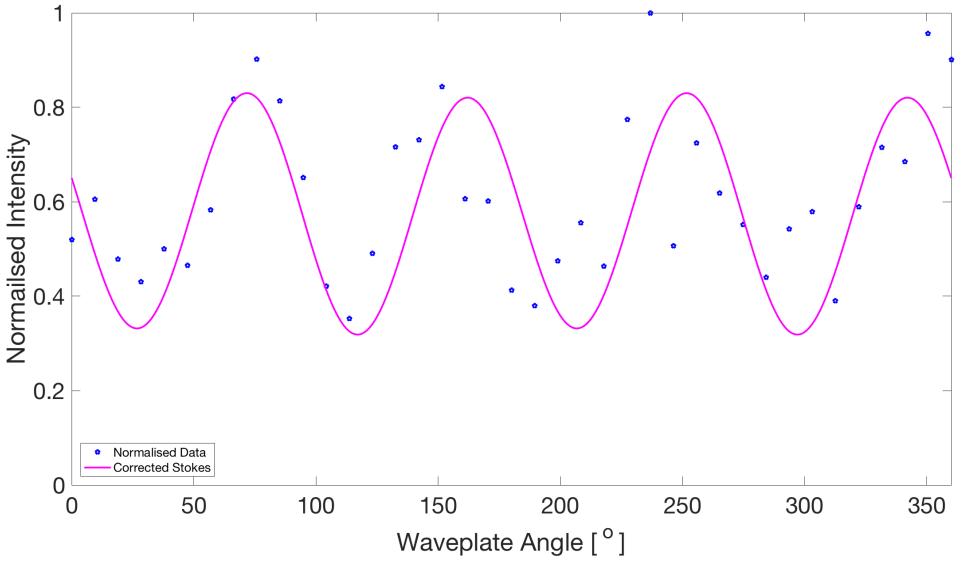

FIGURE 4.13: Normalised CQD intensity versus QWP angle with modelled intensity calculated from the corresponding Stokes parameters.

linearly horizontally polarised. The data was recorded using the same method and increments used previously, where the intensity was normalised by the maximum recorded value of intensity, figure 4.13. The scatter plot, as expected, follows the same oscillatory periodic function as previously.

Figure 4.13 displays the intensity as a function of QWP rotational angle where the Stokes vector has been calculated for the data analysis reveals preponderantly -45^0 polarisation. The shift from linear horizontal polarisation to preponderantly -45^0 polarisation is likely due to the shift in pump spot location. This would suggest that the polarisation of the VCSEL is set by the anisotropy of the CQD film; although this would warrant further studies in order to be 100% sure.

However, as can be seen by the oscillation period, the polarisation is still linear. The Stokes parameters were calculated as previous and resulted in a Stokes vector,

$$S = \begin{pmatrix} 1.00 \\ 0.17 \\ -0.53 \\ 0.01 \end{pmatrix} \left[S_{ELP} = \begin{pmatrix} 1.00 \\ 0.30 \\ -0.95 \\ 0.02 \end{pmatrix} \right]. \tag{4.25}$$

This Stokes vector differs from the previous measurement. There is no longer a linear horizontal polarisation but the value of S indicates a preponderantly linear -45^0 polarisation. Again this results in the observation of linear behaviour as is

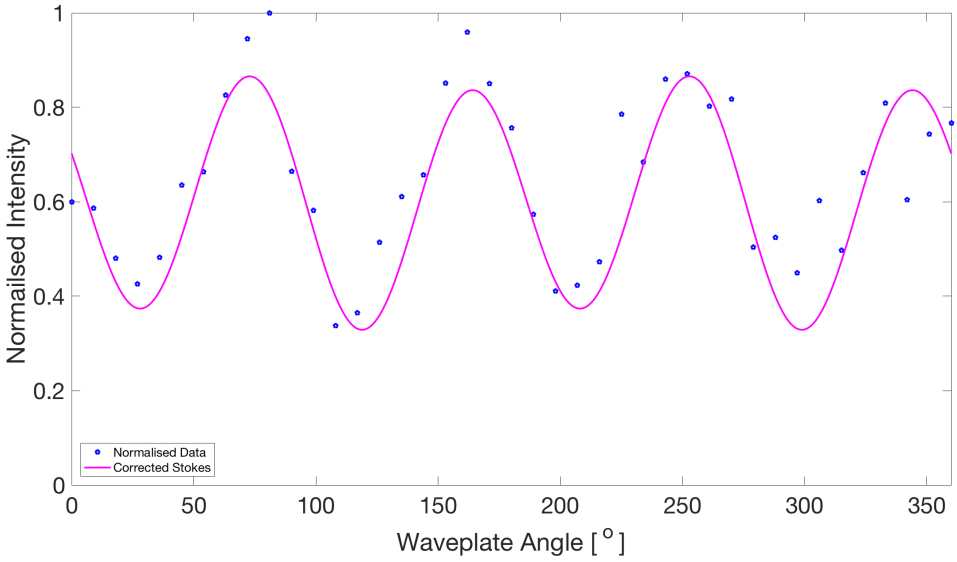

FIGURE 4.14: Normalised CQD intensity from LCP optical pump source versus QWP angle with modelled intensity calculated from the corresponding Stokes parameters.

expected from the previous study, section 4.5.2.2. The fit of this calculated Stokes parameter was again overlaid and as before fit the raw data well. The DOP is also calculated, equation 4.24, and for the fit $P = 0.56$ (again taking into account the PL contribution as well as pump fluctuations and probably slight multimodal behaviour causing some data points to spike).

Moving on from here, the new QWP was set to an angle of 315^0 (-45^0) to the QWP normal resulting in the optical pump beam being left circularly polarised (LCP). The same experimental procedure was followed as before and the Stokes parameters, fitted to the data and DOP calculated, figure 4.14. The Stokes vector is,

$$S = \begin{pmatrix} 1.00 \\ 0.32 \\ -0.73 \\ 0.04 \end{pmatrix} \left[S_{LCP} = \begin{pmatrix} 1.00 \\ 0.40 \\ -0.91 \\ 0.05 \end{pmatrix} \right], \tag{4.26}$$

and the DOP is calculated as $P = 0.79$ and fitted over the raw data, with $\psi = 123^0$ from the vertical. The same operation was observed as when the additional wave-plate had no phase change. The oscillation again indicating linear nature with the polarisation being preponderantly linear -45^0 as earlier.

The wave-plate was then set to an angle of 45^0 to the optical axis resulting in the incoming light being right circularly polarised (RCP). The same experimental

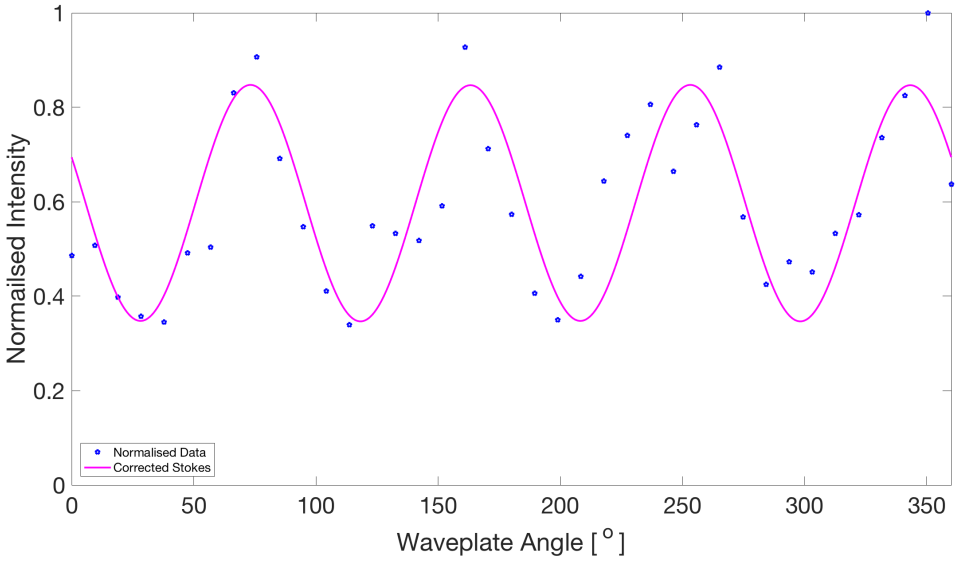

FIGURE 4.15: Normalised CQD intensity from RCP optical pump source versus QWP angle with modelled intensity calculated from the corresponding Stokes parameters at resolution of 0.13 nm.

procedure and calculations were performed where the Stokes vector was found to be,

$$S = \begin{pmatrix} 1.00 \\ 0.32 \\ -0.76 \\ 0.00 \end{pmatrix} \left[S_{RCP} = \begin{pmatrix} 1.00 \\ 0.39 \\ -0.92 \\ 0.00 \end{pmatrix} \right], \tag{4.27}$$

with is $P = 0.82$ with $\psi = 124^0$ from the vertical, again representing a preponderantly linear -45^0. Figure 4.15 displays the data and Stokes parameter fit.

The data demonstrates that when optically excited with either right or left circularly polarisation the CQD-VCSEL is still linearly polarised. This indicates that the pump polarisation does not affect the VCSEL polarisation. The latter is probably fixed by the cavity anisotropy. It also indicates that no spin states is favoured upon pumping or that if it is the states decohere (spin flip) rapidly. We note though that RCP and LCP pumping halved the unpolarised component compared to the linear pump (see equation 4.23). Spin excitation seems to affect the PL and this might warrant further investigation.

4.6 Conclusion

Solution processed alloyed-core/shell CdS_xSe_{1-x}/ZnS quantum dots have been exploited for the fabrication of a yellow-orange VCSEL, at wavelength ranges difficult to obtain with epitaxial technology. With a large 250 μm pump spot, highly multimodal laser emission was achieved with centre emission at 591.1 nm where through visually fine tuning displaying thresholds as low as 2.1 mJ/cm^2. The emission displayed spatio-temporal instabilities with the formation of spatially-localised beam akin to solitons. Single peak emission at 590.6 nm obtained in certain conditions was observed by reducing the excitation beam to 110 μm in radius with a threshold of 8.5 mJ/cm^2. The latter emission was linearly polarised. A study of polarisation-controlled excitation showed that the pump polarisation had no effect on the polarisation of the VCSEL emission but might have an effect on the PL.

Since this work, similar studies on solution processed VCSELs have been very recently reported on utilising Perovskite CQDs [73], however, the study reported in this thesis was completed before they were published. The CQD-VCSEL here was also excited using ns pulses, whereas [73] report on using fs excitation. Patel *et al*, also exploit the fs regime, opening CQD reseach into open cavity lasers utilising CdSe/CdS CQDs [99, 100]. Here they achieved single mode emission and the ability to fine tune the emission wavelength over a 25nm range by altering the cavity length. The paper also makes claim that colloidal NPs would improve performance due to their reduced Auger recombination rates and large emission cross-sections. However, the work presented in this thesis, to the authors best knowledge, detailing the polarisation studies of CQD VCSELs, section 4.5, has not been attempted/reported on by other groups; although similar work has been studied in single GaN nanowires [101].

References

[1] Jack L. Jewell, Y. H. Lee, J. P. Harbison, A. Scherer, and L. T. Florez. Vertical-Cavity Surface-Emitting Lasers: Design, Growth, Fabrication, Characterization. *IEEE Journal of Quantum Electronics*, 27(6):1332–1346, 1991. ISSN 15581713. doi: 10.1109/3.89950.

[2] P.M. Ilroy, Atsushi Kurobe, and Yutaka Uematsu. Analysis and application of theoretical gain curves to the design of multi-quantum-well lasers. *IEEE Journal of Quantum Electronics*, 21(12):1958–1963, dec 1985. ISSN 0018-9197. doi: 10.1109/JQE.1985.1072606. URL `http://ieeexplore.ieee.org/document/1072606/`.

[3] Haruhisa Soda, Ken-ichi Iga, Chiyuki Kitahara, and Yasuharu Suematsu. GaInAsP / InP Surface Emitting Injection Lasers. *Japanese Journal of Applied Physics*, 18(12):2329–2330, 1979.

[4] Kenichi Iga, Takayuki Nishimur, Katsumi Yagi, Takao Yamaguchi, and Tatsuhiko Niina. Room temperature pulsed oscillation of GaAlAs/GaAs surface emitting junction laser grown by MBE. *Japanese Journal of Applied Physics*, 25(6 R):924–925, 1986. ISSN 13474065. doi: 10.1143/JJAP.25.924.

[5] Fumio Koyama, Susumu Kinoshita, and Kenichi Iga. Room-temperature continuous wave lasing characteristics of a GaAs vertical cavity surface-emitting laser. *Applied Physics Letters*, 55(3):221–222, 1989. ISSN 00036951. doi: 10.1063/1.101913.

[6] J. M. Dallesasse and N. Holonyak. Native-oxide stripe-geometry AlxGa1-xAs-GaAs quantum well heterostructure lasers. *Applied Physics Letters*, 58(4):394–396, 1991. ISSN 00036951. doi: 10.1063/1.104645.

[7] D. L. Huffaker, D. G. Deppe, K. Kumar, and T. J. Rogers. Native-oxide defined ring contact for low threshold vertical-cavity lasers. *Applied Physics Letters*, 65(1):97–99, 1994. ISSN 00036951. doi: 10.1063/1.113087.

[8] K D Choquette, R P Schneider jr., K L Lear, and K M Geib. Low threshold voltage vertical-cavity lasers fabricated by Selective oxidation. *Electronics Letters*, 30(24):2043–2044, 1994. ISSN 00135194. doi: 10.1049/el:19941421.

[9] Michael H. MacDougal, P. Daniel Dapkus, Vasily Pudikov, Hanmin Zhao, and Gye Mo Yang. Ultralow threshold current vertical-cavity surface-emitting lasers with AlAs oxide-GaAs distributed Bragg reflectors. *IEEE Photonics Technology Letters*, 7(3):229–231, 1995. ISSN 10411135. doi: 10.1109/68.372729.

[10] K. L. Lear, K. D. Choquette, R.P. Schneider, S.P. Kilcoyne, and K.M. Geib. Selectively oxidised vertical cavity surface emitting lasers with 50% power conversion efficiency. *Electronic Letters*, 31(3):208–209, 1995. ISSN 0013-5194.

[11] Kent D. Choquette, K. L. Lear, R. P. Schneider, K. M. Geib, J. J. Figiel, and Robert Hull. Fabrication and performance of selectively oxidized vertical-cavity lasers. *IEEE Photonics Technology Letters*, 7(11):1237–1239, 1995. ISSN 10411135. doi: 10.1109/68.473457.

[12] Ebinazar B. Namdas, Minghong Tong, Peter Ledochowitsch, Sarah R. Mednick, Jonathan D. Yuen, Daniel Moses, and Alan J. Heeger. Low Thresholds in Polymer Lasers on Conductive Substrates by Distributed Feedback Nanoimprinting: Progress Toward Electrically Pumped Plastic Lasers. *Advanced Materials*, 21(7):799–802, feb 2009. ISSN 09359648. doi: 10.1002/adma.200802436. URL `http://doi.wiley.com/10.1002/adma.200802436`.

[13] J.L. Jewell, Y.H. Lee, S. Walker, A. Scherer, J.P. Harbison, L.T. Florez, and S.L. McCall. Low-threshold electrically pumped vertical-cavity surface-emitting microlasers. *Electronics Letters*, 25(17):1123–1124, 1989. ISSN 00135194. doi: 10.1049/el:19890754. URL `http://digital-library.theiet.org/content/journals/10.1049/el{_}19890754`.

[14] Yuh-shiuan Liu, A F M Saniul Haq, Karan Mehta, Tsung-ting Kao, Shuo Wang, Hongen Xie, Shyh-chiang Shen, P Douglas Yoder, Fernando A Ponce, Theeradetch Detchprohm, and Russell D Dupuis. Optically pumped vertical-cavity surface-emitting laser at 374.5nm with an electrically conducting n-DBR. *Applied Physics Express*, 9(11):1–4, 2016.

[15] Michael C.Y. Huang, Y. Zhou, and Connie J. Chang-Hasnain. A surface-emitting laser incorporating a high-index-contrast subwavelength grating. *Nature Photonics*, 1(5):297–297, 2007. ISSN 1749-4885. doi: 10.1038/nphoton.2007.73.

[16] Connie J. Chang-Hasnain. Tunable VCSEL. *IEEE Journal on Selected Topics in Quantum Electronics*, 6(6):978–987, 2000. ISSN 1077260X. doi: 10.1109/2944.902146.

[17] Weiyong Mao, Jia Guo, Wuli Yang, Changchun Wang, Jia He, and Jiyao Chen. Synthesis of high-quality near-infrared-emitting CdTeS alloyed quantum dots via the hydrothermal method. *Nanotechnology*, 18(48):485611, dec 2007. ISSN 0957-4484. doi: 10.1088/0957-4484/18/48/485611. URL `http://stacks.iop.org/0957-4484/18/i=48/a=485611?key=crossref.bc3a5ea18392a10b65bdabbbebbb5fd0`.

[18] Cheng Wang, Ravi Raghunathan, Kevin Schires, Sze-Chun Chan, Luke F. Lester, and Frédéric Grillot. Optically injected InAs/GaAs quantum dot laser for tunable photonic microwave generation. *Optics Letters*, 41(6):1153, mar 2016. ISSN 0146-9592. doi: 10.1364/OL.41.001153. URL `https://www.osapublishing.org/abstract.cfm?URI=ol-41-6-1153`.

[19] N.N. Ledentsov, A.R. Kovsh, A.E. Zhukov, N.A. Maleev, S.S. Mikhrin, A.P. Vasil'ev, E.S. Semenova, M.V. Maximov, Yu.M., Shemyakov, N.V Kryzhanovskaya, , VM. Ustinov, and D. Bimberg. High performance quantum dot lasers on GaAs substrates operating in 1.5 m range. *Electronics Letters*, 39(15):1126–1128, 2003.

[20] V.M Ustinov, A.E Zhukov, N.A Maleev, A.R Kovsh, S.S Mikhrin, B.V Volovik, Yu.G Musikhin, Yu.M Shernyakov, M.V Maximov, A.F Tsatsul'nikov, N.N Ledentsov, Zh.I Alferov, J.A Lott, and D Bimberg. 1.3μm InAs/GaAs quantum dot lasers and VCSELs grown by molecular beam epitaxy. *Journal of Crystal Growth*, 227-228:1155–1161, 2001. ISSN 00220248. doi: 10.1016/S0022-0248(01)01006-5. URL `http://www.sciencedirect.com/science/article/pii/S0022024801010065`.

[21] C Affolderbach, A Nagel, S Knappe, C Jung, D Wiedenmann, and R Wynands. Nonlinear spectroscopy with a vertical-cavity surface-emitting laser (VCSEL). *Applied Physics B: Lasers and Optics*, 70:407–413, 2000. ISSN 0946-2171. doi: 10.1007/s003400050066.

[22] T. Svensson, M. Andersson, L. Rippe, S. Svanberg, S. Andersson-Engels, J. Johansson, and S. Folestad. VCSEL-based oxygen spectroscopy for structural analysis of pharmaceutical solids. *Applied Physics B: Lasers and Optics*, 90(2):345–354, 2008. ISSN 09462171. doi: 10.1007/s00340-007-2901-6.

[23] Gurneesh Jatana, Sam Geckler, David Koeberlein, and William Partridge. Design and development of a probe-based multiplexed multi-species absorption spectroscopy sensor for characterizing transient gas-parameter distributions in the intake systems of I.C. engines. *Sensors and Actuators B: Chemical*, 240:1197–1204, 2017. ISSN 09254005. doi: 10.1016/j.snb.2016.08.183. URL `http://linkinghub.elsevier.com/retrieve/pii/S0925400516314162`.

[24] Benjamin Kögel, Hubert Halbritter, Sandro Jatta, Markus Maute, Gerhard Böhm, Markus Christian Amann, Maximilian Lackner, Michael Schwarzott, Franz Winter, and Peter Meissner. Simultaneous spectroscopy of NH3 and CO using a $>$ 50 nm continuously tunable MEMS-VCSEL. *IEEE Sensors Journal*, 7(11):1483–1488, 2007. ISSN 1530437X. doi: 10.1109/JSEN.2007.907055.

[25] Takehiko Tawara, Hideki Gotoh, Tetsuya Akasaka, Naoki Kobayashi, and Tadashi Saitoh. Low-threshold lasing of InGaN vertical-cavity surface-emitting lasers with dielectric distributed Bragg reflectors. *Applied Physics Letters*, 83(5):830–832, 2003. ISSN 00036951. doi: 10.1063/1.1596728.

[26] Y.-K. Song, H. Zhou, M. Diagne, A. V. Nurmikko, R. P. Schneider, C. P. Kuo, M. R. Krames, R. S. Kern, C. Carter-Coman, and F. A. Kish. A quasicontinuous wave, optically pumped violet vertical cavity surface emitting laser. *Applied Physics Letters*, 76(13): 1662, 2000. ISSN 00036951. doi: 10.1063/1.126128. URL `http://scitation.aip.org/content/aip/journal/apl/76/13/10.1063/1.126128`.

[27] Karin Hedsten, Jordi Fonollosa, Peter Enoksson, Peter Modh, Jörgen Bengtsson, Duncan S. Sutherland, and Alexandre Dmitriev. Optical label-free nanoplasmonic biosensing using a vertical-cavity surface-emitting laser and charge-coupled device. *Analytical Chemistry*, 82(4):1535–1539, 2010. ISSN 00032700. doi: 10.1021/ac9025169.

[28] Tatevik Chalyan, Laura Pasquardini, Davide Gandolfi, Romain Guider, Alina Samusenko, Manuela Zanetti, Georg Pucker, Cecilia Pederzolli, and Lorenzo Pavesi. Aptamer- and

Fab'- Functionalized Microring Resonators for Aflatoxin M1 Detection. *IEEE Journal of Selected Topics in Quantum Electronics*, 23(2):350–357, mar 2017. ISSN 1077-260X. doi: 10.1109/JSTQE.2016.2609100. URL `http://ieeexplore.ieee.org/document/7565645/`.

[29] Ahmed Al-Samaneh, Marwan Bou Sanayeh, Wolfgang Schwarz, Dietmar Wahl, and Rainer Michalzik. Vertical-cavity lasers for miniaturized atomic clocks. *SPIE Newsroom*, (100): 10–12, 2011. doi: 10.1117/2.1201108.003824.

[30] M. Schreck, F. Hörmann, H. Roll, J. K N Lindner, and B. Stritzker. Diamond nucleation on iridium buffer layers and subsequent textured growth: A route for the realization of single-crystal diamond films. *Applied Physics Letters*, 78(2):192–194, 2001. ISSN 00036951. doi: 10.1063/1.1337648.

[31] Moonsang Lee, Dmitry Mikulik, and Sungsoo Park. Thick GaN growth via GaN nanodot formation by HVPE. *CrystEngComm*, (0001), 2017. ISSN 1466-8033. doi: 10.1039/C6CE02125E. URL `http://xlink.rsc.org/?DOI=C6CE02125E`.

[32] Richard Nötzel, Klaus H Ploog, Jiang Wu, Siming Chen, Alwyn Seeds, Klaus H Ploog, and Richard Nötzel. Self-organized growth of quantum-dot structures. *Semiconductor Science and Technology*, 11(10), 1996.

[33] R. S. Wagner and W. C. Ellis. Vapor-liquid-solid mechanism of single crystal growth. *Applied Physics Letters*, 4(5):89–90, 1964. ISSN 00036951. doi: 10.1063/1.1753975.

[34] John Simon, Kevin L Schulte, Nikhil Jain, Michelle Young, Matthew R Young, David L Young, and Aaron J Ptak. Upright and Inverted Single Junction GaAs Solar Cells Grown by Hydride Vapor Phase Epitaxy. *Proceedings of the 43rd IEEE Photovoltaics Specialists Conference*, 7(1):4–7, 2016. doi: 10.1109/JPHOTOV.2016.2614122.

[35] A. Kębłowski, M. Kopytko, K. Młynarczyk, W. Gawron, J. Piotrowski, P. Martyniuk, and A. Rogalski. Investigation of hillocks formation on (100) HgCdTe layers grown by MOCVD on GaAs epi-ready substrates. *Infrared Physics & Technology*, pages 1–7, 2017. ISSN 13504495. doi: 10.1016/j.infrared.2017.01.004. URL `http://linkinghub.elsevier.com/retrieve/pii/S1350449516303991`.

[36] A. J. Ptak, D. J. Friedman, and S. W. Johnston. A comparison of MBE- and MOCVD-grown InGaAsN. *MBE 2002 - 2002 12th International Conference on Molecular Beam Epitaxy*, 251:291–292, 2002. ISSN 00220248. doi: 10.1109/MBE.2002.1037874.

[37] Nikolai N. Ledentsov, M. Grundmann, F. Heinrichsdorff, Dieter Bimberg, V. M. Ustinov, A. E. Zhukov, M. V. Maximov, Zh I. Alferov, and J. A. Lott. Quantum-dot heterostructure lasers. *IEEE Journal on Selected Topics in Quantum Electronics*, 6(3):439–451, 2000. ISSN 1077260X. doi: 10.1109/2944.865099.

[38] Feng Gao, Shuai Luo, Hai-Ming Ji, Song-Tao Liu, Dan Lu, Chen Ji, and Tao Yang. Single-section mode-locked 1.55-μm InAs/InP quantum dot lasers grown by MOVPE. *Optics*

Communications, 370:18–21, 2016. ISSN 00304018. doi: 10.1016/j.optcom.2016.02.061. URL http://linkinghub.elsevier.com/retrieve/pii/S0030401816301535.

[39] Supachok Thainoi, Suwit Kiravittaya, Thanavorn Poempool, Zon, Noppadon Nuntawong, Suwat Sopitpan, Songphol Kanjanachuchai, Somchai Ratanathammaphan, and Somsak Panyakeow. Molecular beam epitaxy growth of InSb/GaAs quantum nanostructures. *Journal of Crystal Growth*, (November 2016):1–4, 2017. ISSN 00220248. doi: 10.1016/j.jcrysgro.2017.01.011. URL http://linkinghub.elsevier.com/retrieve/pii/S0022024817300179.

[40] Bin Li, Yipu Xia, Wingkin Ho, and Maohai Xie. Suspended Ga2Se3 film and epitaxial Bi2Se3(221) on GaSb(001) by molecular-beam epitaxy. *Journal of Crystal Growth*, 459 (November 2016):76–80, 2017. ISSN 00220248. doi: 10.1016/j.jcrysgro.2016.11.057. URL http://linkinghub.elsevier.com/retrieve/pii/S0022024816307461.

[41] Andrew R Barron. Molecular Beam Epitaxy. (100):1–7. ISSN 00368075. doi: 10.1016/B978-0-12-387839-7.00029-4.

[42] J Hegarty. GaAs-AIGaAs DFB. *Electronics Letters*, 32(3):219–221, 1996.

[43] P. Zhou, Julian Cheng, C. F. Schaus, S. Z. Sun, K. Zheng, E. Armour, C. Hains, Wei Hsin, D. R. Myers, and G. A. Vawter. Low series resistance high-efficiency GaAs/AlGaAs vertical-cavity surface-emitting lasers with continuously graded mirrors grown by MOCVD. *IEEE Photonics Technology Letters*, 3(7):591–593, 1991. ISSN 10411135. doi: 10.1109/68.87923.

[44] Y. Qian, Z. H. Zhu, Y. H. Lo, D. L. Huffaker, D. G. Deppe, H. Q. Hou, B. E. Hammons, W. Lin, and Y. K. Tu. Long wavelength (1.3 μm) vertical-cavity surface-emitting lasers with a wafer-bonded mirror and an oxygen-implanted confinement region. *Applied Physics Letters*, 71(1):25, 1997. ISSN 00036951. doi: 10.1063/1.119459. URL http://scitation.aip.org/content/aip/journal/apl/71/1/10.1063/1.119459.

[45] Stephane Calvez, Jennifer E. Hastie, Mircea Guina, Oleg G. Okhotnikov, and Martin D. Dawson. Semiconductor disk lasers for the generation of visible and ultraviolet radiation. *Laser and Photonics Reviews*, 3(5):407–434, 2009. ISSN 18638880. doi: 10.1002/lpor.200810042.

[46] M. Weyers and A. Knigge, M. Zorn, H. Wenzel and G. Trankle. High efficiency AIGalnP-based 650 nm vertical-cavity surface-emitting lasers. *Electronic Letters*, 37(20):1222–1223, 2001.

[47] R. P. Schneider, M. Hagerott Crawford, K. D. Choquette, K. L. Lear, S. P. Kilcoyne, and J. J. Figiel. Improved AlGaInP-based red (670-690 nm) surface-emitting lasers with novel C-doped short-cavity epitaxial design. *Applied Physics Letters*, 67:329, 1995. ISSN 00036951. doi: 10.1063/1.115434.

[48] Eli Kapon and Alexei Sirbu. Power-efficient answer. *Nat. Photonics*, vol(January):27–29, 2009. ISSN 1749-4885. doi: 10.1038/nphoton.2008.266.

[49] V. Jayaraman, T. J. Goodnough, T. L. Beam, F. M. Ahedo, and R. A. Maurice. Continuous-wave operation of single-transverse-mode 1310-nm VCSELs up to 115oC. *IEEE Photonics Technology Letters*, 12(12):1595–1597, 2000. ISSN 10411135. doi: 10.1109/68.896318.

[50] Alexandru Mereuta, Vladimir Iakovlev, Andrei Caliman, Alexei Syrbu, Senior Member, Paul Royo, Alok Rudra, and Eli Kapon. In(Al)GaAs AlGaAs Wafer Fused VCSELs Emitting at 2-m Wavelength. *Technology*, 20(1):24–26, 2008.

[51] Kenichi Iga. Surface-emitting laser - Its birth and generation of new optoelectronics field. *IEEE Journal on Selected Topics in Quantum Electronics*, 6(6):1201–1215, 2000. ISSN 1077260X. doi: 10.1109/2944.902168.

[52] D Feezell, D.A. Buell, and L.A. Coldren. InP-Based 1.31.6m VCSELs With Selectively Etched Tunnel-Junction Apertures on a Wavelength Flexible Platform. *IEEE Photonics Technology Letters*, 17(10):2017–2019, oct 2005. ISSN 1041-1135. doi: 10.1109/LPT.2005.854357. URL `http://ieeexplore.ieee.org/document/1512258/`.

[53] Theeradetch Detchprohm, Yuh-Shiuan Liu, Karan Mehta, Shuo Wang, Hongen Xie, Tsung-Ting Kao, Shyh-Chiang Shen, Paul D Yoder, Fernando A Ponce, and Russell D Dupuis. Sub 250 nm deep-UV AlGaN/AlN distributed Bragg reflectors. *Citation: Appl. Phys. Lett*, 110, 2017. ISSN 00036951. doi: 10.1063/1.4973581. URL `http://dx.doi.org/10.1063/1.4973581{%}0Ahttp://aip.scitation.org/toc/apl/110/1`.

[54] S. Kalusniak, S. Sadofev, S. Halm, and F. Henneberger. Vertical cavity surface emitting laser action of an all monolithic ZnO-based microcavity. *Applied Physics Letters*, 98(1), 2011. ISSN 00036951. doi: 10.1063/1.3533800.

[55] H Jeon, V Kozlov, P Kelkar, A V Nurmikko, D C Grillo, J Han, G C Hua, and R L Gunshor. Room-temperature optically pumped blue-green vertical cavity surface emitting laser. 67(12):1668–1670, 2001. ISSN 0003-6951. doi: 10.1063/1.115051.

[56] P. D. Floyd, J. L. Merz, H. Luo, J. K. Yamada, Yokogawa Yoichi, and Furdyna Toshiya. Optically pumped blue-green vertical cavity surface emitting lasers. *Electronics Letters*, 31(2):106, 1995. ISSN 00135194. doi: 10.1049/el:19950075. URL `http://link.aip.org/link/ELLEAK/v31/i2/p106/s1{&}Agg=doi`.

[57] Daiji Kasahara, Daisuke Morita, Takao Kosugi, Kyosuke Nakagawa, Jun Kawamata, Yu Higuchi, Hiroaki Matsumura, and Takashi Mukai. Demonstration of blue and green GaN-based vertical-cavity surface-emitting lasers by current injection at room temperature. *Applied Physics Express*, 4(7), 2011. ISSN 18820778. doi: 10.1143/APEX.4.072103.

[58] Guoen Weng and Mike Cooke. Yellow-green indium gallium nitride quantum dot laser. 11 (6):60–61, 2016.

[59] Guoen Weng, Yang Mei, Jianping Liu, Werner Hofmann, Leiying Ying, Jiangyong Zhang, Yikun Bu, Zengcheng Li, and Baoping Zhang. Low threshold continuous-wave lasing of yellow-green InGaN-QD vertical-cavity surface-emitting lasers. 24(14):15546–15553, 2016.

[60] Hung Hsun Huang and Yuh Renn Wu. Light emission polarization properties of semipolar InGaN/GaN quantum well. *Journal of Applied Physics*, 107(5), 2010. ISSN 00218979. doi: 10.1063/1.3327794.

[61] Mohammed Nadir. Characterization of GaN-based Quantum Dots within Vertical-Cavity Surface-Emitting Lasers for realizing Green Lasers by Simulations. pages 161–162, 2016.

[62] Elaine Taylor, Paul R. Edwards, and Robert W. Martin. Colorimetry and efficiency of white LEDs: Spectral width dependence. *Physica Status Solidi (A) Applications and Materials Science*, 209(3):461–464, 2012. ISSN 18626300. doi: 10.1002/pssa.201100449.

[63] J Simon, N T Pelekanos, C Adelmann, E Martinez-Guerrero, R Andre, B Daudin, L S Dang, and H Mariette. Direct comparison of recombination dynamics in cubic and hexagonal GaN/AlN quantum dots. *Physical Review B*, 68(3):35312, 2003. ISSN 0163-1829. doi: 10.1103/PhysRevB.68.035312. URL `http://prb.aps.org/abstract/PRB/v68/i3/e035312{%}5Cnpapers2://publication/doi/10.1103/PhysRevB.68.035312`.

[64] P Waltereit, O Brandt, A Trampert, HT T Grahn, J Menniger, M Ramsteiner, M Reiche, and KH H Ploog. Nitride semiconductors free of electrostatic fields for efficient white light-emitting diodes. *Nature*, 406(6798):865–868, 2000. ISSN 1476-4687. doi: 10.1038/35022529.

[65] Yu Higuchi, Kunimichi Omae, Hiroaki Matsumura, and Takashi Mukai. Room-temperature CW lasing of a GaN-based vertical-cavity surface-emitting laser by current injection. *Applied Physics Express*, 1(12):1211021–1211023, 2008. ISSN 18820778. doi: 10.1143/APEX.1.121102.

[66] Wen Jie Liu, Xiao Long Hu, Lei Ying Ying, Jiang Yong Zhang, and Bao Ping Zhang. Room temperature continuous wave lasing of electrically injected GaN-based vertical cavity surface emitting lasers. *Applied Physics Letters*, 104(25):1–5, 2014. ISSN 00036951. doi: 10.1063/1.4885384. URL `http://dx.doi.org/10.1063/1.4885384`.

[67] Kunimichi Omae, Yu Higuchi, Kyosuke Nakagawa, Hiroaki Matsumura, and Takashi Mukai. Improvement in lasing characteristics of GaN-based vertical-cavity surface-emitting lasers fabricated using a GaN substrate. *Applied Physics Express*, 2(5), 2009. ISSN 18820778. doi: 10.1143/APEX.2.052101.

[68] Yang Mei, Guo-En Weng, Bao-Ping Zhang, Jian-Ping Liu, Werner Hofmann, Lei-Ying Ying, Jiang-Yong Zhang, Zeng-Cheng Li, Hui Yang, and Hao-Chung Kuo. Quantum dot vertical-cavity surface-emitting lasers covering the green gap'. *Light: Science & Applications*, 6(1):e16199, 2016. ISSN 2047-7538. doi: 10.1038/lsa.2016.199. URL `http://www.nature.com/doifinder/10.1038/lsa.2016.199`.

[69] Cuong Dang and Arto Nurmikko. Beyond quantum dot LEDs: Optical gain and laser action in red, green, and blue colors. *MRS Bulletin*, 38(09):737–742, 2013. ISSN 0883-7694. doi: 10.1557/mrs.2013.183. URL `http://www.journals.cambridge.org/abstract{_}S0883769413001838`.

[70] Cuong Dang, Joonhee Lee, Craig Breen, Jonathan S. Steckel, Seth Coe-Sullivan, and Arto Nurmikko. Red, green and blue lasing enabled by single-exciton gain in colloidal quantum dot films. *Nature Nanotechnology*, 7(5):335–339, apr 2012. ISSN 1748-3387. doi: 10.1038/nnano.2012.61. URL http://www.ncbi.nlm.nih.gov/pubmed/22543426http://www.nature.com/doifinder/10.1038/nnano.2012.61.

[71] N. Valappil, M. Luberto, V. M. Menon, I. Zeylikovich, T. K. Gayen, J. Franco, B. B. Das, and R. R. Alfano. Solution processed microcavity structures with embedded quantum dots. *Photonics and Nanostructures - Fundamentals and Applications*, 5(4):184–188, 2007. ISSN 15694410. doi: 10.1016/j.photonics.2007.07.003.

[72] Burak Guzelturk, Yusuf Kelestemur, Kivanc Gungor, Aydan Yeltik, Mehmet Zafer Akgul, Yue Wang, Rui Chen, Cuong Dang, Handong Sun, and Hilmi Volkan Demir. Stable and Low-Threshold Optical Gain in CdSe/CdS Quantum Dots: An All-Colloidal Frequency Up-Converted Laser. *Advanced Materials*, 27(17):2741–2746, 2015. ISSN 09359648. doi: 10.1002/adma.201500418. URL http://doi.wiley.com/10.1002/adma.201500418.

[73] Yue Wang, Xiaoming Li, Venkatram Nalla, Haibo Zeng, and Handong Sun. Solution-Processed Low Threshold Vertical Cavity Surface Emitting Lasers from All-Inorganic Perovskite Nanocrystals. *Advanced Functional Materials*, 201605088:1605088, 2017. ISSN 1616301X. doi: 10.1002/adfm.201605088. URL http://doi.wiley.com/10.1002/adfm.201605088.

[74] Oussama Mhibik, Sébastien Chénais, Sébastien Forget, Christophe Defranoux, and Sébastien Sanaur. Inkjet-printed vertically emitting solid-state organic lasers. *Journal of Applied Physics*, 119(17):173101, 2016. ISSN 0021-8979. doi: 10.1063/1.4946826. URL http://scitation.aip.org/content/aip/journal/jap/119/17/10.1063/1.4946826.

[75] Kannatassen Appavoo, Xiaoze Liu, Vinod Menon, and Matthew Y. Sfeir. Excitonic Lasing in Solution-Processed Subwavelength Nanosphere Assemblies. *Nano Letters*, 16(3):2004–2010, 2016. ISSN 15306992. doi: 10.1021/acs.nanolett.5b05274.

[76] V. M. Menon, M. Luberto, N. V. Valappil, and S. Chatterjee. Lasing from InGaP quantum dots in a spin-coated flexible microcavity. *Optics Express*, 16(24):19535, nov 2008. ISSN 1094-4087. doi: 10.1364/OE.16.019535. URL http://www.ncbi.nlm.nih.gov/pubmed/19030039https://www.osapublishing.org/oe/abstract.cfm?uri=oe-16-24-19535.

[77] Young Shin Park, Wan Ki Bae, Jeffrey M. Pietryga, and Victor I. Klimov. Auger recombination of biexcitons and negative and positive trions in individual quantum dots. *ACS Nano*, 8(7):7288–7296, 2014. ISSN 1936086X. doi: 10.1021/nn5023473.

[78] Hans Jürgen Eisler, Vikram C. Sundar, Moungi G. Bawendi, Michael Walsh, Henry I. Smith, and Victor Klimov. Color-selective semiconductor nanocrystal laser. *Applied Physics Letters*, 80(24):4614–4616, 2002. ISSN 00036951. doi: 10.1063/1.1485125.

[79] Yujie Chen, Benoit Guilhabert, Johannes Herrnsdorf, Yanfeng Zhang, Allan R. Mackintosh, Richard a. Pethrick, Erdan Gu, Nicolas Laurand, and Martin D. Dawson. Flexible distributed-feedback colloidal quantum dot laser. *Applied Physics Letters*, 99(24):

241103, 2011. ISSN 00036951. doi: 10.1063/1.3659305. URL http://scitation.aip.org/content/aip/journal/apl/99/24/10.1063/1.3659305.

[80] A. V. Malko, A. A. Mikhailovsky, M. A. Petruska, J. A. Hollingsworth, H. Htoon, M. G. Bawendi, and V. I. Klimov. From amplified spontaneous emission to microring lasing using nanocrystal quantum dot solids. *Applied Physics Letters*, 81(7):1303, 2002. ISSN 00036951. doi: 10.1063/1.1497708. URL http://scitation.aip.org/content/aip/journal/apl/81/7/10.1063/1.1497708.

[81] Burak Guzelturk, Yusuf Kelestemur, Murat Olutas, Savas Delikanli, and Hilmi Volkan Demir. Amplified Spontaneous Emission and Lasing in Colloidal Nanoplatelets. *ACS Nano*, 8(7):6599–6605, jul 2014. ISSN 1936-0851. doi: 10.1021/nn5022296. URL http://pubs.acs.org/doi/abs/10.1021/nn5022296.

[82] Max Born and Emil Wolf. *Principles of Optics*. 7th edition, 1999. ISBN 9780521642224. doi: 10.1080/713826373.

[83] Shun Lien Chuang. *Physics of Photonic Devices*. John Wiley & Sons Inc, 2nd edition, 2009. ISBN 9788578110796. doi: 10.1017/CBO9781107415324.004.

[84] Stephane Barland, Jorge R Tredicce, Massimo Brambilla, Luigi a Lugiato, Salvador Balle, Massimo Giudici, Tommaso Maggipinto, Lorenzo Spinelli, Giovanna Tissoni, Thomas Knödl, Michael Miller, and Roland Jäger. Cavity solitons as pixels in semiconductor microcavities. *Nature*, 419(6908):699–702, 2002. ISSN 0028-0836. doi: 10.1038/nature01049. URL http://www.nature.com/nature/journal/v419/n6908/abs/nature01049.html{%}5Cnhttp://www.ncbi.nlm.nih.gov/pubmed/12384692.

[85] K. Thyagarajan and Ajoy Ghatak. *Lasers: Fundamentals and Applications*. Springer, 2nd edition, 2010. ISBN 9788578110796. doi: 10.1017/CBO9781107415324.004.

[86] Frank Träger. *Springer Handbook of Laser and optics*. Springer, 2nd edition, 2012. ISBN 9788578110796. doi: 10.1017/CBO9781107415324.004.

[87] M. Marconi, J. Javaloyes, S. Barland, S. Balle, and M. Giudici. Vectorial dissipative solitons in vertical-cavity surface-emitting lasers with delays. *Nature Photonics*, 9(7):450–455, 2015. ISSN 1749-4885. doi: 10.1038/nphoton.2015.92. URL http://www.nature.com/doifinder/10.1038/nphoton.2015.92.

[88] Ph Grelu, S. Chouli, J. M. Soto-Crespo, W. Chang, A. Ankiewicz, and N. Akhmediev. Dissipative solitons for mode-locked fiber lasers. *2010 Photonics Global Conference, PGC 2010*, 6(February), 2010. ISSN 1749-4885. doi: 10.1109/PGC.2010.5706017.

[89] F. Prati, G. Tissoni, C. McIntyre, and G. L. Oppo. Static and dynamic properties of cavity solitons in VCSELs with optical injection. *European Physical Journal D*, 59(1):139–147, 2010. ISSN 14346060. doi: 10.1140/epjd/e2010-00128-2.

[90] Tobias Schemmelmann, Felix Tabbert, Alexander Pimenov, Andrei G. Vladimirov, and Svetlana V. Gurevich. Delayed feedback control of self-mobile cavity solitons in a wide-aperture laser with a saturable absorber. pages 1–10, 2017. URL http://arxiv.org/abs/1704.08869.

[91] Xavier Hachair, Francesco Pedaci, Emilie Caboche, Stphane Barland, Massimo Giudici, J. R. Tredicce, Franco Prati, Giovanna Tissoni, Reza Kheradmand, Luigi A. Lugiato, Igor Protsenko, and Massimo Brambilla. Cavity solitons in a driven VCSEL above threshold. *IEEE Journal on Selected Topics in Quantum Electronics*, 12(3):339–350, 2006. ISSN 1077260X. doi: 10.1109/JSTQE.2006.872711.

[92] F. Prati, P. Caccia, G. Tissoni, L. A. Lugiato, K. Mahmoud Aghdami, and H. Tajalli. Effects of carrier radiative recombination on a VCSEL-based cavity soliton laser. *Applied Physics B: Lasers and Optics*, 88(3):405–410, 2007. ISSN 09462171. doi: 10.1007/s00340-007-2711-x.

[93] M. Sich, D. N. Krizhanovskii, M. S. Skolnick, A. V. Gorbach, R. Hartley, D. V. Skryabin, E. A. Cerda-Méndez, K. Biermann, R. Hey, and P. V. Santos. Observation of bright polariton solitons in a semiconductor microcavity. *Nature Photonics*, 6(1):50–55, 2011. ISSN 1749-4885. doi: 10.1038/nphoton.2011.267. URL http://www.nature.com/doifinder/10.1038/nphoton.2011.267.

[94] S. Barland, M. Brambilla, L. Columbo, L. Furfaro, M. Giudici, X. Hachair, R. Kheradmand, L. a. Lugiato, T. Maggipinto, G. Tissoni, and J. Tredicce. Cavity solitons in a VCSEL: reconfigurable micropixel arrays. *Europhysics News*, 34(4):136–139, 2003. ISSN 0531-7479. doi: 10.1051/epn:2003403. URL http://www.europhysicsnews.org/10.1051/epn:2003403.

[95] Beth Schaefer, Edward Collett, Robert Smyth, Daniel Barrett, and Beth Fraher. Measuring the Stokes polarization parameters. *American Journal of Physics*, 75(2):163–168, feb 2007. ISSN 0002-9505. doi: 10.1119/1.2386162. URL http://link.aip.org/link/AJPIAS/v75/i2/p163/s1{&}Agg=doihttp://aapt.scitation.org/doi/10.1119/1.2386162.

[96] G D Scholes and D L Andrews. Resonance energy transfer and quantum dots. *Phys. Rev. B*, 72(12):125331, 2005. ISSN 1098-0121. doi: 10.1103/PhysRevB.72.125331.

[97] Gregory D. Scholes. Selection rules for probing biexcitons and electron spin transitions in isotropic quantum dot ensembles. *Journal of Chemical Physics*, 121(20):10104–10110, 2004. ISSN 00219606. doi: 10.1063/1.1808414.

[98] Feng Kuo Hsu, Wei Xie, Yi Shan Lee, Sheng Di Lin, and Chih Wei Lai. Ultrafast spin-polarized lasing in a highly photoexcited semiconductor microcavity at room temperature. *Physical Review B - Condensed Matter and Materials Physics*, 91(19):1–15, 2015. ISSN 1550235X. doi: 10.1103/PhysRevB.91.195312.

[99] Robin K Patel, Aurélien A P Trichet, David M Coles, Philip R Dolan, Simon M Fairclough, Edman Tsang, Marina A Leontiadou, David J Binks, Eunjoo Jang, Hyosook

Jang, Robert A Taylor, Sotiris Christodoulou, Iwan Moreels, and Jason M Smith. Gain Spectroscopy and Tunable Single Mode Lasing of Solution-Based Quantum Dots and Nanoplatelets Using Tunable Open Microcavities. In *Lasers and Electro-Optics*, pages 4–5, 2016. ISBN 9781943580118. doi: 10.1002/adom.201500363.

[100] Robin K Patel, Aurélien A P Trichet, David M Coles, Philip R Dolan, Simon M Fairclough, Marina A Leontiadou, S C Edman Tsang, David J Binks, Eunjoo Jang, Hyosook Jang, Robert A Taylor, and Jason M Smith. Gain Spectroscopy of Solution-Based Semiconductor Nanocrystals in Tunable Optical Microcavities. *Advanced Optical Materials*, 4(2):285–290, 2016. ISSN 2195-1071. doi: 10.1002/adom.201500363. URL `http://dx.doi.org/10.1002/adom.201500363`.

[101] A. Hurtado, H. Xu, J. B. Wright, Sheng Liu, Q. Li, G. T. Wang, T. S. Luk, J. J. Figiel, K. Cross, G. Balakrishnan, L. F. Lester, and I. Brener. Polarization switching in GaN nanowire lasers. *Applied Physics Letters*, 103(25), 2013. ISSN 00036951. doi: 10.1063/1.4835115.

Chapter 5

Organic semiconductor lasers

This chapter reports on studies of two types of organic semiconductor materials for use in solution-processed lasers. The first part of the chapter focuses on the polymer "Super Yellow", polyphenylenevinylene (PPV), (SY), usually used in OLEDs, with the demonstration of DFB lasers in ambient conditions and when immersed in polar solvents. The motivation behind these experiments was to explore the possibility for DFB laser biosensing; a priori, SY has some attractive properties for such application. However, challenges of SY lasers for sensing were found and highlighted. DFB lasers encapsulated with PVA, spin-on glass and parylene (a bio-compatible barrier polymer) are also demonstrated. The second part of the chapter deals with newly designed and synthesised oligofluorene based macromolecules, Blue 4 and Blue 6. These are light-emitting molecules with sizes similar to CQDs. ASE with random laser phenomena is shown in thin-films of these new organic materials. A DFB laser made with Blue 4 is also demonstrated.

5.1 Introduction

With the previous sections of this thesis concentrating on inorganic semiconducting nanocrystals, this part delves into the exploration of nanostructured organic semiconductors (OSs) for laser applications. OSs are also solution based processable [1–5], allow mechanically-flexible formats of devices [6, 7] and have application in biochemical analysis [8, 9]. Regrettably, OSs are prone to degradation effects [3], in particularly thermal and photodegradation, which can limit their use in

some applications [10–20]. These issues can be mitigated by for example increasing the thermal conductivity of the device structure as well as by using optical pumping at low repetition rates [21]. Oxidisation of the OS gain material causing breakdown or changes of the conjugated bonds [20, 22, 23] is often the main mechanism of photodegradation. Encapsulation of the OS is the solution to alleviate this problem [13, 23–25]. Encapsulation protects the OS from the environment of operation and can extend the operational lifetime of the device. Encapsulation is often done by over-coating the OS with another material that acts as a barrier. An alternative is to create nanocomposites by blending the OS in a host matrix.

In the first part of this chapter, the copolymer Super Yellow (SY) is investigated as a potential gain material for laser-based refractive index biosensor [26]. Here, films made of nanocomposites of SY are shown to produce ASE, a precursor of laser emission. Laser emission is demonstrated in neat SY films formed on a distributed feedback grating. The devices were then submerged in glycerol solutions of varying refractive indices studying shifts in the emission wavelength - this is a first step to assess the suitability of SY for laser-based refractive index sensing. Finally, the laser devices were encapsulated with either a PVA, SoG and parylene layer (see section 2.3.4) to observe if an increase in operational performance occurred.

The second part of the chapter explores new OS materials, so-called Blue 4 and Blue 6 macromolecules. These are molecules of similar sizes to CQDs based on oligofluorenes as the active units. Their synthesis was done by the Department of Chemistry at the University of Strathclyde. The π-conjugated oligofluorene are attached to an adamantine core that is rigid. Compared to the star-shape oligofluorene truxene macromolecules [6, 23, 27], the chain attachments are no longer planar but adopt a tetrahedral geometry with an overall star shaped molecule containing triarylamine functionality at the end of the arms. These materials were tested as visible laser materials. They produced random lasing when in neat thin film spun cast onto a planar glass substrate and also single transverse mode laser emission when incorporated with a DFB cavity. The initial measurements of the Blue 4 and Blue 6 materials seem to have great potential to incorporate into refractive index sensing as they produce low operational thresholds in thin-films allowing for surface functionalisation.

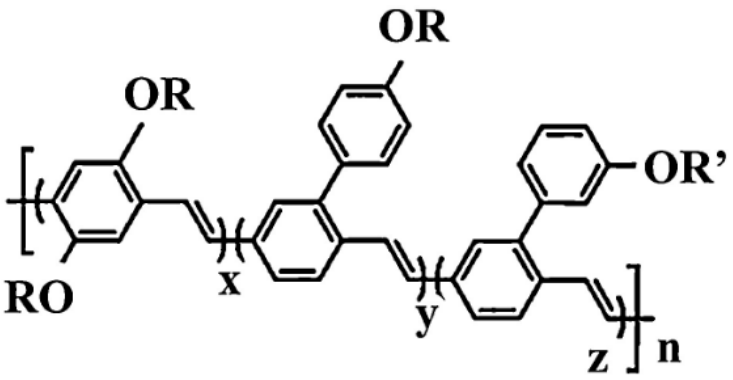

FIGURE 5.1: Molecular structure of Super Yellow [29].

5.2 Super Yellow

The copolymer polyphenylenevinylene (PPV) derivative aka SY was investigated. This is a PPV derivative that has high PL efficiency (PLQY). SY is also known for its charge transporting properties [1] and long operational lifetime under electrical pumping [28]. The molecular structure of SY is shown in figure 5.1 [29]. SY luminesces under electronic pumping (producing electroluminescence) as well as under optical pumping (PL). Optical (fs) pulse pumping has been employed for laser operation [32]. SY has been researched for innovative lighting technologies and has successfully been employed in organic light emitting diodes (OLEDs, also known as light emitting polymer diodes (PLEDs)) [1, 2, 5, 28–30, 33–36], ultra-thin LEDs [30], organic field-effect transistors (OTFTs) [8], light emitting field effect transistors (LEFETs) [31, 32, 35] and light emitting electrochemical cells [28]. It has been utilised as part of an optical concentrator for visible light communications [37, 38] and as the gain layer of a DFB laser [32]. Our motivation here, which sets our study apart, is to demonstrate laser fabrication and demonstration in a completely ambient environment and to assess if the resulting lasers are potentially suitable for biomolecular detection based on refractive index sensing.

SY has been reported to produce high quality thin films with higher PLQY than other PPV derivatives [28, 30]. SY lasers were reported with low values of threshold energy [32]. In addition, SY has a relatively high refractive index (n$\sim$1.86 at 570 nm) that, in principle, can lead to a higher sensitivity for a DFB laser implemented as an evanescent sensor to detect changes in the refractive index at the laser surface. In such a DFB laser biosensor, the device surface is functionalised in order to capture specific analytes in a given environment (see figure 5.2). If analytes

are captured the effective refractive index is altered, resulting in a shift in the emission wavelength (from the Bragg equation, equation 2.8). It has been shown in [39, 40] that a gain layer with a high refractive index was desirable for the sensitivity. SY with its combination of high PLQY, low reported laser threshold and high refractive index (for an OS) is therefore a priori attractive for DFB laser biosensing.

There are challenges ahead however. The majority of reports of SY devices in the literature are for operation in an oxygen deprived environment - by placing the device inside a vacuum chamber or in a nitrogen atmosphere for example. There are accounts of operation in ambient conditions, however, some where the SY film is itself encapsulated before oxygen contact and others where only the PL capability was used [42, 43]. In addition, examples of optical excitation have utilised ultrafast pumping in the fs and ps regimes [32, 44]. These result in having bulky pump sources that are not suited for applications. Herein, while initial assessments for sensing were conducted on neat SY lasers, three different encapsulating materials were then tested on the lasers: PVA, spin-on-glass and parylene.

5.2.1 Design and fabrication of devices

SY (from Merck) was initially in powder. The molecular weight is 1939000 g/mol. It was then diluted in chloroform or dichloromethane (DCM) solvents.

For the detection of ASE the SY was dispersed in chloroform and mixed with Poly (methyl methacrylate) (PMMA) at 1.6:1 ratio by weight also to a concentration of 20 mg.mL^{-1} creating a blend. This was done initially to facilitate the fabrication of smooth films to sustain ASE. The solution was then spun cast at 8krpm onto a glass substrate (20 x 20 mm) and the spectra detected at the edge, section 2.4.1; this is the same procedure as in Chapter 3. We used this approach to "debug" the process and inform us if we could get ASE with our apparatus.

Neat films of SY were then deposited onto a DFB cavity formed from the optical adhesive Norland 65 (NOA 65) that has a refractive index of approximately 1.52. The grating structure was created utilising soft-lithography through the same procedure described in section 2.3.1. Before deposition, the SY was placed into a glass cuvette, weighed and diluted at a concentration of 7 mg.mL^{-1} in chloroform. The cuvette was then placed on a magnetic stirrer until all SY was diluted. Once

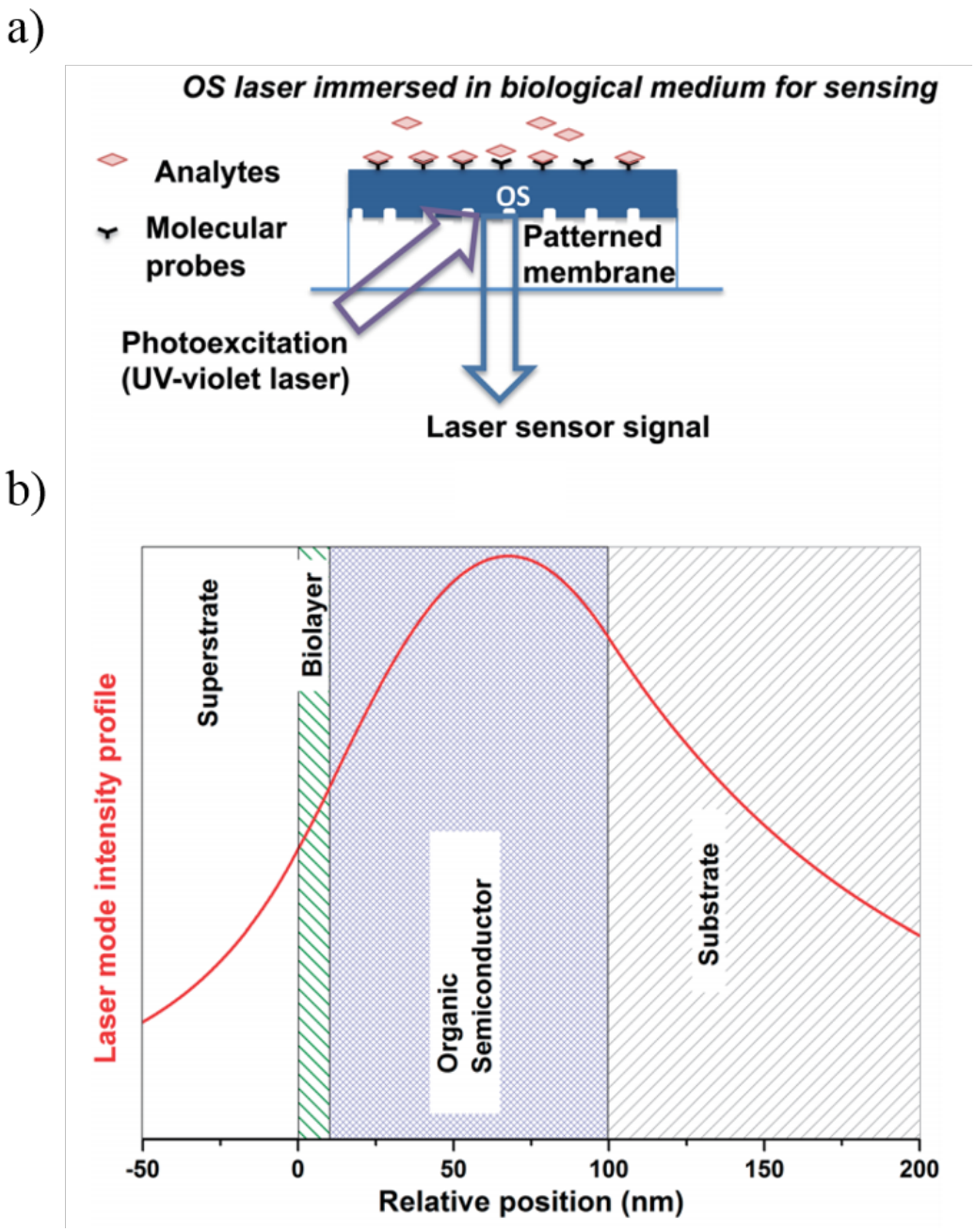

FIGURE 5.2: a) Schematic depicting the implementation of an OS laser sensor; the laser surface is functionalised to capture specific analytes, and b) laser mode intensity overlap of the multi-region laser structure, from [41], where the evanescent part of the laser mode interacts with analytes on the surface.

diluted the SY undergoes gelation under transport, a sign that SY contains high chain regularity. This is where the solution undergoes a change in viscosity and loses fluidity. Once the grating was finished, the SY was spun cast onto the DFB surface over at a range of spin speeds ranging from 2-8krpm. DCM, a lower boiling point solvent, was also employed during this investigation to examine the effects of SY with increasing film thickness. SY/DCM films were made both by drop coating and by rolling the SY onto to DFB grating [45] to increase uniformity and surface coverage over the grating as the SY/DCM did not disperse over the grating easily. SY/chloroform films were made by spin coating.

The SY DFB laser samples were tested initially in air. Following this, operation when submerged in deionised (DI) water, and eventually in glycerol solutions, was tested while monitoring the emission wavelength. This was done to give an indication on the capability of the devices to operate in a polar liquid and to detect changes in the bulk refractive index of such an environment - a first step towards biosensing.

Glycerol was purchased from Sigma Aldrich diluted at 99% in DI water. This was diluted down to concentrations of 5%, 10%, 15%, 20%, 30%, 40%, 50% and 60% in DI water (refractive indices ranging from 1.35 (5%) to 1.43 (60%)). Doing so enables the obtention of glycerol solutions with a refractive index proportional to the glycerol concentration. Immersing the laser in such solutions alters the effective refractive index, which should in turn shift the wavelength emission, as described by equation 2.8.

For immersion in different liquids, the SY lasers were secured onto an inner face of a cuboid quartz cuvette. A laser was attached with a transparent optical adhesive (Kapton tape, $100\mu m$) with the cuvette and the laser acetate substrate being in contact. This allowed the SY surface to be exposed to the liquid environment, either DI water or glycerol solution. The laser was optically excited through the back at an angle of approximately 10^0 to the normal. The laser emission was collected from the back, figure 5.3.

Encapsulation of SY lasers with PVA (section 2.3.4), spin-on-glass and parylene was also explored. The PVA was dispersed at 50 mg.mL^{-1} in DI water and spin coated at 3.2krpm on the SY laser surface of the sample to give a 180 nm PVA film. The device was then annealed at 30^0C for 72 hours. Spin-on Glass (SoG, from Desert Silicon) is based on titanate that has high dielectric constant, strength

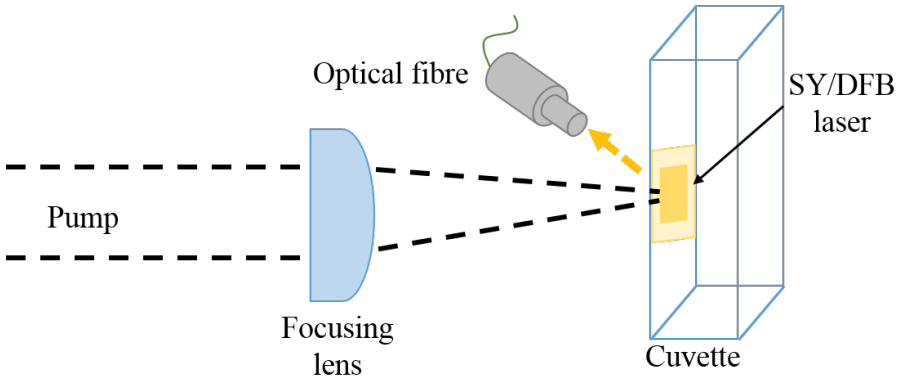

FIGURE 5.3: Optical setup for varying effective refractive index of SY/DFB lasers.

and high refractive index (n = 2.1). It was spun cast at 3.5krpm resulting in a 200 nm encapsulating film. This was then annealed for 72 hours at 30^0C. Higher temperature was not used to preserve the SY. The final encapsulant explored was parylene, which is a biologically compatible polymer. Parylene is deposited under vacuum at the molecular level where films are essentially grown layer by layer by a monomer gas. These methods created bi-layered wave guiding structures potentially improving confinement of the laser mode in addition to the reduction of surface scattering losses and acting as an oxygen barrier.

5.2.2 Measurements

5.2.2.1 PL

Figure 5.4a shows the emission spectra acquired through edge detection of a film of SY. This can be compared to the (normalised) absorption and electroluminescence spectra from Merck in figure 5.4b. Merck prepared the SY in toluene at 5 mg.mL^{-1} where it was spun cast onto an OLED device in a nitrogen atmosphere. It can be seen that both of the intrinsic PL profiles have a similar shape with 2 peaks at approximately 570 nm and 600 nm. In figure 5.4a the SY diluted to 6mg.mL^{-1} in toluene and was spun cast at 1krpm for 60 seconds. The first peak occurs at 582.0nm and the second, lower intensity peak occurs at 638.7 nm, a 56.7 nm separation. Both peaks being more prominent than in figure 5.4b. This shift has been seen to depend on the concentration of SY and has also been attributed to electron-vibrational mode interaction that varies with temperatures [44]. It can

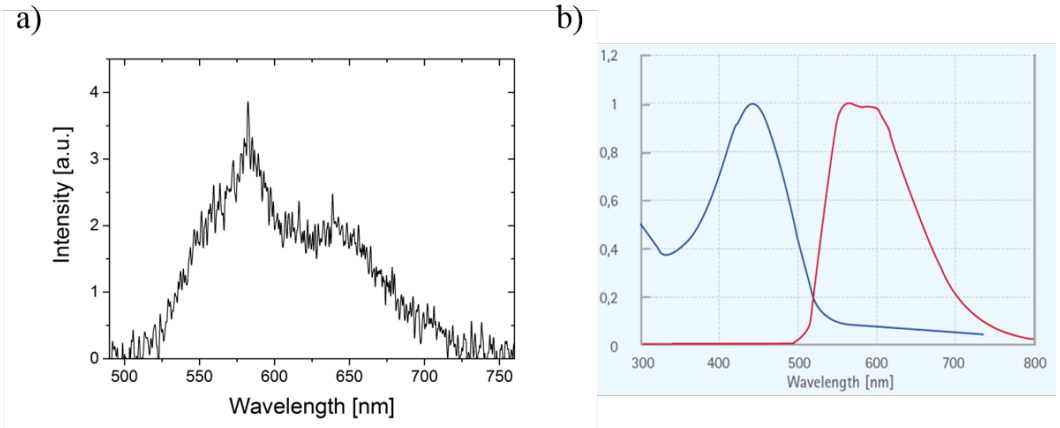

FIGURE 5.4: a) Photoluminescence spectra of Super Yellow film spun cast on planar glass substrate diluted at 6 mg.mL^{-1} in toluene b) absorption and electroluminescence spectra from Merck data sheet.

also be seen that there is a relatively large Stokes shift with the absorption and emission only just overlying creating a promising condition for lasing.

5.2.2.2 ASE and laser characterisations

The SY film (ASE) and the initial DFB lasers in air were optically pumped with a stripe and characterised as discussed in section 2.4. This was done with SY dispersed in both solvents (initally with chloroform and then DCM). The pump geometry was then altered to be a spot (as to mimic the refractive index sensing setup employed within the group [26]). Encapsulation of the devices was then explored to investigate if an improvement in operational lifetime and threshold is observed.

For the further laser tests under immersion in liquids of different refractive indices, the device was excited with a spot through the back (substrate) as shown in figure 5.3. The emission was detected as well through the back. A measurement of the emission spectrum (at a pump level of 100 μJ) in air was first taken for reference. DI water was then added and the spectrum recorded again. After the DI water the laser was submerged in glycerol starting at 5% working up to 60%. Between every glycerol increment the SY/DFB was rinsed with fresh DI water before the next concentration was added. The pump spot and energy remained the same throughout. In addition to these measurements the emission in air was taken between each stage of the DI water rinse to observe any change in the emission.

5.2.3 Results

5.2.3.1 ASE

As mentioned earlier, the next characteristic of a material to explore in the quest for laser operation is to characterise ASE (if there is an occurrence). The detection of ASE signifies the materials potential use as a gain medium for lasers. Figure 5.5a shows the emission spectra of the SY (diluted at 20mg.mL^{-1} in a PMMA matrix (1.6:1 chloroform) spun cast at 8krpm for 60 seconds) in thin film format. The spectra can be seen to narrow for increasing energy, transitioning from pure PL at low pump energies to ASE above a threshold energy has been passed, section 1.3.5. Figure 5.5a shows the ASE developing at 583.7nm, and is located approximately centrally between the PL peaks (557.8 and 608.4nm), with a FWHM of 9 nm.

Figure 5.5b is the corresponding energy transfer function giving the ASE threshold energy of approximately 22 μJ (corresponding to an energy per pulse of 440nJ/pulse where [32] reported ASE occurring at 315nJ/pulse in a SY/PVA/quartz sample under 100fs pulses and a stripe width of 2.5 mm by ~ 350 μm). SY displays high threshold energy when compared with other organic semiconductors such as BBEPH-PPV typically threshold energies around 0.4 μJ.

5.2.3.2 DFB operation

After the demonstration of ASE in thin films the next stage is to develop an operational laser. SY lasers made from SY in DCM (boiling point 39^0C) and chloroform (boiling point 61^0C) were made and compared. Lasers made from SY in DCM are discussed first.

When the SY/DCM DFB lasers were fabricated by drop-coating, the output of the devices produced relatively weak multimodal emission, which is attributed to non-uniformity in the film. Spin casting the solution proved difficult due to the viscosity of the material as it did not cover enough of the grating structure. It appeared as a faint "yellow" mark where the solution had been deposited and the rest spun off. Therefore, we had to use a rolling coating method discussed in [45]. The SY DCM mixture was deposited onto the grating surface and a glass pipette was then rolled over the surface to improve the film quality and surface coverage.

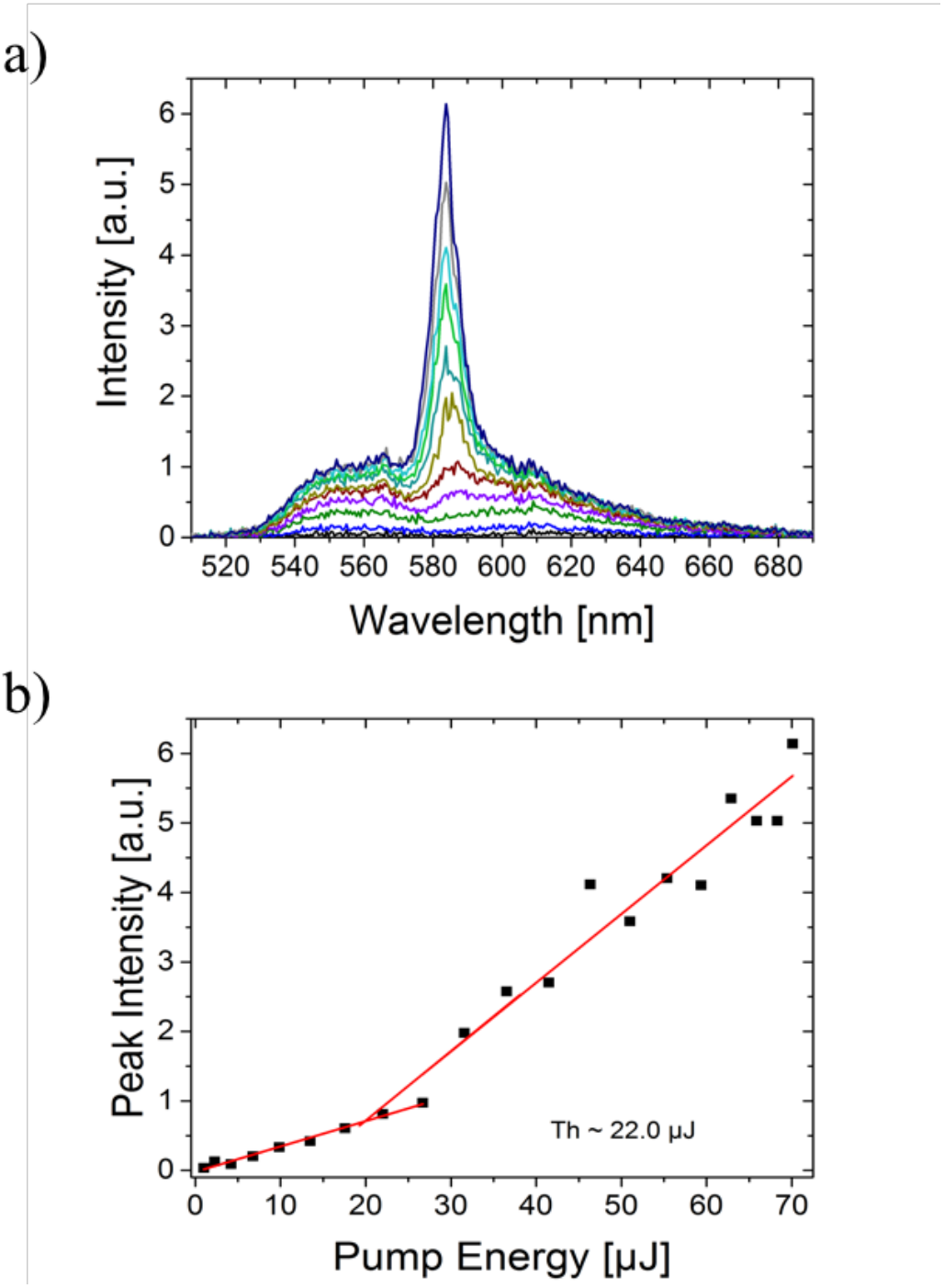

FIGURE 5.5: a) ASE spectra for nanosecond pumped nanocomposite SY film (20mg.mL^{-1} in PMMA chloroform matrix) spun cast onto planar glass substrate excited at pump energies ranging 1 μJ to 70 μJ, b) corresponding transfer function of ASE with threshold energy of 22 μJ.

Figure 5.6a shows the evolution of the spectrum with the fluence and the corresponding transfer function of such a laser. Figure 5.6b is the transfer function. The threshold energy is at approximately 0.52 μJ. The threshold is lower here because the SY is in neat form and there is a DFB cavity. From the spectra it is clear that the laser is operating multi-mode with competition of modes occurring. The main peak wavelength is at 584.5 nm for a FWHM of 0.80 nm (a secondary peak at 585.1nm has a FWHM of 0.43 nm). When compared to the SY in chloroform spun cast at 2krpm this is an 8.3nm blue shift attributed to the inhomogeneous SY film (discussed next).

The SY in chloroform lasers were fabricated by spin casting at different spin speeds (2-7 krpm). The emission spectra (with the transfer function in inset) for each spin rate can be seen in figure 5.7. The corresponding emission wavelengths, FWHM and threshold energies are displayed in table 5.1. The value for the wavelength at peak emission remains somewhat constant as the spin rate increases. This indicates that there is no significant change in the average film thicknesses over the excitation stripe with spin-coating speed (it does not mean the film is flat or homogenous). Typically the thickness should decrease with the spin speed, at least up to a point. It should also be noted we found the SY is a difficult material to work with and this could contribute to the non-uniformity in the film as AFM measurements seem to indicate (figure 5.8). Little to no variance in the film thickness with the spin speed was found (data not presented here). With the addition of working with a viscous solution, the SY deposition over the grating structure might not be ideal. The solution remains gel-like and with the use of chloroform (having a low boiling point) it is possible that the solvent evaporates upon deposition. This would leave a non-uniform film where the excess/"dilute" material is spun off. The lasers' linewidth also remains roughly consistent with the average being 2.3 nm limited here by the resolution (2.5 nm). Due to the stripe length and non-uniformity in the SY film, stripe excitation is not ideal. Reducing the stripe to a spot allows for a more precise location on the SY film to be excited (as well as mimicking the biosensing setup in our group). SY/chloroform films also permits an "easier" fabrication process by spin coating.

To mitigate the effect of non-uniformity in the film, the excitation was changed from a stripe to a spot (approximate radius of 130 μm) - the device being excited in the centre of the sample. Using a spot over a stripe is also beneficial for other reasons. A narrower spot can reduce the number of oscillating modes, narrowing

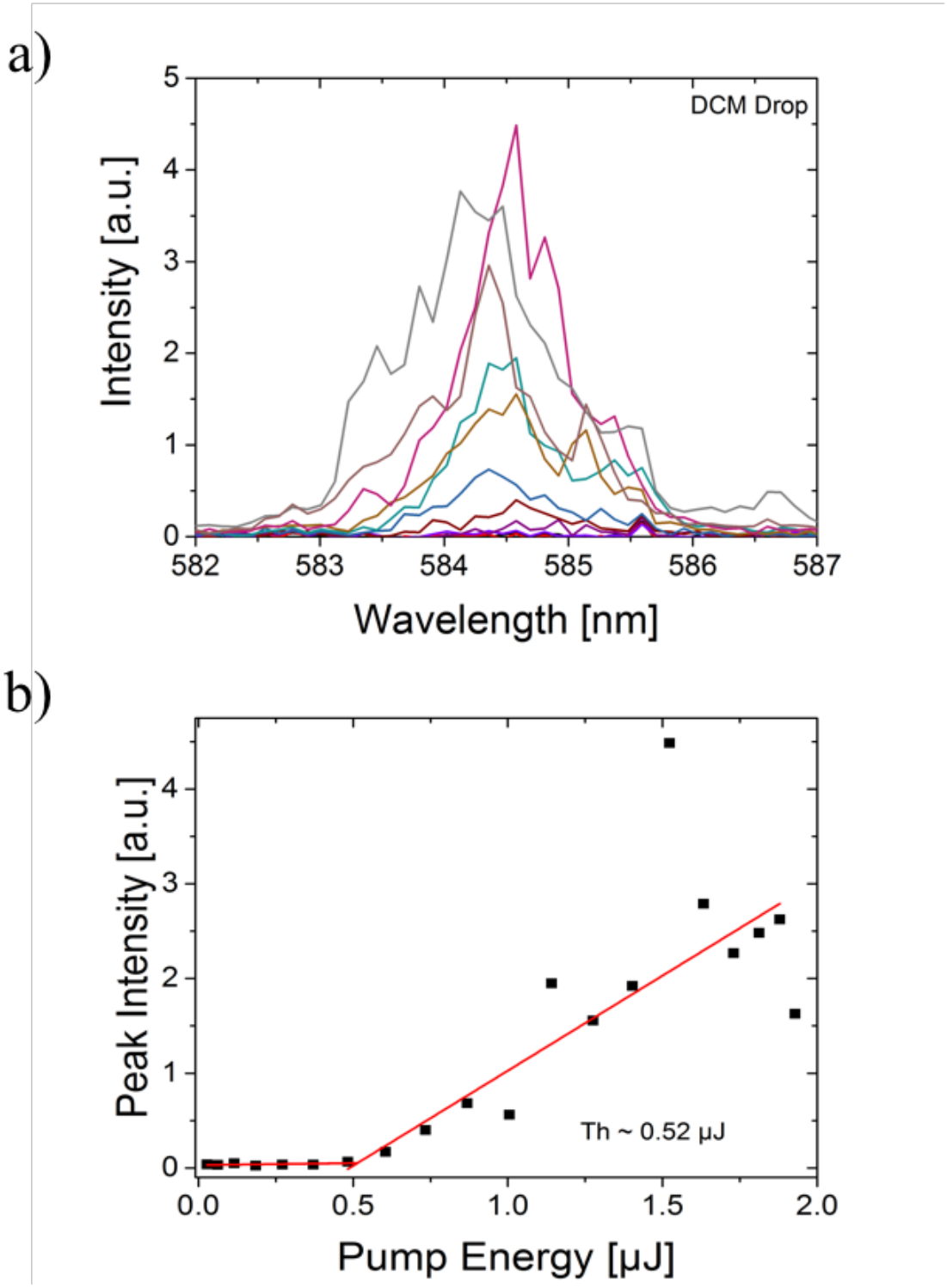

FIGURE 5.6: Super Yellow diluted at 6mg.mL^{-1} in DCM drop cast onto NOA 65 grating. The film was then rolled with a glass cuvette increasing surface area and uniformity where a) is the emission spectra excited over a pump range of 0.03 μJ to 2 μJ and b) the corresponding transfer function with threshold energy 0.52 μJ.

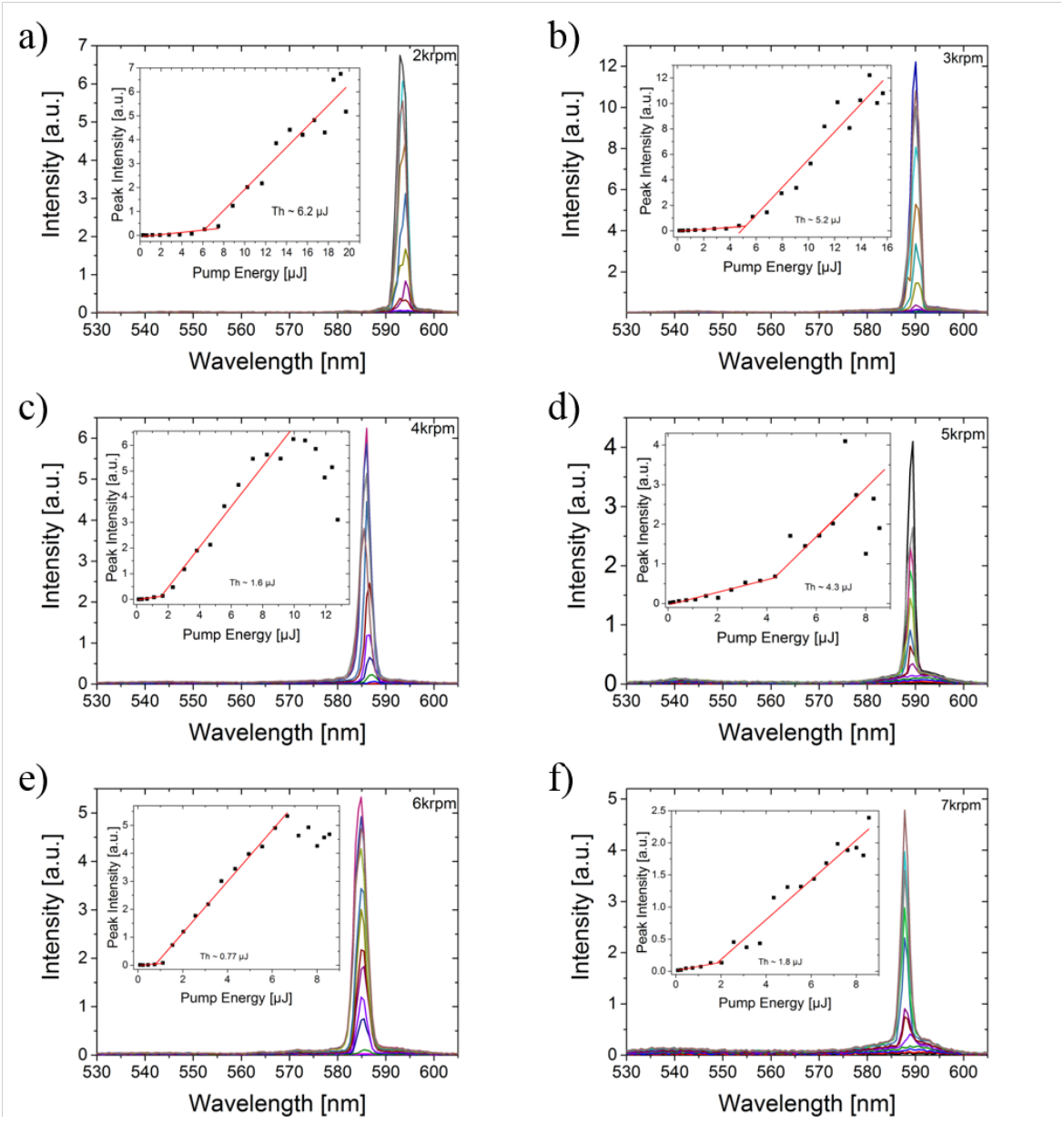

FIGURE 5.7: Lasers spectra under different pump energy for samples made from SY diluted in chloroform at 7mg.mL^{-1} spun cast over a range of spin rates onto an adhesive grating, period 350 nm. Lasers are excited with a stripe. Insets display the corresponding transfer functions for each spin speed and are displayed in table 5.1.

TABLE 5.1: Optical parameters is SY/DFB laser when excited by a stripe. Error in the wavelength is ± half of the resolution (1.3nm).

Spin rate (krpm)	Emission Wavelength (nm)	Threshold Energy (μJ)	FWHM (nm)
2	592.9	6.2 ± 0.6	2.1
3	590.1	5.2 ± 0.6	2.1
4	586.0	1.6 ± 0.2	2.3
5	589.5	4.3 ± 0.4	2.2
6	584.9	0.8 ± 0.1	3.1
7	587.8	1.8 ± 0.3	1.9

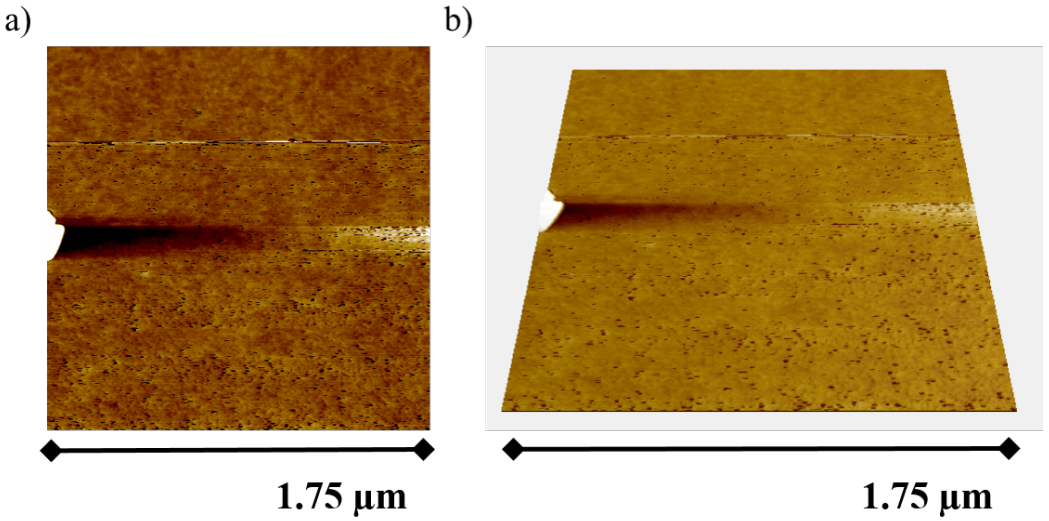

FIGURE 5.8: a) AFM image of SY thin film diluted at 5mg.mL^{-1} in toluene spun cast at 4krpm. Indentation (scratch) is from measuring film thickness. b) 3D representation of a.

the linewidth. In saying this, here a one-dimensional grating is used, so a fine stripe oriented perpendicular to the grating structure could give the same result, if the film was smooth enough. One issue with pumping with a spot, in the one-dimensional grating case, is that it can cause the threshold energy to increase if the excitation area is significantly decreased, due to the decrease in the feedback.

Figure 5.9 shows the emission spectra for the SY/DFB laser spun cast at 7krpm excited with the pump laser focused to a spot - the transfer function is given in inset. Devices prepared with spin speeds of 5krpm, 6krpm and 8krpm were also tested. Main results are displayed in table 5.2. Here it can be seen that the emission wavelength follows the expected trend of blue shifting with increasing spin speed (decreasing thickness, hence decreasing n_{eff}). The increasing spin speed also leads to an increase in the threshold energy. The peak wavelengths,

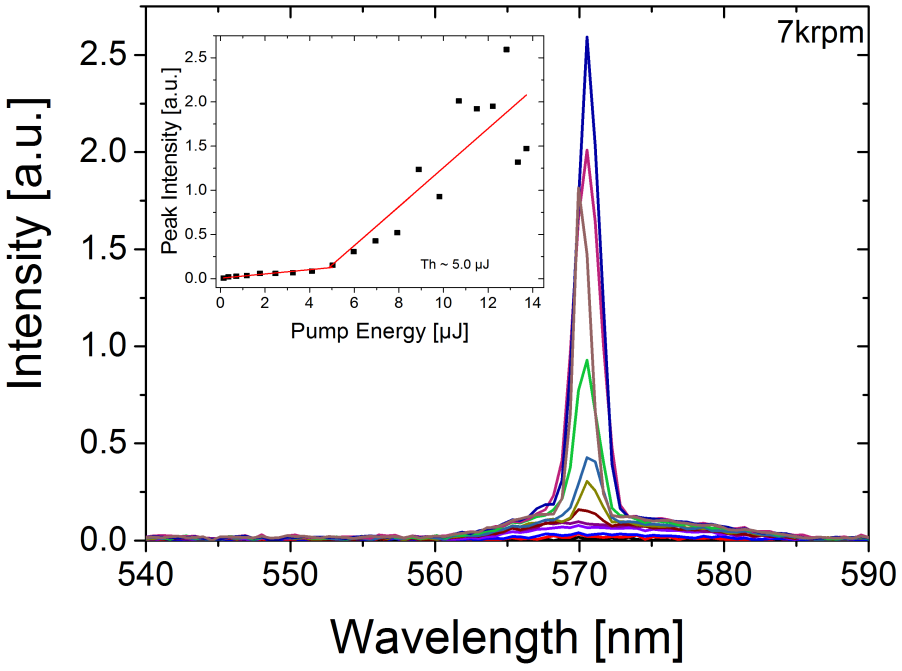

FIGURE 5.9: SY/DFB laser with film spun cast at 7krpm optically excited over a range of 0.1μJ to 14μJ via spot pump geometry, inset: corresponding transfer function.

TABLE 5.2: Optical parameters of SY/DFB laser when excited by a spot. Error in the wavelength is ± half of the resolution (1.3nm).

Spin rate (krpm)	Emission Wavelength (nm)	Threshold Energy (μJ)	FWHM (nm)
5	580.3	0.5 ± 0.04	1.6
6	578.0	1.2 ± 0.05	2.0
7	570.5	5.0 ± 0.3	1.4
8	571.1	3.4 ± 0.2	1.6

threshold energies and linewidths can be found in table 5.2. There is no significant difference between the 7krpm and the 8krpm samples meaning the film thickness of the 7 and 8krpm samples is approximately equal. It can also be seen that the FWHM remains roughly constant giving average linewidth limited again by the resolution.

The SY/DFB lasers were then measured immersed in DI water. There is a red shift caused by the increase effective refractive index change when water is added that can be seen in figure 5.10.

The inserts show that the threshold energies increase as the spin rate is increased.

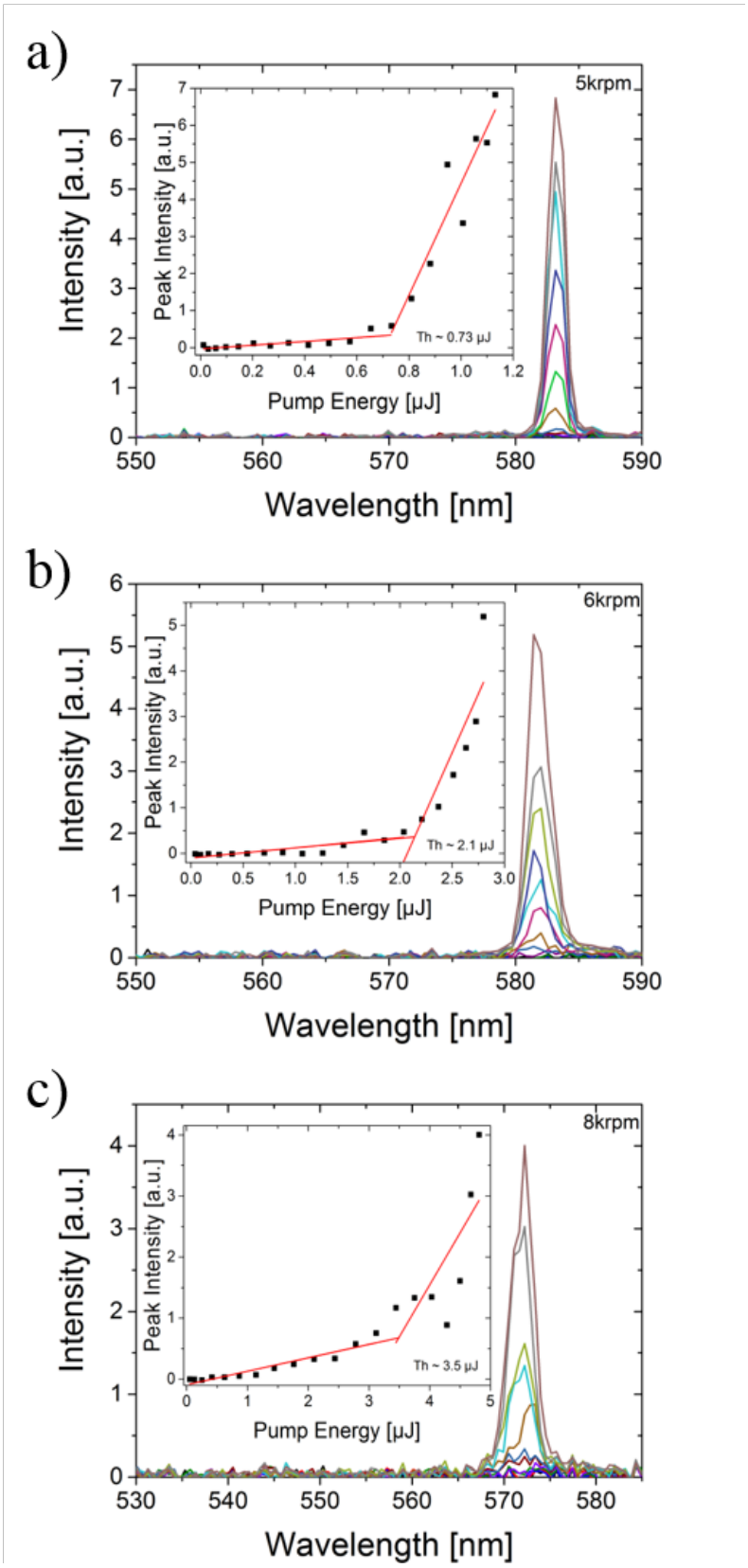

FIGURE 5.10: SY/DFB lasers attached to a quartz cuvette and submerged in DI water spectra for 3 different spin speeds of SY film, a) 5krpm, b) 6krpm and c) 8krpm. Insets are the corresponding transfer functions.

TABLE 5.3: Optical parameters of SY/DFB laser submerged in DI water noting the change in emission wavelength. Error in the wavelength is ± half of the resolution (1.3nm).

Spin rate (krpm)	Emission Wavelength (nm)	Threshold Energy (μJ)	FWHM (nm)	$\Delta\lambda$ (nm)
5	583.2	0.73 ± 0.4	1.6	2.9
6	581.4	2.1 ± 0.2	2.1	3.5
8	572.2	3.5 ± 0.5	2.9	1.2

Again this shows that alteration of the effective refractive index alters the threshold energy, however, not as significant as before. When applying the methods in section 2.5 the laser mode propagates within the DI water, barely entering the SY film (taking $n_{H_20} = 1.33$ and $n_{SY} = 1.86$ at 570 nm). The emission wavelengths, threshold energies and peak shift ($\Delta\lambda$) can be seen in table 5.3 (note 7krpm was not measured as spectra was undetectable).

Note that for all the laser measurements reported here, the spectrum blue shifts as the pump energy increases. In CQDs this was attributed to the saturation of absorption, section 4.4.3, and the effect is similar here.

5.2.3.3 Glycerol measurements

Building on the emission shift observed when the SY/DFB laser was submerged in DI water a range of effective refractive index was examined in order to validate SY as a material for refractive index sensing. Here the spectral resolution was 0.13 nm. The device was secured inside the same quartz cuvette as before and the spectrum was recorded observing if any shift due to the addition of liquid in the cuvette. The concentrations of glycerol-in-DI-water solutions used in the measurements were 5, 10, 15, 20, 30, 40, 50 and 60%. Once one concentration had been measured the glycerol was removed from the cuvette and the SY/DFB rinsed with DI water to ensure that it was completely removed. The DI water was then removed, the spectra in air measured again and the next glycerol concentration added. The SY/DFB laser was pumped with the same energy and location throughout these measurements.

Figure 5.11 displays the data recorded for the glycerol measurements. Looking at figure 5.11 it can be seen that there is a noticeable red shift from the SY/DFB laser emitting in air. The measurements in glycerol undergo the same shift but

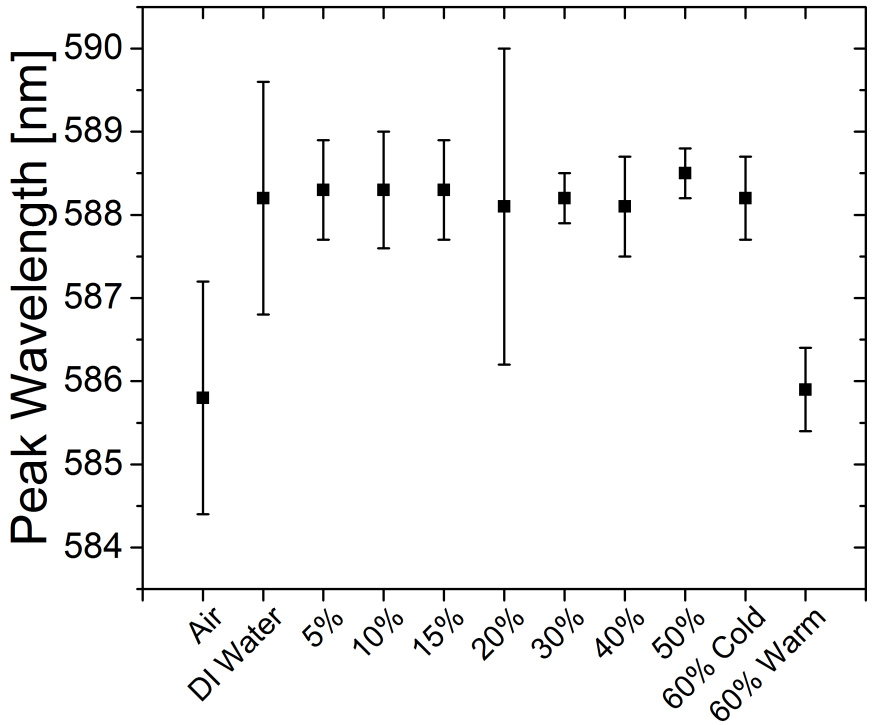

FIGURE 5.11: SY/DFB emission where the laser mode wavelength is represented versus effective refractive index. The error bars represent the wavelength range incorporating the multimodal nature when present.

with increasing concentrations remain relatively constant. Figure 5.11 displays the data in a scatter plot for ease of sight. These peak values can be seen in table 5.4. Note, the reason there are a hot and cold 60% as curiosity arose to whether there was a shift change observable with temperature. This shows that SY refractive index does have a correlation with temperature [46].

Unfortunately, the glycerol measurements show that SY is not an ideal as a gain material in refractive index sensing devices. Under a varying refractive index the emission wavelength remains approximately constant where ideally a shift would be observed between increasing glycerol concentration. The shift between air and water is also less than that has been reported for Truxene [26]. We attribute these results to the difficulty in making high quality films. The property of SY might also suffer for immersion in polar solvent. Degradation of the laser performance over time is also a problem. Stability issues, operational lifetime, are addressed where device encapsulation has been used to reduce this issue [23, 47, 48].

TABLE 5.4: Optical parameters of SY/DFB laser when submerged in different concentrations of glycerol. Error in the wavelength is ± half of the resolution.

Medium	Peak Wavelength (nm)	FWHM (nm)	$\Delta\lambda$ from air (nm)
Air	585.8	0.4	0
DI water	588.2	0.2	2.6
5%	588.3	0.3	2.4
10%	588.3	0.4	2.4
15%	588.3	0.2	2.4
20%	588.1	0.5	2.2
30%	588.2	0.3	2.4
40%	588.1	0.3	2.2
50%	588.5	0.2	2.7
60% cold	588.2	0.3	2.3
60% warm	585.9	0.3	0.1

5.2.3.4 Encapsulation of laser devices

With our SY lasers having a low operational lifetime (low photostability) steps were taken in an attempt to improve on it. As seen in Chapter 3, section 3.4.2, encapsulating the device is beneficial to operation and lifetime. To re-emphasise on what was previously discussed the encapsulant behaves as an oxygen barrier and aids in the confinement of the laser mode. Until now, to the best of the authors knowledge, experiments with SY has been carried out by avoiding exposure to the ambient environment, in one way or another [42, 43].

Figure 5.12a displays the spectrum and corresponding transfer function for a neat SY/DFB laser, in ambient conditions. Note as SY is not a stable material in oxygen and devices see variance of emission quality. The non-encapsulated device spectra appear "untidy" (measured using the spectrometer at resolution 0.13 nm). The maximum value of intensity occurs at 579.5 nm. Taking this as the central position the transfer function, inset, results in a threshold energy of 0.68 μJ.

The device was then encapsulated with PVA, as done in section 3.4.2, which was again chosen to have a film thickness of 180 nm. Figure 5.12b shows the encapsulant layer reduces the multimodal nature of the device. Whereas with the CQDs, section 3.2.2, the addition of the PVA layer reduced the value for lasing threshold, here the opposite is true. The threshold energy is a similar value of 1.1 μJ. Here, although the laser mode is symmetrised more with the PVA layer, the reduction in the number of modes shows a lower scattering, probably

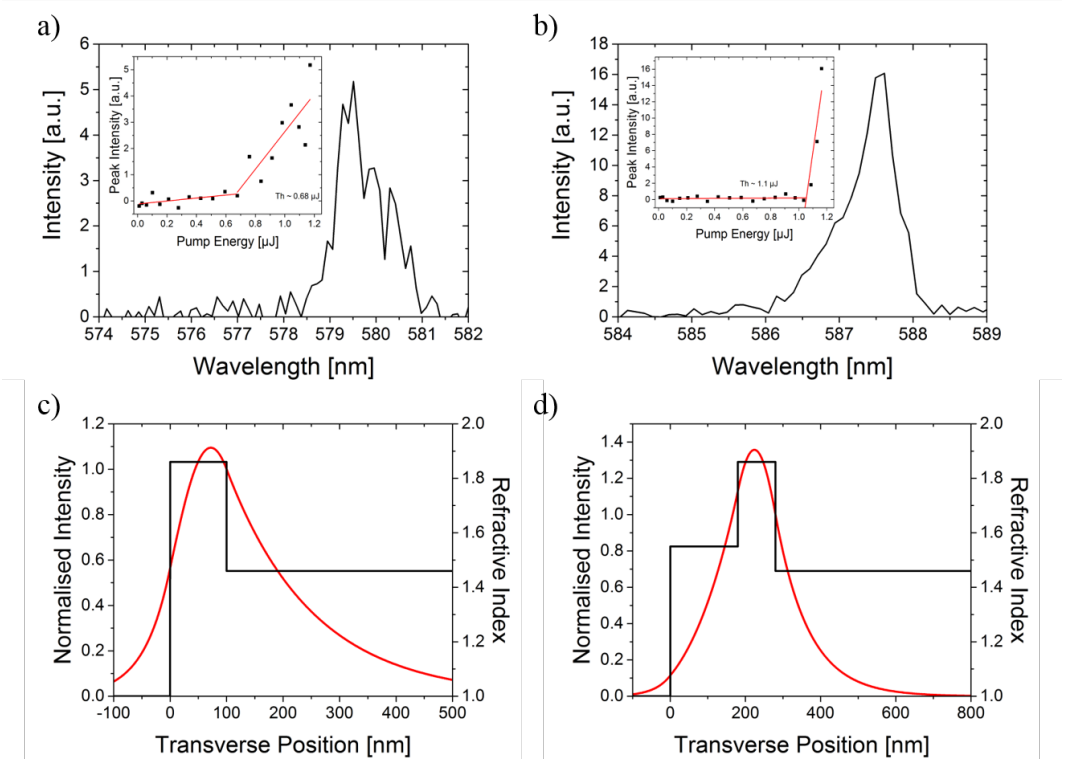

FIGURE 5.12: SY/DFB laser excited over an energy range 0.01μJ to 1.2μJ where a) is the raw emission spectra and b) is the spectra after encapsulation with 180nm thick PVA. Insets display the corresponding transfer functions. c) and d) are models of the mode confinement of the devices discussed in section 2.5.1.

at the film interfaces. While figure 5.12d displays greater modal confinement, the model does not take into account the grating structure. The addition of the PVA decreases the field interaction with the substrate where the grating actually is. This can reduce the cavity feedback leading to an increase in threshold. However, now a distinct kick can be observed in the transfer function, inset figure 5.12b, when lasing is achieved suggesting that it increases confinement within the guiding structure. This seems legitimate as the spectra characteristics reduce to a more prominent emission. Occurring at 587.6nm, the emission is red shifted by 8.1nm compared to the non-encapsulated device. This is due to the increase in the modal effective refractive index as discussed in the next paragraph. It is expected that PVA encapsulation should improve the photosatbility. However, due to the rate at which of device death a photodegradation study could not be completed.

The modal confinement for each of these structures was modelled. Figures 5.12c shows the mode profile for the SY thin film without encapsulation. Here the refractive index of SY is taken to be 1.86 [34] resulting in an effective refractive

index of 1.53. The mode is not centred in the SY film and there is a large overlap with the NOA 65. There is also an overlap with air and SY. Here, the SY film thickness is taken to be 100 μm. SY produces very thin films and a uniform layer at larger thickness would prove difficult in neat films (SY films were measured by AFM measurements who found that there was not much variance in film thickness over varying spin rates and other groups have reported SY diluted in toluene spun at 1.5 krpm produces a 50nm film [28]). With the addition of the PVA layer, figure 5.12d, the modal confinement increases in comparison and is centred within the gain layer (the overlap increases from 35% to 41% with increased coverage of the laser mode in the SY film). In addition to this the encapsulation results in the red shifted spectra. This is due to a higher effective refractive index, approximately 1.59, that using equation 2.9 the Bragg condition occurs at longer wavelengths. Again, if the SY film could be increased in thickness would increase the devices performance.

SoG was also utilised when testing encapsulation effects. As opposed to PVA, it would allow for encapsulated materials to be operated in aqueous solutions - PVA is soluble in water. Containing inorganic constituent, it should also help in heat dissipation. The material itself is spin on titanate and is an interlayer dielectric film that gives uniform coatings. It has a high refractive index of 1.45 and is a transparent coating. Spinning at 3.5krpm will give a 200nm film (from http://www.desertsilicon.com/). Figure 5.13 displays the model confinement of a SoG encapsulated device using the same parameters as previously. Again, once encapsulated, the devices show a strong confinement with the mode being localised within the gain material. As before, when the thickness of the SY layer is increased the strength of the mode increases. The procedure is to then anneal for 5 minutes at 200^0C. Typical organic semiconductors cannot tolerate high temperatures and anywhere near this temperature would destroy them. SY has had a number of high temperature investigations of temperature up to 80^0C [49].

In our investigation the SoG was annealed as PVA, at 30^0C for 72 hours, as previous success has been shown with π-conjugated poly[2, 5 - bis(2',5 - bis(2" - ethylhexyloxy) phenyl) - p - phenylene vinylene] (BBEHP-PPV). However, this is not the case with the SY. So far the effects have been detrimental to the operational lifetime killing the laser emission before the spectra can be recorded; no laser operation was obseved. Once the process is revisited and the annealing

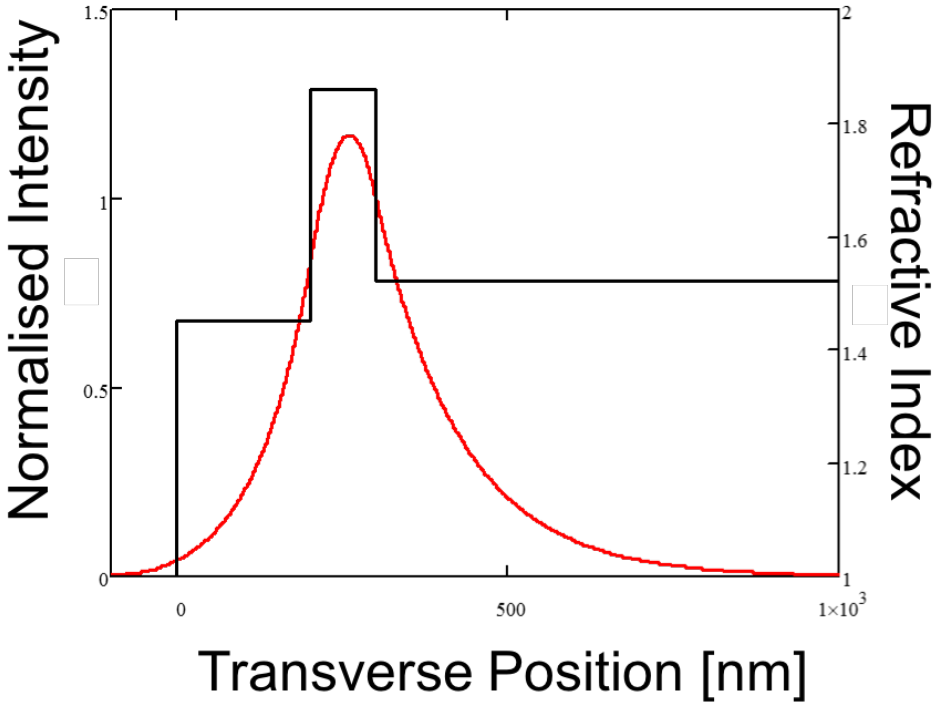

FIGURE 5.13: Model of the modal confinement if SoG if successfully utilised in the lab.

temperature increased, SoG may be prove advantageous as has been shown the quantum dots where it was annealed at 100^0C [50].

Parylene is used in many medical equipment, for example in prosthesiss, making it ideal for the final encapsulation test. There are three different types of parylene where parylene C was applied (n $\sim$ 1.64). Parylene C is an ideal material to use for bio-sensing application as it is known to be biologically accepted [51–54]. It is a good moisture barrier utilised in printed circuit boards and has been used in other medical devices such as pacemakers and prosthetic limbs.

The spectra of a non-encapsulated SY laser (to be coated with parylene) were recorded over a range of pump energies and can be seen in figure 5.14a. The emission is multimodal centred at 578.0nm with the peak value having a FWHM of 0.67 nm. The corresponding transfer function is shown in the figures inset where threshold is achieved at approximately 1.9 μJ. Parylene is deposited at room temperature onto the laser using a specialised vacuum deposition tool (section 5.2.1). The typical film thickness deposited with this tool is 3000 nm.

Figure 5.14b displays the device's spectra after it has been successfully encapsulated with parylene. Straight away it can be seen that the laser emission is more

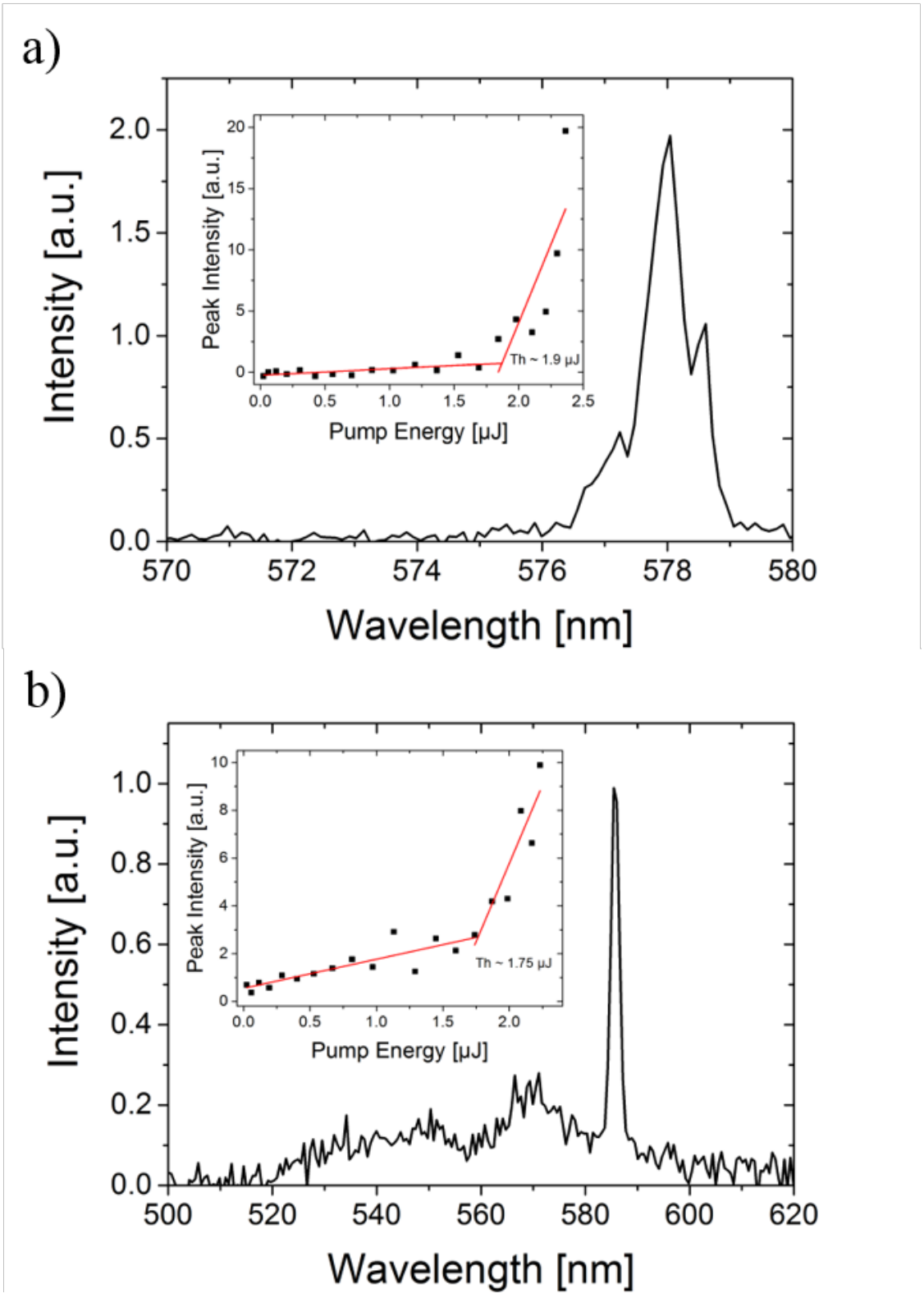

FIGURE 5.14: SY/DFB spectra (excited over a pump range of 0.02 μJ to 2.4 μJ) a) before and b) after encapsulation with 3000nm thick parylene. Insets display the corresponding transfer functions.

defined and centred at 585.5 nm. This is a 7.5nm red shift when compared to the neat device. The transfer function also displays a slightly lower threshold of approximately 1.75 μJ. An argument could be made that the multimodal nature of the neat sample makes its threshold higher due to the competition of modes. Within the resolution of the measurement, it can be said that the spectral FWHM does not change. The intensity of emission was not high enough to observe the spectra at a higher resolution.

The encapsulation methods employed in this chapter have shown to directly affect the laser oscillation in SY/DFB devices. A 180nm PVA layer symmetrises the laser mode creating a larger overlap and reducing the number of modes. Due to a reduction in scattering at the material interfaces. A SoG layer, at first instance, is detrimental to SY DFB devices, killing laser oscillation. However, additional studies are needed to validate this statement. When a SY/DFB device is encapsulated with parylene C the threshold is seen to reduce creating a smoother lasing spectra.

5.3 Blue 4 and 6

Blue 4 and Blue 6 materials were fabricated in the Pure and Applied Chemistry group at the University of Strathclyde. The materials are based on oligofluorenes and were initially designed to be used in OLEDs. Blue 4 absorbs at 367nm and emits at 443 nm, Blue 6 absorbs at 356nm and emits at both 399 nm and 420 nm. The corresponding spectra can be seen in figure 5.15 that also depicts the molecular structures for each material. In powder form Blue 4 has a photoluminescent quantum yield (PLQY) of 33% and Blue 6 of 17%. The following sections will describe the optical characterisation of the materials demonstrating their laser capabilities.

5.3.1 Preparation

Both Blue 4 and Blue 6 samples (thin films) were prepared in the same manner. The molecules, initially in powder form, were diluted in toluene at the following concentrations: 10 mg.mL^{-1} and 20 mg.mL^{-1} for Blue 4 and 20 mg.mL^{-1} for Blue 6. The solutions were spun cast at different spin rates onto planar glass substrates,

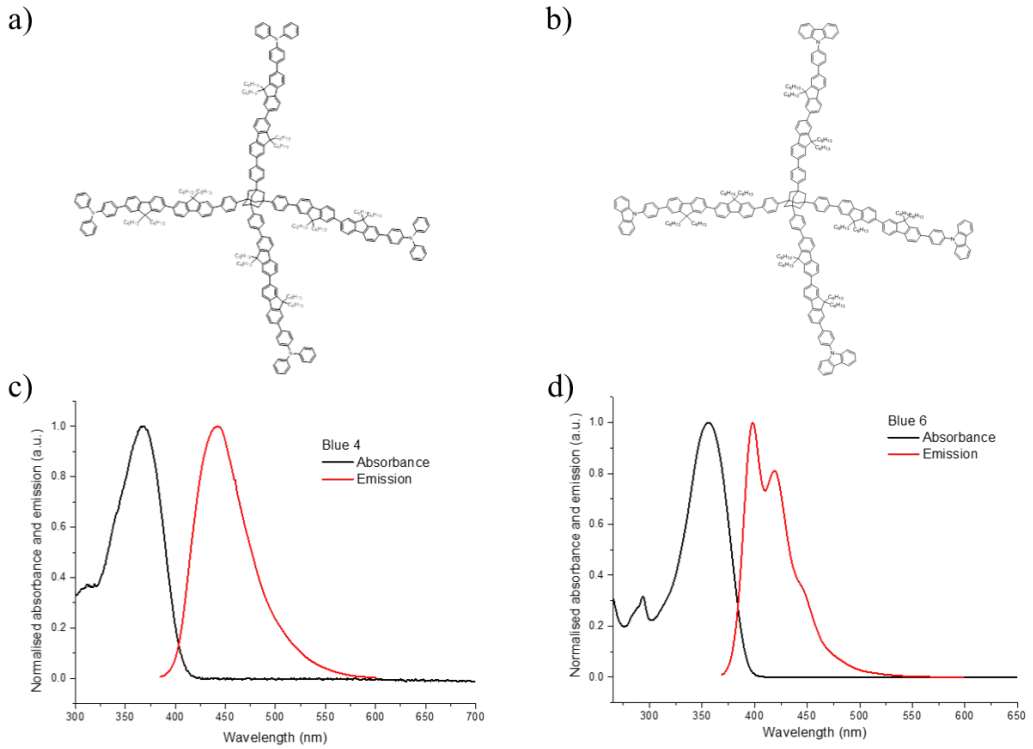

FIGURE 5.15: a) The molecular structure for Blue 4, b) the molecular structure of Blue 6, c) the absorption and emission profiles of Blue 4 and d) absorption and emission profiles of Blue 6.

n∼1.46, to create thin films of different density and/or thicknesses. The edge emission for the same optical excitation conditions (see optical characterisation below) was studied for all samples.

For DFB lasers, thin-films were formed onto 276 nm periodic grating structures, using the same procedure as above (see also Chapter 2).

5.3.2 Optical characterisation of Blue 4 and Blue 6

For characterising the Blue 4 and Blue 6 thin films the same Nd: YAG solid state laser was used as the optical pump source, section 2.4. The thin films were tested in a variable stripe setup where the beam size is controlled by an adjusting slit set for most of the measurements to a fixed size of 0.15cm x 0.01cm. For the measurement of the gain of the 4krpm Blue 4 film the stripe length was varied.

For characterisation of the DFB laser structures a larger pump stripe (both in length and width) where the stripe was created using a 1cm by 1cm cylindrical lens focused (∼0.74 cm by ∼0.1 cm) onto the polymers surface.

TABLE 5.5: Blue 4 diluted at 10 mg.mL^{-1} in toluene thin film spin rates, peak wavelength and threshold fluences.

Spin rate (krpm)	λ_{main} (nm)	F ($\mu J/cm^2$)
1	440.3	290
2	433.9	2150
3	439.2	20680

5.4 Results

5.4.1 Blue 4

5.4.1.1 ASE and random lasing in thin films

The main ASE characteristics (peak wavelength and the fluence for ASE threshold) of the Blue 4 films made from an initial solution concentration of 10 mg.mL^{-1} in toluene can be seen in table 5.5. The samples are identified by the spinning speed utilised for their fabrication (1, 2 and 3 krpm). The peak wavelengths of the edge emission indicated correspond to the point of maximum intensity.

The spectra of the 2krpm sample for different pump excitation level can be seen in figure 5.16a. Above a certain excitation level, a dominant spectral peak occurs at 433.9 nm with a FWHM of 0.3 nm. The evolution with the pump fluence of the intensity of this peak, integrated over the region 433.5nm to 433.9 nm, is plotted in figure 5.16b. It displays a characteristic threshold at $\sim$ 2150 $\mu J/cm^2$ above which the intensity initially increases exponentially before saturating for pump fluence above $\sim$ 4500 $\mu J/cm^2$. It is above the ASE threshold that narrowing of the spectrum with a dominant narrow peak appears. This state is attributed to the phenomenon of "random lasing" that is triggered by ASE in a scattering medium. ASE is characterised by a threshold-like function in the edge intensity accompanied by a narrowing of the emission spectrum as seen here, but the spectral narrowing is usually not as pronounced. A typical ASE spectrum has a FWHM around 5 to 20 nm (depending on material and pumping conditions), section 1.3.5. If significant scattering is present however, narrower spectral peaks can appear and are identified as "random lasing" modes (see Chapter 2). The wavelength of the dominant mode remains constant when the fluence is increased. However, at higher fluence, additional random lasing peaks appear across the range 430 nm to 438 nm. The spectrum is different when pumping a different spot on the sample (i.e.

TABLE 5.6: Blue 4 diluted at 20 mg.mL^{-1} in toluene thin film spin rates, peak wavelength and threshold fluences.

Spin rate (krpm)	λ_{main} (nm)	F ($\mu J/cm^2$)
2	445.9	122
4	443.0	174
5	442.1	189
6	443.7	189
8	437 (/445 after annealing)	470 (/149 after annealing)

the random lasing modes are at different wavelengths, although the ASE is in the same wavelength range) but the overall behaviour remains the same.

The red line in figure 5.16b, is a guide to the eye. There is ASE saturation for pump above ∼4500 $\mu J/cm^2$. This intensity saturation behaviour is attributed to depletion of the material gain. At higher pump energies a shoulder also appears at around 440nm, centred at 442.8 nm. This could be the result of excitation of another vibronic energy level being obtained and can be seen in other samples.

The 1krpm sample has a similar behaviour but has an ASE/random lasing threshold that is lower. The ASE develops between 437nm and 443nm, i.e. slightly red-shifted compared to the 2krpm, figure 5.17. The lower threshold and red-shift are attributed to a thicker film. The 3 krpm on the other hand barely reaches the ASE regime - the estimated threshold being above 20 mJ/cm^2. The film is probably below, or very close to, the cut-off thickness and no efficient guiding occurs.

The second concentration of Blue 4 studied was 20 mg.mL^{-1} in toluene and the main ASE/RL characteristics of the samples are given in table 5.6.

The spectra and integrated intensity as a function of pump energy of the 8krpm sample can be seen in figure 5.18. We note that the ASE develops at a similar wavelength than the 1krpm - 10mg.mL^{-1} sample while the threshold is slightly lower (∼470 $\mu J/cm^2$). From the spectra in figure 5.18, it can be seen that there are 2 main random laser peaks. The initial peak occurs 436.8nm and has a FWHM of 1.2 nm. This is the dominant mode, having the highest spectral intensity reading, until an excitation energy fluence of ∼4500 $\mu J/cm^2$. After this the 438.4nm mode with FWHM 0.8nm, becomes dominant. Other modes can be seen to appear as well and competition is inevitable. There is gain saturation for fluence above 4000 $\mu J/cm^2$.

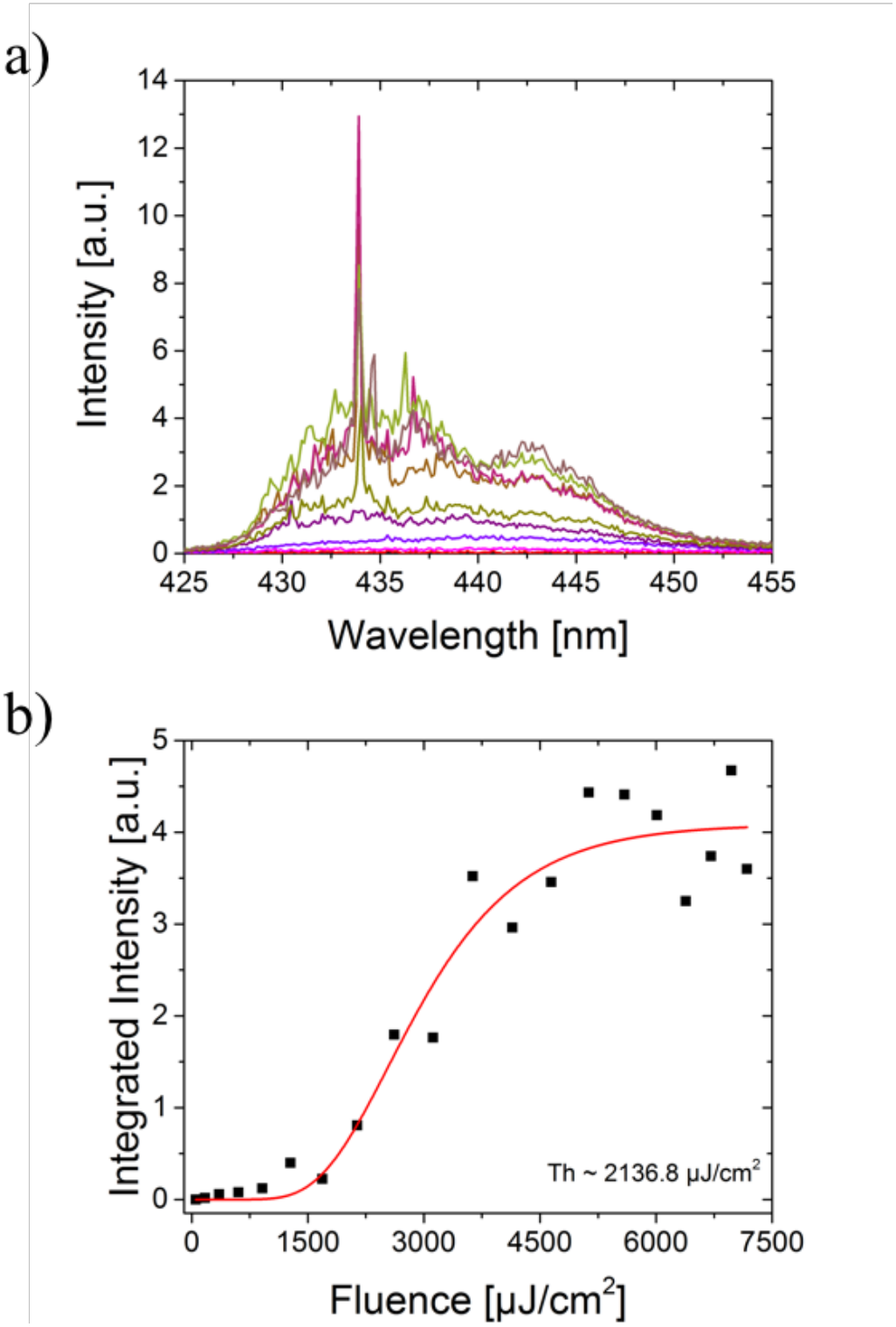

FIGURE 5.16: 2krpm Blue 4 film (10 mg.mL^{-1} in toluene) spectrum at different pump fluence (53 $\mu J/cm^2$ to 7170 $\mu J/cm^2$). a) A random lasing mode at 433.9 nm, FWHM of 0.3 nm, dominates. b) Integrated intensity versus pump fluence the red line is a guide to the eye.

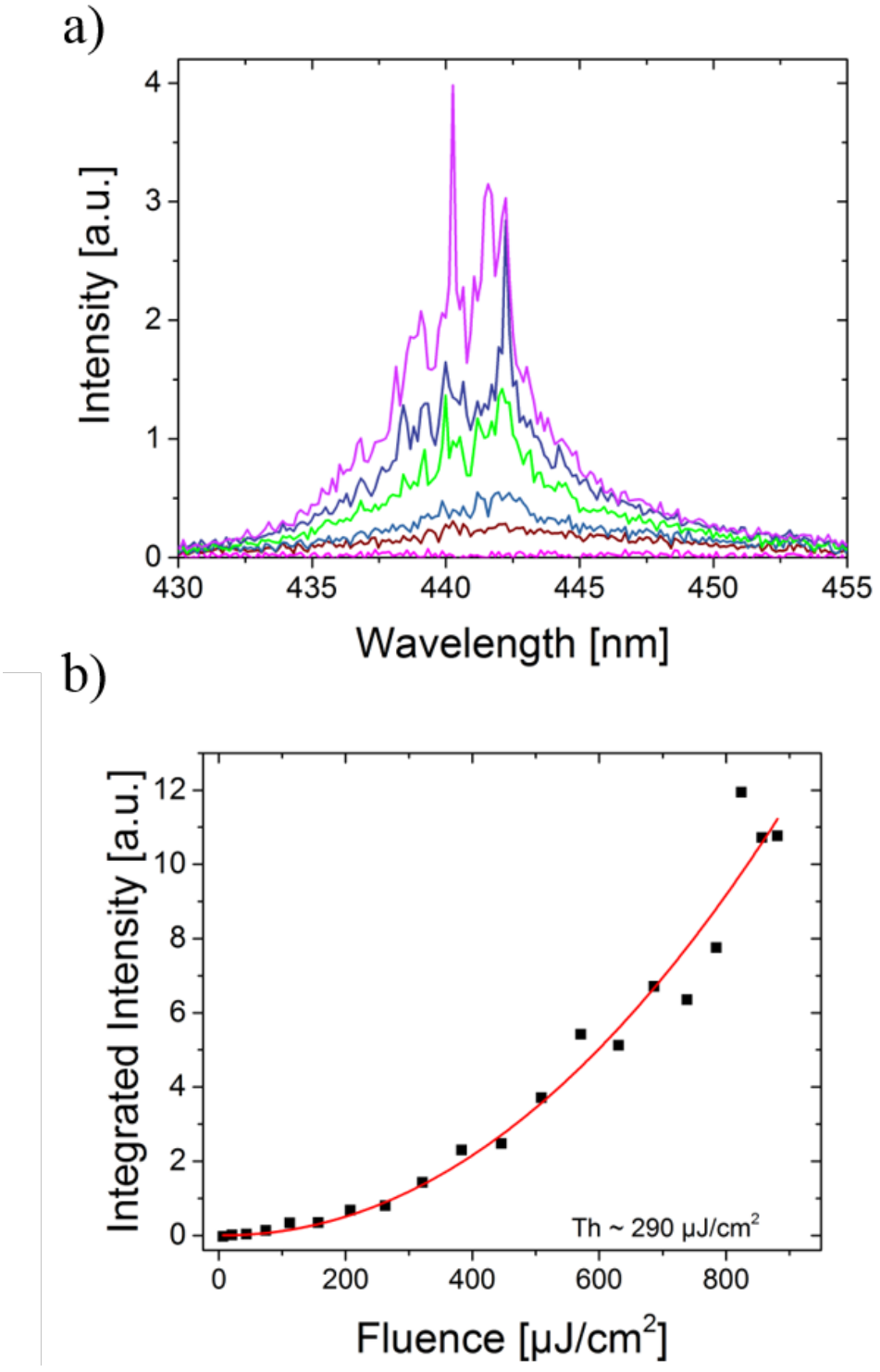

FIGURE 5.17: Blue 4 at 10mg.mL^{-1} spun cast onto planar glass substrate at 1krpm excited over a pump range of 6 $\mu J/cm^2$ to 880 $\mu J/cm^2$. a) Main random lasing mode occurring at 440.3nm with FWHM of 0.6 nm and b) the corresponding transfer function.

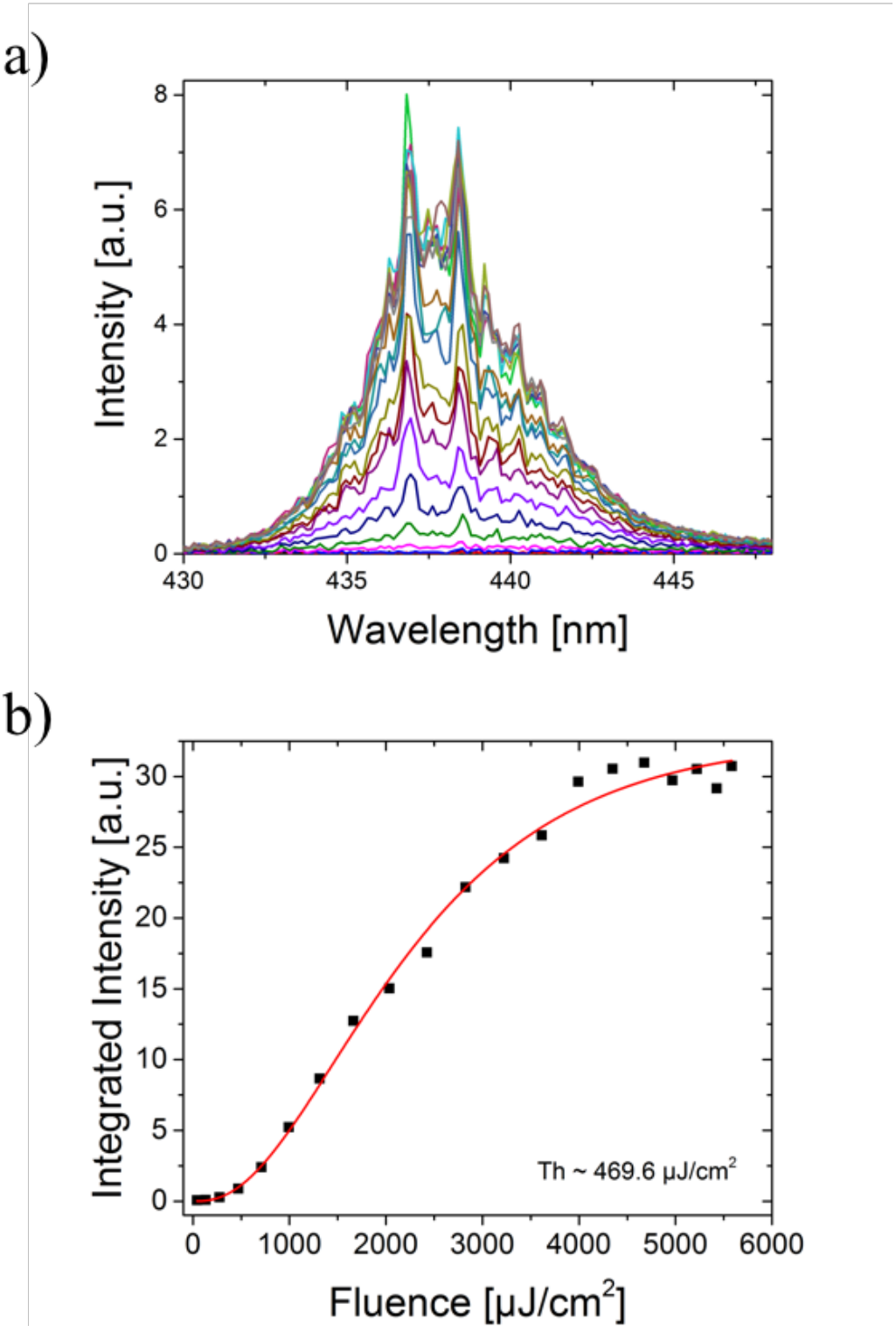

FIGURE 5.18: 8krpm Blue 4 film (20 mg.mL^{-1} in toluene); a) spectrum at different fluence values (ranging over 40 $\mu J/cm^2$ to 5580 $\mu J/cm^2$) showing 2 main peaks occurring at 438.4nm and 436.8nm; b) integrated intensity versus pump fluence.

Overall, the trend is for the ASE threshold to increase with spin-rate, which is consistent with a thinner film (a thinner film translating into a lower overlap between the guided modes and the material, hence a lower modal gain). With the exception of the 8krpm sample, all samples made from 20 mg.mL^{-1} solution have the ASE developing between 442 nm and 446 nm (second vibronic transition), i.e. red-shifted when compared to the 10 mg.mL^{-1} samples. Again, this is consistent with a stronger interaction of the guided modes with the Blue 4 material. This is due the increase in concentration giving a thicker film.

For indication the modal gain of the 4krpm sample was measured using the variable stripe length approach. The gain was calculated to be 20.6 $\pm$ 0.4 cm^{-1}, at approximately 0.18 μJ ($\sim$ 66 $\mu J/cm^2$), similar to what is expected when compared with oligofluorene truxene [27, 55]. This would vary under different conditions, such as a higher pump energy. Here, the intensity was recorded at a specific excitation stripe length. The stripe was then expanded and again the intensity recorded. This was done for a number of increments until the slit, used to control stripe length, was fully open. The recorded intensity was then plotted as a function of strip length, figure 5.19 [56–58]. The gain is calculated on Origin by fitting,

$$y = A\frac{e^{gx} - 1}{g}. \tag{5.1}$$

Here the 2krpm saturates at $\sim$ 612 $\mu J/cm^2$, 4 and 5 krpm sample does not reach saturation, the 6krpm sample reaches saturation at $\sim$ 945 $\mu J/cm^2$, and the 8krpm sample at $\sim$ 4680 $\mu J/cm^2$. There is also a trend in the evolution of the pump level for the onset of ASE saturation. Saturation happens at lower pump fluence for lower spin speeds. Because saturation is caused by depletion of the gain (population inversion) of the material by strongly amplified modes, this will occur at higher pumping level for thinner films.

5.4.1.2 Solvent annealing

The 8krpm sample was then left in a toluene atmosphere for 1 week to observe if any possible alterations of the arrangement of the molecules within the film could be inferred from the edge emission measurements. Figure 5.20a displays the evolution of the spectra of this sample. It is clear that there is now a periodic

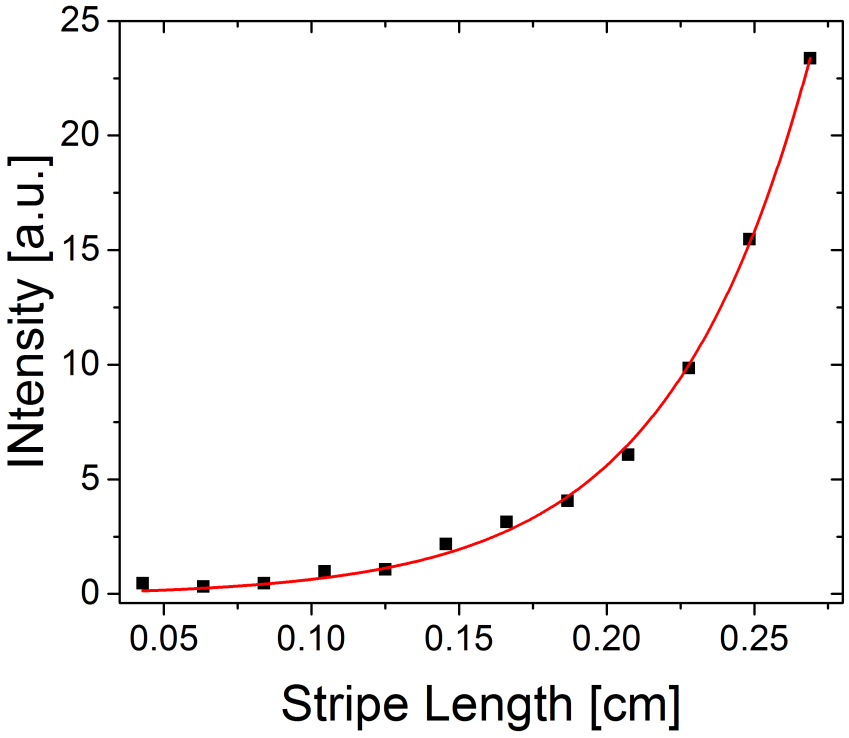

FIGURE 5.19: Variable stripe length (VSL) gain measurement on 4krpm thin film of Blue 4 optically excited at 17 μJ giving a gain coefficient of 20 cm^{-1}.

modulation of the ASE spectrum, akin to a Fabry-Pérot effect. The creation of a structure inducing feedback/scattering in the stripe direction having a characteristic length of 50 to 70 microns could explain such a periodic spectrum. This was observed over a number of different locations measured on the sample but the exact origin of the behaviour is not known. The threshold energy has also decreased to ~149 $\mu J/cm^2$. The packing density of the Blue 4 molecules in the film has possibly increased and/or the overall scattering decreased which would explain the reduction in the ASE threshold. Narrow peaks start to develop at the maxima of the ASE periodicity, as the fluence is increased.

No definitive conclusions can be made at the moment apart from the fact that annealing has an effect on the overall ASE characteristics.

5.4.1.3 DFB laser

With the demonstration of ASE and random lasing occurring in the Blue 4 films, such films were deposited onto NOA 65 grating structures to define DFB laser

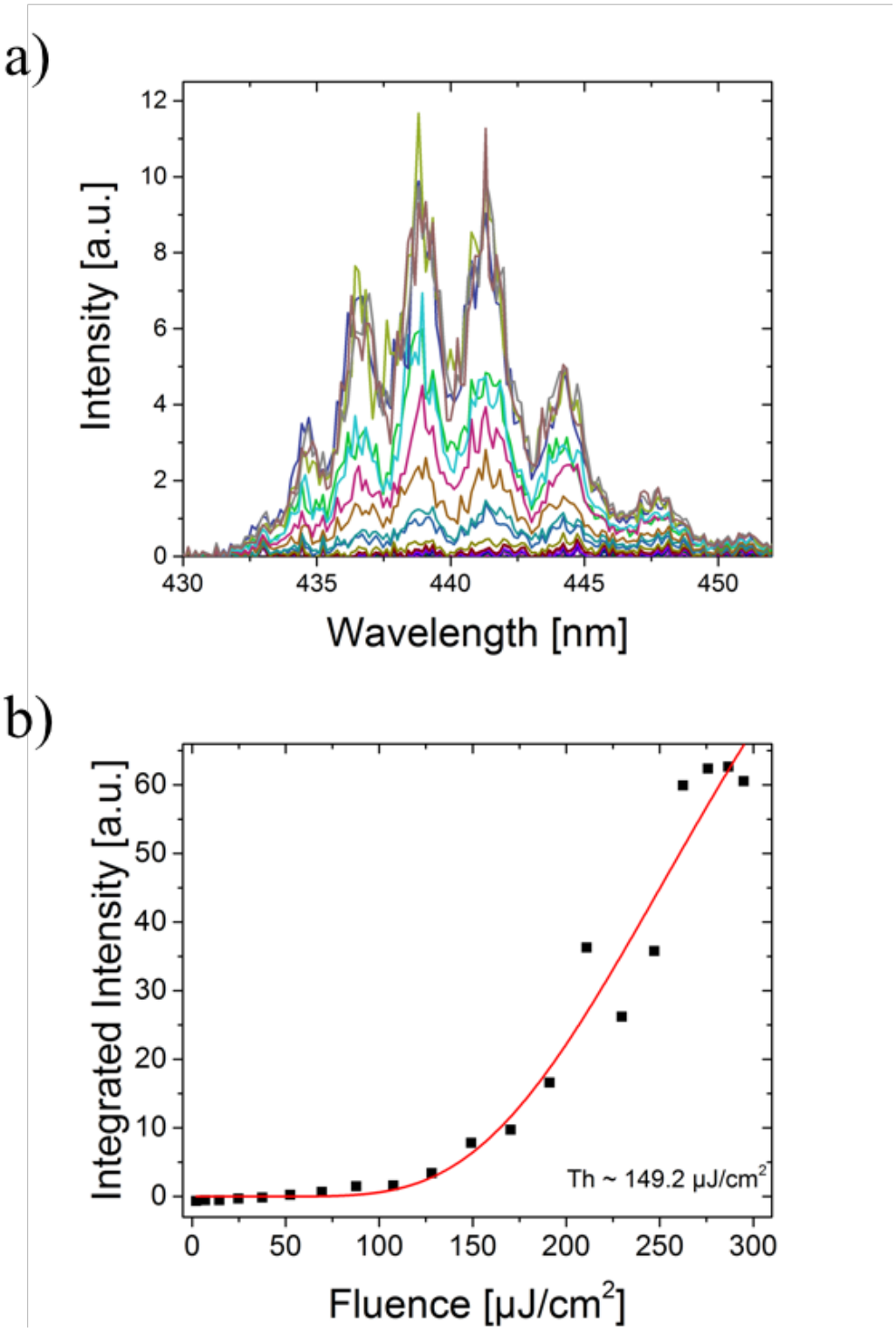

FIGURE 5.20: Sample annealed in a toluene atmosphere for 1 week. a) Spectra (for pump fluencies ranging from 2 $\mu J/cm^2$ to 300 $\mu J/cm^2$); b) Integrated intensity versus pump fluence.

TABLE 5.7: DFB laser based on Blue 4 diluted at 20 mg.mL^{-1} in toluene - spin rate, emission wavelength and threshold.

Spin rate (krpm)	λ_{main} (nm)	$E_{th,main}$ (μJ)
5	452.2	3.10
6	439.3	0.15
7	431.6	0.35
8	434.6	3.20

structures. This was again done over a range of spin speed where the properties can be seen in table 5.7.

The laser wavelengths tend to blue shift with decreasing film thickness, as expected. The only exception being the samples with lower spin rates that have a multimodal emission. Spectral analysis of lower spin rates shows very little detectable emission resulting in the corresponding transfer functions being unclear to whether there is photoluminescence or gain observed (as the emission is at a similar level to the noise). This could be due to the film thickness being too thin for resonance to occur with the cavity structure for the corresponding grating period. Figure 5.21 displays the results of the Blue 4 DFB laser with a 6krpm spin rate. The figure displays single mode emission and is centred at 439.3 nm with a FWHM of 0.35 nm. Figure 5.21b displays the transfer function of the laser emission, figure 5.21a, with threshold energy 0.15μJ.

5.5 Blue 6

5.5.1 ASE and random lasing in thin films

Blue 6 was tested. It was dispersed in toluene at a concentration of 20 mg.mL^{-1}. Again, optical characterisation of the thin films was carried out for a few different deposition spin rates. Table 5.8 list the main values found. No trend can be extracted from these values. All samples develop ASE/random lasing like for Blue 4 where the films were then applied to the same grating structures as with Blue 4 (Λ = 276nm, NOA 65), although no lasing was demonstrated.

Figure 5.22a displays the spectra for the 5krpm sample. Here the main random lasing peak can be seen at 422.3nm with a FWHM of 0.49 nm. From the spectral

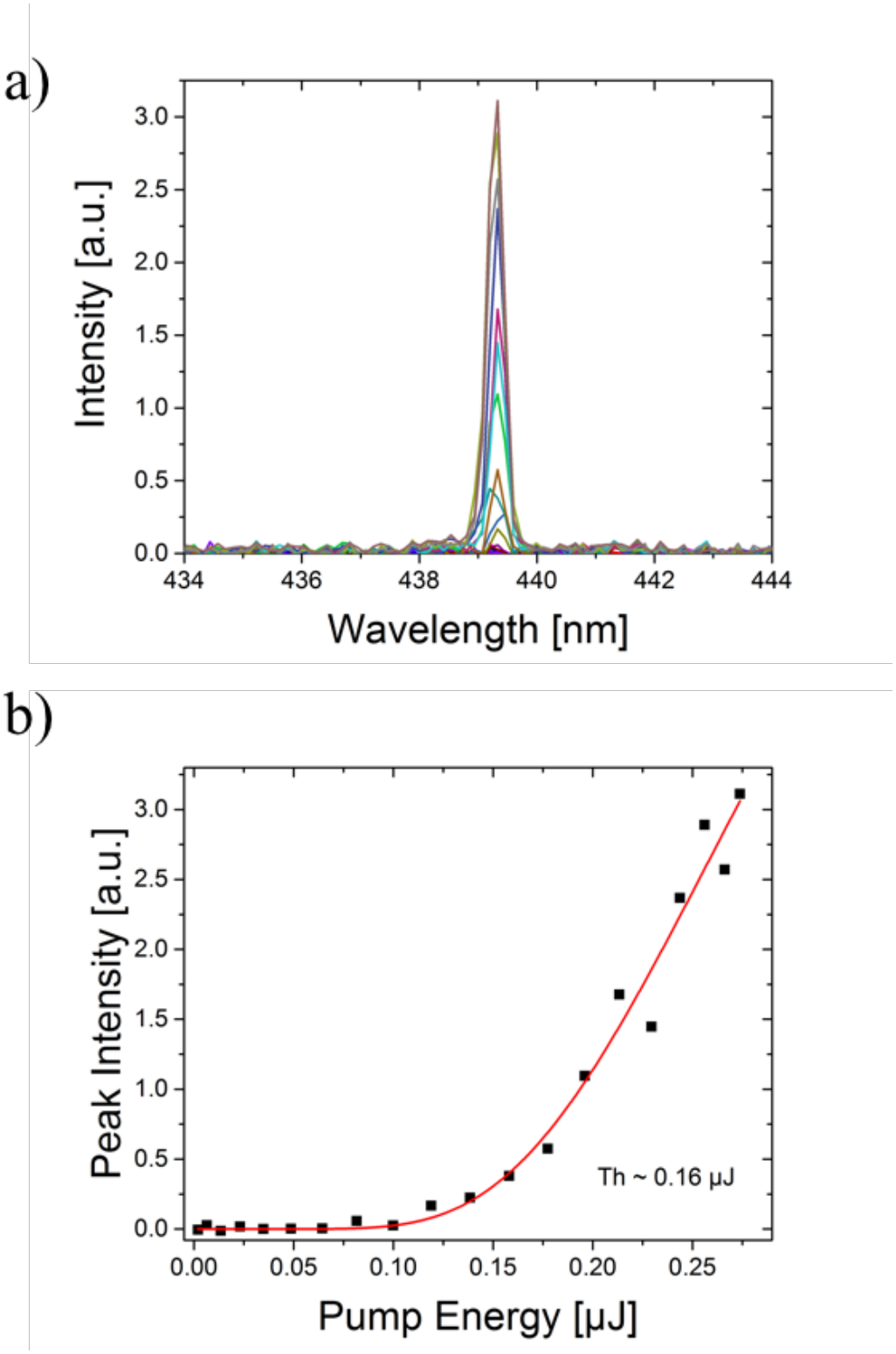

FIGURE 5.21: Blue 4 DFB laser, spin rate 6krpm, grating NOA 65, 276nm period, a) spectra (excited over a pump range 0.002 μJ to 0.3 μJ) and b) the corresponding transfer function.

TABLE 5.8: Blue 6 diluted at 20 mg.mL^{-1} in toluene thin film spin rates, peak emitting wavelength and threshold fluencies'.

Spin rate (krpm)	λ_{main} (nm)	$E_{th,main}$ (μJ)
4	423.9	298
5	422.3	258
6	424.7	165
7	424.7	157
8	424.3	279

evolution it is the dominant mode throughout. Figure 5.22b displays the integrated intensity of this peak giving a threshold fluence of $\sim$258 $\mu J/cm^2$.

5.6 Conclusion

This chapter reported on experiments of Super Yellow polymer and Blue 4 and Blue 6 oligofluorene materials for use in lasers.

Super Yellow is a well-known soluble phenyl-substituted polyphenylenevinylene (PPV) copolymer that has been utilised mainly for its photoluminescent qualities. Used for OLEDs SY has also been beneficial for LEFETs and colour conversion of LEDs. SY is known to have high chain regularity, can withstand temperatures greater than room temperature and has even demonstrated lasing in DFB formats. When applied as thin film its properties are a priori ideal for DFB laser-based refractive index sensing.

DFB laser oscillation using a neat film of SY was reported. Operation in liquids was demonstrated. An assessment of the capability for bulk refractive sensing was carried out by monitoring the laser wavelength when immersed in liquids of different refractive indices. Bulk refractive index sensitivity of around 10 nm per refractive index unit, which does not compare favourably with organic DFB laser sensor made with other materials; where Haughey *et al* report a 21nm sensitivity per refractive index unit with Truxene [26]. However, inhomogeneities of the SY film here led to a multimodal emission that severely limited the resolution and repeatability and prevented optimisation and more precise studies. Photosatbility is also an issue. Further work is needed where the SY film is formed by techniques other than spin-coating.

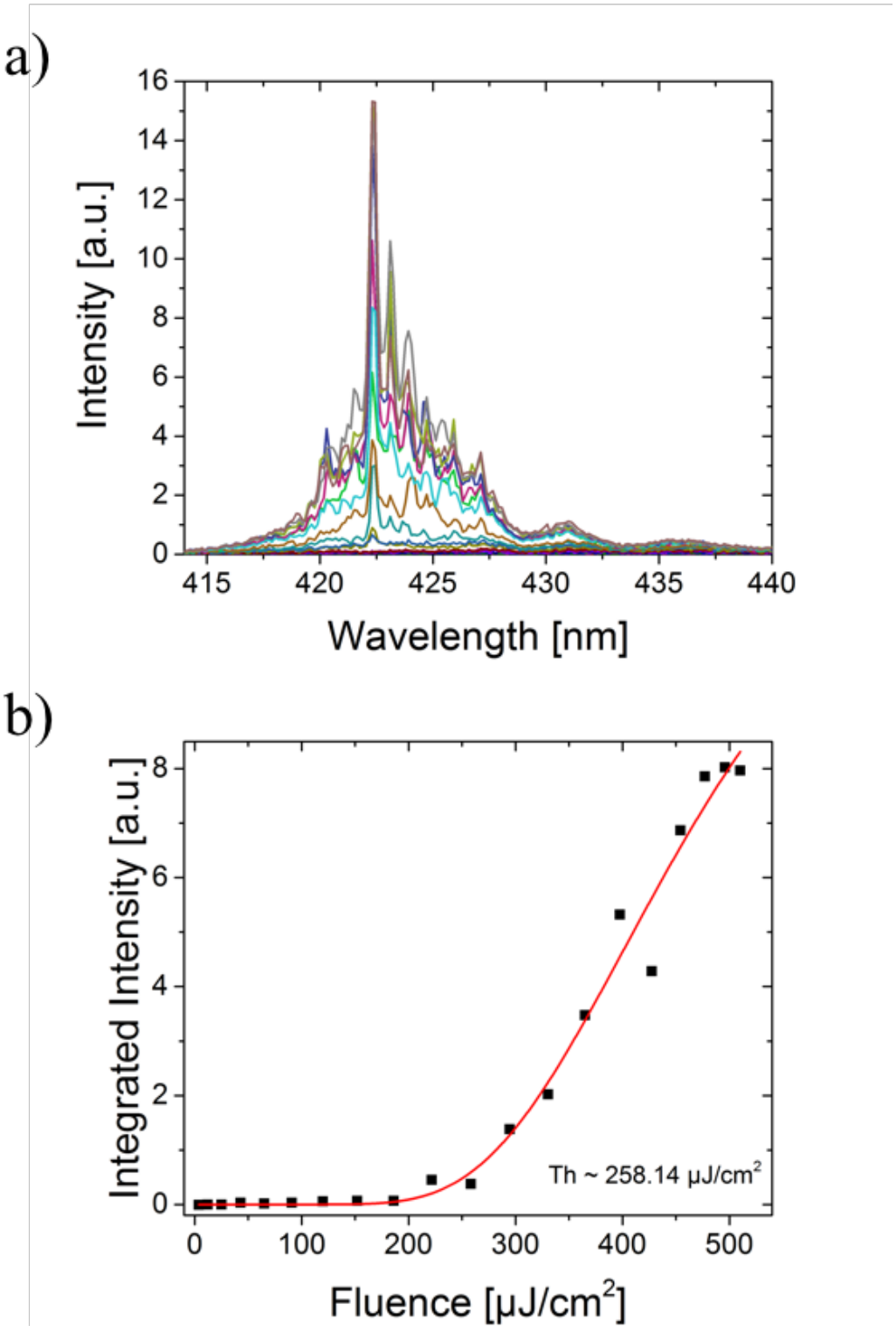

FIGURE 5.22: 5krpm spin rate of Blue 6 film diluted at 20 mg.mL^{-1} in toluene. a) Spectral evolution (excited over a pump fluence range 3 $\mu J/cm^2$ to 510 $\mu J/cm^2$) with the main mode occurring at 422.3 nm and b) transfer function of integrated intensity verse pump fluence.

SY DFB lasers encapsulated with PVA and parylene were demonstrated. The PVA/SY/DFB laser produced a threshold of $\sim 1.1 \mu J$ emitting at 587.6 nm and the parylene/SY/DFB laser produced a threshold of $\sim$ 1.75 μJ at 585.5 nm. The latter could improve photostability and overall performance, while paving the way for incorporation and utilisation of lasers within a biological environment.

Blue 4 and Blue 6 oligofluorene macromolecules were also reported in this chapter. Films of both showed ASE with random lasing phenomena, probably caused by scattering due to the nature of the materials. Blue 4 was also demonstrated in a DFB laser.

Blue 4 was initially tested at 2 concentrations in thin films spun cast on planar glass substrates. These produced ASE in the form of random lasing. At 10 mg.mL^{-1} the films are not thick or dense enough to consistently support propagation explaining the difference in spectra and ASE thresholds. Blue 4 film formed from 20mg.mL^{-1} solutions have lower ASE thresholds. The ASE intensity is found to saturate at the higher spin rates while the threshold increases. This is due to the thinner films producing less modal confinement within the gain region. One Blue 4 sample annealed in a toluene atmosphere for 1 week, displayed reduced ASE threshold as well as a change in the measured spectra. These changes are attributed to changes in the spatial arrangement of the Blue 4 molecules within the film, although no definitive conclusion can be made at this stage. A single mode Blue 4 DFB laser was demonstrated.

Blue 6 was tested in thin films made from 20 mg.mL^{-1} solutions. Again random lasing was observed. No trend with the spin rates was seen with the emission wavelength and threshold energies remaining constant. The grating periodicity was not adequate to demonstrate a Blue 6 DFB laser (Blue 6 has emission at lower wavelengths in comparison to Blue 4).

References

[1] Salvatore Gambino, Ashu K. Bansal, and Ifor D W Samuel. Photophysical and charge-transporting properties of the copolymer Super Yellow. *Organic Electronics: physics, materials, applications*, 14(8):1980–1987, 2013. ISSN 15661199. doi: 10.1016/j.orgel.2013.03.038. URL http://dx.doi.org/10.1016/j.orgel.2013.03.038.

[2] Min Zhang, Stefan Höfle, Jens Czolk, Adrian Mertens, and Alexander Colsmann. All-solution processed transparent organic light emitting diodes. *Nanoscale*, 7:20009–20014, 2015. ISSN 2040-3364. doi: 10.1039/C5NR05820A. URL http://pubs.rsc.org/en/Content/ArticleLanding/2015/NR/C5NR05820A.

[3] Johannes Herrnsdorf, Benoit Guilhabert, Yujie Chen, Alexander Kanibolotsky, Allan Mackintosh, Richard Pethrick, Peter Skabara, Erdan Gu, Nicolas Laurand, and Martin Dawson. Flexible blue-emitting encapsulated organic semiconductor DFB laser. *Optics Express*, 18(25):25535, dec 2010. ISSN 1094-4087. doi: 10.1364/OE.18.025535. URL http://www.ncbi.nlm.nih.gov/pubmed/21164899https://www.osapublishing.org/oe/abstract.cfm?uri=oe-18-25-25535.

[4] B. Guilhabert, N. Laurand, J. Herrnsdorf, Y. Chen, a. L. Kanibolotsky, C. Orofino, P. J. Skabara, and M. D. Dawson. Mechanically Flexible Organic Semiconductor Laser Array. *IEEE Photonics Journal*, 4(3):684–690, jun 2012. ISSN 1943-0655. doi: 10.1109/JPHOT.2012.2195651. URL http://ieeexplore.ieee.org/lpdocs/epic03/wrapper.htm?arnumber=6188505.

[5] Boris Riedel, Julian Hauss, Markus Aichholz, Andre Gall, Uli Lemmer, and Martina Gerken. Polymer light emitting diodes containing nanoparticle clusters for improved efficiency. *Organic Electronics: physics, materials, applications*, 11(7):1172–1175, 2010. ISSN 15661199. doi: 10.1016/j.orgel.2010.04.017. URL http://dx.doi.org/10.1016/j.orgel.2010.04.017.

[6] Benoit Guilhabert, Nicolas Laurand, Johannes Herrnsdorf, Yujie Chen, Allan R Mackintosh, Alexander L Kanibolotsky, Erdan Gu, Peter J Skabara, R A Pethrick, and Martin D Dawson. Amplified spontaneous emission in free-standing membranes incorporating star-shaped monodisperse π-conjugated truxene oligomers. *Journal of Optics*, 12(3):035503, mar 2010. ISSN 2040-8978. doi: 10.1088/2040-8978/12/3/035503. URL http://stacks.iop.org/2040-8986/12/i=3/a=035503?key=crossref.f2d55d4b545464bef95062e56601aa92.

[7] C. Foucher, B. Guilhabert, N. Laurand, and M. D. Dawson. Wavelength-tunable colloidal quantum dot laser on ultra-thin flexible glass. *Applied Physics Letters*, 104(14):141108, apr 2014. ISSN 0003-6951. doi: 10.1063/1.4871372. URL `http://scitation.aip.org/content/aip/journal/apl/104/14/10.1063/1.4871372`.

[8] Magnus Berggren and Agneta Richter-Dahlfors. Organic bioelectronics. *Advanced Materials*, 19(20):3201–3213, 2007. ISSN 09359648. doi: 10.1002/adma.200700419.

[9] Maria D. Angione, Rosa Pilolli, Serafina Cotrone, Maria Magliulo, Antonia Mallardi, Gerardo Palazzo, Luigia Sabbatini, Daniel Fine, Ananth Dodabalapur, Nicola Cioffi, and Luisa Torsi. Carbon based materials for electronic bio-sensing. *Materials Today*, 14 (9):424–433, 2011. ISSN 13697021. doi: 10.1016/S1369-7021(11)70187-0. URL `http://dx.doi.org/10.1016/S1369-7021(11)70187-0`.

[10] Shufang Zheng, Jun Lu, Jingjing Shi, and Xue Duan. Two-dimensional confined electron donoracceptor co-intercalated inorganic/organic nanocomposites: an effective photocatalyst for dye degradation. *RSC Adv.*, 7(5):2789–2795, 2017. ISSN 2046-2069. doi: 10.1039/C6RA25534E. URL `http://xlink.rsc.org/?DOI=C6RA25534E`.

[11] S. C. Yan, Z. S. Li, and Z. G. Zou. Photodegradation Performance of g-C3N4 Fabricated by Directly Heating Melamine S. *Langmuir*, 25(17):10397–10401, 2009. ISSN 07437463. doi: 10.1021/la900923z.

[12] H. Neugebauer, C. Brabec, J. C. Hummelen, and N. S. Sariciftci. Stability and photodegradation mechanisms of conjugated polymer/fullerene plastic solar cells. *Solar Energy Materials and Solar Cells*, 61(1):35–42, 2000. ISSN 09270248. doi: 10.1016/S0927-0248(99)00094-X.

[13] Christoph Vannahme, Sönke Klinkhammer, Mads Brøkner Christiansen, Alexander Kolew, Anders Kristensen, Uli Lemmer, and Timo Mappes. All-polymer organic semiconductor laser chips: parallel fabrication and encapsulation. *Optics express*, 18(24):24881–24887, 2010. ISSN 1094-4087. doi: 10.1364/OE.18.024881.

[14] Wei Yang Chou and Horng Long Cheng. An orientation-controlled pentacene film aligned by photoaligned polyimide for organic thin-film transistor applications. *Advanced Functional Materials*, 14(8):811–815, 2004. ISSN 1616301X. doi: 10.1002/adfm.200305047.

[15] Wei Zhao, Ti Cao, and John M. White. On the origin of green emission in polyfluorene polymers: The roles of thermal oxidation degradation and crosslinking. *Advanced Functional Materials*, 14(8):783–790, 2004. ISSN 1616301X. doi: 10.1002/adfm.200305173.

[16] M Atreya, S Li, E T Kang, K G Neoh, Z H Ma, K L Tan, and W Huang. Stability studies of poly(2-methoxy-5-(2'-ethyl hexyloxy)-p-(phenylene vinylene) [MEH-PPV]. *Polymer Degradation and Stability*, 65:287–296, 1999. ISSN 0141-3910. doi: http://dx.doi.org/10.1016/S0141-3910(99)00018-X.

[17] E. Yariv and R. Reisfeld. Laser properties of pyrromethene dyes in sol-gel glasses. *Optical Materials*, 13(1):49–54, 1999. ISSN 09253467. doi: 10.1016/S0925-3467(99)00010-5.

[18] Manuel G Ramirez, Pedro G Boj, Victor Navarro-Fuster, Igor Vragovic, José M Villalvilla, Ibon Alonso, Vera Trabadelo, Santos Merino, and María A. Díaz-García. Efficient organic distributed feedback lasers with imprinted active films. *Optics Express*, 19(23):22443–22454, 2011. ISSN 1094-4087. doi: 10.1364/OE.19.022443.

[19] V. Trabadelo, A. Juarros, A. Retolaza, S. Merino, M. G. Ramírez, V. Navarro-Fuster, J. M. Villalvilla, P. G. Boj, J. A. Quintana, and M. A. Díaz-García. Highly photostable solid-state organic distributed feedback laser fabricated via thermal nanoimprint lithography. *Microelectronic Engineering*, 87(5-8):1428–1430, 2010. ISSN 01679317. doi: 10.1016/j.mee.2009.11.142. URL `http://dx.doi.org/10.1016/j.mee.2009.11.142`.

[20] Victor Navarro-Fuster, Eva M. Calzado, Pedro G. Boj, José A. Quintana, José M. Villalvilla, María A. Díaz-García, Vera Trabadelo, Aritz Juarros, Aritz Retolaza, and Santos Merino. Highly photostable organic distributed feedback laser emitting at 573 nm. *Applied Physics Letters*, 97(17):1–4, 2010. ISSN 00036951. doi: 10.1063/1.3506500.

[21] G. H Kim, L Shao, K Zhang, and K P Pipe. Engineered doping of organic semiconductors for enhanced thermoelectric efficiency. *Nature materials*, 12(8):719–23, 2013. ISSN 1476-1122. doi: 10.1038/nmat3635. URL `http://www.ncbi.nlm.nih.gov/pubmed/23644522`.

[22] Van Duong Ta, Rui Chen, and Han Dong Sun. Self-assembled flexible microlasers. *Advanced Materials*, 24(10), 2012. ISSN 09359648. doi: 10.1002/adma.201103409.

[23] C. Foucher, B. Guilhabert, A. L. Kanibolotsky, P. J. Skabara, N. Laurand, and M. D. Dawson. Highly-photostable and mechanically flexible all-organic semiconductor lasers. *Optical Materials Express*, 3(5):584, apr 2013. ISSN 2159-3930. doi: 10.1364/OME.3.000584. URL `http://www.opticsinfobase.org/abstract.cfm?URI=ome-3-5-584`.

[24] Andrea Camposeo, Pompilio Del Carro, Luana Persano, and Dario Pisignano. Electrically tunable organic distributed feedback lasers embedding nonlinear optical molecules. *Advanced Materials*, 24(35):221–225, 2012. ISSN 09359648. doi: 10.1002/adma.201201453.

[25] Graziela V L Gomes, Mirella R. Sola, Luis F P Marostegan, Camila G. Jange, Camila P S Cazado, Ana C. Pinheiro, Antonio A. Vicente, and Samantha C. Pinho. Physico-chemical stability and in vitro digestibility of beta-carotene-loaded lipid nanoparticles of cupuacu butter (Theobroma grandiflorum) produced by the phase inversion temperature (PIT) method. *Journal of Food Engineering*, 192:93–102, 2017. ISSN 02608774. doi: 10.1016/j.jfoodeng.2016.08.001.

[26] A Haughey, B Guilhabert, A L Kanibolotsky, P J Skabara, G A Burley, M D Dawson, and N Laurand. Sensors and Actuators B : Chemical An organic semiconductor laser based on star-shaped truxene-core oligomers for refractive index sensing. *Sensors & Actuators: B. Chemical*, 185:132–139, 2013. ISSN 0925-4005. doi: 10.1016/j.snb.2013.04.026. URL `http://dx.doi.org/10.1016/j.snb.2013.04.026`.

[27] Ruidong Xia, Wen Yong Lai, Peter A. Levermore, Wei Huang, and Donal D C Bradley. Low-threshold distributed-feed back lasers based on pyrene-cored starburst molecules with

1,3,6,8attached oligo(9,9-Dialkylfluorene) arms. *Advanced Functional Materials*, 19(17): 2844–2850, 2009. ISSN 1616301X. doi: 10.1002/adfm.200900503.

[28] Yan Shao, Guillermo C. Bazan, and Alan J. Heeger. Long-lifetime polymer light-emitting electrochemical cells. *Advanced Materials*, 19(3):365–370, 2007. ISSN 09359648. doi: 10.1002/adma.200602087.

[29] M. U. Hassan, Yee Chen Liu, Kamran Ul Hasan, H. Butt, Jui Fen Chang, and R. H. Friend. Highly efficient PLEDs based on poly(9,9-dioctylfluorene) and Super Yellow blend with Cs2CO3 modified cathode. *Applied Materials Today*, 1(1):45–51, 2015. ISSN 23529407. doi: 10.1016/j.apmt.2015.08.005. URL `http://dx.doi.org/10.1016/j.apmt.2015.08.005`.

[30] Samantha Burns, Jennifer MacLeod, Thu Trang Do, Prashant Sonar, and Soniya D. Yambem. Effect of thermal annealing Super Yellow emissive layer on efficiency of OLEDs. *Scientific Reports*, 7:40805, 2017. ISSN 2045-2322. doi: 10.1038/srep40805. URL `http://www.nature.com/articles/srep40805`.

[31] Ebinazar B Namdas, Ifor D W Samuel, Deepak Shukla, Dianne M Meyer, Yanming Sun, Ben B Y Hsu, Daniel Moses, Alan J Heeger, Ebinazar B Namdas, Ifor D W Samuel, Deepak Shukla, and Dianne M Meyer. Organic light emitting complementary inverters Organic light emitting complementary inverters. *Applied Physics Letters*, 96(4), 2010. doi: 10.1063/1.3293293.

[32] Ebinazar B. Namdas, Minghong Tong, Peter Ledochowitsch, Sarah R. Mednick, Jonathan D. Yuen, Daniel Moses, and Alan J. Heeger. Low Thresholds in Polymer Lasers on Conductive Substrates by Distributed Feedback Nanoimprinting: Progress Toward Electrically Pumped Plastic Lasers. *Advanced Materials*, 21(7):799–802, feb 2009. ISSN 09359648. doi: 10.1002/adma.200802436. URL `http://doi.wiley.com/10.1002/adma.200802436`.

[33] Herbert Lifka, Cristina Tanase, Dave Mcculloch, Peter Van De Weijer, and Ian French. Ultra-Thin Flexible OLED Device. *Electronics*, pages 1599–1602, 2007. ISSN 0097966X. doi: 10.1889/1.2785625.

[34] Bernd Gruska and Sven Peters. Organic Light Emitting Diodes. *Homo*, 20: 1–12, 2005. URL `http://stacks.iop.org/0268-1242/20/i=8/a=019?key=crossref.836d1fce9166742cca3efc60051978b2`.

[35] Mujeeb Ullah, Kristen Tandy, Jun Li, Zugui Shi, Paul L. Burn, Paul Meredith, and Ebinazar B. Namdas. High-Mobility, Heterostructure Light-Emitting Transistors and Complementary Inverters. *ACS Photonics*, 1(10):954–959, oct 2014. ISSN 2330-4022. doi: 10.1021/ph500300n. URL `http://pubs.acs.org/doi/abs/10.1021/ph500300n`.

[36] X. Gong, D. Moses, A. J. Heeger, S. Liu, and A. K.-Y. Jen. High-performance polymer light-emitting diodes fabricated with a polymer hole injection layer. *Applied Physics Letters*, 83(1):183, 2003. ISSN 00036951. doi: 10.1063/1.1589185. URL `http://scitation.aip.org/content/aip/journal/apl/83/1/10.1063/1.1589185`.

[37] Sujan Rajbhandari, Jonathan J D Mckendry, Johannes Herrnsdorf, Hyunchae Chun, Grahame Faulkner, Harald Haas, Ian M Watson, Dominic O Brien, and Martin D Dawson. A review of Gallium Nitride LEDs for multi-gigabit-per-second visible light data communications. *Semiconductor Science and Technology*, 32(2):1–44, 2016. ISSN 0268-1242. doi: 10.1088/1361-6641/32/2/023001.

[38] Hyunchae Chun, Pavlos Manousiadis, Sujan Rajbhandari, Dimali a. Vithanage, Grahame Faulkner, Dobroslav Tsonev, Jonathan James Donald McKendry, Stefan Videv, Enyuan Xie, Erdan Gu, Martin D. Dawson, Harald Haas, Graham A. Turnbull, Ifor D. W. Samuel, and Dominic C. O'Brien. Visible Light Communication Using a Blue GaN μLED and Fluorescent Polymer Color Converter. *IEEE Photonics Technology Letters*, 26(20):2035–2038, 2014. ISSN 1041-1135. doi: 10.1109/LPT.2014.2345256. URL `http://ieeexplore.ieee.org/lpdocs/epic03/wrapper.htm?arnumber=6871350`.

[39] I D W Samuel and G A Turnbull. Organic semiconductor lasers. *Chem. Rev.*, 107(4): 1272–1295, 2007. ISSN 0009-2665. doi: 10.1021/cr050152i. URL `http://www.ncbi.nlm.nih.gov/pubmed/17385928`.

[40] Victor Navarro-Fuster, Igor Vragovic, Eva M. Calzado, Pedro G. Boj, Jose a. Quintana, Jose M. Villalvilla, Aritz Retolaza, Aritz Juarros, Deitze Otaduy, Santos Merino, and Maria a. Diaz-Garcia. Film thickness and grating depth variation in organic second-order distributed feedback lasers. *Journal of Applied Physics*, 112(4):043104, 2012. ISSN 00218979. doi: 10.1063/1.4745047. URL `http://scitation.aip.org/content/aip/journal/jap/112/4/10.1063/1.4745047`.

[41] Anne-Marie Haughey, Caroline Foucher, Benoit Guilhabert, Alexander L Kanibolotsky, Peter J Skabara, Glenn Burley, Martin D Dawson, and Nicolas Laurand. Hybrid organic semiconductor lasers for bio-molecular sensing. In *Faraday Discussions*, volume 174, pages 369–381, 2014. doi: 10.1039/c4fd00091a.

[42] Fabio Cucinotta, Fabio Carniato, Andre Devaux, Luisa De Cola, and Leonardo Marchese. Efficient photoinduced energy transfer in a newly developed hybrid SBA-15 photonic antenna. *Chemistry - A European Journal*, 18(48):15310–15315, 2012. ISSN 09476539. doi: 10.1002/chem.201202505.

[43] Fabio Cucinotta, Fabio Carniato, Geo Paul, Silvia Bracco, Chiara Bisio, Stefano Caldarelli, and Leonardo Marchese. Incorporation of a semiconductive polymer into mesoporous SBA-15 platelets: Toward new luminescent hybrid materials. *Chemistry of Materials*, 23(11): 2803–2809, 2011. ISSN 08974756. doi: 10.1021/cm103670w.

[44] E. W. Snedden, L. a. Cury, K. N. Bourdakos, and a. P. Monkman. High photoluminescence quantum yield due to intramolecular energy transfer in the Super Yellow conjugated copolymer. *Chemical Physics Letters*, 490(1-3):76–79, 2010. ISSN 00092614. doi: 10.1016/j.cplett.2010.03.030. URL `http://dx.doi.org/10.1016/j.cplett.2010.03.030`.

[45] Shinya Maenosono, Tatsuya Okubo, and Yukio Yamaguchi. Overview of Nanoparticle Array Formation by Wet Coating. *Journal of Nanoparticle Research*, 5(1/2):5–15, apr 2003. ISSN

1388-0764. doi: 10.1023/A:1024418931756. URL http://link.springer.com/10.1023/A:1024418931756.

[46] Johannes Herrnsdorf, Benoit Guilhabert, Jonathan McKendry, Zheng Gong, David Massoubre, Yujie Chen, Shuailong Zhang, Alexander L. Kanibolotsky, Allan R. Mackintosh, Peter J. Skabara, Anthony E. Kelly, Erdan Gu, Nicolas Laurand, and Martin D. Dawson. Hybrid GaN/organic polymer photonic crystal LED. In *IEEE Photonic Society 24th Annual Meeting*, volume 3, pages 389–390. IEEE, oct 2011. ISBN 978-1-4244-8939-8. doi: 10.1109/PHO.2011.6110591. URL http://ieeexplore.ieee.org/lpdocs/epic03/wrapper.htm?arnumber=6110591http://ieeexplore.ieee.org/document/6110591/.

[47] C. Foucher, B. Guilhabert, J. Herrnsdorf, N. Laurand, and M. D. Dawson. Diode-pumped, mechanically-flexible polymer DFB laser encapsulated by glass membranes. *Optics Express*, 22(20):24160, sep 2014. ISSN 1094-4087. doi: 10.1364/OE.22.024160. URL http://www.opticsinfobase.org/abstract.cfm?URI=oe-22-20-24160.

[48] L. J. McLellan, B. Guilhabert, N. Laurand, and M. D. Dawson. CdSxSe1-x/ZnS semiconductor nanocrystal laser with sub 10kW/cmˆ2 threshold and 40nJ emission output at 600 nm. *Optics Express*, 24(2):A146, 2016. ISSN 1094-4087. doi: 10.1364/OE.24.00A146. URL https://www.osapublishing.org/abstract.cfm?URI=oe-24-2-A146.

[49] P L Santos, B B A Costa, K S Araujo, L a Cury, E W Snedden, K N Bourdakos, F B Dias, and A P Monkman. Measurement of interchain and intrachain exciton hopping barriers in luminescent polymer. *Journal of Physics: Condensed Matter*, 24:015801, 2011. ISSN 0953-8984. doi: 10.1088/0953-8984/24/1/015801.

[50] Michael M. Adachi, Fengjia Fan, Daniel P. Sellan, Sjoerd Hoogland, Oleksandr Voznyy, Arjan J. Houtepen, Kevin D. Parrish, Pongsakorn Kanjanaboos, Jonathan A. Malen, and Edward H. Sargent. Microsecond-sustained lasing from colloidal quantum dot solids. *Nature Communications*, 6:8694, 2015. ISSN 2041-1723. doi: 10.1038/ncomms9694. URL http://www.nature.com/doifinder/10.1038/ncomms9694.

[51] Yoshihide Fukaya, Yuki Obama, Shu Hotta, and Takeshi Yamao. Spectrally narrowed emissions from organic crystals mounted on transfer-printed parylene diffraction gratings Spectrally narrowed emissions from organic crystals mounted on transfer-printed parylene diffraction gratings. *Japanese Journal of Applied Physics*, 53(1S), 2013.

[52] Damien C. Rodger, James D. Weiland, Mark S. Humayun, and Yu Chong Tai. Scalable high lead-count parylene package for retinal prostheses. *Sensors and Actuators, B: Chemical*, 117(1):107–114, 2006. ISSN 09254005. doi: 10.1016/j.snb.2005.11.010.

[53] Gerald E. Loeb, M. J. Bak, E. M. Schmidt, and M. Salcman. Parylene as a Chronically Stable, Reproducible Microelectrode Insulator. *IEEE Transactions on Biomedical Engineering*, BME-24(2):121–128, 1977. ISSN 15582531. doi: 10.1109/TBME.1977.326115.

[54] Sushmitha Kuppusami and Reza H Oskouei. Parylene Coatings in Medical Devices and Implants : A Review. *Universal Journal of Biomedical Engineering*, 3(2):9–14, 2015. doi: 10.13189/ujbe.2015.030201.

[55] Georgios Tsiminis, Yue Wang, Paul E. Shaw, Alexander L. Kanibolotsky, Igor F. Perepichka, Martin D. Dawson, Peter J. Skabara, Graham A. Turnbull, and Ifor D W Samuel. Low-threshold organic laser based on an oligofluorene truxene with low optical losses. *Applied Physics Letters*, 94(24):1–4, 2009. ISSN 00036951. doi: 10.1063/1.3152782.

[56] Johannes Herrnsdorf, Yujie Chen, Benoit Guilhabert, Nicolas Laurand, and Martin D. Dawson. Stripe Excitation of High Gain Media With Disorder. *IEEE Journal of Quantum Electronics*, 48(9):1184–1192, sep 2012. ISSN 0018-9197. doi: 10.1109/JQE.2012.2204959. URL `http://ieeexplore.ieee.org/lpdocs/epic03/wrapper.htm?arnumber=6220842`.

[57] Victor I. Klimov, Sergei A. Ivanov, Jagjit Nanda, Marc Achermann, Ilya Bezel, John A. McGuire, and Andrei Piryatinski. Single-exciton optical gain in semiconductor nanocrystals. *Nature*, 447(7143):441–446, may 2007. ISSN 0028-0836. doi: 10.1038/nature05839. URL `http://www.ncbi.nlm.nih.gov/pubmed/17522678http://www.nature.com/doifinder/10.1038/nature05839`.

[58] Hyochul Kim, Kyung-Sang Cho, Heejeong Jeong, Jineun Kim, Chang-Won Lee, Weon-kyu Koh, Young-Geun Roh, Sung Woo Hwang, and Yeonsang Park. Single-Mode Lasing from a Monolithic Microcavity with Few-Monolayer-Thick Quantum Dot Films. *ACS Photonics*, page acsphotonics.6b00327, 2016. ISSN 2330-4022. doi: 10.1021/acsphotonics.6b00327. URL `http://pubs.acs.org/doi/abs/10.1021/acsphotonics.6b00327`.

Part III

Conclusion and Outlook

Chapter 6

Conclusion and outlook

6.1 Summary

This thesis is focused on colloidal quantum dot laser technology primarily through the use hybrid organic/inorganic structures in order to progress its usability for applications. The main objective was to improve the threshold performance of CQD lasers. CQDs offer the ability for solution-processing, emission wavelength over the entire visible spectrum tuned typically via the size of their physical diameter, composition, or a combination of both. Low thresholds with 5ns long pulse pumping were achieved using a bi-layer CQD DFB cavity. Reported thresholds are in principle low enough that laser diode pumping can now be considered. A CQD VCSEL emitting in the yellow/orange was then demonstrated in the same pumping temporal regime and its polarisation dependence on the pump spin studied. While the focus was on CQDs, solution-processed organic semiconductor materials were also utilised with laser-based sensing applications in mind.

All devices exploited within this research are solution-processable, potentially low cost and allow operational emission throughout the visible spectrum. The ease of fabrication would allow for simplicity and flexibility in the manufacturing of photonic devices being applicable to their use on multiple substrates and platforms; materials are compatible with soft-lithography and compatible with conformable technology.

In chapter 3 the main objective of improving CQD laser performance (to partly close the gap with OSs) was addressed. Here, it was shown that the alloyed-core/shell CQDs achieved DFB laser operation, under 5ns long pulse excitation regime, with threshold approximately a factor of five times smaller than previous studies of core/shell CQDs under the same pump conditions. This was reduced further through encapsulation that reduced scattering at the surface of the CQD gain layer and by using an alloyed-core/shell CQD structure. Reported threshold are in principle low enough that laser oscillation could be accomplished via laser diode pumping. The encapsulation also increased photostability.

Chapter 4 then explored the use of the CQDs in VCSEL format. A wedged design allowed for the side injection of the CQD gain material, in solution form, between two DBRs. Once the solvent had evaporated the devices were again optically excited with 5ns pumping and laser emission at approximately 590 nm was achieved. The device was investigated under two pump spot sizes. The polarisation of the CQD-VCSEL device was also explored leading to the Stoke's parameters being calculated. This lead on to observe if the CQD-VCSEL had any polarisation spin-dependency dependent on the pump.

The last experimental chapter (chapter 5) goes on to explore the use of (i) an existing copolymer Super Yellow in a new format and (ii) two new materials fabricated in the Pure and Applied Chemistry Group at the university. Super Yellow has previously been seen to demonstrate laser operation, and due to its high refractive index properties is a priori an ideal candidate for refractive index sensing devices. To the author's knowledge, is the only completely ambient fabrication and operation of a single transverse mode DFB laser. The DFB grating was fabricated using soft-lithography techniques with an optical adhesive and master grating. The device was examined under varying effective refractive index conditions and in encapsulated media. Unfortunately, the limited operational lifetime of the material and the inhomogeneity in the films made it difficult to properly assess its true capability for bio-sensing. Initial bulk refractive index performance obtained was lower than what is typically obtained with oligofluorene truxene or other organic laser materials.

The Blue 4 and Blue 6 materials, fabricated by Dr Neil Findley, were straightforward to work with. In the initial characterisation steps both materials were seen to produce random lasing in thin films. This was demonstrated over a range of different spin rates i.e. different film thicknesses. When employed as a gain

medium in DFB lasers, Blue 4 displayed strong single mode emission. The gratings were made up of the same optical adhesive as for Super Yellow but with a smaller periodicity. Unfortunately, DFB lasing of Blue 6 was not achieved. This is due to an in inadequate grating period for its emission profile, equation 2.9, where it is believe that the material will produce gain in DFB format.

In conclusion, the work presented in this thesis brings the operation of colloidal quantum dot lasers closer to real-world application showing the potential for diode-pumped (low-cost and compact) photostable laser operation. It also shows the use of these gain materials in different laser formats opening up potential applications in different fields. The thesis also brings some light on the challenges to overcome to use SY as a DFB laser biosensor material and assess the capability of Blue 4 and Blue 6 oligofluorene as laser materials.

6.2 Prospectives for solution-processed lasers

From the PVA/CQD/DFB results reported in this thesis, it can be seen that thresholds have reached a low enough level to achieve laser diode pumping. Operation of this type would allow compact systems and is the logical next step in the exploration of CQD DFB lasers. Since our demonstrations, a couple of reports in the literature have looked at even longer pulse duration with quasi-CW demonstrations and diode pumping has been reported [1]. What these and our studies show is that progress in threshold performance is obtained by advances in the CQD materials themselves but also in the design and quality of the laser cavity structures.

6.2.1 CQD laser cavities

We have seen that lowering the loss in a planar laser structure can be obtained by overcoating the gain layer. In a vertical cavity laser, this could be obtained by reducing the gain region thickness (which would necessitate high gain CQDs) and increasing the DBR reflectivity. Another way is to utilise an external cavity for mode control as was done in [2]. Such a cavity opens up applications in sensing but also could enable high brightness emission akin to the work done with other materials: semiconductor disk lasers (SDLs) with epitaxial semiconductor

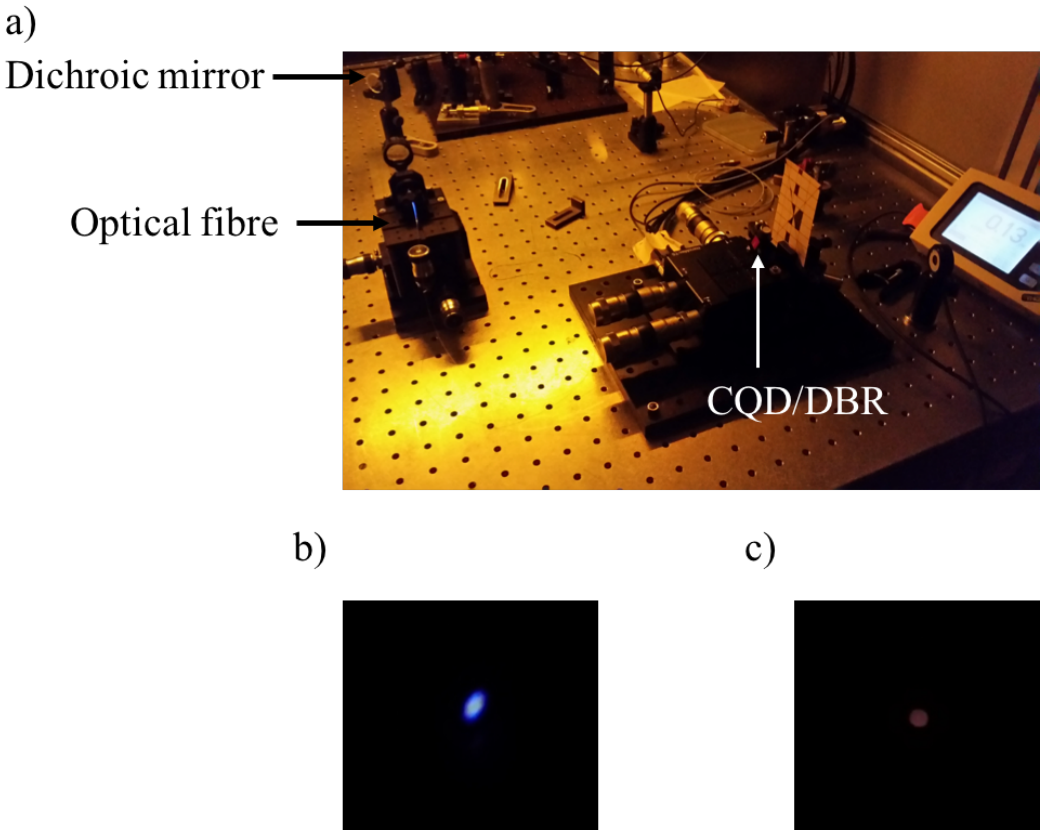

FIGURE 6.1: a) Optical setup showing injected pump, b) successful coupling of pump and c) CQD emission.

structures and VECSOLs with organic dyes. Having an external cavity also enables tuning of wavelength by moving one cavity mirror with respect to the other [3]. Such investigation could be carried out in our laboratory, for example by using a DBR-coated fibre as in [4]. Initial steps that we took can be seen in figure 6.1 where the optical setup used in the investigation, with coupling of the pump, is depicted along with the pump emission exiting the fibre and CQD excitation. A broadband DBR was coated with CQDs (intrinsic PL at 630nm). The Nd: YAG used through this thesis was coupled into an optical fibre. The light was sent onto the CQD surface where the CQD emission was couple back into the fibre. Using a dichroic mirror the CQD emission and pump light were separated where the emission is collected by another optical fibre behind the dichroic mirror connected to a spectrometer. Once CQD detection is achieved, the end of the optical fibre, use to pump and collect, will be coated with a dielectric film. This would allow resonance to occur where, with the position of the fibre, would lead to tunable emission.

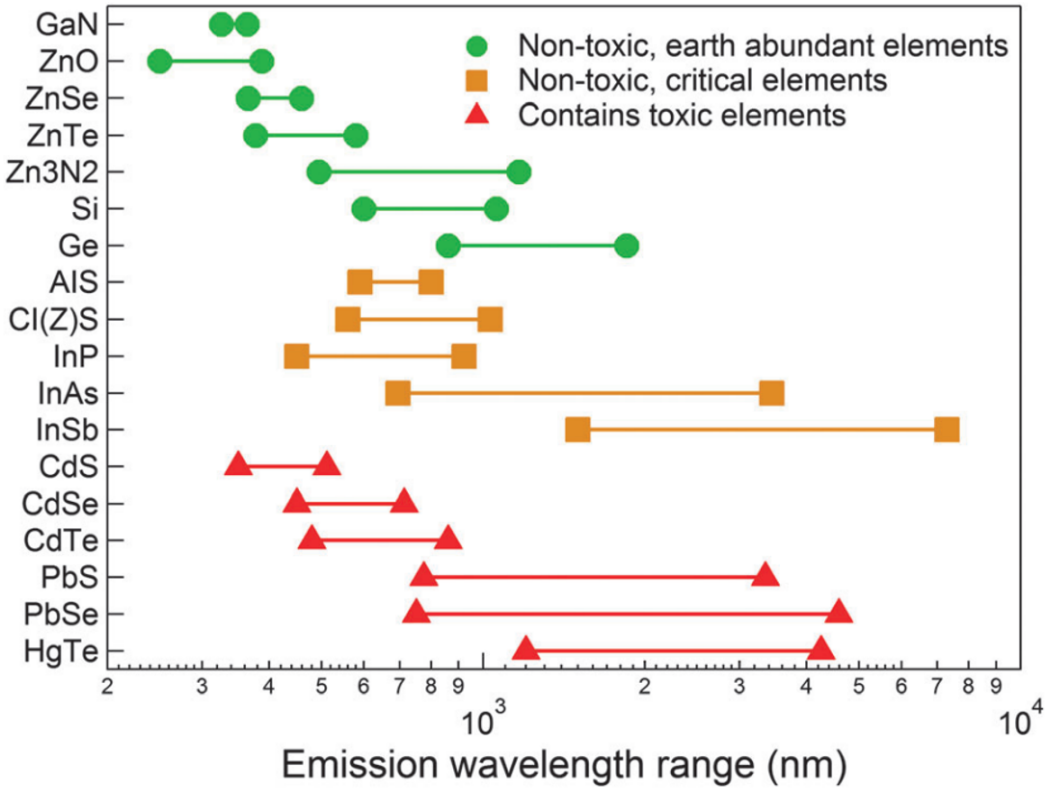

FIGURE 6.2: Taken from [9] plot depicts the emission tunability of selected CQD materials.

6.2.2 CQD laser materials

CQD materials are being exploited more and more in photonic applications. As discussed in Chapter 1, the advancement of this material as a technology has rapidly progressed since the demonstration of optical gain in films [5]. Starting out as a core NC, a semiconductor shell was added improving features such as PLQY and ease of film fabrication. CQDs offer a balance between performance and sustainability as fabrication through solution-based synthesis is low-cost and scalable. Optoelectronic properties are tunable during this procedure allowing customisation of the optimising their performance.

The majority of reports on CQDs are based off of carcinogenic heavy-metal based semiconducting materials, in particular Cd. Cd based CQDs benefit from a mature, well researched synthesis process enabling them to be monodispersed with high PLQY. These synthesis procedures have extended into different geometries of NC, such as nano-platelets [6] and solution processed quantum wells [7, 8]. Figure 6.2, from [9], displays the emission wavelengths of selected CQD materials where the red elements represent materials containing toxic elements.

This advancement in the synthesis techniques have driven application in soft lithography allowing Cd based CQDs to be used as an effective visible gain material. Where, utilising a two-dimensional 2nd order DFB cavity, CW lasing has been claimed [1]. Once CW pumping is established the next step would be to employ LED pumping as has been demonstrated for OS DFB lasers [10]. Other laser formats have also been reported, in particular VCSELs. Dang *et al* reported injected Cd based CQDs into wedged DBRs producing a red emitting device under fs pulse pumping [11]. Patel *et al* expanded this work into open cavities allowing for the emission wavelength to be tuned by the cavity length, remaining in fs pumping [2]. The work presented in this thesis builds on VCSEL structures and achieved an orange emission, a wavelength difficult to obtain through traditional methods, under ns pumping. The next step would be to bridge the gap by achieving faster and faster pump pulse rate with the end goal of a CW device.

Development of nanoplatelets for visible gain materials will advanced this technology as they retain many of the properties of CQDs, such as tuning their emission wavelength by variation of their size. These differ as they have a larger absorption cross-section and have shown a reduction in non-radiative Auger-recombination [2].

With CQDs also being looked at for commercial products, non-toxic (Cd-free) alternative materials have been investigated. The most common material investigated is InP where high PLQY has been achieved. These are primarily used in colour conversion films for LEDs [12] and solid-state lighting [13]. Unfortunately, no InP CQD based lasers have been reported. The green elements is figure 6.2 represent non-toxic CQD materials and the orange elements non-toxic materials containing InP.

Expanding on the different materials, Perovskite quantum dots have recently found popularity. These are based off of Caesium and Lead, $CsPbX_3$ (X being Br, Cl or I), and display large and perfect crystalline structures that improve their optoelectronic properties (others are based off of $MPbX_3$ (M being an organic)). Traction has been gained as Perovskites offer solution processing, cheap synthesis and high efficiencies, with a broad-band absorption and long exciton diffusion length [14]. This has lead to applications such in colour conversion and photovoltaic cells (i.e. solar cells). Perovskites have also demonstrated laser operation in VCSELs when employed as a bulk structure [14] and in colloidal form [15]. The latter utilises fs pulsed pumping and was reported after the work in Chapter 4 was completed.

Again, progression would involve increasing the pump duration until CW pumping was obtained allowing for compact devices to me made.

References

[1] Fengjia Fan, Oleksandr Voznyy, P Randy, Kristopher T Bicanic, Michael M Adachi, James R Mcbride, Kemar R Reid, Young-shin Park, Xiyan Li, Ankit Jain, Rafael Quintero-bermudez, Mayuran Saravanapavanantham, Min Liu, Marek Korkusinski, Pawel Hawrylak, Victor I Klimov, Sandra J Rosenthal, Sjoerd Hoogland, and Edward H Sargent. Continuous-wave lasing in colloidal quantum dot solids enabled by facet-selective epitaxy. *Nature*, 544(7648): 1–18, 2017. ISSN 0028-0836. doi: 10.1038/nature21424. URL `http://dx.doi.org/10.1038/nature21424`.

[2] Robin K Patel, Aurélien A P Trichet, David M Coles, Philip R Dolan, Simon M Fairclough, Marina A Leontiadou, S C Edman Tsang, David J Binks, Eunjoo Jang, Hyosook Jang, Robert A Taylor, and Jason M Smith. Gain Spectroscopy of Solution-Based Semiconductor Nanocrystals in Tunable Optical Microcavities. *Advanced Optical Materials*, 4(2):285–290, 2016. ISSN 2195-1071. doi: 10.1002/adom.201500363. URL `http://dx.doi.org/10.1002/adom.201500363`.

[3] Oussama Mhibik, Tatiana Leang, Alain Siove, Sebastien Forget, and Sebastien Chenais. Broadly tunable (440-670 nm) solid-state organic laser with disposable capsules. *Applied Physics Letters*, 102(4), 2013. ISSN 00036951. doi: 10.1063/1.4790294.

[4] N. Laurand, S. Calvez, M.D. Dawson, T. Jouhti, J. Konttinen, and M. Pessa. Fiber-tunable dilute-nitride VCSEL. *Physica Status Solidi (C)*, 2(11):3895–3898, 2005. ISSN 1610-1634. doi: 10.1002/pssc.200562016. URL `http://doi.wiley.com/10.1002/pssc.200562016`.

[5] V. I. Klimov. Optical Gain and Stimulated Emission in Nanocrystal Quantum Dots. *Science*, 290(5490):314–317, oct 2000. ISSN 00368075. doi: 10.1126/science.290.5490.314. URL `http://www.sciencemag.org/cgi/doi/10.1126/science.290.5490.314`.

[6] Yusuf Kelestemur, Murat Olutas, Savas Delikanli, Burak Guzelturk, Mehmet Zafer Akgul, and Hilmi Volkan Demir. Type-II Colloidal Quantum Wells: CdSe/CdTe Core/Crown Heteronanoplatelets. *Journal of Physical Chemistry C*, 119:21772185, 2015. ISSN 1932-7447. doi: 10.1021/jp510466k.

[7] Joel Q. Grim, Sotirios Christodoulou, Francesco Di Stasio, Roman Krahne, Roberto Cingolani, Liberato Manna, and Iwan Moreels. Continuous-wave biexciton lasing at room temperature using solution-processed quantum wells. *Nature Nanotechnology*, 9(11):891–895, oct 2014. ISSN 1748-3387. doi: 10.1038/nnano.2014.213. URL `http://www.ncbi.nlm.nih.gov/pubmed/25282045http://www.nature.com/doifinder/10.1038/nnano.2014.213`.

[8] Erfan Baghani, Stephen K. O'Leary, Igor Fedin, Dmitri V. Talapin, and Matthew Pelton. Auger-Limited Carrier Recombination and Relaxation in CdSe Colloidal Quantum Wells. *The Journal of Physical Chemistry Letters*, page 150302175751004, 2015. ISSN 1948-7185. doi: 10.1021/acs.jpclett.5b00143. URL `http://pubs.acs.org/doi/abs/10.1021/acs.jpclett.5b00143`.

[9] Joel Q. Grim, Liberato Manna, and Iwan Moreels. A sustainable future for photonic colloidal nanocrystals. *Chem. Soc. Rev.*, 44(16):5897–5914, 2015. ISSN 0306-0012. doi: 10.1039/C5CS00285K. URL `http://xlink.rsc.org/?DOI=C5CS00285K`.

[10] Johannes Herrnsdorf, Yue Wang, Jonathan J D Mckendry, Zheng Gong, David Massoubre, Benoit Guilhabert, Georgios Tsiminis, Graham A. Turnbull, Ifor D W Samuel, Nicolas Laurand, Erdan Gu, and Martin D. Dawson. Micro-LED pumped polymer laser: A discussion of future pump sources for organic lasers. *Laser and Photonics Reviews*, 7(6):1065–1078, 2013. ISSN 18638880. doi: 10.1002/lpor.201300110.

[11] Cuong Dang, Joonhee Lee, Craig Breen, Jonathan S. Steckel, Seth Coe-Sullivan, and Arto Nurmikko. Red, green and blue lasing enabled by single-exciton gain in colloidal quantum dot films. *Nature Nanotechnology*, 7(5):335–339, apr 2012. ISSN 1748-3387. doi: 10.1038/nnano.2012.61. URL `http://www.ncbi.nlm.nih.gov/pubmed/22543426http://www.nature.com/doifinder/10.1038/nnano.2012.61`.

[12] Xuyong Yang, Dewei Zhao, Kheng Swee Leck, Swee Tiam Tan, Yu Xin Tang, Junliang Zhao, Hilmi Volkan Demir, and Xiao Wei Sun. Full visible range covering InP/ZnS nanocrystals with high photometric performance and their application to white quantum dot light-emitting diodes. *Advanced materials (Deerfield Beach, Fla.)*, 24(30):4180–5, aug 2012. ISSN 1521-4095. doi: 10.1002/adma.201104990. URL `http://www.ncbi.nlm.nih.gov/pubmed/22544765`.

[13] Evren Mutlugun, Pedro Ludwig Hernandez-Martinez, Cuneyt Eroglu, Yasemin Coskun, Talha Erdem, Vijay K Sharma, Emre Unal, Subhendu K Panda, Stephen G Hickey, Nikolai Gaponik, Alexander Eychmüller, and Hilmi Volkan Demir. Large-area (over 50 cm 50 cm) freestanding films of colloidal InP/ZnS quantum dots. *Nano letters*, 12(8):3986–93, aug 2012. ISSN 1530-6992. doi: 10.1021/nl301198k. URL `http://www.ncbi.nlm.nih.gov/pubmed/22783904`.

[14] Van Cao Nguyen, Hiroyuki Katsuki, Fumio Sasaki, and Hisao Yanagi. Optically pumped lasing in single crystals of organometal halide perovskites prepared by cast-capping method. *Applied Physics Letters*, 108(26):10–15, 2016. ISSN 00036951. doi: 10.1063/1.4954965. URL `http://dx.doi.org/10.1063/1.4954965`.

[15] Yue Wang, Xiaoming Li, Venkatram Nalla, Haibo Zeng, and Handong Sun. Solution-Processed Low Threshold Vertical Cavity Surface Emitting Lasers from All-Inorganic Perovskite Nanocrystals. *Advanced Functional Materials*, 201605088:1605088, 2017. ISSN 1616301X. doi: 10.1002/adfm.201605088. URL `http://doi.wiley.com/10.1002/adfm.201605088`.

List of Publications

Peer-reviewed archived papers

[1] **Luke Jonathan McLellan**, Benoit Guilhabert, Nicolas Laurand and Martin D. Dawson, *"CdS_xSe_{1-x}/ZnS semiconductor nanocrystal laser with sub $10kW/cm^2$ threshold and 40nJ emission output at 600 nm"*, Opt. Express 24, A146 (2016).

[2] Benoit Guilhabert, Caroline Foucher, **Luke Jonathan McLellan**, Anne-Marie Haughey, Y Gao, Johannes Herrnsdorf, Evren Mutlugun, Hilmi Volkan Demir, Nicolas Laurand and Martin D. Dawson, *"Advances in collodal quantum dot distributed feedback lasers hybridized on glass membranes"*, IEEE Photonics Conference 2014, 627-628.

[3] **Luke Jonathan McLellan** Benoit Guilhabert, Nicolas Laurand and Martin D. Dawson, *"Alloyed-core colloidal quantum dot DFB laser with encapsulated gain region"*, IEEE Photonics Conference 2015, 170-171.

Conferences

(Presenter highlighted by bold letters)

[4] **Luke Jonathan McLellan** Benoit Guilhabert, Nicolas Laurand and Martin D. Dawson, *"Alloyed-core CdSeS/ZnS colloidal quantum dots for solution-processed lasers"* (oral), Colloidal Quantum Dot and Nanocrystals Conference 2014.

[5] **Luke Jonathan McLellan** Benoit Guilhabert, Nicolas Laurand and Martin D. Dawson, *"Nanosecond-pumped bi-layered yellow colloidal quantum dot laser with enhanced photostability"* (poster), QD2016 2016.

[6] **Luke Jonathan McLellan** Benoit Guilhabert, Nicolas Laurand and Martin D. Dawson, *"CdS_xSe_{1-x}/ZnS CQD VCSELs"* (poster), Photon 12 2016.

Awards

Rank Bursary Travel Award, Photon 16.
Second Year Physics Poster Prize, University of Strathclyde, 2015.